Doctoral Dissertation
博士論文

Impacts of Cosmological and Stellar Magnetic Fields on Nucleosynthesis (and related Physical Processes)
(宇宙・恒星磁場が元素合成（および関連する物理過程）に及ぼす影響)

A Dissertation Submitted for the Degree of Doctor of Philosophy

July 2021
令和 3 年 7 月博士 (理学) 申請

Department of Astronomy, Graduate School of Science, The University of Tokyo
東京大学大学院理学系研究科天文学専攻

Yudong LUO
羅　煜東

Abstract

In this thesis, I mainly discuss the influence of magnetic fields on the nuclear astrophysics in both weak- and strong-strength cases. The transverse momentum components of $e^{\pm}$ inside the astrophysical plasma are quantized in magnetic field, results in a change of the thermodynamic condition of the plasma and further affect the weak interaction rates as well as the screening correction to the Coulomb potential of bare nuclei. On the other hand, nuclear weak reactions strongly depend on the background temperature and density of the reactant nuclei species, these are easily affected by the dynamical evolution of magnetic fields due to the induced energy fluctuations, results in a further change of the nucleosynthesis path.

Specifically, for the weak primordial magnetic field (PMF) in the early universe, its impacts on the Big Bang Nucleosynthesis (BBN) is investigated. In Chapter 2, I explore the screening effects arising from the relativistic magnetized plasma in the early universe, and correct the electron capture rates by including the screening potential. By taking into the influence on $e^{\pm}$ momentum phase space during BBN, the epoch at which the PMF was generated is constrained. The possibility of solving deuterium abundance underestimation problem from PMF is also discussed. Considering both screening corrections and Landau quantization effect to the weak interaction rates, a consistency between the predicted abundances and the latest observational constraints of deuterium and ^{4}He is found in the context of PMF.

Then, the impacts on the BBN from the presence of a stochastic PMF whose strength is spatially inhomogeneous distributed is investigated. A uniform total energy density and a Gaussian distribution of field strength is assumed. In this case, domains of different temperatures exist in the BBN epoch due to variations of the local PMF. I show that in such a case, the effective distribution function of particle velocities averaged over domains of different temperatures deviates from the Maxwell–Boltzmann distribution. This deviation is related to the scale-invariant strength of the PMF energy density ρ_{Bc} and the fluctuation parameter σ_B. BBN network calculations are performed by taking into account the PMF strength distribution. The inhomogeneous PMF strength reduces the ^{7}Be production and enhance

D production. I analyze the averaged thermonuclear reaction rates compared with those of a single temperature and find that the averaged charged-particle reaction rates are very different. Finally, the parameters ρ_{Bc} and σ_B are constrained from observed abundances of ^{4}He and D and find that the "cosmic Li problem" could be alleviated. More reliable conclusions could be obtained from a more realistic study on dynamical PMF evolution with BBN, therefore, I derive the cosmological relativistic MHD equations that could be applied to "two-fluid" approximation. The generation mechanism of inhomogeneous PMF from collisions among different phases of the plasma is also discussed extensively. I calculate a static multi-zone PMF model with BBN nuclear reaction network encoded, the results show that an inhomogeneous PMF generated from neutrino decoupling could reduce the ^{7}Li abundance dramatically without violating other elemental observations.

In Chapter 3, for the strong astrophysical magnetic field, the Coulomb screening and weak interactions in magnetized non-degenerate plasma are investigated. The characteristic plasma screening lengths at high temperatures and at high magnetic fields is explored. I estimated the screening potential as well as the changes in weak interaction rates at high fields. High fields could result in the increased β-decay rates as the electron and positron spectra are dominated by Landau levels. Finally, the effects studied here are evaluated in a simple *r*-process model. It is found that relativistic Coulomb screening has a small effect on the final abundance distribution. While the changes in weak interaction rates in strong magnetic fields can have an effect on the *r*-process evolution and abundance distribution, the field strength required to have a significant effect may be larger than what is currently thought to be typical of the *r*-process environment in collapsar jets or neutron star mergers. If *r*-process exists in fields $> 10^{14}$ G, effects from fields on weak decays would be significant.

The magnetized degenerate astrophysical plasma is also studied. A relativistic Hartree self-consistent field method is applied to calculate the screening potential. A profile from a 15 $M_\odot$ core collapsing SNe progenitor is applied in order to evaluate the electron capture rates of ^{54}Fe and ^{70}Zn. It is found that the screening potential at high field is enhanced when compared with the previous study. For the case that field is high enough and only the lowest Landau level is allowed, a two orders of magnitude reduction of the electron capture rates are found in high density region. Such deviations of the ^{54}Fe and ^{70}Zn electron capture rates are essential since these two isotopes determine the neutron richness of the progenitor model as well as the iron core mass, which are crucial for SNe explosion calculation. The reduction of electron capture rates under strongly magnetized degenerated plasma could also potentially deviate the neutrino absorption rate and the neutrino spectrum.

Acknowledgements

First of all, I would like to express my sincere thanks to my supervisor, Prof. Toshitaka Kajino for leading me to the exciting world of nuclear astrophysics and cosmology. During my five years in his group, I learned a lot on both science and daily life. His advice, continuous support, and patience are the most precious treasure in my whole life. Then, I am deeply grateful to Prof. Motohiko Kusakabe for all the generous help, fruitful discussions and collaborations, he never gets tired of my questions, from him, I learned the details determine success or failure. I would like to extend my grateful to Prof. Grant J. Mathews, Prof. A. Baha Balantekin, Prof. Michael Famiano and Dr. Suqing Hou for their suggestions and contributions to my research projects, I enjoyed discussions and collaborations with them very much. I also thank Prof. Myung-Ki Cheoun, Prof. Tomoyuki Maruyama, Prof. Satoshi Chiba, Prof. Toshio Suzuki and many other professors in COSNAP group for their excellent and inspired colloquiums, seminars and lectures, I acquired board cutting edge knowledge from them. I would like to extend my thank to Prof. Kazunori Kohri, his suggestions and comments on my research are very valuable. For Prof. Fumitaka Nakamura, I would like to thank his help and support when Prof. Kajino is absent in NAOJ.

I thank Dr. Chao Chen for the enlightening discussions on cosmology and black hole, we are good friends since the undergraduate days, the collaboration with him is always joyful and pleased. For the senior and junior members of the COSNAP group, Dr. Shota Shibagaki, Dr. Yutaka Hirai, Dr. Hirokazu Sasaki, Dr. Kanji Mori, Mr. Yuta Yamazaki, Mr. Xingqun Yao and Mr. Zhenyu He, I thank their warm encouragements and kind help for my life, I enjoyed studying and parties with them. I also thank all the members of the Division of Science in NAOJ for supporting me and their precious suggestions on my research and presentations, they always organize very excellent colloquiums, workshops and I had so many unforgettable memories during my five-year staying.

I would like to express my gratitude to Prof. Shisheng Zhang, Prof. Renxing Xu, Prof. Jianjun He, Prof. Jianrong Shi, Prof. Isao Tanihata, Prof. Hiroshi Watanabe, Prof. Alan Coc, Prof. Shigeru Kubono, Prof. Tohru Motobayashi, Prof. Satoru Terashima, Dr. Hongliang Yan, Dr. Nobuya Nishimura, Dr. Seiya Hayakawa and Dr. Ertao Li, their advises on my presentations are priceless, the discussion with them during conferences broaden my view about nuclear physics, astronomy and astrophysics. I thank Prof. Tomonori Totani, Prof. Yutaro Sekimoto, Prof. Hideyuki Umeda, Prof. Nozomu Tominaga and Prof. Hidetoshi Yamaguchi for their comments and suggestions on my thesis. I also would like to extend my gratitude to Dr. Xiaoting Fu, Dr. Zhiyu Zhang, Dr. Lizhi Xie, Dr. Jingjing Shi and Mr. Mingjie Jian for organizing the studying group of astronomical observations, they also always encourage me during the thesis writing time, I also learned how to enjoy science from them. I thank Dr. Hongfu Li and Dr. Guangxin Zhang, as seniors, they offered me many help on my studies and gave me precious suggestions about the future life as well. I also thank Ms. Shuyang Fu, she always show great hospitality and kindness when I visit Beihang University.

There are many friends I would like to thank, their supports also mean a lot to me. I thank Mr. Jianfei Cao for helping me and my family, he always cheers me up when I feel depressed. I thank Dr. Yibo Yang and Dr. Da Gao for the encouragements, I thank Mr. Zhennan Luo, Mr. Shumeng Zhang, Mr. Cancan Gong, Mr. Qing Liu and Mr. Sakuya, chilling with them is always fun. I thank Mr. Aiden Campbell, Mr. Ondrej Macek, Ms. Charlotte Kurz, Mr. Alexander Leibik, Dr. Giacomo Berton,

Mr. Theo Hudelist, Ms. Francesca, Ms. Erica Ruzza and Ms. Marlene, the days spent with them in Belfast and Innsbruck were so great.

I would like to offer my special thank to my girlfriend, Ms. Ruijing Yin who never gets angry for my childish behaviors and helps me for the daily life, without her tremendous understanding and encouragement in the past few years, it would be impossible for me to complete my study. Finally, I thank my mother and grandparents, who always give me strength to reach for the stars and chase my dreams, on their love and care from childhood, I could never be able to repay.

This thesis was supported by KAKENHI Grant No. 19J22167 from Japan Society for the Promotion of Science, I thank their financial support on my research and my daily expense.

Contents

List of Figures

List of Tables

List of Abbreviations

AGB	**A**symptotic **G**iant **B**ranch
BBN	**B**ig **B**ang **N**ucleosynthesis
CM	**C**enter **M**ass
CMB	**C**osmic **M**icrowave **B**ackgroud
EOS	**E**quation **O**f **S**tate
FRW	**F**riedmann-**R**obertson-**W**alker
GCE	**G**alactic **C**hemical **E**volution
GT	**G**amow-**T**eller
IGM	**I**nter**G**alactic **M**edium
IGMF	**I**nter**G**alactic **M**agnetic **F**ield
ISM	**I**nter**S**tellar **M**edium
LLL	**L**owest **L**andau **L**evel
LSS	**L**arge **S**cale **S**tructure
MB	**M**axwell-**B**oltzmann
MHD	**M**agneto**H**ydro**D**ynamics
NSE	**N**uclear **S**tatistical **E**quilibrium
NSM	**N**eutron **S**tar **M**erger
PMF	**P**rimordial **M**agnetic **F**ield
SNe	**S**uper**N**ova**e**
TF	**T**homas-**F**ermi

Chapter 1

Introduction

1.1 General Aspect

The modern nuclear astrophysics provides a powerful tool to seek for the origin of atomic elements in the cosmic and galactic evolution, and also serves as a probe of the fundamental laws and the principles in physics. The present nuclear astrophysics was first built on the pioneering paper published in 1957 by Margaret Burbidge, Geoffrey Burbidge, William A. Fowler, and Fred Hoyle (Burbidge et al., 1957). Since then, for more than a half century, many refined works have enriched nuclear astrophysics at such an impressive level as those seen at present day. This progress has been made by the synergy of rapid developments of interdisciplinary fields of science which include observational astronomy based on space and ground-based large telescopes, theoretical astronomy and astrophysics, experimental and theoretical nuclear and particle physics, and so on.

The cosmic chemical evolution started from the Big Bang nucleosynthesis in the first three minutes of the early universe (Fig. 1.1). The first generations of stars (Population III stars) formed from primordial gas, therefore they are considered to be very massive stars having relatively short lifetime. Nuclear and particle processes in stars generate nuclear energy that makes stars shine. Massive stars produce various nuclei during the evolutionary process of internal structure formation which consists of different layers with different chemical compositions of atomic elements and lose their mass as stellar winds. They finally culminate their evolution as supernova at the end of their life. The supernova ejecta and the released heat enrich the interstellar medium, and these stellar ashes thereby provide the source for the next generations of stars. The fundamental physical processes of nuclear and particle reactions underlie this cycle of cosmic and galactic evolution.

Fig. 1.1 illustrates how elements are cycling in the universe. The light elements are mainly produced in the *Big Bang Nucleosynthesis* (BBN), it provides the primordial material (i.e., mainly ^{1}H, ^{2}H, ^{4}He and ^{7}Li) for the formation of Pop III stars. Then nuclear and particle processes inside stars always go through the same path, therefore the synthesis of heavier elements (heavier than ^{7}Li but lighter than ^{56}Fe) today is considered to arise mainly from the life cycles of stars, but normal stellar evolution only produces nuclei with nuclear mass up to $A \sim 56$ because the iron has the largest binding energy. nuclei with nuclear mass $A > 56$ could not form via the stellar evolution. These heavy nuclei beyond iron peak are recognized to originate from the final stage evolution of the intermediate-mass *Asymptotic Giant Branch* (AGB) stars, i.e., the slow neutron capture process (*s*-process), and also from the explosions of massive stars, i.e., the rapid neutron capture process (*r*-process). Finally, the stars died with strong ejection of elements into the interstellar gas trigger the next production cycle of elements. It is remarkably successful to describe the

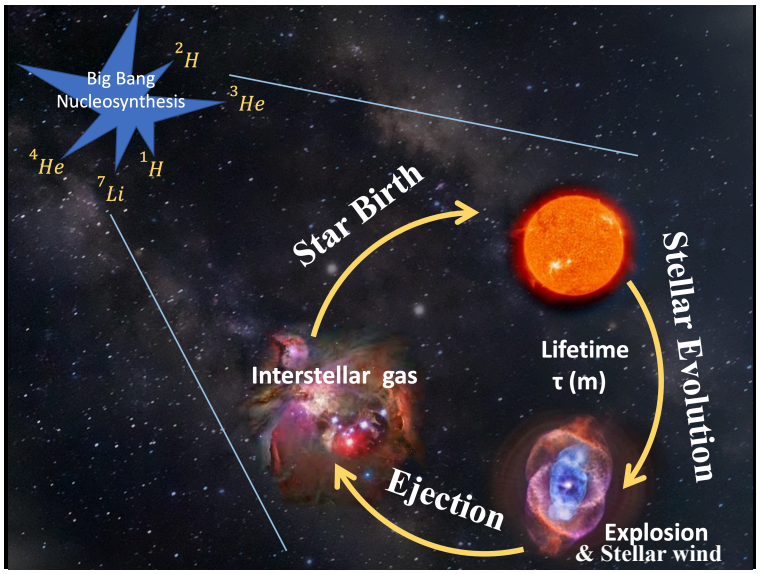

FIGURE 1.1: The cycle of elements in the universe, big bang nucleosynthesis provides the ingredient for the Pop III stars, then later, the old star evolved and ejected the material into interstellar gas to form the next generation stars and so on.

nuclear processes in several astrophysical phenomena such as the hot Big-Bang expansion of the early universe, stellar evolution and explosion of massive stars, which are based on our understanding of quantum mechanical properties of hundreds of atomic nuclei.

The astrophysical environments for nucleosynthesis are mostly the relativistic plasma which contains leptons, neutrinos, photons, and atomic nuclei. These species of elementary particles determine the thermodynamic conditions of the plasma (i.e., density, pressure, temperature), which are the key parameters for both astrophysical evolution and the nuclear reactions for nucleosynthesis studies. In most situations, the nuclei are in the non-relativistic state and could 'feel' the condition of the environment through the many body interactions. Therefore, the comprehensive study of the plasma could deepen the understanding of both nuclear physics and astrophysics. Moreover, magnetic field energy, along with nuclear energy and gravitational energy, are the three most representative and biggest energies in the universe. The magnetic fields widely exist in many astrophysical sites. In this thesis, I focus on the investigation of magnetized plasma in both the early universe and *supernovae* (SNe), try to make clear the impacts of the magnetic fields on the particle interactions which could affect strongly the nucleosynthesis. Specifically, I apply such studies to the two unsolved problems in astronomy and astrophysics: The first is the overproduction problem of primordial Big-Bang ^{7}Li abundance, and the second is the *r*-process nucleosynthesis in SNe. Our theoretical predictions of nuclear abundances in BBN and SNe r-process by taking account of magnetic fields effects will be compared with astronomical observations. This will in turn be able to constrain the magnetic field properties in these astrophysical plasma.

In the first part of this chapter, I briefly introduce the basic concepts of thermonuclear reaction and weak interaction. The interaction rates are strongly coupled with the properties of the environment. On the one hand, the dynamical evolution of magnetic field could trigger a turbulent plasma motion and further affects the thermonuclear reaction rates via the background energy fluctuations; on the other

hand, the electrons and positrons which are the main ingredients of weak interaction move differently in the magnetized plasma compared with field-free situation. In the second part of this chapter, the underlying physics of BBN and the *r*-process nucleosynthesis are explained, which are the two main nucleosynthetic sites that I will discuss in detail through the thesis.

1.2 Nuclear Electroweak Interactions

1.2.1 Thermonuclear Reactions Network

Consider a reaction which involves four species, i.e., $i + j \rightarrow k + l$, where both the projectile (i) and the target (j) are represented by particles with rest mass m_i and m_j (here the case that either of i or j is photon is not considered). The number of reactions per unit volume and time is given by $r = n_i n_j \sigma v$, or, more generally (Clayton, 1983; Fowler, Caughlan, and Zimmerman, 1967),

$$r_{i,j} = \int \sigma \mid \boldsymbol{v}_i - \boldsymbol{v}_j \mid \mathrm{d}n_i^3 \mathrm{d}n_j^3. \tag{1.1}$$

Like most fields of physics, nucleosynthesis requires both theoretical and experimental activities. Here σ is the cross section which is determined by the experiments (detailed discussion in Appendix A), the target number density is given by n_i and the projectile number density is given by n_j. $\mid v_i - v_j \mid$ is the relative velocity amplitude between target and projectile nuclei. It is reasonable to assume that the distribution of nucleus velocity (or kinetic energy) in an astrophysical plasma obey the *Maxwell-Boltzmann* (MB) distribution since the nucleus in general have the rest mass $\sim$ GeV, so they are non-relativistic in most cases. Applying the MB distribution, the reaction rates per unit volume of thermodynamical equilibrium state are given by (Fowler, Caughlan, and Zimmerman, 1967; Clayton, 1983)

$$\mathrm{d}n_i = n_i \Big(\frac{m_i}{2\pi kT}\Big)^{3/2} \exp\Big(-\frac{m_i v_i^2}{2kT}\Big) \mathrm{d}^3 v_i, \tag{1.2}$$

where T is the background temperature and k is the Boltzmann constant. Then the reaction rate per nuclei $\langle \sigma v \rangle$ over the velocity distribution is

$$\langle \sigma v \rangle_{i,j} = \Big(\frac{8}{m_{ij}\pi}\Big)^{1/2} (kT)^{-3/2} \int_0^\infty E\sigma(E) \exp\Big(-\frac{E}{kT}\Big) \mathrm{d}E, \tag{1.3}$$

where m_{ij} is the reduced mass of two nuclei, then the total reaction rate r_{ij} per volume time reads

$$r_{ij} = \frac{n_i n_j}{1 + \delta_{ij}} \langle \sigma v \rangle_{ij}. \tag{1.4}$$

Here, the factor δ_{ij} is used to account for double-counting when nuclei i and j are the same species. It is customary to use the concept of astrophysical S-factors by factoring out the approximate value of tunneling through the Coulomb barrier for reactions between charged nucleus. For a charged particle reaction involving two particles with charge Z_1 and Z_2, cross section $\sigma(E)$ strongly (exponentially) decreases as the relative kinetic energy E of the particles due to the increasing difficulty of the particles to tunnel through the Coulomb barrier, and the value is approximately given by $\exp(-2\pi\eta)$, which is called the Gamow factor. $\eta = Z_1 Z_2 e^2/v$ is the so-called Sommerfeld parameter, where v is the relative kinetic velocity of the particles.

On the other hand, as the energy E increases, the MB distribution function decreases exponentially, therefore, the integrand in Eq. 1.3 is peaked in an energy region which is often called by Gamow window. The peak energy in this window is the Gamow energy. The cross sections are proportional to $\pi\lambda^2 \propto 1/E$ multiplied by the Gamow factor. Therefore, the fusion cross sections could be factorized as

$$\sigma(E)_{\text{charged}} = \frac{\exp\left(-2\pi\eta\right)}{E} S(E) \tag{1.5}$$

where the factor $S(E)$ is the astrophysical S-factor and has a much smoother dependence with the *center mass* (CM) kinetic energy than $\sigma(E)$. Since S-factors are rather smooth at the low astrophysical energies, usually the expression of it is expanded around $E = 0$ (Bahcall, 1989), i.e.

$$S = S(0)\Big(1 + \frac{5kT}{36E_0}\Big) + E_0 \frac{dS(0)}{dE}\Big(1 + \frac{15kT}{36E_0}\Big) + ..., \tag{1.6}$$

here $E_0/kT = (\pi Z_1 Z_2 \alpha/\sqrt{2})^{2/3}(\mu/kT)^{1/3}$ is the Gamow energy and μ the reduced mass of two nuclei species with charges Z_1, Z_2 respectively. For neutron induced reactions, the transmission probability of a neutron through the nuclear potential surface is proportional to the inverse of the velocity v within the assumption of a sharp potential surface (Bertulani and Kajino, 2016). Hence, the cross section is usually expressed as

$$\sigma(E)_{\text{neutral}} = \frac{R(E)}{v}, \tag{1.7}$$

where $R(E)$ is also a smoother dependence on E.

The above formulas could be easily applied to the photon-induced reactions. Although Eq. 1.1 does not holds if one of the reactant is a photon, since the relative velocity is always the speed of light c, one can use time-reversal symmetry to relate the photodisintegration reaction cross section to a photon capture reaction. The reaction rate $r_{i\gamma} = \lambda_{i\gamma} n_i$ is given by (Iliadis, 2007)

$$r_{i\gamma} = \lambda_{i\gamma} n_i = n_i \frac{Z_k Z_l}{Z_i}\Big(\frac{m_k m_l}{m_i}\Big)^{3/2}\Big(\frac{m_u kT}{2\pi\hbar^2}\Big)^{3/2}\langle\sigma v\rangle_{kl} \exp\Big(-\frac{Q_{kl}}{kT}\Big), \tag{1.8}$$

where $\lambda_{i\gamma}$ is averaged over a Planck distribution of photons at temperature T, m_u is the atomic mass unit, i.e. $m_u = m_{^{12}\text{C}}/12$, $Q_{kl} = (m_k + m_l - m_i)c^2$. The average $\langle\sigma v\rangle_{kl}$ is now related to the inverse reaction rate for radiative capture. $Z(T) = \sum_i (2J_i + 1)\exp\left(-E_i/kT\right)$ are statistical weights, and m_i are the mass numbers of the participating nuclei. Here only the equations are provided, detailed derivation can be found in Appendix A. For non-resonant reactions induced by the weak interaction, such as $(p, e^+\nu)$, neutrino scattering or electron capture reaction, they are the smallest among all cross sections. Radiative capture reactions, such as (p,γ) or (α,γ) reaction, have also small cross sections because they involve the electromagnetic interaction.

For the reverse reaction, $k + l \rightarrow i + j$, the cross section could be derived from the reciprocity theorem (Born, 1949):

$$\frac{\sigma_{kl\rightarrow ij}}{\sigma_{ij\rightarrow kl}} = \frac{(2j_i + 1)(2j_j + 1)}{(2j_k + 1)(2j_l + 1)} \frac{m_{ij}E_{ij}}{m_{kl}E_{kl}} \frac{(1 + \delta_{kl})}{(1 + \delta_{ij})}, \tag{1.9}$$

where j is the particle spin, E_{ij} and E_{kl} are the CM kinetic energies for the forward

and reverse reactions. Since the kinetic energy E_{23} is related to the E_{ij} as $E_{kl} = E_{ij} + Q_{ij\to kl}$, the ratio of reaction rate for particle-induced reaction is

$$\frac{N_A\langle\sigma v\rangle_{kl\to ij}}{N_A\langle\sigma v\rangle_{ij\to kl}} = \frac{(2j_i+1)(2j_j+1)(1+\delta_{kl})}{(2j_k+1)(2j_l+1)(1+\delta_{ij})}\Big(\frac{m_{ij}}{m_{kl}}\Big)^{3/2} e^{-Q_{ij\to kl}/kT}. \tag{1.10}$$

As for a photon-induced reaction $\gamma + k \to i + j$, since photons have the spin of 2, the reverse cross section is given by (Kolb and Turner, 1990; Iliadis, 2007; Bertulani and Kajino, 2016)

$$\frac{\sigma_{\gamma k\to ij}}{\sigma_{ij\to\gamma k}} = \frac{(2j_i+1)(2j_j+1)}{2(2j_k+1)}\frac{2m_{ij}c^2E_{ij}}{E_\gamma^2}\frac{1}{(1+\delta_{ij})}, \tag{1.11}$$

then the ratio between forward and reverse reaction is

$$\frac{\lambda_\gamma(k)}{N_A\langle\sigma v\rangle_{ij\to\gamma k}} = \frac{\frac{8\pi}{h^3c^2}\int_0^\infty \frac{E_\gamma^2}{e^{E_\gamma/kT}-1}\frac{(2j_i+1)(2j_j+1)}{(2j_k+1)(1+\delta_{ij})}\frac{m_{ij}c^2E_{ij}}{E_\gamma^2}\sigma_{ij\to\gamma k}dE_\gamma}{(\frac{8}{\pi m_{ij}})^{1/2}\frac{N_A}{(kT)^{3/2}}\int_0^\infty E_{ij}\sigma_{ij\to\gamma k}e^{-E_{ij}/kT}dE_{ij}}, \tag{1.12}$$

where $\lambda_\gamma(k)$ is

$$\frac{8\pi}{h^3c^2}\int_0^\infty \frac{E_\gamma^2}{e^{E_\gamma/kT}-1}\sigma_{\gamma k\to ij}dE_\gamma. \tag{1.13}$$

Nucleosynthesis is a dynamical process since the realistic evolution of astrophysical sites always contains the time dependence of temperature, density and entropy. The time evolution of the number density n_i, is governed by the number of reactions creating or destroying i per volume and time: consider only reaction between two nuclei 0 and 1, i.e., $0 + 1 \to 2 + 3$, the rate of change of the abundance of nuclei 0 due to the reaction with nuclei 1 can be expressed as

$$\Big(\frac{dn_0}{dt}\Big)_1 = -\lambda_1(0)n_0 = -\frac{n_0}{\tau_1(0)}, \tag{1.14}$$

here $\tau = 1/\lambda$ is defined as the mean lifetime of a nuclear species. By using Eq. 1.4, Eq. 1.14 may also read

$$\Big(\frac{dn_0}{dt}\Big)_1 = -(1+\delta_{01})r_{01} = -(1+\delta_{01})\frac{n_0n_1\langle\sigma v\rangle_{01}}{1+\delta_{01}} = -n_0n_1\langle\sigma v\rangle_{01}(T) \tag{1.15}$$

here δ_{01} appears since for identical nuclei each reaction destroys two particles. In general, the sources of number density change are several nuclear processes, then the number density evolution of nuclei i is given by the differential equation (Kolb and Turner, 1990; Iliadis, 2007; Bertulani and Kajino, 2016)

$$\Big(\frac{\partial n_i}{\partial t}\Big)_\rho = \sum_j N_j^i r_j + \sum_{j,k} N_{j,k}^i r_{j,k} + \sum_{j,k,l} N_{j,k,l}^i r_{j,k,l}. \tag{1.16}$$

The physical meaning is that the time evolution of number density n_i, is governed by the number of reactions creating and destroying i per volume and per unit time. Here, the number change of nuclear species i via created or destroyed in the reaction $j + k + l + ... \longleftrightarrow i$ is defined as $N^i_{j,k,l,...}$. The N^is can be negative or positive numbers. The first term is due to the destruction or decay of the nuclear species $i \to j$ due to either photodisintegration, electron and positron capture or neutrino induced reactions ($r_j = \lambda_j n_j$). The second term is due to two-particle reactions (Eq. 1.4), and the

last term is due to three-particle reactions. Usually, number density of nuclei species i depends on volume, therefore, it is necessary to introduce the abundance of one species i to exclude changes due to volume expansion or contraction:

$$Y_i = \frac{n_i}{\rho N_A}, \tag{1.17}$$

where N_A is the Avogadro's number. For a nuclei with mass number A_i, $A_i Y_i$ denotes its mass fraction, so that $\sum A_i Y_i = 1$. Then Eq. 1.16 can be expressed in terms of Y_i (Bertulani and Kajino, 2016):

$$\begin{aligned}\dot{Y}_i = &\sum_j N^i_j \lambda_j(T) Y_j + \sum_{j,k} N^i_{j,k} \rho N_A \langle j,k \rangle (T) Y_j Y_k \\ &+ \sum_{j,k,l} N^i_{j,k,l} \rho^2 N_A^2 \langle j,k,l \rangle (T) Y_j Y_k Y_l.\end{aligned} \tag{1.18}$$

In the real calculation, we have to consider the evolution of all the nuclear species since the production of one reaction could become the reactant of another reaction. So one can set up a bunch of equations same as Eq. 1.18, such a system which include temperature, density and couple of non-linear differential equations is called nuclear reaction network. It is possible to solve it analytically (Esmailzadeh, Starkman, and Dimopoulos, 1991), but in most case, the numerical method is applied, some other methods are described in detail by Hix and Meyer (2006).

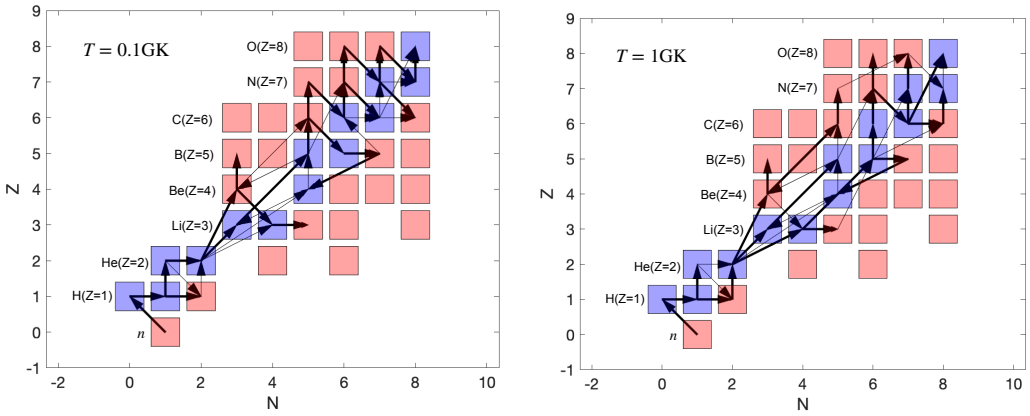

FIGURE 1.2: Abundance flow for the standard BBN calculation at different temperature. The left panel corresponds to $T = 0.1\ GK$ and the right one corresponds to $T = 1.0\ GK$. The blue boxes represent the stable nuclides while the red ones are the unstable nuclides. The thick arrow on both panels represents the strong flow while the thin arrow stands for the weak one.

Fig. 1.2 shows an example of the abundance flow based on the real nuclear reaction network of standard BBN. In this figure, the temperatures are set as 0.1 GK and 1 GK, respectively. Clearly under different temperature, the abundance flow goes through different path on the nuclides chart with different magnitude, this is because the reaction rates are functions of temperature and the number density of the reactant nuclei species. In the astrophysical magnetized plasma, these quantities could evolve along with magnetic field fluctuations, results in a further influence on the nuclear reaction network, so the study on the magnetized plasma properties could help to perform accurate nuclear network calculations and obtain the reliable theoretical elemental abundance yields.

1.2.2 Weak Interactions

Besides the thermonuclear reaction, another important process is the weak interaction: 1). in the early universe before the BBN starts, the neutrons and protons have equal number density because of the balanced weak interaction via $n \leftrightarrow p$. As temperature decreases, the weak interaction decoupled when its rate Γ equals to Hubble expansion rate, and the number density ratio between neutrons and protons at the decoupling epoch determines the final ^{4}He abundance of BBN. 2). During the stellar evolution, the nuclear burning could produce the radioactive nuclides, which further decay via weak interactions and form other nuclide. So the competition between weak interaction rate and the production rate is critical to determine the nucleosynthetic path in the burning stage. 3). At the end phase of the life of massive stars, the electron capture by the iron group nuclei in the core could reduce the pressure support, the emitted neutrinos via weak interactions also affect the energy budget of stars and thus modify the stellar evolution and explosion models. From the nucleosynthetic side, the weak interactions could reduce the electron fraction Y_e, which is important for the nucleosynthesis during the late burning stages in massive stars and during explosion (Langanke and Martinez-Pinedo, 2003; Heger et al., 2001; McLaughlin, Fuller, and Wilson, 1996).

The simplest weak interactions are the neutron-proton conversion:

$$p + e^- \longleftrightarrow n + \nu_e, \tag{1.19}$$

$$n + e^+ \longleftrightarrow p + \bar{\nu}_e, \tag{1.20}$$

$$n \longleftrightarrow p + e^- + \bar{\nu}_e. \tag{1.21}$$

The probability of an electron (or positron) carries a momentum value between $\boldsymbol{p}$ and $\boldsymbol{p} + d\boldsymbol{p}$ can be written in terms of $N(\boldsymbol{p})d\boldsymbol{p}$, the exact expression is given by the Fermi golden rule

$$d\lambda = N(\boldsymbol{p})d\boldsymbol{p} = 2\pi |\int \phi_f^* H \phi_i dV|^2 \frac{dn}{dE_0} = 2\pi |H_{fi}|^2 \frac{dn}{dE_0}, \tag{1.22}$$

the ϕ_i and ϕ_f are the initial and final wave function before and after the weak interaction, respectively. H is the Hamiltonian associated with the interaction, and dV is the unit volume. dn/dE_0 represents the density of final states in terms of energy. The interaction Hamiltonian is given by (Lee and Yang, 1957)

$$\frac{g_V}{\sqrt{2}}[\bar{u}_p \gamma_\mu (1 - \alpha\gamma_5) u_n][\bar{u}_e \gamma^\mu (1 - \gamma_5)\bar{v}_\nu] + h.c.; \tag{1.23}$$

where g_V is the vector coupling constant, $\bar{u}_p$, u_n, $\bar{u}_e$ and $\bar{v}_\nu$ are the proton, neutron, electron and neutrino operators, respectively. γs are the Dirac Matrices, $\alpha = g_A/g_V$ where g_A is the axial-vector coupling constant. $|H_{fi}|^2$ can be written in terms of the M matrix, where $|M|^2$ describe the transition probability:

$$|H_{fi}|^2 = \frac{g_V^2 (1 + 3\alpha^2)|M|^2}{V}, \tag{1.24}$$

Then the density of final states reads

$$dn = f_{FD}(E_e; T) f_{FD}(E_\nu; T) \frac{V d^3\boldsymbol{p}}{(2\pi\hbar)^3} \frac{V d^3\boldsymbol{q}}{(2\pi\hbar)^3}, \tag{1.25}$$

where $\boldsymbol{p}$ and $\boldsymbol{q}$ denote for the momentum of the final particles and f_{FD} is the Fermi-Dirac distribution. Consider the neutron decays: $n \rightarrow p + e^- + \bar{\nu}_e$, the energy conservation gives us $E_\nu + E_e = m_n - m_p = E_0 \equiv Q$, therefore, the momentum-space volume element $d^3\boldsymbol{p}$ becomes $4\pi p^2 dp$ and the neutrino momentum volume element $d^3\boldsymbol{q}$ becomes $(E_0 - E_e)^2 dE_\nu$. So the density of final state is

$$\frac{dn}{dQ} = \frac{(4\pi)^2 V^2}{(2\pi\hbar)^6} p^2 dp (Q - E_e)^2 \tag{1.26}$$

Then, combine it with Eq. 1.22, also include the Pauli exclusion principle, finally one can obtain

$$\lambda = \int d\lambda = \frac{g_V^2(1+3\alpha^2)}{2\pi^3\hbar^7 c^3} \int [1 - f_{FD}(E_e;T)][1 - f_{FD}(E_\nu;T)] p^2 (Q - E_e)^2 dp. \tag{1.27}$$

For other interactions in Eq. 1.19, basically the same manner can be followed, and the results were summarized as follows (Weinberg, 1972):

$$\lambda_{n+\nu_e \rightarrow p+e^-} = \frac{g_V^2 + 3g_A^2}{2\pi^3\hbar^7} \int v_e E_e^2 p_\nu^2 dp_\nu dp_\nu g(E_e;T_e) f_{FD}(E_\nu;T_\nu) \tag{1.28}$$

$$\lambda_{n+e^+ \rightarrow p+\bar{\nu}_e} = \frac{g_V^2 + 3g_A^2}{2\pi^3\hbar^7} \int E_\nu^2 p_e^2 dp_e f_{FD}(E_e;T_e) g(E_\nu;T_\nu) \tag{1.29}$$

$$\lambda_{n \rightarrow p+e^-+\bar{\nu}_e} = \frac{g_V^2 + 3g_A^2}{2\pi^3\hbar^7} \int v_e E_e^2 E_\nu^2 dp_\nu g(E_e;T_e) g(E_\nu;T_\nu) \tag{1.30}$$

$$\lambda_{p+e^- \rightarrow n+\nu_e} = \frac{g_V^2 + 3g_A^2}{2\pi^3\hbar^7} \int E_\nu^2 p_e^2 dp_e f_{FD}(E_e;T_e) g(E_\nu;T_\nu) \tag{1.31}$$

$$\lambda_{p+\bar{\nu}_e \rightarrow n+e^+} = \frac{g_V^2 + 3g_A^2}{2\pi^3\hbar^7} \int v_e E_e^2 p_\nu^2 dp_\nu g(E_e;T_e) f_{FD}(E_\nu;T_\nu) \tag{1.32}$$

$$\lambda_{p+e^-+\bar{\nu}_e \rightarrow n} = \frac{g_V^2 + 3g_A^2}{2\pi^3\hbar^7} \int v_e E_e^2 p_\nu^2 dp_\nu f_{FD}(E_e;T_e) f_{FD}(E_\nu;T_\nu) \tag{1.33}$$

where $g(E;T)$ is denoted as the Pauli blocking factor. The relations between E_e and E_ν are

$$E_e - E_\nu = Q \quad for\ p + e^- \longleftrightarrow n + \nu_e \tag{1.34}$$

$$E_\nu - E_e = Q \quad for\ n + e^+ \longleftrightarrow p + \bar{\nu}_e \tag{1.35}$$

$$E_\nu + E_e = Q \quad for\ n \longleftrightarrow p + e^- + \bar{\nu}_e. \tag{1.36}$$

Be ware that the integrals are taken over the positive values of p_e and p_ν. It is worthy to mention here $|M|^2$ has been omitted. For the simple neutron proton conversion, $|M|^2$ usually has the value between $1 \sim 3$, and all the integrals should be normalized to neutron decay lifetime time measurement.

The situation of weak interactions that involve nucleon is more complicated:

$$ {}^{A}_{Z}X_N \rightarrow {}^{A}_{Z+1}X'_{N-1} + e^- + \bar{\nu}_e \quad (\beta^- \; decay) \tag{1.37} $$
$$ {}^{A}_{Z}X_N \rightarrow {}^{A}_{Z-1}X'_{N+1} + e^+ + \nu_e \quad (\beta^+ \; decay) \tag{1.38} $$
$$ {}^{A}_{Z}X_N + e^- \rightarrow {}^{A}_{Z-1}X'_{N+1} + \nu_e \quad (e^- \; capture) \tag{1.39} $$
$$ {}^{A}_{Z}X_N + e^+ \rightarrow {}^{A}_{Z+1}X'_{N+1} + \bar{\nu}_e \quad (e^+ \; capture) \tag{1.40} $$
$$ {}^{A}_{Z}X_N + \nu_e \rightarrow {}^{A}_{Z+1}X'_{N-1} + e^- \quad (\nu \; capture) \tag{1.41} $$
$$ {}^{A}_{Z}X_N + \bar{\nu}_e \rightarrow {}^{A}_{Z-1}X'_{N+1} + e^+ \quad (\bar{\nu} \; capture) \tag{1.42} $$

In the $n \leftrightarrow p$ case, the matrix elements are simple because of the simple nuclear structure of protons and neutrons. In general, the matrix elements are independent from the lepton energies since the non-relativistic treatment of nucleons and the assumption of a constant lepton wave function over the nuclear volume. However, the β-decay rate in two different matrix elements with different strengths could contribute to the overall transition probability, such transition is called allowed transition. The allowed transition can be further divided into two components with each one has the different matrix element with different strength:

$$ |H_{if}|^2 = \frac{g_V^2 M_F^2 + g_A^2 M_{GT}^2}{V^2}, \tag{1.43} $$

here, M_F and M_{GT} correspond to the Fermi and Gamow-Teller matrix element, respectively. The allowed transitions can only occur if certain selection rules are satisfied for the nuclear spin (J_i, J_f) and parities (π_i, π_f) which i and f stand for the initial and final states. For the Fermi transition, it could occur when

$$ \Delta J = |J_i - J_f| = 0; \quad \pi_i = \pi_f \tag{1.44} $$

While the *Gamow Teller* (GT) transition only occur when

$$ \Delta J = |J_i - J_f| = 0 \; or \; 1 \;\; (J_i, J_f) \neq 0; \quad \pi_i = \pi_f. \tag{1.45} $$

The transition from $0 \rightarrow 0$ and $\pi_i = \pi_f$ corresponds to pure Fermi transition and $\Delta J = 1$ and $\pi_i = \pi_f$ corresponds to the pure GT transition, respectively. Moreover, for the heavier isotopes, the angular momentum and parity selection rules could prevent these transitions, therefore, it is necessary to consider the energy-dependent matrix elements, i.e., the forbidden transition. The forbidden transitions has lower probability compared to the allowed one, and its degree depends on the non-vanishing nuclear matrix element. Also, unlike the neutron and proton interactions, here the wave function of electron (positron) should have a distortion due to the Coulomb barrier of the nuclei. Therefore, there is an extra the correction factor called Fermi function $F(Z', p)$, which depends on the electron (positron) momentum and the charge of the daughter nuclei (Langanke and Martinez-Pinedo, 2003). For example, the β^- decay rate is given by:

$$ d\Gamma_{\beta^-} = \frac{g_V^2 M_F^2 + g_A^2 M_{GT}^2}{2\pi^3 \hbar^7 c^3} F(Z+1, p_e)[1 - f_{FD}(E_e; T)][1 - f_{FD}(E_\nu; T)] p_e^2 (Q - E_e) dp_e, \tag{1.46} $$

the approximate expression of $F(Z,\omega)$ is

$$F(Z,\omega) = 2(1+\gamma)(2pR)^{-2(1-\gamma)}\frac{|\Gamma(\gamma+iy)|^2}{|\Gamma(2\gamma+1)|^2}e^{\pi y} \tag{1.47}$$

where $\gamma = \sqrt{1-(\alpha Z)^2}$, $y = \alpha Z\omega/p$, α is the fine structure constant, and R is the nuclear radius. The nuclear weak interaction rates are summarized below

$$\Gamma_{\beta^-} = \frac{g_V^2 M_F^2 + g_A^2 M_{GT}^2}{2\pi^3\hbar^7c^3}\int p_e^2(Q-E_e)^2 dp_e F(Z+1,p_e)g(E_e;T)g(E_\nu;T), \tag{1.48}$$

$$\Gamma_{\beta^+} = \frac{g_V^2 M_F^2 + g_A^2 M_{GT}^2}{2\pi^3\hbar^7c^3}\int p_e^2(Q-E_e)^2 dp_e F(-Z+1,p_e)g(E_e;T)g(E_\nu;T), \tag{1.49}$$

$$\Gamma_{EC} = \frac{g_V^2 M_F^2 + g_A^2 M_{GT}^2}{2\pi^3\hbar^7c^3}\int p_e^2(Q+E_e)^2 dp_e F(Z,p_e)f_{FD}(E_e;T)g(E_\nu;T), \tag{1.50}$$

$$\Gamma_{PC} = \frac{g_V^2 M_F^2 + g_A^2 M_{GT}^2}{2\pi^3\hbar^7c^3}\int p_e^2(Q+E_e)^2 dp_e F(-Z,p_e)f_{FD}(E_e;T)g(E_\nu;T), \tag{1.51}$$

$$\Gamma_{\nu C} = \frac{g_V^2 M_F^2 + g_A^2 M_{GT}^2}{2\pi^3\hbar^7c^3}\int p_e(Q-E_\nu)p_\nu^2 dp_\nu F(Z+1,p_e)g(E_e;T)f_{FD}(E_\nu;T), \tag{1.52}$$

$$\Gamma_{\bar{\nu}C} = \frac{g_V^2 M_F^2 + g_A^2 M_{GT}^2}{2\pi^3\hbar^7c^3}\int p_e(Q-E_\nu)p_\nu^2 dp_\nu F(-Z+1,p_e)g(E_e;T)f_{FD}(E_\nu;T), \tag{1.53}$$

Finally, the calculation of the weak interactions rates reduces to the evaluation on the transition matrix elements. The study on the weak interactions in nuclear astrophysics started from almost 50 years ago (Mazurek, Truran, and Cameron, 1974; Yokoi, Neo, and Nomoto, 1979), after that, the detailed weak interaction rate calculations are performed by Fuller, Fowler, and Newman (1980), Fuller, Fowler, and Newman (1982a), Fuller, Fowler, and Newman (1982b), and Fuller, Fowler, and Newman (1985) (FFN papers), they calculated the interaction rate table for certain temperature and density grids, which becomes the key ingredients to study the stellar and explosive nucleosynthesis. Also, in FFN papers, the importance of the GT transition is explored: in the laboratory, the parent nuclei usually lie in the ground state, therefore the β^- transitions proceed to all energetically accessible states in the daughter nuclei, so that the decay time, i.e., the summation of all transition probabilities for all β^- branches is independent from the temperature and density. However, in the stars, due to the finite temperature, states corresponds to the GT resonances could be built on the ground, the first excited states in the inverse direction (i.e., electron capture) are thermally populated, which leads to transitions with large M_{GT} element and a increased phase space. These facts stimulate the later studies on the nuclear structure, i.e., the calculation of the GT transition between many nuclear states which finally contribute to the rates. The degree of freedom increase drastically with the number of nucleons, so many methods have been developed to calculate the interaction rate in different regions on the nuclides chart, for light nuclides ($A \leq 10$), the exact calculations by using nucleon-nucleon interaction or the effective-field theory could provide the reliable results (Carlson and Schiavilla, 1998); for heavier nuclides, the shell model is the main tool in general (Talmi and Barrett, 1994).

In conclusion, the calculations of weak interactions in the astrophysical sites, as discussed, should take into account the properties of the cosmological and(or) astrophysical cites such as temperature, density and the electron plasma impacts. The

strong magnetic field could deviated the motion of the electron due to the Landau quantization and further affect the momentum phase space. Such impacts on the electron plasma could change the weak interaction rate significantly but have not been studied in detail.

1.3 The First Few Minutes

The present-day method to probe the cosmology theory, including but not limited to the observations and analysis of SNe, large scale distribution of galaxies, cosmic microwave background radiation and the primordial elemental abundances. The most promising cosmological model is the (hot) Big-Bang theory, a prevailing cosmological model which is consistence with most of those observational facts so far. The evolution of the universe in hot Big-bang is based upon the *Friedmann-Robertson-Walker* (FRW) general relativistic cosmological theory, it is such a robust theory that is possible to make sensible speculations about the universe at time as early as 10^{-43} sec after the big bang, this theory could hold even for the fundamental interactions at energies approaching the Planck scale (10^{19} GeV). The present day standard model of particle physics, the SU(3)$\otimes$SU(2)$\otimes$U(1) gauge theory of the strong and electroweak interactions, can provide a fundamental theory of quarks and leptons and has been tested up to energies approaching 1 TeV. In addition, some interesting and important theoretical predictions have been made about particle physics at very short distances, e.g., grand unification (Georgi and Glashow, 1974), supersymmetry (Friedan, Qiu, and Shenker, 1984), superstring theory (Gervais and Sakita, 1971), etc. It is these theories of fundamental physics at extra-high energies which allow us to speculate about the earliest history of the universe, and the verification of these theory already be put on the scientific to-do list.

However, the earliest phases of the big bang are still subjects under arguments. The extrapolation backwards in time will yields an infinite density and temperature at a 0 time start point in the past (Hawking and Ellis, 1973). This singularity itself is the real 'Big Bang', the birth of the universe, however, general relativity theory is not a suitable description of the laws of physics for the singularity with infinite density and temperature. Therefore, the current model is based on the regime where general relativity can be extended. i.e time is beyond the end of the Planck epoch: $t > t_{Pl} = 10^{-43}$ sec. In the most common accepted models, our universe was filled homogeneously and isotropically with infinite energy density, temperatures and pressures in the beginning. Once it started to evolve, it was experience very rapidly expanding and cooling history. Approximately 10^{-34} sec after the expansion, a phase transition caused a cosmic inflation. In this period, the universe grew exponentially and such growing can solve the horizon problem effectively (Lyth and Riotto, 1999). After inflation, reheating occurred until the universe was cool enough for the production of a quark-gluon plasma as well as all other elementary particles at T$>$ 1 TeV (Wands, 2007). At this temperature, all the particles were at relativistic speeds with the random motions, therefore all kinds of the particle-antiparticle pairs were being continuously created and destroyed, i.e., they are indistinguishable between each other. At T$\sim$ 1 TeV, the conservation of baryon number can be violated by baryogenesis, this process led to a tiny excess of quarks and leptons over anti-quarks and anti-leptons of the order of one part in 30 million. After that, the baryon starts form, and in Table.1.1, the brief time-line of the history of the Universe in Big-Bang theory until present day is presented.

TABLE 1.1: The timeline of the Universe evolution in Big-Bang model. This table is taken from Baumann (2009)

Events	**Time**	**Energy**
Planck Epoch	$< 10^{-43}$ s	10^{18} GeV
Grand Unification	$\sim 10^{-36}$ s	10^{15} GeV
Inflation	$\gtrsim 10^{-34}$ s	$\lesssim 10^{15}$ GeV
Baryogenesis	$< 10^{-10}$ s	> 1 TeV
Electroweak Unification	10^{-10} s	1TeV
Quark-Hadron Phase Transition	10^{-4} s	100 MeV
Nucleon Freeze-Out	0.01 s	10MeV
Neutrino Decoupling	1 s	1 MeV
BBN	3 min	0.1 MeV
Recombination	10^5 yrs	0.1 eV
Dark Ages	$10^5 \sim 10^8$ yrs	
Galaxy Formation	$\sim 6 \times 10^8$ yrs	
Solar System	$\sim 8 \times 10^9$ yrs	
Albert Einstein born	1.38×10^{10} yrs	

After temperature decreases below 1MeV, the universe cooled down sufficiently to allow the formation of subatomic particles after the initial exponential expansion, this epoch is called the BBN or primordial nucleosynthesis, which is the key process to form the component of normal matter. The main productions are the isotopes of light nuclei: ^{1}H, ^{2}H (D), ^{3}H, ^{3}He, ^{4}He and mass number $A = 7$ nuclei (including both ^{7}Be and ^{7}Li). The epoch of this process is believed to have occurred from roughly 10 seconds to 20 minutes after the Big Bang (Mathews, Kusakabe, and Kajino, 2017; Cyburt et al., 2016; Steigman, 2007; Fields and Olive, 2006). It is one of the most important epoch in cosmological history since the way to cook light elements is quite simple but not trivial: a network calculation of nuclear reactions among primordial elements in a space-time characterized by general relativity, the micro-physics is characterized by particle interactions which are described within the standard model of particle physics (Bertulani and Kajino, 2016). As one of the most strongest evidences to support the hot Big-Bang theory, BBN can predict the production of light nuclei isotopes including ^{1}H during the early universe. Therefore the observation of light elemental abundance, combine with the theoretical calculation, is a good probe to testify the present-day physics theory.

The modern concept of cosmological evolution developed along tandem tracks of both theory and observation. Of course, the most important milestone was in 1916 when Albert Einstein published his theory of general relativity, it provided us with a unified theory of gravity as a geometric property of space-time (Einstein, 1948):

$$G_{\mu\nu} = \frac{8\pi G}{c^4} T_{\mu\nu} \tag{1.54}$$

here, $G_{\mu\nu}$ represents the Einstein Tensor $G_{\mu\nu} = R_{\mu\nu} - 1/2 g_{\mu\nu} R$, $g_{\mu\nu}$ is the metric tensor, $T_{\mu\nu}$ is the energy-momentum tensor. In general, the left hand side of Eq. 1.54 describes the curvature of the space-time with $G_{\mu\nu} \propto R^{-2}$ which can be affected by the energy or momentum of the matter. However, for the low mass, the Newtonian

mechanics is a quite good approximation, therefore, naturally, for the cosmic scale, general relativity should take control.

After Einstein proposing his gravity, the following progress in cosmology is the cosmological solution of general relativity which was established by Alexander Friedmann in 1922 (Friedmann, 1922). His equations (Friedmann equations) describe the universe in Friedmann-Lemaître-Robertson-Walker (FLRW) metric and a perfect fluid with a given energy density ρ and pressure p. The FLRW metric describes a homogeneous, isotropic and keep expanding (or contracting, depends on models) universe. The Friedmann equations, together with the FLRW metric, are also called FRW cosmology. There is one assumption in FRM cosmology which is known as cosmological principle: the Universe is globally homogeneous and isotropic with no preferred point, i.e. each point is geometrically equivalent and the space is spherically symmetric around any point (Kolb and Turner, 1990; Liddle and Lyth, 2000; Peacock, 1999). Within this principle and consider the flat universe, the Friedmann equations are

$$H^2 \equiv \left(\frac{\dot{a}}{a}\right)^2 = \frac{8\pi G\rho}{3}; \tag{1.55}$$

$$\frac{\ddot{a}}{a} = -\frac{4\pi G}{3}\Big(\rho + 3p\Big). \tag{1.56}$$

Here, H is the Hubble parameter, $a(t)$ is the scaler factor, G is the gravitational constant (hereafter in this thesis, natural units are used, i.e. $\hbar = c = 1$). These two are the equations describe the dynamical evolution of the universe. The number density n, energy density ρ and entropy density s, they obey the following relation (detailed derivation see Appendix C):

$$n = \frac{\xi(3)}{\pi^2} g' T^3 \ (Boson); \quad \frac{3\xi(3)}{4\pi^2} g' T^3 \ (Fermion) \tag{1.57}$$

$$\rho = \frac{\pi^2}{30} g T^4 \ (Boson); \quad \frac{7\pi^2}{240} g T^4 \ (Fermion) \tag{1.58}$$

$$\tag{1.59}$$

$$s = \frac{p+\rho}{T} \ (For\ both\ fermion\ and\ boson), \tag{1.60}$$

where $\xi(3)$ is the Riemman Zeta function, factors g' and g are corresponds to the degrees of freedom for bosons b and fermions f:

$$g'(T) = g_b(T) + \frac{3}{4} g_f(T); \tag{1.61}$$

$$g(T) = g_b(T) + \frac{7}{8} g_f(T). \tag{1.62}$$

The factors $3/4$ and $7/8$ are due to the different fermionic and bosonic energy distributions in the integrals used to obtain n, ρ and s. In cosmology, it is also generally assumed that a conservation of the co-moving entropy holds (Weinberg, 2008),

$$\frac{d(sa^3)}{dt} = 0 \Longrightarrow s \propto \frac{1}{a^3} \Longrightarrow T \propto \frac{1}{a}. \tag{1.63}$$

As discussed in Sect. 1.2, the nuclear reaction network depends on the evolution of the environment (Temperature and number density of the nuclei). From Eq. 1.63, temperature drops during the expansion, the expansion mechanism of the universe

itself is described by Eq. 1.55 and Eq. 1.56. Eq. 1.57 to Eq. 1.60 ensure the conservation law during the evolution. For the number density of the nuclei in the early universe, it is given by the important parameter baryon-to-photon ratio $\eta := n_B/n_\gamma$ which can be inferred from the observed anisotropy of the CMB power spectrum (Planck Collaboration et al., 2016a; Hinshaw et al., 2013). Then by including Eq. 1.18, one could obtain the general picture of the BBN.

The origin idea of the BBN is proposed more than hundred years ago by the famous "Alpha-Bethe-Gamow" paper, in that paper, the universe starts from a hot and dense environment, all the elements exist today were formed during the early time, then the universe expanded and cooled down until present day (Alpher, Bethe, and Gamow, 1948). Although the main site for the formation of elements was proved to be stellar evolution, such shallow model still predicted the light element production, the relic of radiation background blackbody spectrum and the few Kelvin cosmic temperature. Then after the discovery of CMB radiation, such big-bang theory becomes the prime universe model, based on it, the modern BBN theory was developed.

The initial condition of BBN is when $t \sim 0.01$s and $T \sim 10$MeV, at that time the thermal energies were $kT \sim 10\text{MeV} \gg 2m_ec^2$. Before this epoch, the main components of the relativistic cosmological plasma are γ (photons), $e^\pm$, three neutrino families and baryons. Photons are massless so they kept coupled in the cosmological plasma until redshift $T \sim 3500$K when electrons captured by protons to form the Hydrogen atoms. The neutrinos and electrons are in equilibrium via the weak interactions $\nu\bar{\nu} \leftrightarrow e^\pm$ and $\nu e \leftrightarrow \nu e$. The non-relativistic nuclei are in the *nuclear statistical equilibrium* (NSE), i.e., the production rate of a nuclear species $A(Z)$ larger than the expansion rate, so that only existing baryons were neutrons n and protons p. It is also noticed that $n_n = n_p$ because the balance between neutrons and protons is preserved by the weak interactions, i.e., electrons, positrons and neutrinos were in chemical equilibrium by means of charged- and neutral-current interactions:

$$p + e^- \longleftrightarrow n + \nu_e, \tag{1.64}$$

$$n + e^+ \longleftrightarrow p + \bar{\nu}_e, \tag{1.65}$$

$$n \longleftrightarrow p + e^- + \bar{\nu}_e. \tag{1.66}$$

One of the important concept is decoupling: If the interaction rate Γ is smaller than the Hubble expansion rate H, then the reactant cannot meet each other in the universe, therefore the equal rate epoch (i.e., the time when reaction rate $\Gamma = H$) is defined as the decoupling time. For the interactions between neutrinos and electrons (positrons), The decoupling epoch is given by

$$\frac{\Gamma_{int}}{H} = \frac{G_F^2 T^5}{T^2/m_{pl}} \sim \left(\frac{T}{1\text{MeV}}\right)^3, \tag{1.67}$$

so right at the starting point of BBN: $t \sim 0.01$ s, neutrino family decoupled from the relativistic plasma. For proton and neutron, the NSE ensure that

$$\mu_n + \mu_\nu = \mu_p + \mu_e, \tag{1.68}$$

then according to the Boltzmann-Gibbs statistics, the neutron-to-proton ratio should be (Bertulani and Kajino, 2016)

$$\frac{n}{p} := \frac{n_n}{n_p} = \frac{e^{-(m_n+\mu_n)/kT}}{e^{-(m_p+\mu_p)/kT}} = e^{-Q/kT+(\mu_e-\mu_\nu)} \tag{1.69}$$

where $Q = \Delta m = m_n - m_p = 1.294\text{MeV}$, due to the presumption of charge neutrality of the universe, one can infer that $\mu_e/kT \sim n_e/n_\gamma \sim \eta \sim 10^{-10}$, moreover, electron chemical potential of the early universe is as the same order as magnitude with μ_ν, therefore, the second term of Eq. 1.69 can be ignored, which provide us with $n/p = \exp[-Q/kT]$. Similar to the neutrino decoupling, the weak interaction decoupling epoch can be calculated from the weak interaction rate that discussed in Sect. 1.2.2. $\Gamma_{n\leftrightarrow p} \sim G_F^2 T^5$, however, since neutrinos have already decoupled, then the Hubble expansion rate is given by $5.5T^2/m_{pl}$, so we have

$$\frac{\Gamma_{n\leftrightarrow p}}{H} = \left(\frac{T}{0.8\text{MeV}}\right)^3, \tag{1.70}$$

and from Eq. 1.69, we can calculate that the neutron to proton ratio at the weak interaction decoupling epoch is

$$\frac{n}{p} := e^{-Q/kT} \sim \frac{1}{6}. \tag{1.71}$$

This value is essential to BBN since it determines the 'freeze out' neutron and proton number ratio, and such ratio decides the later on ^{4}He abundance because almost all the neutrons in the early universe are ingredient of ^{4}He. It is also worthy to mention that shortly after the weak interaction decoupling, electrons and positrons start to annihilate (at $T \backsimeq m_e/3 = 0.27\,\text{MeV}$), and for some reasons, our universe kept excess number of the electron. Since neutrinos were free particles (i.e., no interactions), $e^\pm$ annihilation can only transfer their entropy to the photons and hence heated up temperature of photons (i.e. background radiation temperature) relative to that of the neutrinos by a factor of $(11/4)^{1/3}$ (Weinberg, 2008). After the annihilation, the degree of freedom g_* has decreased to its value today, 3.36.

After the freeze out of neutrons and protons, the n/p ratio does not remain as a constant since the neutron β-decay will continuously decrease the number of neutrons in a timescale of about 10 minutes. This process will finally drive the n/p ratio to 1/7 (Steigman, 2007). However the thermal energies were still too high so that the nuclei reaction cannot occur until temperature drops to 300keV ($t = 100s$). The first nuclei, deuterium (d) was also formed during this epoch via radiative capture reaction:

$$n + p \longleftrightarrow \text{d} + \gamma. \tag{1.72}$$

Deuteron is the lightest two-nucleon system, which has only one bound-state with binding energy of 2.24 MeV. The ratio of $n + p$ pairs to the d number density is also determined by Boltzmann-Gibbs statistics

$$\frac{N_{n+p\to d+\gamma}}{N_{d+\gamma}} = \frac{n_d n_\gamma \exp[-\Delta m/kT]}{n_p n_n}, \tag{1.73}$$

this reaction is very fast since it is electromagnetic interaction, therefore, one can assume it is in equilibrium during the early universe so that half of the neutron will be in the deuteron, i.e., $n_d \sim n_n$, so that $n_p/n_\gamma \sim \eta$ and $\exp[-\Delta m/kT] \sim \eta \sim 10^{-9}$,

from which one can obtain the temperature for deuterium formation is $T_{deuteron} \sim 1.25 \times 10^9$ K with $t_d \sim 100$ s. It is also need to mention that the start point of this reaction is at $T \sim 0.1$ MeV rather than 2.24 MeV which is the binding energy of deuteron. This is because that the plasma of the early Universe is dilute (η value is small). The cross section of Eq. 1.72 at the BBN energies $0.02 < E < 0.2$ MeV, is not well known experimentally, however, it is possible to determined by detailed balance from its inverse reaction $\gamma + d \rightarrow p + n$ (Salpeter, 1951; Bethe and Longmire, 1950; Schiff, 1950; Marshall and Guth, 1950; Blatt and Jackson, 1949; Bethe, 1949).

Once d is formed, the other nuclear reactions proceed quickly:

$$d(n,\gamma)^3\mathrm{H},\ \ d(d,p)^3\mathrm{H},\ \ d(p,\gamma)^3\mathrm{He},\ \ d(d,n)^3\mathrm{He},\ \ ^3\mathrm{He}(n,p)^3\mathrm{H} \tag{1.74}$$

The $d(n,\gamma)^3$H cannot contribute a lot to the ^{3}H production since at $E_n = 30.5$ keV, the cross section for this reaction is 2.23 ± 0.34 μb (Nagai et al., 2006), for an electromagnetic process, this is very small as expected. The $d(d,p)^3$H reaction has been extensively measured experimentally with a latest measurement of the S-factor of $S(0) = 55.3$ keV·b within a 5% error (Tumino et al., 2014). The reaction $d(p,\gamma)^3$He has been studied both experimentally and theoretically (Kievsky et al., 2008; Casella et al., 2002; Marcucci et al., 2005; Viviani et al., 2000; Ma et al., 1997). The most common used S-factor at $E = 10$ keV is $S = 0.286$ keV·b (Marcucci et al., 2005). The S-factor of $d(d,n)^3$He from the recent measurement reports is $S(0) = 58.6$ keV·b within a 5% error (Tumino et al., 2014). Cross section for the reaction $^3\mathrm{He}(n,p)^3\mathrm{H}$ have been measured and fits by using R-matrix (Brune et al., 1999). Recent study (Adahchour and Descouvemont, 2003) suggests that the cross section of this reaction near the threshold is affected by a 0^+ s-wave resonance in ^{4}He strongly. Therefore, a deviation of the cross section from the typical $1/v$ law for neutron induced reactions will occur. However, $R(E)$ in Eq. 1.7 is relatively constant at the low energy region, the value of $(\sigma E^{1/2})_{E=0} = 0.7$ MeV$^{1/2}$·b.

The main production of the BBN is the ^{4}He, which cannot be formed until temperatures cool down to ~ 100 keV, ^{4}He produced via

$$^3\mathrm{H}(p,\gamma)^4\mathrm{He},\ \ ^3\mathrm{H}(d,n)^4\mathrm{He},\ \ ^3\mathrm{He}(n,\gamma)^4\mathrm{He},\ \ ^3\mathrm{He}(d,p)^4\mathrm{He},\ \ ^3\mathrm{He}(^3\mathrm{He},2p)^4\mathrm{He} \tag{1.75}$$

Shortly before the temperature approaches to $T = 0.3$ MeV, ^{4}He falls below the equilibrium state, this is due to the reaction rates of those reactions are not fast enough to sustain the equilibrium amount of ^{4}He. The reaction rates proportional to $n_A\langle\sigma v\rangle$, for the reactions in Eq. 1.75, the abundance of D, ^{3}H and ^{3}He are exceed their equilibrium abundance but still too dilute to maintain that of ^{4}He. On the other hand, Coulomb barrier reduction is significant (Kolb and Turner, 1990):

$$\langle\sigma v\rangle \propto \exp\Big[-2\frac{A_1A_2}{A_1+A_2}(Z_1Z_2)^{2/3}T^{-1/3}\Big], \tag{1.76}$$

hence after $T \sim 100$ keV, the reactions in Eq. 1.75 can produce the sufficient ^{4}He. Then assume that all neutrons finally wind up in ^{4}He, then the mass fraction of ^{4}He, i.e. Y_p, can be estimate as

$$Y_p \sim \frac{4(n_n/2)}{n_n+n_p} = \frac{2(n/p)}{1+(n/p)}, \tag{1.77}$$

plug in the $n/p \sim 1/7$, $Y_p \sim 0.25$ can be obtained.

Beside ^{3}He and ^{4}He, there are also tiny amounts of ^{7}Li and ^{7}Be will be produced via

$$^4\text{He}(^3\text{H},\gamma)^7\text{Li}, \quad ^4\text{He}(^3\text{He},\gamma)^7\text{Be}. \tag{1.78}$$

The S-factor of ^{7}Li produced reaction is $S(0) = 0.107$ keV·b (Brune, Kavanagh, and Rolfs, 1994). The cross section of ^{7}Be production reaction are very scattered at the measured energies, only an estimated value of $S(0) = 0.4$ keV·b at $E_{CM} = 50$ keV can be obtained. The final step of BBN is ^{7}Be(n,p)^{7}Li, that is when BBN should stop as the universe expands, cools down, and it becomes increasingly more difficult for the nuclear fusion reactions to proceed. At about redshift $z \sim 3 \times 10^4$, the cosmological recombination of ^{7}Be^{4+} ions occurs, then ^{7}Be nucleus instantaneously captures the orbital electron with the half-life $t_{1/2} = 106$ d, and is converted to 7Li: ^{7}Be(e^-,ν_e)^{7}Li. In conclusion, only extremely small amounts of elements heavier than Li isotopes are formed compared to those produced in stars during the later evolution of the universe.

All the light elemental abundances are strongly depend on the baryon-to-photon ratio η: once increase value of η, then a higher BBN temperature T_{BBN} is obtained and also a larger n/p ratio (Steigman, 2007). Thus, larger η yields larger ^{4}He abundance. D and ^{3}He can be treat as 'catalysts' since once they are produced, immediately are consumed, so they are keeping the equilibrium value which depends on the rate of their production and destruction. For ^{7}Li, it can be created and destroyed by

$$^4\text{He}(^3\text{H},\gamma)^7\text{Li}; \quad ^7\text{Li}(p,\gamma)^4\text{He}, \tag{1.79}$$

The ^{7}Li destruction reaction has a larger Coulomb barrier compare with production, therefore, for a lower η value, it will enhance the creation of ^{7}Li than destruction. On the other hand, for larger η, ^{7}Li production changes because more ^{3}He is produced, the reaction ^{4}He(^{3}He,γ)^{7}Be also becomes more important due to the Coulomb barrier at high temperature. There are also very few neutrons around to deplete ^{7}Be by ^{7}Be(n,α)α reactions. Therefore, ^{7}Li produced via the decay of ^{7}Be is also occurring at high T and large η.

Finally, in Fig. 1.3, light elemental abundances as functions of temperature $T_9 := T/10^9$ K is presented. Here, a BBN nuclear reaction network code based on Refs. (Kawano, 1992; Smith, Kawano, and Malaney, 1993) is used and I have updated the reaction rates of nuclei with mass numbers $A \leq 10$ using the JINA REACLIB Database (Descouvemont et al., 2004; Cyburt et al., 2010; Coc et al., 2015). The neutron lifetime is 880.2 ± 1.0 s, corresponds to the central value of the Particle Data Group (Patrignani, 2016). The baryon-to-photon ratio η is taken to be $\eta_{10} \equiv \eta/10^{-10} = (6.16 \pm 0.02)$ corresponding to the baryon density $\Omega_b h^2 = 0.0224 \pm 0.0001$ in the standard ΛCDM model determined from Planck analysis of Ref. (Aghanim, 2020). The effect of the conversion of primordial ^{7}Be to ^{7}Li via the electron capture decay is also taken into account in the current calculation. Once the cosmological recombination of ^{7}Be^{4+} ions occurs at $z \sim 3 \times 10^4$, the ^{7}Be nucleus instantaneously captures the orbital electron with the half-life $T_{1/2} = 106$ d, and is converted to ^{7}Li (Khatri and Sunyaev, 2011). In conclusion, the light elemental synthesis in the early universe is well described by the standard model of BBN. There are mainly three parameters: the effective neutrino number, N_ν; the neutron lifetime τ_n; and the baryon to photon ratio (the baryonic density) of the Universe, η. All these three parameters have been fairly well determined from experiments (Patrignani, 2016; Descouvemont et al., 2004; Coc et al., 2015) and the analysis of cosmic microwave background (CMB) power spectrum analysis (Bennett, 2013; Planck Collaboration et al., 2016a). The recent progress on the nuclear physics also push the theoretical calculations of

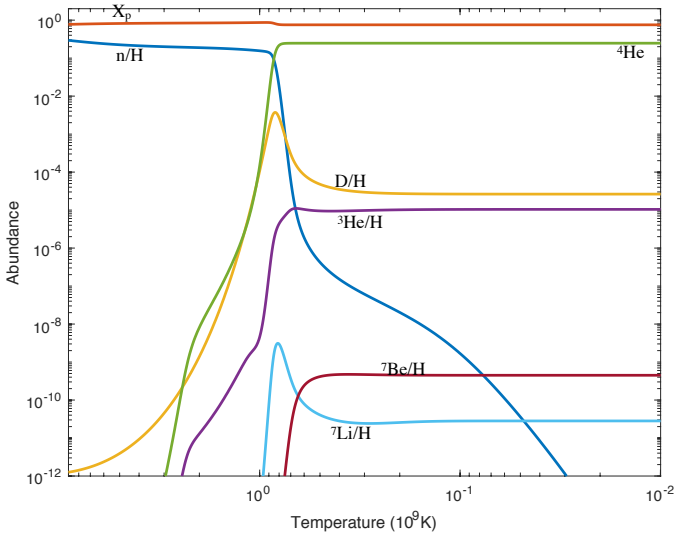

FIGURE 1.3: Time evolution of primordial elemental abundances. After weak interaction decoupling, the neutrons decay to protons so that n/H keep decrease. At around $T_9 = 1$, the deuteron starts forming, and shortly after deuteronformation, ^{3}He, ^{4}He, ^{7}Li and ^{7}Be are rapidly produced, finally, temperature drop down to the nuclear reaction needed, and almost all the neutron turn into ^{4}He at $T_9 \sim 10^{-1}$.

light element abundances in the standard BBN to an accuracy of 1% (Cyburt et al., 2016; Mathews, Kusakabe, and Kajino, 2017).

Moreover, the observational data of primordial light elements have also been improved for several decades, ^{4}He could be produced in stars, so the constraints on the primordial ^{4}He abundance come from observations of metal-poor extragalactic HII regions. The observed emission lines are extrapolated to the zero metallicity, the recent observation of the additional atomic infrared line even further improve the accuracy (Izotov, Thuan, and Guseva, 2014; Aver, Olive, and Skillman, 2015). The D is a fragile isotope since the binding energy is only 2.224MeV, and it can only be destroyed in the stellar evolution. The primordial D abundance is constrained with observations of high-redshift Lyman-α absorption systems towards quasars. Although the observed data show a significant scatter in the past (Pettini and Cooke, 2012), the recent re-analysis and cross check with the cosmic merger tree model of structure formation has shown a plateau for redshift $z > 2$, and such value can be treated as the primordial abundance. The ^{3}He abundances in Galactic HII regions are determined using the 8.665 GHz hyperfine transition of ^{3}He$^+$ ion. The ^{3}He abundance can change via the *Galactic chemical evolution* (GCE) although the net effect of GCE is not constrained sufficiently since stars can both destroy and synthesize ^{3}He. But it is worth to stress here that the^{3}He abundance is not expected has decreased significantly over galactic history as this would require that a large fraction of Galactic baryonic material have participated in star formations and experienced ^{3}He destruction, while the present interstellar deuterium abundance limits the amount of astration to not more than about a factor of two.

For ^{7}Li, since it can also be produced from the cosmic ray spallation, the stellar evolution and novae explosion, it is difficult to track the real "primordial" abundance of ^{7}Li. The present results are obtained from the Pop II metal-poor stars whose surface has temperature $5700 < T_{eff} < 6800$ K so that Li on surface is not depleted effectively (Fu et al., 2018). The ^{7}Li abundances observed from these stars form a so

called "Spite plateau", i.e., A(^{7}Li)=2.23 dex [1] (Sbordone, 2010).

The comparison between the standard BBN predictions and the observed elemental abundances is in Fig. 1.4, the predicted abundances (solid line in each panel) depends on the baryon-to-photon ratio η ($\eta_{10} = \eta \times 10^{10}$) which constrained from CMB anisotropy analysis from Aghanim (2020) (vertical blue band). The observed element abundances are shown in horizontal green band for each panel: (1)Y_p (mass fraction of ^{4}He) : $0.2409 - 0.2489$ (Aver, Olive, and Skillman, 2010); (2)D/H: $2.50 - 2.55 \times 10^{-5}$, or $2.40 - 2.88 \times 10^{-5}$ from 1σ and 2σ of Cooke, Pettini, and Steidel (2018), separately; (3)^{3}He/H: $0.9 - 1.3 \times 10^{-5}$ (Bania, Rood, and Balser, 2002);(4)^{7}Li/H: $1.27 - 1.89 \times 10^{-10}$ (1σ from Sbordone, 2010), or $1.06 - 2.35 \times 10^{-10}$ (2σ from Sbordone, 2010). From the figure, there is excellent agreement between BBN and the observed primordial abundances of D, ^{3}He and ^{4}He for the observed η value from CMB spectrum. However the theoretical prediction (Li/H$= 5.1 \times 10^{-10}$) is larger than the observed Spite Plateau (Spite and Spite, 1982; Sbordone, 2010) by about a factor of 3, which is the long lasting "cosmic Li Problem".

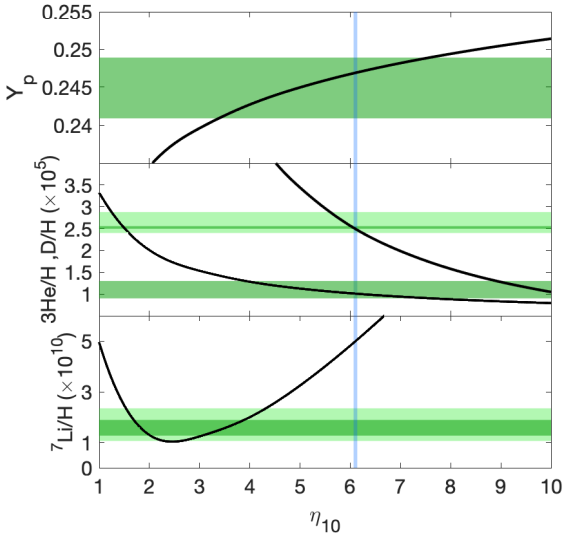

FIGURE 1.4: The primordial element abundance as a function of η_{10}. Observation value of η_{10} is painted as vertical blue band: $\eta_{10} = (6.16 \pm 0.02)$. Horizontal green band shows the observational results of Y_p, D/H and ^{7}Li/H. If the observation is trustful and the standard BBN theory is correct, for each element, the curve should go through the concordance region of both green and blue for each element. Obviously Y_p, ^{3}He/H and D/H satisfy such condition while ^{7}Li/H is over predicted in standard BBN model.

In order to solve this puzzle, many studies have been working on modifying the standard BBN model and(or) including the ^{7}Li depletion mechanism in the stellar evolution. The recent accurate nuclear experiments also indicate low chance to solve it from nuclear physics side. The current status of "cosmic Li problem" are discussed in Chapter 2. However, it is necessary to stress here few recent works (Hou et al., 2017; Bertulani, Fuqua, and Hussein, 2013; Kusakabe et al., 2019) on Tsallis statistics proposed that such a non-extensive distribution function could be a solution to the "cosmic Li Problem". In this framework, an extra parameter q characterizes the deviation from a MB distribution. Several physical sources of the parameter q have

[1] $A(^7\text{Li}) = 12 + \log[N(^7\text{Li})/N(\text{H})]$ where N is number density of atoms and the solar hydrogen abundance is normalized to 10^{12}.

been discussed (Lutz, 2003; Bernui, Tsallis, and Villela, 2007; Rossani and Scarfone, 2000; Livadiotis and McComas, 2010; Pavlos, 2012; Wilk and Wlodarczyk, 2000; Wilk and Wlodarczyk, 2002). One possible explanation for such non-MB distribution is the entropy (or equivalently, the temperature) fluctuations (Wilk and Wlodarczyk, 2000; Wilk and Wlodarczyk, 2002) in the equilibrium state. The relativistic plasma in the early universe may also have strong turbulence, motivated by this, I therefore explore this possibility in a phenomenological model whereby sub-horizon isocurvature temperature fluctuations arise from a fluctuated *primordial magnetic field* (PMF). Previous studies (Cheng, Schramm, and Truran, 1994; Grasso and Rubinstein, 1996; Kernan, Starkman, and Vachaspati, 1996; Yamazaki and Kusakabe, 2012; Kawasaki and Kusakabe, 2012) introduced a constant scale invariant PMF strength within a certain co-moving radius during the BBN epoch. However, as the magnetic field evolves, the strength may not always be homogeneous (e.g. Minoda et al., 2017), the background photon energy density or temperature may not have a universal homogeneous value as assumed in previous BBN studies due to the fluctuations, which finally may leave the imprints in the elemental abundances.

1.4 *r*-process Nucleosynthesis

The Coulomb barrier increases drastically with the increasing of the nuclear charges Z, therefore, the heavy elements are hardly to be formed via the charged particle reactions. However, the observed solar elemental abundances (see Fig. 1.5) beyond iron peak (i.e., $A \leq 60$) indicate that there exists a process that could provide considerable amount of such heavier elements. For the neuron-induced reactions, there is no Coulomb barrier that prevent the reaction occurs. The cross section for such induced reactions even increasing with decreasing incident neutron energy. Such facts lead us to looking for astrophysical sites that the numerous neutron could be emitted and the heavy nuclei are synthesis by exposing in such neutron rich flow, i.e., they could be formed from the light nuclei via the neutron-induced reactions. One of the proof of such scenario is the abundances peak near $A = 84, 138, 208$, which corresponds to the neutron magic number $N = 50, 82, 126$, respectively (see Fig. 1.5). However, one problem is that the neutron is not stable with a lifetime $\tau_n = 881.2$ s, it means that the normal interstellar medium cannot contain much free neutron. So we should further look at the stellar sites: inside stars, there are several nuclear reactions could play the role as the neutron source such as ^{13}C(α,n)^{16}O and ^{22}Ne(α,n)^{25}Mg, so that the free neutrons are possible inside the stars. In order to form neutron rich nuclei, a compete between neutron captures and β^- decay is essential. Mainly there are two different categories, the criterion is that the neutron capture rate with the β^- decay rate. For the process that neutron capture is much slow than the β^- decay, then the nuclei decay to the valley of stability before capture another neutron, so such a process can be achieved only near the valley of stability on the nuclides chart, this is called *s*-process. *s*-process usually occurs in the final stage evolution of AGB stars, the neutron flux usually around $10^5 \sim 10^{11}$ cm^{-2} s^{-1}. The nuclear study on the *s*-process are more accessible form the experiment and theory since the typical *s*-process nucleosynthesis consider somehow mediate evolution stage of the stellar.

If the neutron capture rate is much faster than the β^- decay rate, then huge amount of neutrons can be captured by the nuclei before it decays. such a process can reach the region that far away from the valley of stability and close to the neutron drip line, finally the production can be access to much heavier region on

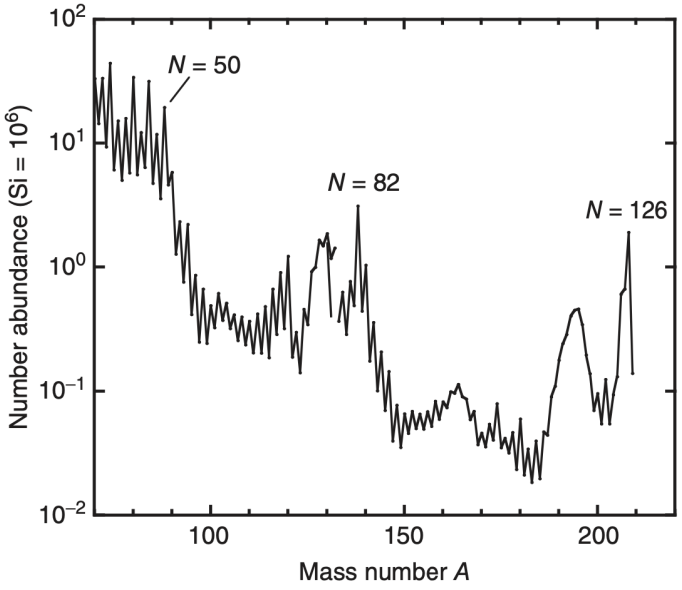

FIGURE 1.5: Solar system abundances (relative to 10^6 Si atoms) of the heavy nuclides. This figure is taken from Lodders (2003).

the nuclides chart such as $A = 280$, it is called *r*-process. The nuclear study on *r*-process is more challenging because it requires huge amount of neutrons since the β^- decay time for nuclides that away from the valley of stability is about 10^{-10} s. Therefore the *r*-process could only occur in a more extreme astrophysical sites such as the core-collapse SNe, or the binary neutron star mergers. In such extreme cases, the density and temperature usually very high in the center and drops quickly during the explosion, also the strong magnetic field has been confirmed in these sites. therefore, the study on the environment of such astrophysical activities can help us with the much accurate calculation of the nucleosynthesis. Another important fact that stimulate the study on *r*-process is the elemental abundance pattern observed in the metal poor stars in Galactic halo. Although the absolute magnitude depends on the metallicities (i.e., the iron abundance [Fe/H], which is approximately can be treated as the stellar age) of the stars, the normalized abundances show the similar pattern as in the solar system. This indicates that the elements are enriched as some regular processes that could provide the material in the *interstellar medium* (ISM) that contents the same abundance ratio and later involved with GCE.

The simplest *r*-process model is that the temperature and number density kept the same value through the nucleosynthesis. The neutron capture rate in a hot, neutron-rich plasma is much larger than the β^- decay rate (i.e., $\lambda_{n,\gamma} >> \lambda_{\beta^-}$), therefore, the elemental abundance evolution is given by

$$\frac{dN(Z,A)}{dt} = -N_n N(Z,A)\langle\sigma v\rangle_{Z,A} + N(Z,A+1)\lambda_\gamma(Z,A+1), \tag{1.80}$$

here, N_n is the neutron number density, $N(Z,A)$ is the number density of isotope ${}^A_Z X_N$, $\langle\sigma v\rangle_{Z,A}$ is the neutron capture rate defined as per particle. λ_γ is the photodisintegration of ${}^{A+1}_Z X_N$. For the high temperature $T > 1$ GK and large amount of neutron flux $N_n > 10^{21}$ cm^{-3}, the neutron capture reaction is balanced ($dN(A,Z)/dt = 0$) so that the number of isotopes are in equilibrium, the number density ratio is given by

the Saha equation (Saha, 1921)

$$\frac{N(Z,A+1)}{N(Z,A)} = N_n \Big(\frac{2\pi}{m_{An}kT}\Big)^{3/2} \frac{2j_{(Z,A+1)}+1}{(2j_{(Z,A)}+1)(2j_n+1)} \frac{G^{norm}_{(Z,A+1)}}{G^{norm}_{(Z,A)}} e^{Q_{n\gamma}/kT}, \tag{1.81}$$

where m_{An} is the reduced mass of reaction $A(n,\gamma)A+1$, j_i is the ground state spin of the isotope i. G^{norm} is the normalized partition function

$$G^{norm}_i = \frac{\sum_\mu g_{i\mu} e^{-E_{i\mu}/kT}}{g_{g.s.}}, \tag{1.82}$$

where $g_{i\mu} = (2J_{i\mu}+1)$ is the statistical weight of state μ in nuclei i, $J_{i\mu}$ is the spin, $E_{i\mu}$ is the excitation energy of state μ. From Eq. 1.81, the abundance ratio $N(Z,A+1)/N(Z,A)$ is mainly decide by the Q-value $Q_{n\gamma}$ (or neutron separation energy, equivalently). Consider a temperature $T = 1.25\,\mathrm{GK}$, neutron density $N_n = 10^{22}\,\mathrm{cm}^{-3}$, and neglect the spin and partition function's contribution, then for the equal abundance of the isotope ${}^{A}_{Z}X_N$ and ${}^{A+1}_{Z}X_N$, we can obtain the Q-value for such condition $Q = 3$ MeV. In reality, the isotope close to the valley of stability has larger Q-value and the isotope close to the neutron drip line has smaller Q-value, then one can predict that start from valley of stability, for a certain isotope chain with charge Z, the abundance increase for nuclei with larger neutron number, then reaches the peak around the nuclei that with the neutron separation energy $Q_{n\gamma} \sim 3$ MeV, then decreases as the isotope close to the neutron drip line. Also, from Eq. 1.81, an increasing in N_n could shifts the most abundant isotope to the neutron rich side (small Q-value), and a higher temperature could move the peak to the less neutron-rich side (large Q-value). A much quantitative equation for a certain isotope x_m which is produced after m neutron captures on x_0 could be obtained from the successive application of the Saha equations:

$$N_x m = N_x 0 \frac{N_n^m}{\theta^m} \Big(\frac{M_x m}{M_x 0 M n^m}\Big)^{3/2} \frac{g_x m}{g_x 0 g_n^m} \frac{G^{norm}_{xm}}{G^{norm}_{x0}} \exp\Big[\frac{1}{kT}\sum_{j=0}^{m-1} Q_{xj(n,\gamma)}\Big], \tag{1.83}$$

where θ is

$$\theta = \Big(\frac{m_u kT}{2\pi}\Big)^{3/2}. \tag{1.84}$$

The above discussion neglects the effects from the nuclear binding energy. Because of the pairing effect of the nuclear shell structure, the binding energy depends on the neutron numbers in the nuclei: for even number of neutrons, $Q_{n\gamma}$ is larger while for odd number of neutrons, it is opposite. Therefore, the abundance maximum point in each isotopic chain is identified with nuclei with even neutron number. The Q-values close to the valley of stability is much larger and the forward neutron capture reaction rate is significantly enlarged compared with the reverse reaction (i.e., photodisintegration). Although it seems that the nuclei are quickly destroyed in to heavier isotope, it has been proved that the equilibrium condition holds for all isotopes with any significant abundance at equilibrium (Seeger, Fowler, and Clayton, 1965). Then naturally, those abundant isotopes are considered as the waiting points of the r-process abundance flow: the r-process path can only continue via β^- decay, however, since the decay rates are small, the equilibrium could not be broken.

Now one could include the β^- decay in such a model. β^- decay could transfer the abundance flow from one isotopic chain to the next and build the equilibrium of

the next isotopic chain, such transfer is expecting to occur near the neutron drip line since those nuclei has shorter β^- decay lifetime. So one can imaging the repetitive sequence of the β^- decay transfer lead to the rising of the *r*-process path. The total β^- decay of an isotope with charge Z is given by

$$\lambda_Z = \sum_A p(Z,A)\lambda_{\beta^-}(Z,A), \tag{1.85}$$

where the $\lambda_{\beta^-}(Z,A)$ is the decay rates for certain nuclides and $p(Z,A) = N_(Z,A)/N_Z$ is the abundance ratio of nuclei (Z,A) to the total isotopic abundance. So the time evolution of the isotope Z is given by

$$\frac{dN(Z,A)}{dt} = -N_n N(Z,A)\langle\sigma v\rangle_{Z,A} + N(Z,A+1)\lambda_\gamma(Z,A+1). \tag{1.86}$$

where the first term describes the destruction and second term stands for production. Now the situation is clear: Eq. 1.81 and Eq. 1.83 decide the abundance within the isotopic chain while the Eq. 1.86 decide the how the flow evolved accumulate the charge number Z. One general solution is given for the initial condition:

$$N(t=0) = N_0 \quad for \quad Z = Z_0 \tag{1.87}$$
$$N(t=0) = 0 \quad for \quad Z \neq Z_0, \tag{1.88}$$

$$N_z(t) = N_0 e^{-\lambda t} \quad for \quad Z = Z_0 \tag{1.89}$$
$$N_Z(t) = N_0 \sum_{i=Z_0}^{Z} e^{-\lambda_i t}\frac{\lambda_i}{\lambda_Z}\prod_{j\neq i}\frac{\lambda_j}{\lambda_j-\lambda_i} \quad for \quad Z \neq Z_0 N_z = N_0 e^{-\lambda t}. \tag{1.90}$$

For a longer enough time, the β^- flow will become steady and the $dN_Z/dt = 0$ so that

$$\lambda_Z N_Z = \lambda_{Z-1} N_{Z-1} = const. \tag{1.91}$$

which is called the steady flow approximation (Cameron, Cowan, and Truran, 1983; Cameron et al., 1983). Based on this approximation, all the nuclei in the network will approach a steady state abundance in which the rates of production and destruction are in equilibrium, the abundances are given by Eq. 1.83 , Eq. 1.89, and Eq. 1.90 . Then for the isotope with magic number of neutrons (e.g., ${}^A_Z x_N$), due to the neutron shell configuration, the Q-value for $x(n,\gamma)$ drops quickly compared with the isotope $(Z,N-1)$, then $(Z,N+1)$ nuclei has smaller abundance so that x will become the most abundant nuclei in the isotopic chain and represent the waiting point. The later on β^- decay move upward to the $(Z+1,N)$ nuclei, form the next isotope chain, and the waiting point becomes the $(Z+1,N)$ which is also an isotope with the magic number of neutrons.

Such repetitive processes make a sequence of waiting points which encountered at the same magic neutron number N. The *r*-process path has no choice but to move vertically upward in Z to the valley of stability. The closer to the valley of stability, the longer time it takes for the β^- decay: the typical half-lives along the *r*-process path amount to $\tau_{1/2} \sim 0.01 - 0.05$ s, but near neutron magic waiting point close to the stability valley (e.g., ^{130}Cd), it is considerably longer ($\tau_{1/2} \sim 0.2$ s). Hence, the abundance flow build up a relatively large abundances in these isotope.

Fig. 1.6 shows the situation that *r*-process near the magic number nuclides with $N = 82$, this magic number could form a waiting point chain with the increasing

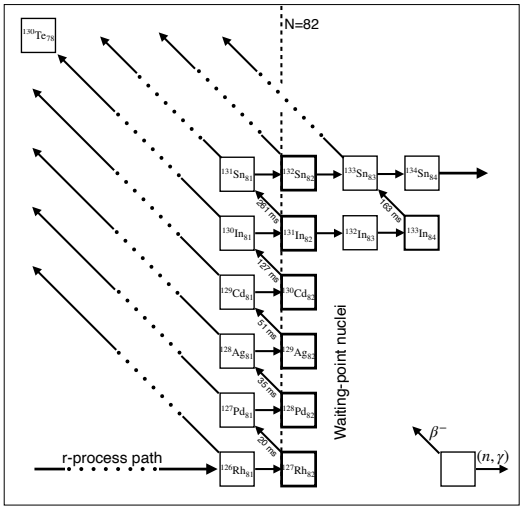

FIGURE 1.6: The *r*-process path around neutron magic number $N = 82$. The waiting point of $N = 82$ ends up at ^{130}Cd because the next isotope with $N = 82$, i.e., ^{131}In is too close to the valley of stability, it has a Q-value ~ 3 MeV, in fact ^{133}In has $Q < 3$ MeV, it is the most abundant isotope on this chain. Therefore elemental flow cross the $N = 82$ line at ^{131}In, and could continue forming heavier nuclei. The ^{130}Cd finally will decay to ^{130}Te which corresponds to $A = 130$ peak in the solar *r*-process abundance distribution.

charge number. However, an interesting situation occurs when the nuclei ^{131}In is reached. Since it is close to the valley of stability, there is the extra stability which reflected in the larger overall neutron-capture Q-values, so that the Q-value of ^{131}In is only slightly below 3 MeV, it does not form the peak of In isotropic chain. In fact, the ^{133}In has the Q-value below 3 MeV, which makes it the most abundant isotope. Therefore, the *r*-process flow will overcome the magic number $N = 82$ when it reaches ^{133}In, moving further to heavier nuclei. The final step of *r*-process is the terminate of neutron flux, after that, the neutron-rich nuclides β^- decay along the lines of constant mass number A to the stable isobars. For the simplicity, the neutron flux is assumed shut down spontaneously after some time τ. Then the final abundance of the isobars with mass number A is

$$N_{r,A} = \sum_Z N_Z(r) p(Z, A). \tag{1.92}$$

For example, the magic number that is discussed above corresponds to the $A \sim 130$ peak.

The aforementioned model is also known as the classic *r*-process model which is the simplest one because: 1). the constant temperature and neutron flux is assumed; 2). the waiting point is only valid for high temperature and neutron density, the steady flow approximation requires that neutron exposure time is much longer than the β^- decay lifetime in order to build the equilibrium state for all the isotopes on the *r*-process path; 3). the sudden termination of neutron flux indicate the spontaneous fall-out of the equilibrium, which in reality is a finite time. However, the elemental abundance peak at $A = 130$ of solar system indicate the validity of the classic model in predicting the origin of the heavy element (Lodders, 2003). One should also notice that the discussion here did not contain the β^- delayed neutron emission (i.e., a neutron unbound state produced by β^- decay which lead to the further neutron

emission) and the fission cycling (i.e., in the higher mass range, fission could become faster than β^- decay, which could recycle the lighter nuclei to the *r*-process). These processes could change the elemental equilibrium abundance as well as the final *r*-process abundance yields, for details, please see (Martínez-Pinedo et al., 2007).

Moreover, it is obvious that the *r*-process nucleosynthesis path strongly depends on the nuclear properties which covered wild range on the nuclides chart from the valley of stability to the neutron drip line. The Q-value of the neutron induced reaction determines the equilibrium isotopic abundance ratio which requires a accuracy information of the nuclei mass (Q-value is calculated from mass difference between two nuclei). β^- decay rates determine the total amount of material for an isotope with given charge Z. For the case without waiting point approximation, the neutron capture cross section also plays important role in deciding the final abundance yields. These properties are studied both theatrically and experimentally (Kajino et al., 2019).

The observed heavy elements distribution in the metal-poor stars has the remarkable agreement with the solar abundance for nuclei with mass number $A > 135$. This indicates that those heave elements were not synthesis in halo stars, they must have been produced by some rapid-evolving process that could eject matter to the IGM very quickly. Such activities are likely linked to massive stars since low-mass stars or intermediate-mass stars evolve on considerably longer time scales. It is also clear that such a site should produce high neutron flux with $N_n > 10^{21}$ cm^{-3}s^{-1} for a short time scale. Also, the temperature should not be high otherwise the photodisintegration process will be dominated and the *r*-process flow could not reach to the heavy region on nuclides chart. There are different potential sites of the *r*-process that could holds for such condition, such as collapsars, which are the supernovae leaving black hole as remnant (Takiwaki, Kotake, and Sato, 2009), neutrino driven wind of core-collapse SNe (Qian and Woosley, 1996), the *magnetohydrodynamic-Jet Supernovae* (MHD-Jet SNe) (Nishimura, Takiwaki, and Thielemann, 2015) and *neutron star mergers* (NSMs) (Metzger et al., 2010).

The recent breakthrough of the *r*-process study is the detection of gravitational wave GW170817 and its electromagnetic counterpart GRB170817 (Abbott, 2017; Abbott et al., 2017). The observed light curve indicate this event as a binary NSM (Metzger et al., 2010). However, except for the light curve color change from blue to red, there is unfortunately no clear evidence for the r-process elements. The first analysis by Smartt et al. (2017) of the optical to near-infrared spectra of this kilonova misidentified the absorption lines of neutral Te I and Cs I. Since these atoms are easily ionized for their low ionization potentials, they are not expected at very high temperatures of the ejecta and outflows from GW170817. Watson et al. (2019) reanalyzed the recorded same spectra carefully and suggested a possible absorption line of the first ionized Sr II. Nevertheless, it is allowed to assume that some *r*-process elements were produced in this specific kilonova associated with GRB170817/GW170817. Although this event is consistent with the present understanding of the NSM, however, it only make minor contribution to the GCE in recent epoch since binary system takes long time to merge, the major sites of providing *r*-process elements in the entire history of GCE are still collapsars and SNe where the relatively light *r*-process elements are believed to be produced. Therefore, it is worthy to carry on a much systematic study of the *r*-process nucleosynthesis. In this thesis, I focus on the magnetized plasma which play an important role in the MHD-Jet SNe. The jet-like explosion could be formed via rapid rotation and a strong initial magnetic field, also, the ejected low Y_e material in the jet emerged from the silicon layers could be the potential site of the *r*-process. I try to clarify the imprints of the strong magnetic field

in the *r*-process nucleosynthesis, finally could lead us to a deeper understanding of the *r*-process elements' origin.

1.5 Purposes of the Thesis

In this Chapter, two nuclear astrophysical sites that magnetic field could play potential important roles are briefly introduced, i.e., the Big-Bang Nucleosynthesis and the *r*-process nucleosynthesis. The nucleosynthetic process strongly depends on the cosmological and astrophysical environments: the thermonuclear reaction rates are determined by the local background temperature and the number density of the nuclear species, these two could have spatial inhomogeneity in the turbulent relativistic magnetized plasma; for the weak interactions, the motion of electron could be easily affected by the electromagnetic force of the plasma. Therefore, it is worthy to investigate the impacts of magnetic field on the plasma in these two sites.

For BBN, since the up-to-date theoretical BBN model and observational constraints on primordial D and ^{4}He abundance have reached an accuracy of 10^{-4} (Aver, Olive, and Skillman, 2010; Cooke, Pettini, and Steidel, 2018), such precise measurements are promising to constrain the PMF property. However, the previous studies on constraining PMF via primordial elemental abundances (Cheng, Schramm, and Truran, 1994; Grasso and Rubinstein, 1996; Kernan, Starkman, and Vachaspati, 1996; Yamazaki and Kusakabe, 2012; Kawasaki and Kusakabe, 2012) only focus on the contribution from magnetic field energy density to the expansion rate (or equivalently, the change of the effective neutrino number), so that only the constraint on co-moving strength of PMF is obtained. In this thesis, the Coulomb screening effect, the thermodynamic condition and the effect of weak interaction rates of the magnetized plasma are extensively investigated in the context of PMF, stringent constraints on the homogeneous PMF strength and its generation time are provided. On the other hand, the present discrepancy of primordial ^{7}Li abundance between the standard theoretical BBN prediction, i.e., $^7\mathrm{Li/H}=(5.623 \pm 0.247) \times 10^{-10}$ from Pitrou et al. (2018) and the observation in the Pop II metal-poor stars, i.e., A(^{7}Li)=2.23 dex (Sbordone, 2010) has been a puzzle for decades. In order to resolve it, many solutions have ever been proposed such as the depletion of Li due to astrophysical activities like diffusion or convective mixing of materials in the surface of metal-poor stars (or dwarf stars) (Richard, Michaud, and Richer, 2005; Piau et al., 2006; Fu et al., 2015), the exotic solutions which involve the extra neutron or photon injection and other cosmological solution (Esposito et al., 2000; Ishida, Kusakabe, and Okada, 2014; Arbey and Mahmoudi, 2008; Kusakabe, Kajino, and Mathews, 2011; Kusakabe et al., 2017). The relic strength of PMF at present day is about nG scale (Planck Collaboration et al., 2016b), however, due to the conservation of the magnetic field flux, PMF could be much stronger up to 10^{13} G before neutrino decoupling in the early universe. Such a strong PMF could lead to a turbulence of the relativistic plasma. As the magnetic field evolves, the PMF strength may not always stays as homogeneous, namely the background photon energy density or temperature may not take a universal homogeneous value as assumed in previous BBN studies due to the fluctuations, which finally leaves the observational imprints in the elemental abundances. This thesis seeks for the observational imprints of inhomogeneous PMF in the BBN elemental abundance prediction and also tries to constrain the properties of the inhomogeneous PMF itself.

For the r-process nucleosynthesis, I focus on the MHD-Jet collapsar and SNe, which are the potential major sites of providing r-process elements in the entire history of GCE. The associated magnetic field in these sites could be as high as 10^{16-17} G (Takiwaki, Kotake, and Sato, 2009; Nishimura, Takiwaki, and Thielemann, 2015; Nakamura et al., 2015), while the effects from relativistic, magnetized plasma have not been fully addressed: the magnetic field could affect the motion of electrons and positrons inside the plasma, which results in a change of their thermodynamics; also, electron momentum transverse to the field direction is quantized into Landau levels, and the phase space integral is replaced by a summation of the finite Landau levels. A few study focused on the magnetic field imprints in the nucleosynthetic yields in these astrophysical sites. In this thesis, the impacts of strong magnetic field on the weak interaction rates inside both low and high density plasma are studied. The screening potential and the weak interactions are extensively studied within strongly magnetized circumstance. For the low density plasma, the result is applied to an example nucleosynthesis process in a MHD collapsar jet. The modification on the β^- decay and electron capture rates leave essential imprints in the r-process abundance flow and the isotopic ratio. For high density plasma, the electron occupation is limited to only the lowest Landau level in phase space, which results in a reduction of the electron capture rates. A profile from the 15 $M_\odot$ core collapsing SNe progenitor model is applied to calculate the electron capture rates of ^{54}Fe and ^{70}Zn since they are the representative nuclides for pre-SNe and post-collapsing and bouncing calculation (Heger et al., 2001; Liebendörfer et al., 2001). At the final phase of the stellar evolution, since the electron captures reduce the electron fraction Y_e, which is a key parameter that determines the neutron-richness, its further evolution in the region above neutrino sphere during bouncing phase also depends on the weak interactions as well (Langanke and Martinez-Pinedo, 2003). It is expected that such a study could clarify the imprints of the strong magnetic field in the final elemental abundance yields as well as the observational signals, which could be used to constrain the magnetic field of the site and vice-versa.

This thesis is arranged in the following way: in Chapter 2, the PMF and its imprints in the BBN are investigated, and both microscopic and macroscopic impacts are studied. The weak screening (screening in a low-density relativistic plasma) potential with a PMF background is calculated, the screening potential suppress the electron kinetic energy, and turns out to give an enhancement of the electron capture rate. By implementing the inhomogeneous PMF on BBN, it is also found that such an inhomogeneity could deviate the primordial elements abundance of BBN and relaxing the "cosmic Li problem". The MHD equations for an expanding relativistic plasma are also derived, which are easily to be encoded to the numerical solution to perform the realistic BBN-PMF calculation. Finally, I summarize present status of the "Cosmic Li Problem" and discuss the possible solution from PMF. In Chapter 3, the influence of strong magnetic field on the r-process nucleosynthesis site is studied, and it is shown that the explosive nucleosynthesis of r-process elements could provide an observational signal for such strong magnetic fields through the screening effect on the change of weak electron-capture rates affected by Landau quantization theoretically. Also as for magnetized degenerate plasma, the strong screening (screening in degenerate plasma) potential is investigated, and the electron capture rates of pf-shell nuclei under the strong magnetic field are also corrected. Those nuclei could affect the final stage evolution of the massive star as well as the collapsing and post-bounce phases of SNe. In Chapter 4, the conclusions and the future aspects are presented.

For the convenience of reading, hereafter in this thesis, I use natural units, i.e. $\hbar = c = 1$ except when we judge instructive to write them explicitly.

Chapter 2

Primordial Magnetic Field & Big Bang Nucleosynthesis[1]

2.1 Introduction

It has been confirmed that nG-scale magnetic fields exist in the Galaxy via both the Faraday rotation ((Davies, 1968) and references therein) and Zeeman effect (Verschuur, 1968; Davies, Booth, and Wilson, 1968) observations. The Observations of intermediate and high redshift galaxies also indicate the existence of such large magnetic fields. Theoretically, the PMFs can be considered as seeds of these Galactic magnetic fields which have amplified via the dynamo mechanism (see e.g., Kronberg (1994), Grasso and Rubinstein (2001), and Widrow et al. (2012) for reviews), a rather large PMF is also possible as a seed due to a short duration time amplification (Kronberg, 1994; Grasso and Rubinstein, 2001; Widrow et al., 2012).

The theoretical studies on PMF are mainly focusing on the generation mechanism and the following magnetic field evolution. During the inflation, the electromagnetic field is conformally coupled with the expanding background, therefore, PMFs are considered to be generated via the breaks of the coupling conformal invariance or the gauge symmetry (Turner and Widrow, 1988; Martin and Yokoyama, 2008; Subramanian, 2010). In the phase transitions, the PMFs can be generated via bubble nucleation which is a very violent event, and likely to lead to turbulence in the cosmic plasma which could further growth to the seeds PMF (Grasso and Riotto, 1998; Caprini, Durrer, and Servant, 2009). Since the horizon during the inflation and phase transitions is much smaller than the typical co-moving length scale of the observed PMF at present day, PMFs generated during inflation and (or) phase transition are usually considered as the homogeneous PMF (Turner and Widrow, 1988; Dolgov, 1993; Demozzi, Mukhanov, and Rubinstein, 2009). Another inhomogeneous PMF could be generated at later epochs: in one model proposed by Dolgov and Grasso (2002), the smaller scale of the PMF fluctuations inside the co-moving horizon is expected to survive during the BBN epoch due to the local imbalance of lepton number. After the PMFs are generated, the growth and scaling behavior of B_{rms} are also interesting. The initial PMF could be treated as the Gaussian random field, with a power-law spectrum normalized by the field strength B_{rms} (Brandenburg, Enqvist, and Olesen, 1996). The requirement of the flux conservation implies that $B_{rms} \propto R^{-2}$, i.e., the magnetic field strength itself is conserved in the co-moving coordinate while the correlator $\langle B(r+x)B(x)\rangle$ could have further evolution until the end of radiation dominated era. The small scale uncorrelated field regions could come into contact during the expansion of the universe, so the detailed MHD study of PMF is necessary. For the early universe, the Prandtl number Re_u ($Re_u \sim v\sigma H^{-1} \sim M_P/T$,

[1] This chapter is based on the paper Luo et al. (2019), and Luo et al. (2020)

where M_P is the Planck mass) is large, therefore turbulence also plays an essential role. There are many pioneer studies on the PMF evolution by including both linear and nonlinear MHD equations (Subramanian, 2016; Brandenburg and Subramanian, 2005; Banerjee and Jedamzik, 2004; Dimopoulos and Davis, 1997; Subramanian and Barrow, 1998; Brandenburg, Enqvist, and Olesen, 1996; Gailis, Frankel, and Dettmann, 1995), the subsequence turbulent decay and damping of the PMF could lead to the present-day possible relic field in the IGM today.

To constrain the relic PMF seeds, one need to look at the *intergalactic medium* (IGM), where the field strength did not suffer much amplification from the *large scale structure* (LSS) formation. By calculating the largest size of eddies that could made by PMF and compare its growing time scale with the cosmic age, the theoretical constraints on the present-day PMF strength and correlation length could be obtained (Adamek et al., 2011). After the epoch of photon last scattering ($z \sim 1100$), the CMB power spectrum provides us with an observable constraint on the relic PMF (Kronberg, 1994; Seshadri and Subramanian, 2009; Caprini et al., 2009; Planck Collaboration et al., 2016b; Jedamzik and Saveliev, 2019) which comes from the anisotropy, distortion and the Faraday rotation in the CMB polarization. PMFs could leave imprints in CMB power spectrum and polarization. The recent measurement of TT, TE and EE modes of CMB polarization spectra from Planck satellite constrained the PMF upper limits as $B_{1\mathrm{Mpc}} \sim 10^{-9}$ G (Planck Collaboration et al., 2016b). Another observational constraint comes from the time delayed γ-rays emission (Taylor, Vovk, and Neronov, 2011): the electromagnetic cascading process during the propagation of the γ-rays in IGM could generate electron-positron pair and their motion could be deviated in the magnetic field, so the following secondary γ-ray emission could interaction with CMB photons and probe the properties of present day's *intergalactic magnetic field* (IGMF). Fig. 2.1 shows the present day's constraints on IGMF for both field strength and correlation scale. The straight lines with arrow show how the PMF are evolved after the generation from different epoch to the present day. The integrated length move with constant velocity due to the free turbulent decay of the PMF until the end of recombination. It is clearly that PMF finally could contribute to a $\sim$ nG IGMF for a co-moving length scale $\sim$ kpc after turbulent decay and dissipation. However, the predicted of the magnetic field ejected by the galaxies or the AGN activity also has the same strength (vertical blue and yellow bands) (Bertone, Vogt, and Ensslin, 2006; Furlanetto and Loeb, 2002), therefore, the origin of the field unfortunately is undistinguished. Moreover, such a result urge us to seek for a probe that could constraint both the magnetic field strength and correlation length in the very early universe without contamination of galactic activities.

The up-to-date theoretical BBN model and observational constraints on primordial elemental abundance have reached an accuracy of 10^{-4}, any change in X_n (neutron fraction) larger than this amount is to be constrained carefully, which is promising to constraint the PMF property, however, the previous study on constraining PMF via primordial elemental abundances Cheng, Schramm, and Truran (1994), Grasso and Rubinstein (1996), Kernan, Starkman, and Vachaspati (1996), Yamazaki and Kusakabe (2012), and Kawasaki and Kusakabe (2012) only provide the 10^{-6}G for a co-moving length scale 1Mpc. These studies on the BBN constraints of PMF only focus on : 1). the magnetic field energy density contributes to the expansion rate (or equivalently, the change of the effective neutrino number), this is the most important effect; 2). the electron phase space is quantized inside the magnetic field. Therefore, their constraints only valid for PMF with coherent scale larger than the horizon at early epoch, so that only the upper limit of the field strength and co-moving scale

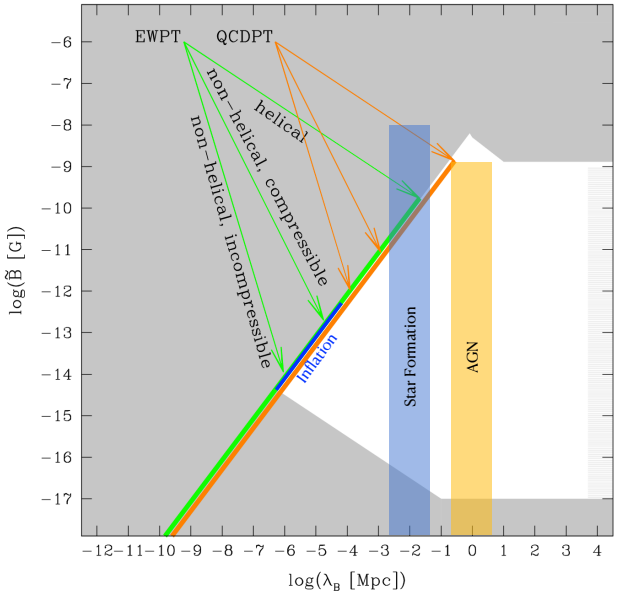

FIGURE 2.1: Constraints on the present day IGMF. The gray-shaded region is excluded by observations, solid lines corresponds to the possible correlation length scale and strength of the relic magnetic fields which are produced in the early universe (namely, inflation, electroweak phase transition and QCD phase transition). The arrows indicate the evolution of the integral scale of the magnetic field after its generation. The yellow and blue shaded region corresponds to the magnetic field produced by AGN and star formation, respectively. This Figure is modified based on Fig. 19 of Durrer and Neronov (2013).

are provided since no dynamical model was included. However, as have been discussed, the PMF can also be inhomogeneous within the horizon scale; also, the dynamical evolution shows the fluctuation of PMF leading to the energy fluctuations which should leave the imprints in the primordial elemental abundances. Therefore, it is important to consider more sophisticate impacts from PMF and develop a dynamical model, which are promising to be used to constrain PMF generation and evolution.

This Chapter is organized as follows. In Section 2.2, I first investigate the microscopic effects of PMF: the screening potential and its correction to the electron capture reaction rate in the early universe are studied, then the thermodynamic condition of the magnetized plasma and the weak interactions within the background PMF are also investigated. I discuss how the PMF affects the prediction of primordial light element abundances and try to provide constraints on the PMF strength and the generation time. In Section 2.3, I consider the inhomogeneous static PMF impacts on BBN, the PMF scale could be under the horizon scale (Dolgov and Grasso, 2002), so energy density of the early universe could be varied spatially, which finally lead to a temperature fluctuation during the BBN epoch. A phenomenological static inhomogeneous PMF model is explored, whereby sub-horizon iso-curvature temperature fluctuations arise from fluctuations in a PMF, the primordial elemental abundances in such a PMF model are also investigated. Moreover, to study more realistic PMF models, it is necessary to consider the dynamical generation and evolution of PMF. In 2.4, I move further on discussing the MHD of the PMF, the full relativistic MHD equations in the early universe were derived, "two-fluid" model

is applied to illustrate how the PMF could be generated during the decoupling of the particles from the relativistic plasma. The numerical solution of such equations could benefit to study the dynamical impact from the PMF on the BBN in the future. Finally, in Section 2.5, I summarize our work and discuss the current status of "cosmic Li problem" and the potential solution from PMF.

2.2 Microscopic Effect from the Primordial Magnetic Field

2.2.1 Weak Screening Correction

Recently, charge screening from both ionized nuclei and electrons in relativistic electron-positron plasmas have been discussed and applied to the determination of thermonuclear reaction rates (Wang, Bertulani, and Balantekin, 2011; Famiano, Balantekin, and Kajino, 2016). This effect turned out to be negligible during the BBN epoch because the plasma is in a high temperature, low density state, and the distance between electrons or positrons and nuclei is so large that the screening effect on the Coulomb potential is not significant. However, at the epoch before weak decoupling, i.e., $t \lesssim 1$sec and $kT > 1$ MeV, the density is much higher compared with the later BBN epoch, and there is also a large number of electrons and positrons. The screening effect in a relativistic electron-positron plasma could affect weak interaction rates by changing the electron and positron energy distributions. Such screening corrections to the electron capture rates have been studied and applied to stellar nucleosynthesis (Itoh et al., 2002); however, this approach is not suitable for the relativistic non-degenerate electron-positron plasma.

In a hot plasma, the background charged particles can create a "screening" effect which reduces the Coulomb barrier between two fusion reactants by reducing the effective charge (Jancovici, 1977; Famiano, Balantekin, and Kajino, 2016). The background charges include the surrounding electrons, positrons, and other nuclei. Classically, the electrostatic potential ϕ of a charge ze in the presence of a background charge density can be computed via the *Poisson-Boltzmann equation*:

$$\nabla^2\phi(r) = -4\pi Ze^2\delta^3(\mathbf{r}) - 4\pi\sum_{z\geq 0} zen_z\left[\exp\left(-\frac{ze\phi(r)}{T}\right) - 1\right] - e\left[N(\mu + e\phi, T) - N(\mu, T)\right], \tag{2.1}$$

where

$$N(\mu, T) = \frac{1}{\pi^2}\int dp\, p^2\left[\frac{1}{e^{(E-\mu)/T}+1} - \frac{1}{e^{(E+\mu)/T}+1}\right] \tag{2.2}$$

is the net lepton number density, T and μ are the temperature and the chemical potential of electrons in units of MeV. The second term of Eq.(2.1) is a sum over all charged nuclei in the medium with charge ze and number density n_z. The last term includes the charge of the electrons and positrons. This is universally used in astrophysical calculations involving nuclear reactions. By expanding Eq. (2.1) to lowest order in potential ϕ, one obtains the solution as the familiar Yukawa potential:

$$\phi(r) = \frac{Z_1 Z_2 e^2}{r}\exp\left(-\frac{r}{\lambda_{TF}}\right). \tag{2.3}$$

For the relativistic electron-positron plasma, the corresponding *Thomas-Fermi length* can be calculated exactly to all orders from the *Schwinger-Dyson equation* for the photon propagator (Famiano, Balantekin, and Kajino, 2016). The characteristic length

scale is:

$$\frac{\pi^2}{\lambda_{TF}^2} = 4\pi e^2 \frac{\partial}{\partial \mu} \int_0^\infty dp\ p^2 \left[\frac{1}{1+\exp{(E-\mu)/T}} - \frac{1}{1+\exp{(E+\mu)/T}} \right], \tag{2.4}$$

where μ is the electron chemical potential.

Screening corrections to β-decay rates have been discussed previously (Takahashi, El Eid, and Hillebrandt, 1978; Fuller, Fowler, and Newman, 1980; Liu, Zhang, and Luo, 2007). The possible importance of the screening effects on the electron capture rates at extremely high densities have also been investigated. However, the plasma is not degenerate (Itoh et al., 1983; Itoh et al., 2002) in the early Universe with a high density and temperature before the completion of the e^+e^- annihilation, and non-degenerate relativistic screening corrections to the electron capture have not been well studied. In the non-degenerate environments, the distance between particles is always much smaller than λ_{TF}, therefore Eq. 2.3 can be expanded to the first order and compared with the Coulomb potential from bare nuclei. The correction to weak screening is shown to be:

$$\Delta V = \phi(r) - V^{bare} \approx \frac{Z_1 Z_2 e^2}{\lambda_{TF}}. \tag{2.5}$$

In the early Universe, weak interactions play an important role in calculating the proton-to-neutron ratio n/p. The predicted ^{4}He mass fraction Y_p is mainly determined by $2n/(n+p)$ (Bertulani and Kajino, 2016) at the epoch of weak decoupling. When the temperature of the Universe is higher than the mass difference between proton and neutron, $q = m_p - m_n$, neutrons and protons are indistinguishable via three main weak interactions:

$$\begin{aligned} n + e^+ &\longleftrightarrow p + \bar{\nu_e}, \\ n + \nu_e &\longleftrightarrow p + e^-, \\ n &\longleftrightarrow p + e^- + \bar{\nu_e}. \end{aligned} \tag{2.6}$$

The cross sections for weak interactions are calculated with the V-A interaction Hamiltonian (Bjorken and Drell, 1964). For electron capture process, i.e., $p + e^- \rightarrow n + \nu_e$, the screening correction [Eq. (2.5)] influences the cross section through a change in the Coulomb potential. The kinetic energies of electrons around protons are shifted due to screening. The electron capture rate on protons, $\Gamma_{pe^-\rightarrow n\nu_e}$, is:

$$\Gamma^{scr}_{pe^-\rightarrow n\nu_e} = \frac{G_F^2 T_\gamma^2 (g_V^2 + 3g_A^2)}{2\pi^3} \int_1^\infty E_\nu^2 \epsilon' \sqrt{\epsilon'^2 - m_e^2}\, d\epsilon'\ f_{FD}(\epsilon'; \mu, T_\gamma) g(E_\nu; \mu_\nu, T_\nu), \tag{2.7}$$

where G_F is the *Fermi coupling constant*, $g_V = 1.4146 \times 10^{-49}$ erg cm^3 and $g_A/g_V \sim -1.262$, E_ν is the neutrino energy, μ_ν is the neutrino chemical potential, T_γ and T_ν represent the photon and neutrino temperatures respectively. The notation f_{FD} is the Fermi-Dirac distribution function:

$$f_{FD}(\epsilon'; \mu, T_\gamma) = \frac{1}{[\exp[(\epsilon' - \mu)/T_\gamma] + 1]}, \tag{2.8}$$

and $g(E_\nu; \mu_\nu, T_\nu) = 1 - f_{FD}(E_\nu; \mu_\nu, T_\nu)$ is the Pauli blocking factor. The screening

correction to the electron kinetic energy is given by $\epsilon' = \epsilon - \Delta V$. The rare three-body reaction, $pe^-\bar{\nu}_e \to n$, is ignored.

2.2.2 Effect on the Weak Interactions Rates

Electrons and positrons are more sensitive to the background magnetic field than the charged baryons because of their smaller masses. The thermodynamics of $e^\pm$ will be affected via Landau quantization, which has already been addressed in Cheng, Schramm, and Truran (1993), Kernan, Starkman, and Vachaspati (1996), and Grasso and Rubinstein (1995). In the presence of a magnetic field, the electron (or positron) energy is given by

$$E_n^2 = p_z^2 + m_e^2 + 2neB, \tag{2.9}$$

After summing over the electron spin, the phase space of electron thermodynamical functions changes to

$$2\frac{d^3p}{(2\pi)^3} f_{FD}(E;\mu,T) \to \sum_{n=0}^{\infty}(2-\delta_{n0})\frac{dp_z}{2\pi}\frac{eB}{2\pi} f_{FD}(E_n;\mu,T), \tag{2.10}$$

where the Fermi-Dirac distribution function is one-dimensional. The transverse momenta are quantized, resulting in the sum in Eq. (2.10).

Fig. 2.2 shows the distribution as a function p_z and n (i.e. phase space of electrons for each Landau level) for various magnetic fields. For weak magnetic fields, difference in the distribution function between two levels is negligible: each distribution approximately equals to the continuous Fermi-Dirac distribution without magnetic fields. For stronger magnetic fields, fermions will occupy lower Landau levels. It has also been pointed out that for strong magnetic field, it is possible to have pair production (Daugherty and Harding, 1983), however here, this possibility is neglected. Including the background magnetic field in the weak interaction rate

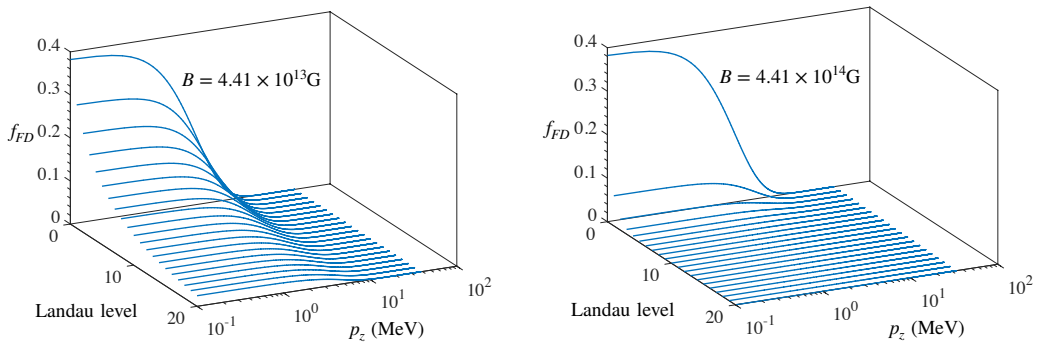

FIGURE 2.2: Fermi distribution functions in the presence of external magnetic fields as a function of Landau level n and longitudinal momentum p_z for two different field strengths.

calculation, Eq. (2.4) becomes

$$\frac{\pi^2}{\lambda_{TF}^2} = 4\pi e^2 \frac{\gamma m_e^2}{2\pi^2}\frac{\partial}{\partial\mu}\sum_{n=0}^{\infty}(2-\delta_{n_0})\int_0^\infty dp_z \Big[\frac{1}{1+\exp{(E_n-\mu)/T}} - \frac{1}{1+\exp{(E_n+\mu)/T}}\Big], \tag{2.11}$$

where γ is the ratio B/B_c with the critical field B_c defined as $B_c \equiv m_e^2/e = 4.41 \times 10^{13}$ G.

Fig. 2.3 shows λ_{TF} as a function of magnetic field strength for three values of temperature. In the case of a weak magnetic field, $B \ll B_c$, λ_{TF} does not significantly change. The change in the distribution functions for different Landau levels is small. For stronger magnetic field strength, $B \gtrsim B_c$, λ_{TF} drops dramatically. Prior to BBN, i.e. $T \gtrsim 1$ MeV, weak interaction rates can be strongly dependent on the magnetic field and the temperature. In this epoch λ_{TF} is expected to be much smaller. One thus expects an increase of ΔV, altering the electron-capture rate. With

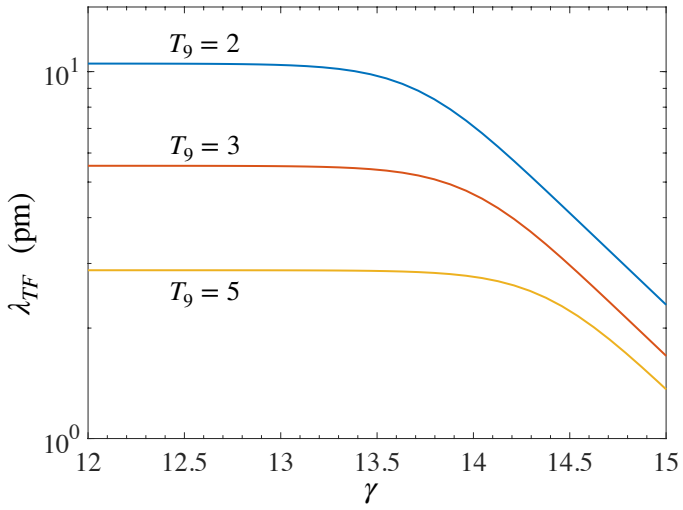

FIGURE 2.3: Thomas-Fermi length, λ_{TF}, as a function of scaled magnetic field strength, γ, for different $T_9 = T/(10^9 \text{ K})$. The parameter γ is defined as $\gamma = eB/m_e^2$. The chemical potential is chosen to be $\mu = 0.1$ MeV.

the background magnetic field, it has been suggested (Cheng, Schramm, and Truran, 1993; Kernan, Starkman, and Vachaspati, 1996; Grasso and Rubinstein, 1995) that the weak interaction rate itself also changes due to the Landau quantization. There has been some debate as to whether the weak rates increase or decrease as a result of the magnetic field (Cheng, Schramm, and Truran, 1993; Kernan, Starkman, and Vachaspati, 1996; Kernan, Starkman, and Vachaspati, 1997). I show here that the rate of the reaction $n + \nu_e \to p + e^-$ decreases as magnetic field strength increases. However, the reaction $n + e^+ \to p + \bar{\nu}_e$ shows the opposite trend and the summation of two results in a total weak interaction rate $\Gamma_{n\to p}$ that is enhanced by the existence of the magnetic field (see Fig. 2.4). Rewriting Eq. (2.7) with the Fermi distribution given by Eq. (3.45), the electron capture rate in a screened plasma is obtained as:

$$\Gamma^{Bscr}_{pe^-\to n\nu_e} = \frac{G_F^2 T_\gamma^2 (g_V^2 + 3g_A^2) eB}{\pi^3} \sum_{n=0}^{\infty} (2 - \delta_{n0}) \times \int_{m_e\sqrt{1+4\gamma n}}^{\infty} \frac{E_\nu^2 \epsilon'}{\sqrt{\epsilon'^2 - m_e^2(1+4\gamma n)}} \, d\epsilon' \, f_{FD}(\epsilon'; \mu, T_\gamma) g(E_\nu; \mu_\nu, T_\nu). \quad (2.12)$$

Fig. 2.5 shows the weak screening correction of both the electron capture $p + e^- \to n + \nu_e$ and the total $p \to n$ rate as a function of T_9. The vertical axis represents the ratio between the interaction rates with and without the screening correction, where

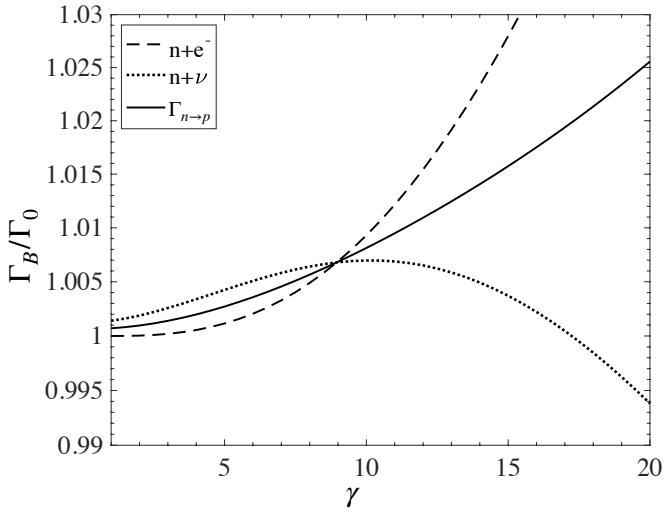

FIGURE 2.4: Weak interaction rate as a function of the scaled magnetic field strength, γ. The dashed line corresponds to the $n + e^+ \to p + \bar{\nu}_e$ rate; the dotted line is the $n + \nu_e \to p + e^-$ rate; and the solid line is the total weak interaction rate $\Gamma_{n\to p}$. For the $n \to p + e^- + \bar{\nu}_e$ rate, we assumed a zero neutrino chemical potential so that this term can be neglected. Here the temperature is set as $T_9 = 10$.

the magnetic field effect on the Fermi distribution is included. The weak screening correction increases the electron capture rate (upper panel). Therefore, the total weak reaction rate $\Gamma_{p\to n}$ increases (lower panel) and finally leads to a higher neutron fraction (see Fig. 2.6 below). For a strong B-field (purple line, $\gamma = 100$), the impact can be over 0.6% at $T_9 \sim 2$. The change itself is small. However, considering the present-day Y_p observation, any corrections which affect weak rates by $\mathcal{O}(10^{-4})$ can be constrained by Y_p abundance observations (Pitrou et al., 2018), which suggests the possibility of using the weak screening correction to constrain the PMF since the weak interaction plays a leading role before BBN started.

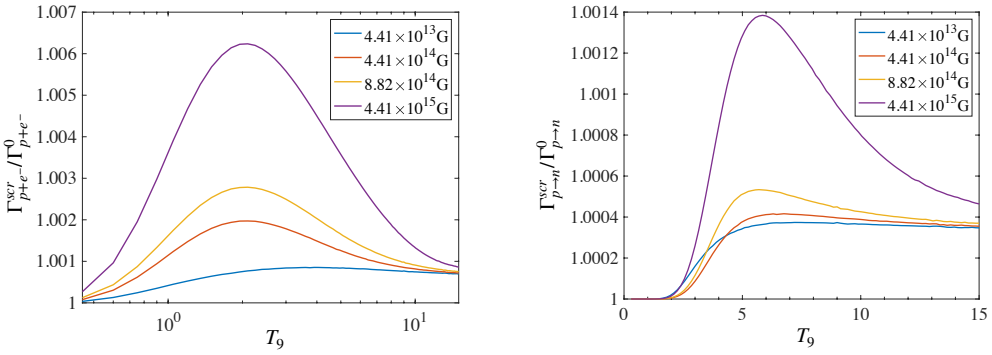

FIGURE 2.5: The screening correction to the $p + e^- \to n + \nu_e$ reaction rate and the total $p \to n$ rate as function of T_9 for various field strengths.

2.2.3 Constraints of Primordial Magnetic Field

This section considers contributions to the final element abundances arising from the weak screening correction of the electron capture rate. Adapting the Thomas-Fermi length formula of Eq. (2.4), the screening corrections are taken into account using Eq. (2.7). A standard BBN nuclear reaction network code (Kawano, 1992; Smith, Kawano, and Malaney, 1993) is used and I have updated the reaction rates of nuclei with mass numbers $A \leq 10$ using the JINA REACLIB Database (Cyburt et al., 2010; Coc et al., 2015). The neutron lifetime is taken as 880.2 ± 1.0 s, corresponding to the central value of the Particle Data Group (Patrignani, 2016). The baryon-to-photon ratio η is taken to be $\eta_{10} \equiv \eta/10^{-10} = (6.16 \pm 0.02)$ calculated using a conversion of the baryon density in the standard ΛCDM model determined from Planck analysis of Aghanim (2020). PMF could also affect the thermodynamics of electrons and positrons since these leptons have larger magnetic momentum compared with charged baryons. The modification on the thermodynamics could further affect the derivatives of photon temperature (i.e., dT_γ/dt) because the conservation of energy requires $d[(\rho_{em} + P_{em})R^3] = R^3 dP_{em}$,with $\rho_{em} = \rho_e + \rho_\gamma$ and $P_{em} = P_e + P_\gamma$ (See detail in Appendix C). In this study, these two impacts from PMF were also included.

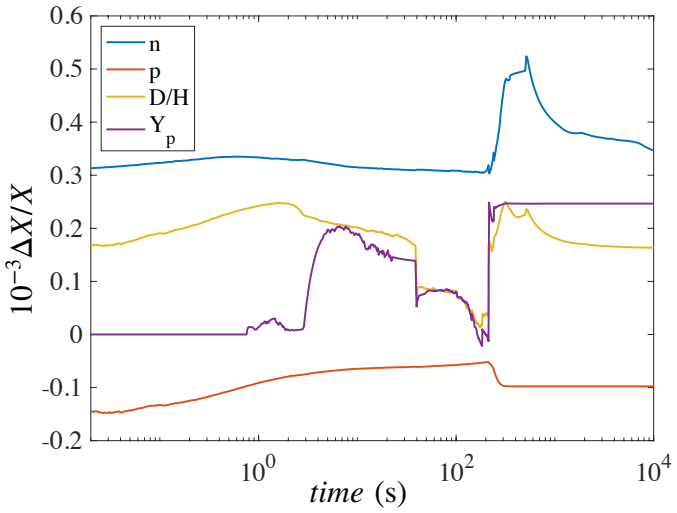

FIGURE 2.6: Relative change of light nuclear abundances (n, p, D/H and Y_p) due to the weak screening correction on the electron capture reaction, i.e. $p + e^- \rightarrow n + \nu_e$, in the BBN network as a function of time. Effects from the magnetic field on the Fermi distribution function at the relevant BBN temperatures are negligible as shown in Figure 2.3.

Fig. 2.6 shows the ratios of final abundances of light nuclei (n, p, D/H and Y_p) with weak screening effects on the electron capture rate to those calculated without screening effects. The quantity Y_p is effectively determined by $2n/(n+p)$ at the ^{4}He synthesis at $t \sim 180$ s. Therefore, the higher neutron fraction naturally leads to a higher ^{4}He mass fraction.

I consider a constraint on generation epoch of the PMF. In this study, the "frozen-in" PMF model is employed, i.e., the PMF energy density decreases as $\rho_{PMF} \propto 1/a^4$ where a is the scale factor of the Universe. Current constraints on the PMF from light element abundance observations can only provide us with an upper limit of the field strength (Grasso and Rubinstein, 1995; Kernan, Starkman, and Vachaspati,

1996; Kawasaki and Kusakabe, 2012). I have investigated three main effects from the PMF on the electron/positron thermodynamics, the time-temperature relation, and thermonuclear reaction rates (Kawasaki and Kusakabe, 2012). The impact on the weak interaction rates are always neglected due to the large uncertainty of past Y_p observations (Kawasaki and Kusakabe, 2012). However, the updated observational constraint on primordial ^{4}He abundance is accurate to within 0.1%.

Fig. 2.7 shows the constraint on the generation epoch and the strength of the PMF. The horizontal axis is the strength of the PMF in unit of B_c at $T_9 = 10$, and the vertical axis is the temperature at which the PMF is generated. Only the PMF generated before the neutrino decoupling at $T \sim 1$ MeV is considered, and vertical axis is only shown above $T_9 = 10$ accordingly. The "frozen-in" PMF generated at different temperatures is encoded into the BBN calculations. The shaded region on the right-upper part of the figures is ruled out by Y_p observations $Y_p = (0.2449 \pm 0.0040)$ (Aver, Olive, and Skillman, 2015). Although the ^{4}He abundance is sensitive to the n/p ratio, for the lately ($T_9 < 15$) generated PMF the constraint is weaker since the weak reaction rates drop quickly when temperature decreases. Thus, such a PMF cannot alter Y_p as significantly as the early generated PMF, which means one can introduce a stronger PMF at later times without changing the calculated ^{4}He abundance. The enhancement of weak interaction rates induces a tighter constraint on the PMF. The weak screening correction to fusion reactions does not make a significant change in BBN due to the low electron-positron density at the BBN epoch.

In Fig. 2.7, all effects from the PMF summarized in Ref. Kawasaki and Kusakabe (2012) have been taken into account (shown in the dark gray region). A more accurate constraint on the B field based on the consideration of the weak interaction rate enhancements via the PMF is shown by the light gray region. It is clearly seen that such effects can provide a narrower constraint on the PMF strength. Because weak interactions decouple at $T \sim 0.8$ MeV, the PMF generated well before this epoch plays an important role in determining the light element abundances. According to Fig. 2.5, the screening corrections can increased with increasing magnetic field. This is also taken into account and indicated by a blue line.

Recent high-accuracy BBN calculations suggest an underproduction of D for $\eta_{10} = 6.10$ when compared to the mean value of the D observation, i.e., D/H= $(2.527 \pm 0.03) \times 10^{-5}$ (Cooke, Pettini, and Steidel, 2018). Uncertainties in nuclear reaction rates for D destruction result in a ~ 1.5 % error in the predicted D abundance, i.e., D/H=$(2.459 \pm 0.036) \times 10^{-5}$ (Pitrou et al., 2018). Therefore, there is a possible discrepancy at $\sim 2\sigma$ level. The solution of such discrepancy from the standpoint of modifications of weak and fusion reactions by the PMF is also considered. I have already shown that the ^{4}He abundance constraint allows a PMF with $\gamma < 0.58$. Moreover, when the D/H constraint is also taken into account, recent observations can actually exhibit clear discrepancy with PMF since both D/H and ^{4}He abundances are enhanced when PMF is included (Grasso and Rubinstein, 1995; Kawasaki and Kusakabe, 2012; Yamazaki and Kusakabe, 2012). Fig. 2.8 shows the contour plot of both D/H and Y_p observational abundance constraints. The green region is the observational constraint D/H $= (2.527 \pm 0.03) \times 10^{-5}$, and it is clear that for the PMF model with strength parameter $\gamma = 0.37 - 0.54$, the D/H prediction is consistent with the observation. Such a PMF is not ruled out by taking account of the Y_p observational constraint as well. If the "D underproduction problem" were confirmed in extensive and more accurate observations in the future, it would be provide an additional explanation for faster cosmic expansion triggered by a large effective number of neutrino families $N_{\rm eff}$ (Cyburt et al., 2016) due to a sterile neutrino or something equivalent to it.

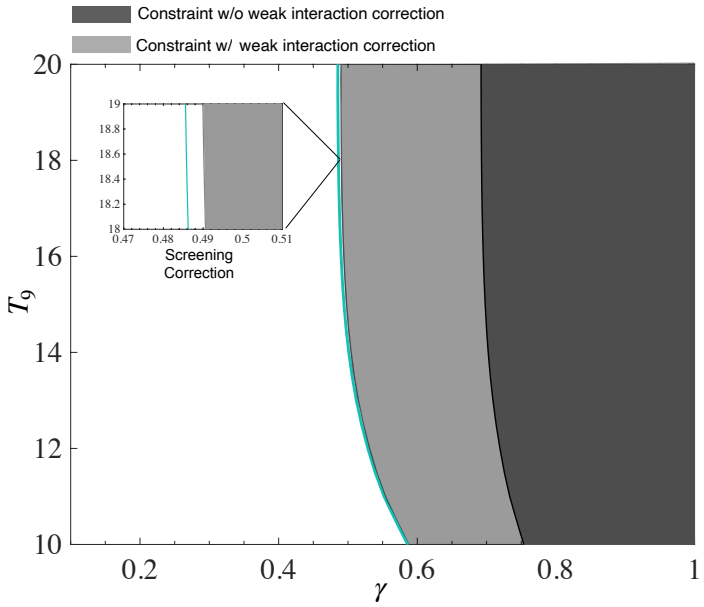

FIGURE 2.7: Constraints of the PMF generation epoch and strength from the Y_p observational value. The light gray shaded region is excluded if the modification of weak reaction rates by the magnetic field is taken into account. The dark gray region is excluded by prior work (Yamazaki and Kusakabe, 2012; Kawasaki and Kusakabe, 2012), in their study the PMF impacts on weak interaction are ignored. The constraint from the screening correction of weak reaction rates is shown by the blue line. This constraint is negligible since the density of electrons and positrons during the BBN epoch is low. Here the γ value of the PMF is taken at $T_9 = 10$.

In Table 2.1, I compare the observational constraints on primordial abundances with the theoretical predictions in three models, i.e., (1) the SBBN, (2) the BBN model with the screening correction, and (3) the BBN model with the screening correction and PMF effects for $\gamma = 0.4$, for example. Although the "D underproduction problem" in the SBBN is not solved in model (2) because of its very small effect, it is solved when a "frozen-in" PMF with strength $\gamma = 0.37 - 0.54$ is introduced in the model (3). Neither the screening effect nor the "frozen-in" PMF model can alleviate the cosmic lithium problem. Uncertainties in the nuclear reaction rates for ^{7}Be production and destruction have been reduced by recent experiments on ^{7}Be destruction reactions. As for the primary destruction reaction ^{7}Be(n,p)^{7}Li, a recent measurement at the neutron time-of-flight (n_TOF) facility of CERN showed that the cross section is significantly higher than previous measurements in the low neutron energy region of $E_n \sim 10^{-2}$ MeV, while it is consistent with the old measurements for higher energies (Damone, 2018). Replacing the old reaction rate by the newly derived rate, the predicted ^{7}Li abundance becomes smaller by at most 12%. The effect of including the first excited state of ^{7}Li in the final state is investigated by the Center for Nuclear Study Radioactive Isotope Beam separator via analyzing Q-value spectra of the ^{7}Be(d,^{7}Li p)^{1}H and ^{7}Be(d,2α)^{1}H reactions, the results show a one-tenth reduction of the final ^{7}Li abundance prediction (Hayakawa et al., 2021). The reaction cross section of ^{7}Be(d,2α)^{1}H has been recently measured in the energy range relevant to BBN (Rijal et al., 2019). The new cross section leads to a 1.4%–8.1% decrease of the primordial ^{7}Li abundance compared to the case without the ^{7}Be(d,2α)^{1}H reaction. The cross

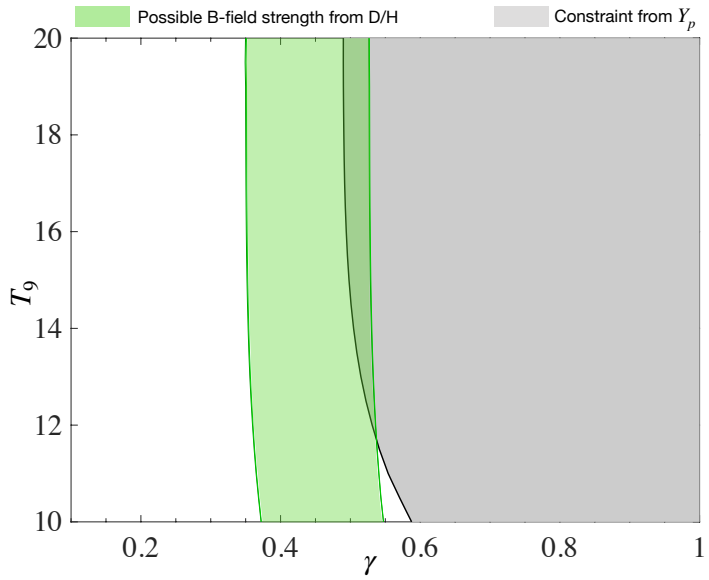

FIGURE 2.8: Range of PMF strength constrained by deuterium abundance observations, i.e., $\mathrm{D/H} = (2.527 \pm 0.03) \times 10^{-5}$. Here the scaled value of the PMF, γ, is taken at $T_9 = 10$. The gray region is excluded by constraints from ^{4}He abundance observations while the green region is allowed by deuterium abundance observations.

section of the reaction ^{7}Be(n,α)^{4}He has also been determined precisely at the n_TOF facility in CERN ($E_n \lesssim 10$ keV) (Barbagallo, 2016), the n_TOF in the Research Center for Nuclear Physics, Osaka University (the center of mass energy $E_{\mathrm{CM}} = 0.20$–0.81 MeV) (Kawabata, 2017), and the EXOTIC facility of Laboratori Nazionali di Legnaro ($E_n = 0.03$–2 MeV) (Lamia, 2019). The contribution of this reaction to the destruction of ^{7}Be during the BBN was found to be negligibly small.

2.2.4 Results & Discussions

In this Section, I investigated weak screening corrections from the PMF and the impact of these corrections on the electron capture rate. The lowest-order screening effect is to shift kinetic energies of electrons and positrons. The impact from such corrections on the BBN is explored , and it is found that an enhancement of the ^{4}He abundance by a factor of $\mathcal{O}(10^{-4})$. Then, I considered the configuration with a background PMF in which the electron and positron energy distributions are altered by Landau quantization. The presence of an external magnetic field results in a shift in the screening potential. Moreover, with the existence of an external magnetic field, the weak screening correction can enhance the electron capture rate by a factor of $\mathcal{O}(10^{-3})$. Such effects on the electron capture rate can be negligible due to the low density at BBN epoch.

The magnetic field results in a reduction of the rate for the reaction $n + \nu_e \to p + e^-$ while the rate for the $n + e^+ \to p + \bar{\nu}_e$ reaction is increased. The net rate $\Gamma_{n\to p}$ turns out to be enhanced by the magnetic field effects. I conclude that such an enhancement of weak reaction rates from the background PMF should be taken into account since the accuracy of present-day theoretical calculations requires detailed treatments of any change of weak reaction rate larger than 0.1%.

TABLE 2.1: Comparison between observations and theoretical predictions for primordial abundances. Here in the theoretical calculation, all the cross sections for nuclei $A < 10$ are adopted from the JINA REACLIB Database (Cyburt et al., 2010; Coc et al., 2015). The neutron lifetime is taken as 880.2 s (Patrignani, 2016), the baryon-to-photon ratio η is taken to be $\eta_{10} \equiv \eta/10^{-10} = (6.094 \pm 0.063)$ (Planck Collaboration et al., 2016a). PMF model with strength parameter $\gamma = 0.4$ is used.

	Observ.	SBBN	BBN + Scr Corr.	BBN + Scr Corr. +PMF
Y_p	0.2449(a) $\pm$0.0040	0.2417 $\pm$0.0001	0.24165 $\pm$0.00005	0.2477 $\pm$0.0001
D/H ($\times 10^{-5}$)	2.527 ± 0.03(b)	2.462 ± 0.042	2.462 ± 0.042	2.545 ± 0.043
$A = 7$ ($\times 10^{-10}$)	$1.58^{+0.35}_{-0.28}$(c)	4.90 ± 0.105	4.90 ± 0.105	4.87 ± 0.11

(a)Aver *et al.* (2015) (Aver, Olive, and Skillman, 2015),(b)Cooke *et al.* (2018) (Cooke, Pettini, and Steidel, 2018),(c)Sbordone *et al.* (2010) (Sbordone, 2010).

Finally, the generation epoch of a "frozen-in" PMF has been constrained by considering its impact on weak interactions. Comparing the theoretical ^{4}He yield with observations, we find that a late PMF generation epoch at $T_9 < 15$ is more favored.

Moreover, the “D underproduction problem” in SBBN could be solved by including the effects of the PMF, resulting in an enhancement of weak reaction rates. Namely, an allowed region which satisfies both of D/H and Y_p observational abundance constraints in the BBN model with the screening correction and PMF effects is found.

However, the “cosmic Li problem” still remains. Possible solutions to this problem include the following scenarios: (1) BBN models with exotic long-lived negatively-charged particles (Jittoh et al., 2007; Bird, Koopmans, and Pospelov, 2008) or a color (Kawasaki and Kusakabe, 2011) can potentially solve the problem. (2) The existence of a sterile neutrino during the BBN can reduce the ^{7}Li abundance significantly only if its mass and lifetime are in specific ranges (Kusakabe et al., 2013; Ishida, Kusakabe, and Okada, 2014). (3) An ambipolar diffusion of abundant $^7Li^+$ ions via the PMF during structure formation can result in Li abundances in structures smaller than the cosmic average value (Kusakabe and Kawasaki, 2015; Kusakabe and Kawasaki, 2019). (4) If population III (Pop III) stars deplete Li with a very large formation rate and if they do not produce Li via the neutrino process, the Li abundance can temporarily decrease in the early structure formation epoch (Piau et al., 2006). However, a recent calculation of the neutrino process in Pop III stars indicates efficient Li production (Heger and Woosley, 2020). In this case, the Li abundance monotonically increases with time, and this scenario does not provide a solution. However, there remain possibilities of significant Li depletion. (5) ^{7}Li could be destroyed in a highly convective pre-main sequence stage via nuclear burning (Fu et al., 2015) and also (6) during the main sequence via atomic diffusion under stellar gravity (Korn et al., 2006).

2.3 Static Stochastic Magnetic Field

2.3.1 Homogeneous Magnetic Energy Density

The origin and evolution of the galactic magnetic field has been a subject of interest for a number of years. From one view point, the galactic magnetic field might be a fossil remnant of PMFs amplified through the galactic dynamo process (Subramanian and Barrow, 1998; Banerjee and Jedamzik, 2004). Several mechanisms have been proposed to explain the origin of a PMF from early cosmological phase transitions (Takahashi et al., 2005; Ichiki et al., 2006; Durrer and Neronov, 2013; Subramanian, 2016; Yamazaki, 2016). However, these scenario cannot account for a large scale magnetic field. The co-moving correlation length scale for these models is at most given by the horizon during the phase transition, which is much smaller than a typical galaxy size at the present day. One possible solution of this problem is a super-horizon PMF generated during inflation (Turner and Widrow, 1988; Dolgov, 1993; Demozzi, Mukhanov, and Rubinstein, 2009). This kind of magnetic field is "frozen-in" with the dominant fluids. Previous studies have shown that such a PMF can slightly change the weak reaction rate and the electron-positron distribution function while their main effect is the enhancement of the cosmic expansion rate (Grasso and Rubinstein, 1996). In this sub-section, this case of a super-horizon scale magnetic field is considered firstly.

A statistically homogeneous and isotropic magnetic field must have a two-point correlation function for the co-moving wave vector (Kandus, Kunze, and Tsagas, 2011)

$$\langle B_i(\boldsymbol{k})B^i(\boldsymbol{k}')\rangle = 2(2\pi)^3 P_{[\mathrm{PMF}]}(k)\delta(\boldsymbol{k}-\boldsymbol{k}'). \tag{2.13}$$

Here, as in previous studies, the power spectrum of the PMF energy density is assumed to be a power law (PL) spectrum.

$$P_{[\mathrm{PMF}]}(k) = Ak^{n_B}, \tag{2.14}$$

where n_B is the power-law index. This PL spectrum is the most common assumption for magnetic fields on cosmological scales.

One can then derive the normalization coefficient A from the variance of the magnetic fields in real space. The co-moving PMF strength B_λ inside a spherical Gaussian radius should be (Mack, Kahniashvili, and Kosowsky, 2002)

$$\langle B^i(\boldsymbol{x})B_i(\boldsymbol{x})\rangle|_\lambda = B_\lambda^2, \tag{2.15}$$

where λ is a typical co-moving length scale for the present-day, usually set as 1 Mpc. Then, applying a Fourier transform to k space and integrating this together with a window function, the co-moving strength B_λ^2 becomes

$$\begin{aligned}\langle B_i(\boldsymbol{x})B^i(\boldsymbol{x})\rangle|_\lambda = B_\lambda^2 =& \frac{1}{(2\pi)^6}\int d^3k \int d^3k' \\ &\times \exp\left(-i\boldsymbol{x}\cdot(\boldsymbol{k}-\boldsymbol{k}')\right)\langle B_i(\boldsymbol{k})B^i(\boldsymbol{k}')\rangle|W_\lambda^2(k)|.\end{aligned} \tag{2.16}$$

Here, the window function $|W(k)| = \exp\left(-\lambda^2\boldsymbol{k}^2/2\right)$ is required to constrain large values of the wave number. This means that large spatial scales of the PMF are taken into account while the smallest scales are cut off. A lower cutoff of the PMFs results from decay of the magnetic field on small scales. Magneto-hydrodynamical (MHD) turbulence generates such a cutoff (Durrer and Neronov, 2013). It has been pointed out (Brandenburg, Enqvist, and Olesen, 1996) that with random initial conditions for

the magnetic field, turbulence can have an inverse cascade that transfers the magnetic energy density from small scales to large scales. From Eqs. (2.13)−(2.16), the final result (Yamazaki and Kusakabe, 2012) for the energy density contributed from a PMF is

$$\begin{aligned}\langle \rho_{\rm B} \rangle =& \frac{\langle B^2 \rangle}{8\pi} = \frac{1}{8\pi} \int_{k_{[min]}}^{k_{[max]}} \frac{dk}{k} \frac{k^3}{2\pi^2} P_{[\rm PMF]}(k) \\ =& \frac{1}{8\pi} \frac{B_\lambda^2}{\Gamma(\frac{n_B+5}{2})} [(\lambda k_{[max]})^{n_B+3} - (\lambda k_{[min]})^{n_B+3}], \end{aligned} \tag{2.17}$$

where $k_{[max]}$ and $k_{[min]}$ are the maximum and minimum wave numbers, respectively. Their values depend on $\lambda/2\pi$. For example, for an averaged magnetic field strength with $\langle \rho_{\rm B} \rangle = 0.2\rho_{\rm rad}$ with $\rho_{\rm rad}$ the radiation energy density after the epoch of $e^\pm$ annihilation, the magnetic field energy density would be given by

$$\langle \rho_{\rm B} \rangle = 0.2 \frac{\pi g_*}{30} T^4 = 0.2 \cdot 4.506 \text{ g cm}^{-3} \Big(\frac{g_*}{3.36264} \Big) \Big(\frac{T}{10^9 \text{K}} \Big)^4, \tag{2.18}$$

where $g_* = 2 + (7/8) \cdot 6 \cdot (4/11)^{4/3} = 3.36264$ is the effective number of statistical degrees of freedom after the epoch of $e^\pm$ annihilation. For $T = 2.73$K at the present day, $\rho_{\rm Bc} = 1.57 \times 10^{-34}$g cm^{-3} $= 1.412 \times 10^{-13}$erg cm^{-3}. With this amount of magnetic energy, the magnetic field would have a present RMS amplitude of $\langle B^2 \rangle_0^{1/2} = 1.88\mu$G.

It is noticed that this magnitude of the PMF strength is much greater than the upper limit of a few nG on a 1 Mpc co-moving scale for both scale, vector and tensor contributions from the magnetic field. Such value is inferred from the Planck analysis on TT, TE and EE modes of CMB polarization spectra (Planck Collaboration et al., 2016b). However, in the present analysis, a lower cutoff of the correlation scale is adopted below the large scales that are constrained by the CMB power spectrum. Previous studies (Durrer and Neronov, 2013; Brandenburg, Enqvist, and Olesen, 1996) pointed out that MHD turbulence can lead to such a cutoff. Moreover, the fluid-viscosity due to neutrinos and photons can induce damping of magnetic fields (Jedamzik, Katalinic, and Olinto, 1998; Subramanian and Barrow, 1998). In fact, the MHD modes with wavelengths smaller than the mean free path of neutrinos and(or) photons are in such a diffusion regime. Such damping process suggests that a PMF on the smaller scales associated with BBN would dissipate by the time of photon last scattering. Hence, a PMF would only affect the CMB power spectrum via the expansion rate. The Planck constraint of $N_{eff} < 3.6$ (95% C.L.) is consistent with the upper limit of $\rho_{\rm Bc}/\rho_{\rm tot} < 0.2$ adopted here.

Previous studies (Yamazaki et al., 2008) used Eq. (2.18) to constrain the ratio of the SI energy density contributed from the PMF based upon the CMB power spectrum. The primordial element abundances can also be computed (Yamazaki, Ichiki, and Takahashi, 2013; Yamazaki, 2016) by introducing this amount of extra energy density contribution to the total energy density. The present day co-moving length scale λ =1 Mpc corresponds to a length of 10^{15}cm during the BBN epoch, which is well beyond the horizon ($10^{10} - 10^{12}$ cm) during BBN. Hence, within the horizon volume, the averaged magnetic energy density mainly affects BBN through the expansion rate

$$\Big(\frac{\dot{a}}{a} \Big)^2 \equiv H^2 = \frac{8\pi G}{3} \rho_{\rm tot} \propto \rho_\gamma + \rho_{\rm B}; \tag{2.19}$$

$$\frac{d\rho}{dt} = -3H\Big(\rho + p\Big), \tag{2.20}$$

where G is the gravitational constant. The quantities ρ and p are the energy density and the pressure respectively. Since $H^{-1} \propto T_{\rm tot}^{-2}$, the epoch of weak decoupling ($H^{-1} = \tau_{\rm wd}$) occurs when

$$(8\pi G)^{-1} T_{\rm tot}^{-2} \sim G_F^{-2} T_\gamma^{-5}. \tag{2.21}$$

The right hand side results from the fact that the weak-reaction cross sections scale as $G_F^2 T_\gamma^2$ and the background particle number density is proportional to T_γ^3. Then if the magnetic energy density is included, the left hand side of Eq. (2.21) will be smaller ($T_\gamma^{-2} > T_{\rm tot}^{-2}$). This leads to a shorter decoupling time or a higher decoupling temperature $T_{\rm wd}$. Since a larger $T_{\rm wd}$ corresponds to larger n/p ratio, the ^{4}He abundance will increase consequently. Fig. 2.9 shows the primordial element abun-

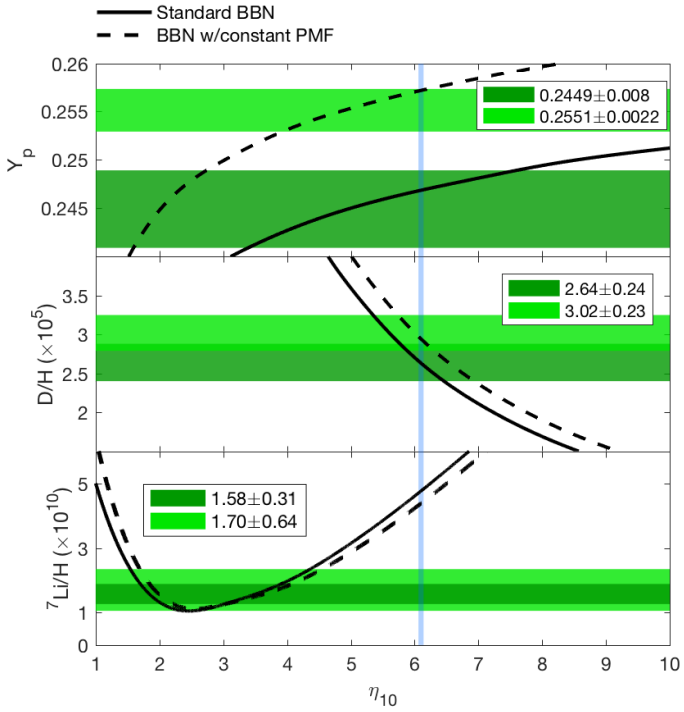

FIGURE 2.9: The calculated isotopic abundances in the SBBN model (solid line) and a BBN model with a constant strength of PMF with $\rho_{\rm B} = 0.13\rho_{\rm tot}$ (dashed line). The observational values are given by green bands for each isotope. The Planck constraint of $\eta \times 10^{10} = 6.16 \pm 0.02$ is given by the vertical blue band. The observed value for each element abundance is given in horizontal painted band. The constraints in the top, middle, and bottom panels are taken from Y_p: Aver, Olive, and Skillman (2010) (dark-green band), Izotov, Thuan, and Guseva (2014) (light-green band); (2)D/H: Cooke, Pettini, and Steidel (2018) (dark-green band), Olive et al. (2012) (light-green band); (3)^{7}Li/H: Sbordone (2010), 1σ (dark-green band) and 2σ (light-green band) respectively.

dances as a function of $\eta_{10} = \eta \times 10^{10}$. The vertical band shows the limits on the baryon to photon ratio derived from the constraints on CMB TT+TE+EE polarization spectra Aghanim, 2020, i.e., $\omega_b h^2 = 0.02236 \pm 0.00015$ in the standard ΛCDM

model. The horizontal shaded bands indicate observational constraints on the element abundances. There remain some ambiguities in the primordial abundances (e.g. Cyburt et al., 2016). Hence, in this work, for each element, two observational constraints are listed to compare with our calculations: (1)Y_p (mass fraction of ^{4}He) : $0.2409 - 0.2489$ (Aver, Olive, and Skillman, 2010), or $0.2551 - 0.2573$ (Izotov, Thuan, and Guseva, 2014); (2)D/H: $2.40 - 2.88 \times 10^{-5}$ (Cooke, Pettini, and Steidel, 2018), or $2.79 - 3.25 \times 10^{-5}$ (Olive et al., 2012); (3)^{7}Li/H: $1.27 - 1.89 \times 10^{-10}$ (1σ from Sbordone, 2010), or $1.06 - 2.35 \times 10^{-10}$ (2σ from Sbordone, 2010).

In Fig. 2.9, Y_p increases as expected when a PMF is introduced. The other primordial elements D, ^{3}He and ^{7}Li are also slightly affected. The amount of PMF energy density is constrained to be $\leq 13\%$ of the total energy density $\rho_{\rm tot}$ in the figure. This is based upon the upper limit to Y_p from the observations of Izotov, Thuan, and Guseva (2014). This is equivalent to a co-moving PMF field strength $\langle B^2 \rangle^{1/2} = 1.51 \mu$G.

2.3.2 Inhomogeneous Magnetic Energy Density

In addition to the effect of a homogeneous PMF energy density, fluctuations of the magnetic field over a wide range of sub-horizon scales will serve as a non-linear driving force that induces the metric fluctuations (Wasserman, 1978). As has already been proposed (Dimopoulos and Davis, 1997; Son, 1999; Dolgov and Grasso, 2002; Banerjee and Jedamzik, 2004), it is possible to have an inhomogeneous sub-horizon PMF in the early Universe. Once the turbulence is produced, an induced MHD dynamo can amplify the field exponentially until equal partition between the plasma turbulent kinetic energy and the PMF energy is eventually reached. This can consequently lead to an inhomogeneity in the energy density (Brandenburg, Enqvist, and Olesen, 1996; Brandenburg, 2001; Christensson, Hindmarsh, and Brandenburg, 2001; Dolgov and Grasso, 2002).

For a magnetic field on small scales, the strength can be damped due to photon and neutrino viscosities. This means that the magnetic field on scales with $L < \sqrt{t_{\rm age}(T)\zeta}$ (Durrer, Ferreira, and Kahniashvili, 2000) dissipates rapidly, where $t_{\rm age}$ is the age of the universe and ζ is the magnetic diffusivity. An estimate of the damping scale due to the viscosity in the magneto-hydrodynamic evolution process is given by splitting long and short wavelength fluctuations in the magnetic field separately (Brandenburg, Enqvist, and Olesen, 1996). Moreover, a magnetic field with scale $L \ll \sqrt{t_{\rm age}(T)\zeta}$ is not easy to generate, while that with $L \gg \sqrt{t_{\rm age}(T)\zeta}$ will not dissipate, and the magnetic field is frozen-in with the dominant fluids (Dendy, 1990). Thus, the survival length scale for the PMF during the BBN epoch with temperature set as 0.3 MeV is $L_{\rm sur} \sim 10^4$ cm (Yamazaki et al., 2012). This is much smaller than the co-moving length scale for which a constraint on the field amplitude is given from the CMB power spectrum, i.e., $1/(1+z)$ Mpc $\sim 10^{15}$ cm for the BBN redshift of $z \sim 10^9$. Therefore, one cannot exclude the possibility of fluctuations in the PMF length scales of the same order as $L_{\rm sur}$. One can also consider that the energy density of the PMF could have some distribution $f(\rho_{\rm B})$ rather than the ideal case with $f(\rho_{\rm B}) = \delta(\rho_{\rm B} - \rho_{\rm Bc})$. The effect of a PMF on baryons and the $e^{\pm}$ plasma has also been studied (Grasso and Rubinstein, 1996; Kawasaki and Kusakabe, 2012). However, the effect they discussed is not very important for the present application since the modification to the distribution functions is proportional to ZeB/T^2. However, if a distribution function $f(\rho_{\rm B})$ exists, then the associated radiation energy density fluctuations can modify the nuclear reaction yields after averaging over all local regions.

Most BBN network calculations have considered the photon energy density to be homogeneous during the entire epoch. Here, however, I consider large-scale energy density fluctuations in the temperature (or equivalently photon energy density). The nuclear reactions occur locally, this means that the local velocity distribution function for baryons is,

$$f_{\rm MB}(v|\beta') = \Big(\frac{m\beta'}{2\pi}\Big)^{3/2} 4\pi v^2 \exp\,(-\frac{\beta' m v^2}{2}). \tag{2.22}$$

Here, β' refers to the inverse temperature $1/kT'$ and T' corresponds to the local temperature. This is just the classical MB distribution which refers to the velocity distribution function of particles for a certain temperature in equilibrium. Since the nucleon gas in the early Universe was dilute, two-body nuclear reactions dominate. The local two-body reaction rate per unit volume can be written as

$$R_{12}(\beta') = \frac{N_1 N_2}{1+\delta_{12}} \langle \sigma v \rangle (\beta'), \tag{2.23}$$

where N_1 and N_2 are the number densities of reacting particles 1 and 2, respectively, δ_{12} is the Kronecker's delta function for avoiding the double counting of identical particles 1 and 2, and $\langle \sigma v \rangle (\beta')$ is the averaged thermonuclear reaction rate for a given temperature written as

$$\langle \sigma v \rangle (\beta') = \int \sigma(E) v f_{\rm MB}(v|\beta') dv = \int \Big(\frac{m\beta'}{2\pi}\Big)^{3/2} 4\pi v^3 \sigma(E) \exp\,(-\frac{\beta' m v^2}{2}) dv, \tag{2.24}$$

where m_{12} is the reduced mass of the system 1+2. Because local fluctuations of the energy density occur due to the inhomogeneous PMF, locally nuclei obey a classical MB distribution with inverse temperature equal to β'. The thermonuclear reaction rates averaged over the set of temperature fluctuations is then given by

$$\begin{aligned} \langle \sigma v \rangle (\beta) &= \int \langle \sigma v \rangle (\beta') f(\beta') d\beta' \\ &= \int \Big[\int \sigma(E) v f_{\rm MB}(v|\beta') dv \Big] f(\beta') d\beta' \\ &= \int \sigma(E) v F(v) dv. \end{aligned} \tag{2.25}$$

In the last equation, a new function $F(v)$ is defined, which is independent of β' as an effective distribution function averaged over the set of temperature fluctuations[2] In principle, the evolution of nuclear abundances should be solved inhomogeneously, i.e. the abundance at a given time depends on locations, i.e., $\mathrm{Y}_i(t,x)$. But in the present calculation, the inhomogeneity of nuclear abundances is neglected, i.e., $\mathrm{Y}_i(t)$. Then, an average distribution function can be defined.

$$F(v) \equiv \int d\beta' f(\beta') f_{\rm MB}(v|\beta'). \tag{2.26}$$

Here, $f(\beta')$ is the distribution function of β' generated from averaging over fluctuations of the energy density. The derivation of this deviation from a classical MB distribution is similar to that deduced in Beck (2001) in terms of Tsallis statistics.

[2]Note: $F(v)$ is the average velocity distribution function over a length scale much longer than the typical size of magnetic domains' but not a real particle velocity distribution.

Now, one can invoke the central limit theorem and simply assume that the distribution function of magnetic energy density $f(\rho_B)$ follows a gaussian distribution with a peak located at the mean value ρ_{Bc} ($\langle\rho_B\rangle$ in Eq. (2.17))

$$f(\rho_B) = \frac{1}{\sqrt{2\pi}\sigma_B^+} \exp\Big[-\frac{(\rho_B - \rho_{Bc})^2}{2\sigma^{+2}_B}\Big]. \tag{2.27}$$

I then introduce the fluctuation parameter σ_B as a dimensionless quantity, i.e., $\sigma_B = \sigma_B^+/\rho_{Bc}$ to describe the fluctuations of the PMF. In the limit of $\sigma_B \to 0$, this is a delta function which corresponds to the homogeneous case. The total energy density is assumed as a uniform quantity for all volumes, but with some fraction contributed from the magnetic energy density:

$$\rho_{tot} = \rho_B + \rho_{rad} = const, \tag{2.28}$$

an effective temperature T_{eff} can be defined as

$$\rho_{tot} = \frac{\pi g_*}{30} T^4_{eff}. \tag{2.29}$$

Since ρ_{tot} is constant, the magnetic energy density can not exceed ρ_{tot} in which case ρ_{rad} would obtain an unphysical negative value. Here, a cut-off is imposed to the distribution function $f(\rho_B)$ ($\rho_B < 0.25\rho_{tot}$). Fig. 2.10 shows Gaussian functions for

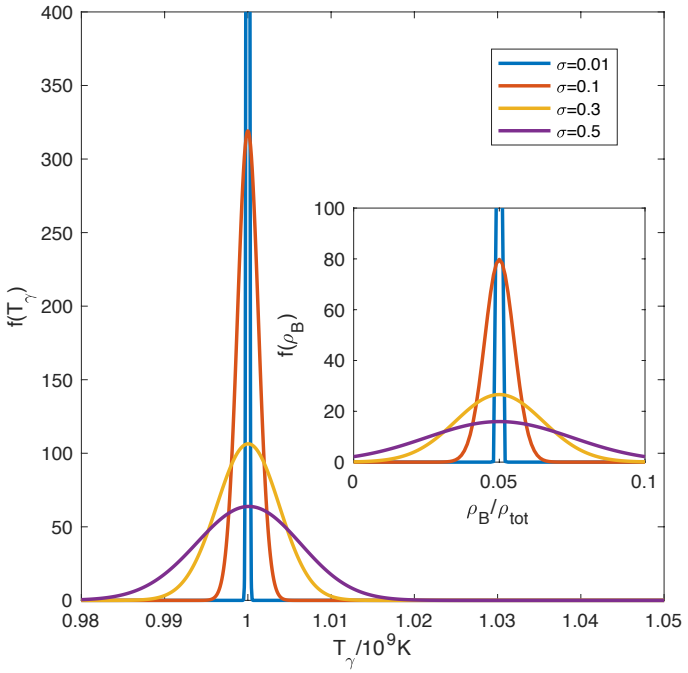

FIGURE 2.10: Temperature distribution under the assumption of an inhomogeneous PMF strength. Here T_γ is in units of $10^9 K$ (centered at $T_9 = 1$) and $\langle\rho_B\rangle$ is taken as 0.05 of ρ_{tot}. When $\sigma_B < 0.01$. the distribution function $f(T_\gamma)$ can approximately be treated as $\delta(T_\gamma - 10^9 K)$.

various values of σ_B. Since it is not expected that a very large inhomogeneity in the magnetic energy density strength during BBN, a narrow distribution $f(\rho_B)$ is required. For $\sigma_B < 0.65$, $f(\rho_B)$ is consistent with our cut-off range for ρ_B. The photon temperature T_γ determines the radiation energy density as $\rho_{rad} \propto T_\gamma^4$, so Eq. (2.28)

becomes

$$\beta = 1/T_\gamma = \Big[T_{\rm eff}^4 - \frac{30}{\pi g_*}\rho_{\rm B}\Big]^{-1/4}. \tag{2.30}$$

The final expression for the distribution function for β is then

$$f(\beta) = \frac{1}{\sqrt{2\pi}\sigma_{\rm B}} \exp\Big[-\frac{(\frac{\pi g_*}{30}(T_{\rm eff}^4 - \beta^{-4}) - \rho_{\rm Bc})^2}{2\sigma_{\rm B}^2}\Big]\frac{2\pi g_*}{15}\beta^{-5}. \tag{2.31}$$

2.3.3 Effect on Reaction Rates

Adopting this as the distribution function, it is shown that the averaged charged particle reactions are affected significantly by the inhomogeneous temperature distribution. For neutron induced reactions, the transmission probability of a neutron through the nuclear potential surface is proportional to the inverse of the velocity v within the assumption of a sharp potential surface (Bertulani and Kajino, 2016). Hence, the cross section is usually expressed as $\sigma(E)_{\rm neutral} = R(E)/v$, where $R(E)$ is a smooth function. Therefore, the change of reaction rates is mainly determined by the deviation of the average distribution function from a MB distribution function. This is not a large effect as shown in Fig. 2.11 (solid straight line and dashed straight line).

For charged particle reactions, the astrophysical S-factor is introduced to rewrite the cross section $\sigma(E)$ in terms of a much smoother dependence on the center of mass energy E :

$$\sigma(E)_{\rm charged} = \frac{\exp\left[-2\pi\eta(E)\right]}{E}S(E), \tag{2.32}$$

where $\exp\left[-2\pi\eta(E)\right]$ approximately expresses the probability to penetrate the Coulomb barrier. This is also known as Gamow factor, $2\pi\eta(E) = \sqrt{E_G/E}$. Eq (2.24) is peaked at the so called Gamow energy $E_G = 2m_{12}(\pi e Z_1 Z_2)^2$.The deviation from a MB distribution function in the inhomogeneous PMF model is not large. However, the impact on reaction rates can increase when taken into account the factor of $\exp\left[-2\pi\eta(E)\right]$ for charged particle reactions as shown in Fig. 2.11. The distribution function (shown by straight lines) in our PMF model looks similar to MB distribution function. However, $\exp\left[-2\pi\eta(E)\right]$ is also a energy dependent function, and the inhomogeneous PMF model suggests an effective reduction of the Gamow window derived by multiplying this term with the average distribution function $F(v)$. In conclusion, for the case of an inhomogeneous PMF during BBN epoch, the effect generated from the distribution of PMF energy density can be divided into two parts: 1) changes in the Hubble expansion rate (see Section 2.3.1) and 2) changes within nuclear reaction rates due to an effective non-MB averaged distribution function when calculate the sum of averaged thermonuclear reaction rates in all domains.

2.3.4 Results & Discussions

I encoded the temperature averaged reaction rates as described in Eqs. (2.25) and (2.31) to calculate the BBN reaction network and compare the results with the observationally inferred abundances for D, ^{4}He and ^{7}Li. The current Particle Data Group world average value $\tau_n = 880.3$ s is used for the neutron lifetime (Olive and Particle Data Group, 2014). The baryonic density of the Universe or η is now deduced to be $\eta_{10} = 6.10 \pm 0.04$ (Planck Collaboration et al., 2016a) from the observations of the anisotropy of the CMB radiation. Fig. 2.12 shows the parameter dependence of the final primordial light element abundances as a function of $\rho_{\rm Bc}$ (left panel) and

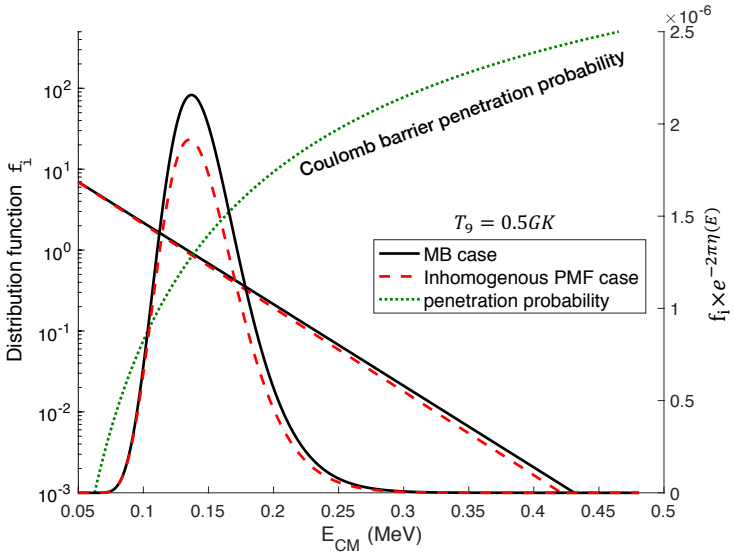

FIGURE 2.11: The deviation of the Gamow window for the ^{3}He(α, γ)^{7}Be reaction in our PMF model from that of the MB case at $t \sim 670s$ which corresponds to $T_9 = 0.5$ in SBBN. Although the deviation of the distribution function itself is not large (solid straight line versus the dashed straight line), the Gamow peak in the PMF model (dashed curve) is suppressed compared with the classical Gamow peak for the homogeneous BBN (solid curve).

σ_B(right panel). In the left panel, element abundances are presented as a function of mean magnetic energy density (ρ_{Bc}) for a fixed value of $\sigma_B = 0.05$. The effect of ρ_{Bc} on the primordial element abundances is consistent with a PMF model with a homogeneous energy density in the previous study of Yamazaki and Kusakabe (2012): ^{4}He is most sensitive to the changes of the cosmic expansion rate, which is equivalent to a change of ρ_{Bc}. The constraint from the observed value of Y_p and D/H implies that the PMF mean energy density has an upper limit of $\rho_{Bc} < 0.13\rho_{tot}$. The right panel shows the element abundances as a function of the fluctuation parameter σ_B. For this panel, it is set as $\rho_{Bc}/\rho_{tot} = 0.13$ which is the upper limit from the Y_p observations. In the case that the fluctuation parameter approaches $\sigma_B \to 0$ (i.e no fluctuation occurs), the result is consistent with the homogeneous energy density PMF model of Yamazaki and Kusakabe (2012). As σ_B increases, the inhomogeneity enhances. This affects the element abundances. It is also generally true that as the D abundance increases, the ^{7}Li production is reduced. In this case, the other primordial abundances are strongly dependent on σ_B, while Y_p remains nearly the same as in the case of the homogeneous PMF model. This is a completely new effect on BBN from a PMF model which includes spatial inhomogeneities in the energy density. Finally, from the Y_p and D constraints, we obtain $\rho_{Bc}/\rho_{tot} = 0.08 - 0.13$ and $\sigma_B = 0.04 - 0.17$ without violating the observational constraints on the ^{4}He and D abundances.

Fig. 2.13 illustrates the light element abundances as a function of η_{10} with the allowed parameter values of ρ_{Bc} and σ_B. In the grey region, the D/H and Y_p calculations are consistent with observations, and the ^{7}Li/H value is reduced to $(3.18 - 3.52) \times 10^{-10}$ compared with SBBN. However, this is still above the Spite plateau (Spite and Spite, 1982; Sbordone, 2010). The calculated primordial element abundances for $\eta_{10} = 6.10$ are shown in Table.2.2. Finally, by keeping $\rho_{Bc}/\rho_{tot} = 0.13$ which is the upper limit for the mean magnetic energy density, it is found that the

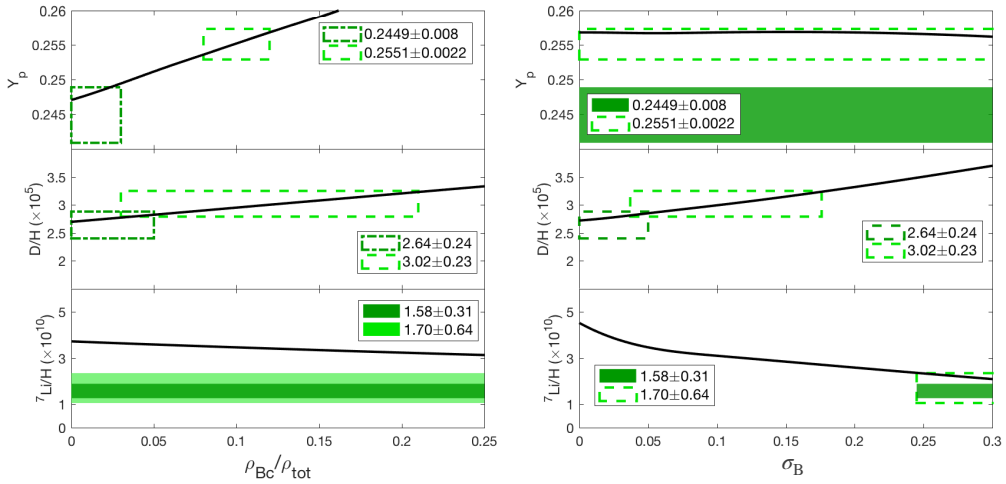

FIGURE 2.12: Abundances of Y_p (mass fraction of ^{4}He), D/H and ^{7}Li/H as a function of ρ_{Bc}(left panel) and σ_B (right panel). In the left panel, the fluctuation parameter σ_B is fixed as 0.05. In right panel, the mean value for the PMF strength is chosen as $1.51\mu G$ thus $\rho_{Bc}/\rho_{tot} = 0.13$. The baryon to photon ratio η is set to the best fit value of $\eta_{10} = 6.16$ from Planck analysis (Aghanim, 2020). In this figure, both boxes and painted patches refer to the observational constraints on elemental abundances. If the calculated curves have an overlap with observational data, boxes are used. Otherwise painted patches are used.

TABLE 2.2: Predicted abundances for the BBN primordial light elements ($\eta_{10} = 6.10$). Observational data are listed for comparison. For the PMF case, $\rho_{Bc}/\rho_{tot} = 0.08 - 0.13$ is set based upon the Y_p and D constraints.

Abundance	SBBN	PMF with $\sigma_B = 0.04 - 0.17$	Observation
$\mathbf{Y_p}$	0.2469	$0.2503 - 0.2536$	0.2551 ± 0.0022
D/H($\times 10^5$)	2.57	$2.75 - 2.96$	3.02 ± 0.23
^{7}Li/H($\times 10^{10}$)	4.91	$3.18 - 3.52$	1.70 ± 0.64

predicted ^{7}Li/H abundance reduces to 1.89×10^{-10} with a fluctuation parameter $\sigma_B = 0.37$ (dash-dotted line in Fig.2.13). Since this parameter region is inside the allowed region of observed η, the 'Lithium Problem' may be solved in this model. However, the D abundance is D/H$= 3.76 \times 10^{-5}$ which is inconsistent with the observational upper limits (Olive et al., 2012; Cooke, Pettini, and Steidel, 2018).

The thermonuclear reaction rates are key factors in determining the final primordial abundances. As shown in Fig. 2.13, D/H is enhanced and ^{7}Li/H reduced as a result of an inhomogeneous PMF energy density model. The $n(p,\gamma)^2$H reaction is the main production mechanism for deuterium, while the ^{2}H(d,n)^{3}He and ^{2}H(d,p)^{3}H reactions are the main destruction channels. For ^{7}Li (or ^{7}Be), the main production reaction is ^{3}He$(\alpha,\gamma)^7$Be. The main destruction process is ^{7}Be$(n,p)^7$Li. In Fig. 2.14, it is shown that the reduction fraction for charged particle reaction rates in our PMF model compared with the SBBN results as a function of temperature. For lower temperature, the reduction is larger than that at higher temperature. Since the reaction ^{3}He$(\alpha,\gamma)^7$Be has the largest Coulomb barrier, the reduction is large compared to the

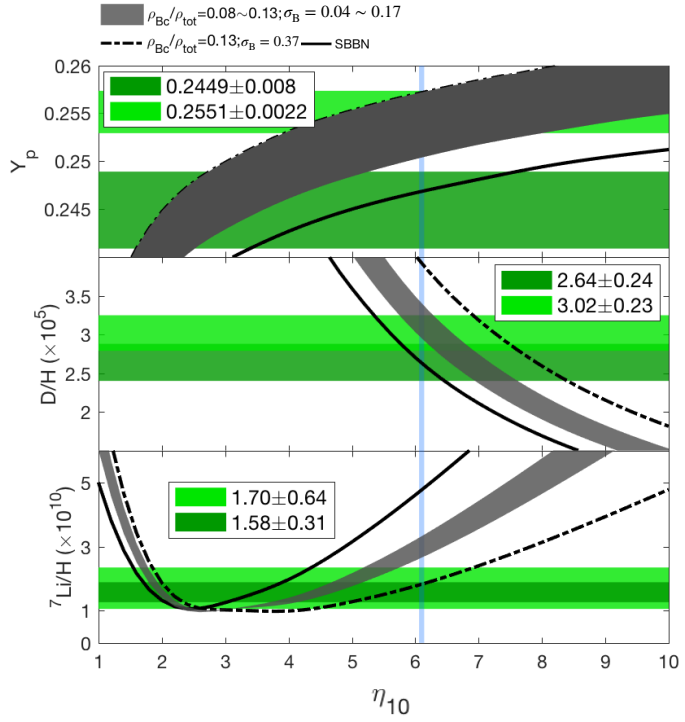

FIGURE 2.13: Abundances of Y_p, D/H and ^{7}Li/H as a function of the baryon to photon ratio η. The boxes show the adopted observational constraints similar to those in Fig. 2.9. This figure shows that larger σ_B values can suppress the production of ^{7}Li but increase the value of D/H. The vertical blue band shows the Planck constraint on η_{10}.

D destruction reactions. For deuteron destruction reactions, i.e., ^{2}H(d,n)^{3}He (dotted line) and ^{2}H(d,p)^{3}H (dash-dotted line), the same trend can be seen in the low energy region since they have the same Gamow energy E_G. The solid line shows a larger reduction for the beryllium production rate ^{3}He$(\alpha,\gamma)^7$Be at low temperature. Because of the stronger Coulomb repulsion for this reaction, a large E_G contributes to a steeper exponential term for charged particle reaction rates (cf. Fig. 2.12).

The extra energy contribution from PMF to the Hubble expansion rate could enhances the D, ^{4}He abundance while reduces the ^{7}Li abundance. The enhancements of D and ^{4}He abundance are due to the earlier weak interaction decoupling time, which results in a larger n/p ratio as well as the earlier freeze out of ^{1}H(n,γ)D reaction, such impacts are discussed in Sect. 2.2. However, the ^{7}Li is not sensitive to such influence, instead, the reduction on ^{7}Li abundance is a non-linear dependence on PMF energy density, which is a consequence from the thermonuclear reaction network. In our inhomogenous PMF model, a homogeneous Hubble expansion rate is used by adding the ρ_{Bc} to the ρ_{tot} which affect the D and ^{4}He abundance, on the other hand, the σ_B decides the width of the inhomogeneity, i.e., effectively, there exists patches with $\rho_B > \rho_{Bc}$, and such an impact could further reduce the ^{7}Li abundance, another impact is from the lower cut-off of the ρ_B to prevent negative PMF energy density, which results in the shifting of effective temperature in the thermonuclear reaction to a lower value. Hence, it is concluded that all 3 elemental abundances are influenced by an inhomogeneous PMF model, specifically, D and ^{4}He are enhanced due to the early decoupling time of weak interaction, and ^{7}Li is suppressed due to the non-linear dependence on the inhomogeneous PMF energy density. Fig. 2.15 shows such a non-linear dependence of the ^{7}Li abundance with

the PMF energy density.

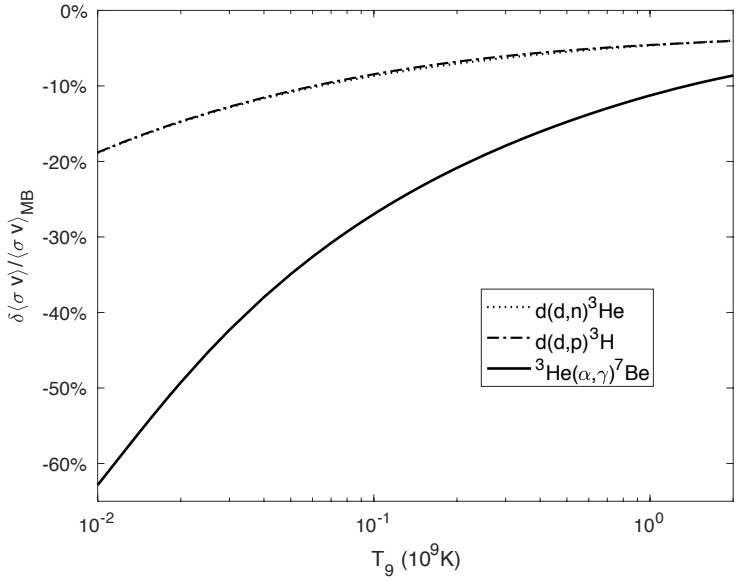

FIGURE 2.14: Ratio of reduction in reaction rates of charged particles from an inhomogeneous strength PMF model compared with the MB case. Here, $\sigma_B = 0.15$.

The above discussion is based on the presumption that no other physical process occurs between BBN and the photon last scattering epoch so that the η value from the Planck analysis is the same as that during BBN. Fig. 2.16 explores the possibility to find a parameter region with a concordance for all light element abundances with a higher value for the baryon-to-photon ratio. The fraction ρ_{Bc}/ρ_{tot} is chosen as 0.11 which is the mean magnetic field strength constrained from the observed mean ^{4}He abundance. In the left panel, the calculated element abundances are shown as functions of η_{10} for the fluctuation parameter $\sigma_B = 0.53$. Although there is no solution to the Li problem within the η_{10} range of Planck (light blue vertical band), at $\eta_{10} = 8.2 \pm 0.1$ (light orange vertical band), all of the elements fall into a region that is consistent with the observational constraints. In the right panel, I expand this result to a parametric study of the fluctuation parameter σ_B. This panel shows contours for light nuclear abundances in the plane of η_{10} and σ_B. The upper limit of $\sigma_B \leq 0.65$ satisfies our upper limit on the contribution of the PMF for the case of $\langle\rho_B\rangle = 0.11\rho_{tot}$. Here, for a larger fluctuation parameter σ_B which is taken to be $0.45 - 0.61$, there is an area (grey-shaded area) in which the abundances of all light elements D, Y_p and ^{7}Li are consistent with observations. However, the baryon-to-photon ratio in this region is $\eta_{10} = 7.59 - 8.97$, which is larger than the Planck observational constraints (light blue vertical band). This larger η value might due to the spatial inhomogeneity of baryon or photon distribution in isothermal fluctuations, i.e., baryon-inhomogeneous BBN models (Applegate, Hogan, and Scherrer, 1987; Alcock, Fuller, and Mathews, 1987; Fuller, Mathews, and Alcock, 1988; Kajino, 1991; Orito et al., 1997; Lara, Kajino, and Mathews, 2006; Nakamura et al., 2017) have pointed out such a scenario. In Sect. 2.4, the full MHD process during BBN could also result in both inhomogeneities of PMF and baryon-number density, and leading to such larger η value consequently.

It is noticed that a dissipation of the PMF between BBN and the last scattering of the background radiation could result in an evolution of the η value (see Sec. IV-B in Yamazaki and Kusakabe, 2012). For example, an 11% increase in the total energy

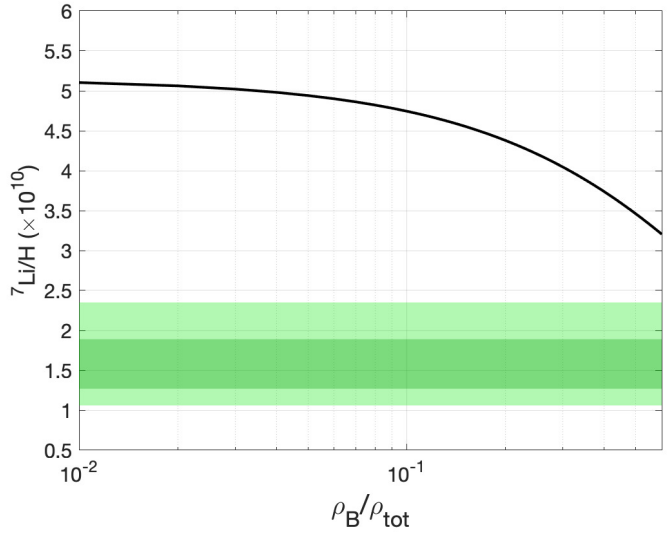

FIGURE 2.15: The non-linear dependence of ^{7}Li abundance on the PMF energy density ρ_B. Due to the non-linearity, the ^{7}Li abundance in patches with $\rho_B > \rho_{Bc}$ is suppressed more than the patches with $\rho_B < \rho_{Bc}$ in such an inhomogeneous PMF model, then, effectively, the averaged ^{7}Li abundance is reduced compared with the homogeneous PMF model with $\rho_B = \rho_{Bc}$.

density by the PMF leads to a 13.5 % increase in the photon number density from the case without dissipative heating. As a result, the η value during BBN would be 13.5% larger than the value after the dissipation. Since this change is not enough to explain the 30% increase required for the high η value in Fig. 2.16 (left panel), the inhomogeneous PMF model alone still cannot completely solve the Li problem.

However, there are other possible astrophysical and cosmological effects that might solve the Li problem: The first is the inhomogeneous PMF model with an amplitude smaller than the best range found in Fig. 2.16 (left panel), coupled with a possible stellar Li depletion. The depletion of ^{7}Li during both pre-main sequence (Fu et al., 2015) and main sequence phases (Richard, Michaud, and Richer, 2005; Korn et al., 2006) of POP II metal poor stars indicates that the current constraints on the ^{7}Li abundance from those stars might be lower than the actual value of primordial ^{7}Li abundance. In such a case, the PMF effects on BBN and its dissipation could be a solution to the Li Problem. The second possible effect is a change in the η value induced by the radiative decay of exotic particles (Kolb and Scherrer, 1982; Scherrer and Turner, 1988a; Scherrer and Turner, 1988b; Feng, Rajaraman, and Takayama, 2003; Ishida, Kusakabe, and Okada, 2014), which is independent of the dissipation of the PMF as discussed above. In this case, the 30% increase of the baryon-to-photon ratio in Fig. 2.16 (left panel) might be acceptable.

2.4 Cosmological Magnetohydrodynamics

2.4.1 Formalism and Basic Equations

In the very early universe that cosmic time $t < 1$ s, the main components of the ultra relativistic primordial plasma are photons and leptons, they interact with each other via electromagnetic or weak interactions on small scale. For the large scale, they are

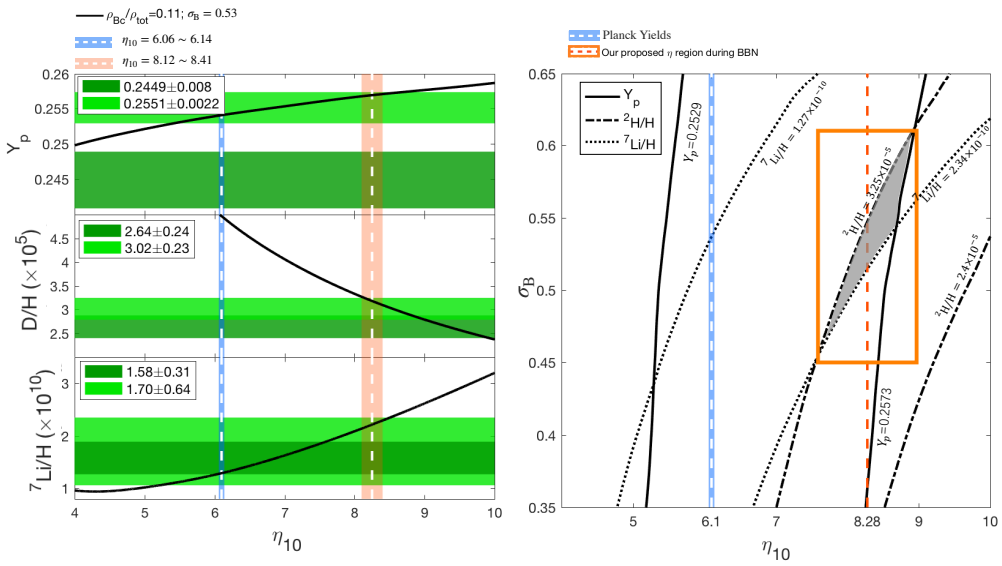

FIGURE 2.16: Primordial element abundances as a function of η_{10} for fixed $\sigma_B = 0.53$ (left panel). The horizontal bands show the observational constraints on abundances. The light blue vertical band is the value inferred from the Planck analysis, and the light orange band shows the possible η_{10} region for which concordance is possible for all three elements. In the right panel, the contour plot for all three elements is presented. The light blue vertical band is the value from the Planck analysis. In the grey region abundances of all three elements are consistent with observational constraints, and the orange rectangle indicates the constraints on η_{10} and σ_B that are consistent with observational constraints on abundances.

in the so called equilibrium state, this is consistent with one of the basic assumption of the standard big bang cosmology model that the universe is homogeneous and isotropic on the large scale. However, on the other hand, it also indicate that the small scale turbulence is possible, especially for the extreme early universe because of the high temperature. The interactions rates are dramatically enhanced in such environment. One of the strong supports is that the observed CMB anisotropy ($\Delta T/T \sim 10^{-5}$) due to the inflationary scalar modes, which indicates the possibility of primary small scale turbulence before the photon last scattering (Aghanim, 2020). Another evidence is that the existence large scale correlated IGMF: one of the theory about its origin is that the strong seed PMF generated in the early epoch then coupling with the cosmic plasma and evolves until present day.

Once the background field is produced, it would further change the motion of the particles (such as electrons and positrons) inevitably, it is possible to generate small scale turbulence locally, and such turbulence could be amplified to large scale and finally leaves the imprints in the CMB spectrum and IGM. the PMF generation mechanism and its observational constraints are discussed previously (see Section 2.1). From the theoretical side, it is essential to study the turbulence itself and also to track the PMF evolution after its generation, for example, if the PMF is homogeneous, the turbulence could tell us how the uncorrelated field regions come into contact with each other during the expansion of the universe. For inhomogeneous PMF, as discussed in Section 2.3, the energy density inhomogeneous distribution is critical to the BBN theoretical yields, it is promising that the observed light elemental abundances could provide new constraints on the fluctuated PMF since the

nuclear reactions are sensitive to the background local temperature. Considering these aspects, it is natural for us to study the MHD affect in an expanding universe (Subramanian and Barrow, 1998; Brandenburg, Enqvist, and Olesen, 1996; Gailis, Frankel, and Dettmann, 1995; Dettmann, Frankel, and Kowalenko, 1993; Gailis et al., 1994).

I begin with the basic equations and the formulas of such dynamical system, although these equations follow closely from that of (Subramanian, 2016; Brandenburg and Subramanian, 2005; Banerjee and Jedamzik, 2004; Dimopoulos and Davis, 1997; Subramanian and Barrow, 1998; Brandenburg, Enqvist, and Olesen, 1996; Gailis, Frankel, and Dettmann, 1995; Dettmann, Frankel, and Kowalenko, 1993; Gailis et al., 1994) which consider the perfect fluid, it is worth to emphasize that the equations presented in this section is written in a more general way which could be applied for other MHD study in the expanding universe. Furthermore, several of the equations in this section are new, as for the inhomogeneous PMF generation, it is discussed in a more concrete pattern compared with the previous study (Dolgov and Grasso, 2002). Also, because the plasma is highly relativistic, previously, only the scenario that no strong collective effects which could give rise to a relativistic fluid velocity is considered, therefore the induced bulk velocities are in general non-relativistic in the previous studies, here the MHD equations in a fully relativistic pattern are derived. The geometry of space-time in general relativity is specified by the metric tensor, the proper time element (i.e.,the interval ds between two infinitesimally independent events) is $ds^2 = g_{\mu\nu}dx^\mu dx^\nu$. Here after, the Greek letters $\mu, \nu, ...$ are the indices for the 4-dimensional space-time coordinates, the English letters $i, j, ...$ are used for the 1+3 decomposed coordinates. The repeated indices are also summarized by Einstein manner.

Start from the cosmological principle (i.e., on large scale, the universe is homogeneous and isotropy), we apply the FLRW metric, so that the proper time element becomes

$$ds^2 = -dt^2 + a(t)^2\Big[\frac{dr^2}{1-kr^2} + r^2(d\theta^2 + sin^2\theta d\phi^2\Big], \tag{2.33}$$

where $0 < \theta < \pi$, $0 < \phi < 2\pi$ are the usual angular in spherical coordinates, and r is the co-moving radius (here below, the $(-,+,+,+)$ manner is used for the Minkowski metric). The expansion of the universe is described by the scale factor $a(t)$. The coefficient $k = 0, -1, +1$ corresponds to a flat, open or closed spatial geometry, respectively. The results of CMB observation and the large scale survey prefer a flat space, therefore $k = 0$ is set, so that the FLRW metric becomes

$$ds^2 = a^2(-d\tau^2 + d\boldsymbol{x}^2) \tag{2.34}$$

where τ is the conformal time (notice that the conformal time is just the definition in terms of mathematical convenient, it has no physical meaning). The energy-momentum tensor of the cosmological fluid reads

$$T^{\mu\nu}_{fl} = (p+\rho)U^\mu U^\nu + pg^{\mu\nu}, \tag{2.35}$$

where p and ρ is the pressure and energy density separately. U^μ is the four velocity, the definition of U^μ is

$$U^\mu := \frac{dX^\mu}{ds} = \frac{dX^\mu}{d\tau}\cdot\frac{d\tau}{ds}, \tag{2.36}$$

where $dX^\mu/d\tau$ is the peculiar velocity (i.e., the velocity relative to the co-moving frame of reference). From Eq. 2.34, the term $d\tau/ds$ gives out the coefficient $a^{-1}\gamma$

where γ is the Lorentz factor. Unlike the ideal cosmological fluid, the four velocity reads $U^\mu = (a^{-1}\gamma, a^{-1}\gamma u^i)$ instead of $(-1, 0)$. The conservation law requires (here after, T_{fl} is denoted as T)

$$T^{\mu\nu}_{\ ;\nu} = \frac{1}{\sqrt{-g}}\frac{\partial}{\partial x^\nu}\left(\sqrt{-g}T^{\mu\nu}\right) + \Gamma^\mu_{\nu\lambda}T^{\nu\lambda} = 0, \tag{2.37}$$

where $\Gamma^\mu_{\nu\lambda}$ is the Christoffel symbol (See Appendix B for the expressions). Then for the $\mu = i$ component, the momentum conservation is

$$T^{i\nu}_{\ ;\nu} = \frac{\partial(\rho_{com} + p_{com})\gamma^2\boldsymbol{u}}{\partial\tau} + \nabla\cdot\Big[(\rho_{com} + p_{com})\gamma^2\boldsymbol{u}\otimes\boldsymbol{u} + p_{com}\mathbf{I}\Big] = 0, \tag{2.38}$$

where the co-moving quantities as $\rho_{com} = a^4\rho$ and $p_{com} = a^4 p$ have been defined. Eq. 2.38 is nothing but the Euler equation in an expanding coordinates. Now consider the imperfect fluid which includes the viscosity, the classic definition of the shear stress term is

$$\mu\Big[\nabla\boldsymbol{u} + (\nabla\boldsymbol{u})^T) - \frac{2}{3}(\nabla\cdot\boldsymbol{u})\mathbf{I}\Big], \tag{2.39}$$

it can be extended easily to the general relativity frame as (Weinberg, 1972):

$$W_{\mu,\nu} = \eta(U_{\mu;\nu} + U_{\nu;\mu} - \frac{2}{3}g_{\mu\nu}U^\sigma_{\ ;\sigma}) \tag{2.40}$$

here, η is the shear viscosity coefficient and it is given by

$$\eta = \frac{4}{15}g\frac{\pi^2}{30}T^4 l_d = \frac{4\rho_d l_d}{15(\rho + p)}, \tag{2.41}$$

where T is the background temperature, g is the degree of freedom, ρ_d and l_d is the density and mean-free-path of the diffusing particles, respectively. Since the viscosity only applies to the spatial coordinates, the projection operator reads

$$H^{\mu\nu} = g^{\mu\nu} + U^\mu U^\nu, \tag{2.42}$$

then the energy momentum tensor including stress tensor from imperfect fluid becomes

$$T^{\mu\nu} = (p + \rho)U^\mu U^\nu + pg^{\mu\nu} - \eta H^{\mu\alpha}H^{\nu\beta}W_{\alpha\beta}. \tag{2.43}$$

Similar to the perfect fluid, the momentum conservation law gives us the Navier-Stocks equation in an expanding coordinates:

$$\begin{aligned} T^{i\nu}_{\ ;\nu} = \frac{\partial(\rho_{com} + p_{com})\gamma^2\boldsymbol{u}}{\partial\tau} &+ \nabla\cdot\Big[(\rho_{com} + p_{com})\gamma^2\boldsymbol{u}\otimes\boldsymbol{u} + p_{com}\mathbf{I}\Big] \\ &- \eta_{com}[\nabla^2\boldsymbol{u} + \frac{1}{3}\nabla(\nabla\cdot\boldsymbol{u})] = 0, \end{aligned} \tag{2.44}$$

where we have defined the co-moving quantity $\eta_{com} = a^3\eta$.

For the $\mu = 0$ component, the energy conservation reads

$$\begin{aligned} T^{0\nu}_{\ ;\nu} = \frac{\partial}{\partial\tau}\Big[\gamma^2(\rho_{com} + p_{com}) - p_{com}\Big] &+ \nabla\cdot\Big[\gamma^2(\rho_{com} + p_{com})\boldsymbol{u} - \eta_{com}\boldsymbol{f}\Big] \\ &= \frac{a'}{a}(\rho_{com} - 3p_{com}), \end{aligned} \tag{2.45}$$

where $\boldsymbol{f}$ is given by

$$\boldsymbol{f} = \nabla\frac{\boldsymbol{u}^2}{2} - \frac{2}{3}\boldsymbol{u}\nabla\cdot\boldsymbol{u}. \tag{2.46}$$

Now consider the electromagnetic energy momentum tensor, i.e.,

$$T^{\mu\nu}_{em} = \frac{1}{4\pi}\Big(F^{\mu\sigma}F^{\nu}_{\ \sigma} - \frac{1}{4}g^{\mu\nu}F_{\lambda\sigma}F^{\lambda\sigma}\Big), \tag{2.47}$$

and

$$F^{\mu\nu}_{\ \ ;\nu} = J^{\mu} \quad F_{[\mu,\nu,\lambda]} = 0, \tag{2.48}$$

which two are nothing but the Maxwell equations. The conservation law of the total energy momentum tensor (i.e., $T + T_{em}$) is written as

$$(T + T_{em})^{\mu\nu}_{\ \ ;\nu} = F^{\mu\nu}g_{\nu\sigma}J^{\sigma}. \tag{2.49}$$

So the $\mu = i$ component of RHS in Eq. 2.49 gives us

$$F^{i\nu}g_{\nu\sigma}J^{\sigma} = \boldsymbol{J}_{com}\times\boldsymbol{B}_{com} = \nabla\Big(\frac{\boldsymbol{B}_{com}\otimes\boldsymbol{B}_{com}}{4\pi} - \frac{\boldsymbol{B}^2_{com}}{8\pi}\Big) \tag{2.50}$$

which corresponds to the Lorentz force (here, the time-derivative of the displacement electric current is omitted). For $\mu = 0$ component, it reads

$$\begin{aligned} F^{0\nu}g_{\nu\sigma}J^{\sigma} =& \boldsymbol{J}_{com}\cdot\boldsymbol{E}_{com} \\ =& -\frac{\partial}{\partial\tau}\frac{B^2_{com}}{8\pi} - \nabla\cdot\Big[\frac{\boldsymbol{B}_{com}\times(\boldsymbol{u}\times\boldsymbol{B}_{com}) + \kappa\boldsymbol{J}_{com}\times\boldsymbol{B}_{com}}{4\pi}\Big] + \kappa\boldsymbol{J}^2_{com} \end{aligned} \tag{2.51}$$

which corresponds to the electromagnetic field energy. Also, the Ohm's law is given by:

$$\boldsymbol{J}_{com} = \sigma(\boldsymbol{E}_{com} + \boldsymbol{u}\times\boldsymbol{B}_{com}) \tag{2.52}$$

where σ is the electrical conductivity. In general, the conductivity is given by $\sigma \sim ne^2\tau_c/T$ where τ_c is the collision time scale. For strong collision, $\tau_c \sim 1/(n\pi b^2)$ where $e^2 b$ corresponds to the potential energy; for a long range force, $\tau_c \sim T^2/(n\pi e^4 ln\Lambda)$ where Λ is a coefficient to be determined (Baym and Heiselberg, 1997). Here in this section, the relativistic electron gas interacts with heavy non-relativistic ions is considered, so η is given by the Coulomb scattering cross section: (Akhiezer et al., 1975)

$$\sigma = \frac{\omega_p^2}{4\pi\sigma_{coll}n_e} \sim \frac{ne^2\tau_c}{T} \sim \frac{T}{3\pi\alpha}, \tag{2.53}$$

where ω_p is the plasma frequency, σ_{coll} is the collision cross section, and α is the fine structure constant.

The results are summarized here, combine Eq. 2.44, Eq. 2.45, Eq. 2.50 and Eq. 2.51 the MHD in the expanding universe is given by the following set of equations:

$$\begin{aligned} \frac{\partial(\rho_{com}+p_{com})\gamma^2\boldsymbol{u}}{\partial\tau} + \nabla\cdot\Big[&(\rho_{com}+p_{com})\gamma^2\boldsymbol{u}\otimes\boldsymbol{u} + p_{com}\mathbf{I} \\ &- \frac{\boldsymbol{B}_{com}\otimes\boldsymbol{B}_{com}}{4\pi} - \frac{\boldsymbol{B}^2_{com}}{8\pi}\Big] \\ =&\eta_{com}[\nabla^2\boldsymbol{u} + \frac{1}{3}\nabla(\nabla\cdot\boldsymbol{u})] \end{aligned} \tag{2.54}$$

$$\frac{\partial}{\partial\tau}\Big[\gamma^2(\rho_{com}+p_{com})-p_{com}+\frac{\boldsymbol{B}_{com}^2}{8\pi}\Big]+\nabla\cdot\Big[\gamma^2(\rho_{com}+p_{com})\boldsymbol{u}-\eta_{com}\boldsymbol{f} + \frac{\boldsymbol{B}_{com}\times(\boldsymbol{u}\times\boldsymbol{B}_{com})+\kappa\boldsymbol{J}_{com}\times\boldsymbol{B}_{com}}{4\pi}\Big] = \frac{a'}{a}(\rho_{com}-3p_{com})+\kappa\boldsymbol{J}_{com}^2 \tag{2.55}$$

$$\frac{\partial\boldsymbol{B}_{com}}{\partial\tau}=\nabla\times(\boldsymbol{u}\times\boldsymbol{B}_{com})-\kappa\nabla\times\boldsymbol{J}_{com}. \tag{2.56}$$

The definition $\kappa = 1/(4\pi\sigma)$ is used to represents the resistivity. All the quantities with lower index *com* corresponds to the co-moving terms:

$$\rho_{com}=\rho\cdot a^4;\quad p_{com}=p\cdot a^4;\quad \boldsymbol{B}_{com}=\boldsymbol{B}\cdot a^2;\quad \boldsymbol{J}_{com}=\boldsymbol{J}\cdot a^3;\quad \eta_{com}=\eta\cdot a^3. \tag{2.57}$$

τ is the proper time and has the relation that $d\tau = dt/a(t)$. It is clear that these equations becomes ordinary non-expanding MHD equations in the non-relativistic limit, i.e., $\gamma = 1$, $p << \rho$ and $a = 1$. These equations are also consistent with previous works: for example, Brandenburg, Enqvist, and Olesen (1996) and Gailis et al. (1994) consider the relativistic MHD equation without viscosity (i.e., $\eta = 0$), Subramanian (2016) considered the imperfect relativistic fluid but with non-relativistic bulk velocity (i.e., $\gamma = 1$), Subramanian and Barrow (1998) also use the similar treatment while they consider the perfect conductor situation so that the last term in Eq. 2.56 becomes 0.

2.4.2 Primordial Magnetic Field Generation from Decoupling

The observed CMB signals indicate a possibility that magnetic field could be generated in the early universe and survive. Grasso and Riotto (1998), Caprini, Durrer, and Servant (2009), Turner and Widrow (1988), Dolgov (1993), and Demozzi, Mukhanov, and Rubinstein (2009) have studied the PMF generated for the case of both quark-hadron phase transition and the electroweak phase transition, although the generated PMF scale cannot explain the large correlated length scale we observed from CMB and IGMF, the following studies of the MHD effect of these seeds field illustrate that the growth patter of the seed field could explain the present day observations: if PMF was generated during inflation epoch, then due to the rapidly expansion of the universe, the large-scale PMF pattern could be satisfied Turner and Widrow, 1988; Martin and Yokoyama, 2008; Subramanian, 2010. It is true that the dynamo itself is well described, which is based on the temporal evolution of a pre-existing field. It is however, difficulty to create the new field from a completely field-free condition, the non-ideal processes should be include in order to explain the origin of magnetic fields. Starting from Biermann (1950), it was noticed that even for the neutral plasma, the small charge current from collisions of different phases in the plasma could grow to the large magnetic field if the currents have non-zero vorticity. Such mechanism later on was applied to many astrophysical site (Mestel and Roxburgh, 1962; Subramanian, Narasimha, and Chitre, 1994; Zaqarashvili, Khodachenko, and Rucker, 2011; Widrow et al., 2012) and stimulate many the studies on the multi-phase properties of the plasma (Braginskii, 1965; Khomenko et al., 2014; Martínez-Gómez, Soler, and Terradas, 2016). In this subsection, the PMF induction scenario based on such multi-phases model is studied, moreover, such mechanism could be manipulated and extended to a more general formalism that describe the magnetic field generation from decoupling species.

Starting from the MHD equations of the incompressible (i.e., $\nabla \cdot \boldsymbol{u} = 0$) relativistic plasma in the early universe, the Eq. 2.54 and Eq. 2.55 read

$$\begin{aligned}\frac{\partial(\rho_{com}+p_{com})\gamma^2\boldsymbol{u}}{\partial\tau}+\nabla\cdot\Big[(\rho_{com}+p_{com})\gamma^2\boldsymbol{u}\otimes\boldsymbol{u}+p_{com}\mathbf{I}\Big]\\ =\eta_{com}\nabla^2\boldsymbol{u}+\boldsymbol{J}_{com}\times\boldsymbol{B}_{com}\end{aligned} \tag{2.58}$$

$$\begin{aligned}\frac{\partial}{\partial\tau}\Big[\gamma^2(\rho_{com}+p_{com})-p_{com}\Big]+\nabla\cdot\Big[\gamma^2(\rho_{com}+p_{com})\boldsymbol{u}-\eta_{com}\frac{\boldsymbol{u}^2}{2}\Big]\\ =\frac{a'}{a}(\rho_{com}-3p_{com})+\boldsymbol{J}_{com}\cdot\boldsymbol{E}_{com}.\end{aligned} \tag{2.59}$$

There are mainly three components in the plasma of the early universe, electrons-positrons (denote as e), the ion component (mainly proton, denote as i) and other neutral components (denote as n). Here, for simplicity, one could consider that always elastic interactions occurred in the plasma, so that only the momentum transfer is possible between different species. In fact, the collision between different species in plasma could transfer the momentum, energy or even charge between each other, please see (Mestel and Roxburgh, 1962; Braginskii, 1965; Spitzer, 1965; Khomenko et al., 2014) for details. For the neutral components, one have:

$$\frac{\partial(\rho^n_{com}+p^n_{com})\gamma^2\boldsymbol{u}_n}{\partial\tau}+\nabla\cdot\Big[(\rho^n_{com}+p^n_{com})\gamma^2\boldsymbol{u}_n\otimes\boldsymbol{u}_n+p^n_{com}\mathbf{I}\Big]=\eta_{com}\nabla^2\boldsymbol{u}_n-C_n, \tag{2.60}$$

where C_n stands for the momentum transfer between neutral and charged components. For the charged e and i components, one should include the electromagnetic field:

$$\begin{aligned}\frac{\partial(\rho^c_{com}+p^c_{com})\gamma^2\boldsymbol{u}_c}{\partial\tau}+\nabla\cdot\Big[(\rho^c_{com}+p^c_{com})\gamma^2\boldsymbol{u}_c\otimes\boldsymbol{u}_c+p^c_{com}\mathbf{I}\Big]\\ =\eta_{com}\nabla^2\boldsymbol{u}_c+C_n+\boldsymbol{J}_{com}\times\boldsymbol{B}_{com}.\end{aligned} \tag{2.61}$$

Here, c stands for the charge components. Clearly the summation of Eq. 2.60 and Eq. 2.61 canceled the momentum transfer so that the whole system still satisfy the momentum conservation law. C_n is defined as (Martínez-Gómez et al., 2021)

$$C_n=\alpha\rho_c\rho_n(\boldsymbol{u}_n-\boldsymbol{u}_c), \tag{2.62}$$

where α is the collisional parameter given by

$$\alpha=\frac{\rho_e\nu_{en}+\rho_i\nu_{in}}{\rho_n\rho_c}, \tag{2.63}$$

where ν corresponds to the collision rates. Such scenario is called 'two-fluid' model. The generic Ohm's law can be derived to describe the generation of the field (Mestel and Roxburgh, 1962; Braginskii, 1965; Spitzer, 1965), the treatment of the fluid here is simple since basically the electrons, positrons and neutrinos are considered as separated fluid components and can only interact with each other via collisions. The generic Ohm's law reads

$$\boldsymbol{E}_{com}+\boldsymbol{u}_c\times\boldsymbol{B}_{com}=-\frac{\nabla p_e}{en_e}+\kappa(\boldsymbol{u}_n-\boldsymbol{u}_c)+\frac{\boldsymbol{J}_{com}\times\boldsymbol{B}_{com}}{en_e}+\frac{m_e}{e^2}\frac{\partial}{\partial\tau}\Big(\frac{\boldsymbol{J}_{com}}{n_e}\Big), \tag{2.64}$$

where the first term on the RHS is the electron pressure gradient, also called Biermann battery term (Biermann, 1950). The second term is the Ohmic term, $\kappa = m_e(\nu_{en} - vin)/e$; the third one is the Hall term and the last one is the inertial term. In general, the last two can be ignored since Hall effect is small and the macroscopic time scales are large compared to the plasma oscillation periods so that time derivative of the induced current negligible. Combining Eq. 2.64 with the magnetic field evolution ($\partial \boldsymbol{B}/\partial\tau = -\nabla \times \boldsymbol{E}$), one could obtain

$$\frac{\partial \boldsymbol{B}_{com}}{\partial\tau} = \nabla \times (\boldsymbol{u}_c \times \boldsymbol{B}_{com}) + \nabla \times \frac{\nabla p_e}{en_e} + \kappa\nabla \times (\boldsymbol{u}_n - \boldsymbol{u}_c). \tag{2.65}$$

Eq. 2.65 describes the magnetic field in an expanding universe from a neutral plasma. At about cosmic temperature $T \sim 1$ MeV in the early universe, the neutrino family gradually decoupled from the relativistic plasma, the neutrinos are mainly interact with electrons and positrons via weak interactions elastically, so the neutrino phase satisfies Eq.2.60, the charged phase satisfies Eq. 2.61 while since the positrons are the main species hold for the positive charge, the collision term α becomes

$$\alpha = \frac{\rho_{e^+}\nu_{e^+n} + \rho_{e^-}\nu_{e^-n}}{\rho_n\rho_c}, \tag{2.66}$$

Therefore the induced electric resistivity κ becomes

$$\kappa = \frac{m_e(\nu_{e^-n} - \nu_{e^+n})}{e}, \tag{2.67}$$

where ν_{e^-n} and ν_{e^+n} represent the collision rate between neutrino-electron and neutrino-positron, respectively. Here the elastic weak interactions ensure the whole system still keep the energy conservation law as collision-free situation (i.e., Eq. 2.59). However, if the interaction is inelastic, then even mass exchange is possible during interaction, so that the energy conservation should also be modified, for detail, see (Khomenko et al., 2014). Plug Eq. 2.67 into Eq. 2.65, one could obtain

$$\frac{\partial \boldsymbol{B}_{com}}{\partial\tau} = \nabla \times (\boldsymbol{u} \times \boldsymbol{B}_{com}) - \frac{m_e(\nu_{e^-n} - \nu_{e^+n})}{e}\nabla \times \boldsymbol{u}_{rel}. \tag{2.68}$$

Here, the collisional term is kept and the others are ignored in Eq. 2.64 since the pressure of the background fluid is homogeneous. Taking the relativistic plasma as the inertial frame of reference, the relative velocity between neutrinos and charged phase is $\boldsymbol{u}_{rel}$. The collision rate ν_{e^+n} and ν_{e^-n} are simply given by the weak interactions:

$$\nu_{e^+n} = n_n\sigma_{ne^+} = \frac{G_F^2 s}{\pi} \sim 3G_F^2T^2 \tag{2.69}$$

while for neutrino-electron interaction, it has

$$\nu_{e^-n} = n_n\sigma_{ne^-} = \frac{G_F^2 s}{3\pi} \sim 10G_F^2T^2. \tag{2.70}$$

In conclusion, the MHD equations for inducing magnetic field are

$$\frac{\partial(\rho^n_{com} + p^n_{com})\gamma^2\boldsymbol{u}_{rel}}{\partial\tau} + \nabla \cdot \Big[(\rho^n_{com} + p^n_{com})\gamma^2\boldsymbol{u}_{rel} \otimes \boldsymbol{u}_{rel} + p^n_{com}\mathbf{I}\Big] = \eta_{com}\nabla^2\boldsymbol{u}_{rel} - C_n \tag{2.71}$$

$$\frac{\partial(\rho^c_{com}+p^c_{com})\gamma^2\boldsymbol{u}_c}{\partial\tau}+\nabla\cdot\Big[(\rho^c_{com}+p^c_{com})\gamma^2\boldsymbol{u}_c\otimes\boldsymbol{u}_c+p^c_{com}\mathbf{I} - \frac{\boldsymbol{B}_{com}\otimes\boldsymbol{B}_{com}}{4\pi}-\frac{\boldsymbol{B}^2_{com}}{8\pi}\Big]=\eta_{com}\nabla^2\boldsymbol{u}_c+C_n \tag{2.72}$$

$$\frac{\partial B_{com}}{\partial\tau}=\nabla\times(\boldsymbol{u}_c\times B_{com})+\frac{m_e(7n_nG_F^2T^2)}{e}\nabla\times\boldsymbol{u}_{rel}. \tag{2.73}$$

Therefore, if the velocity of decoupled species has non-zero vorticity, i.e., $\nabla\times\boldsymbol{u}_{rel}\neq 0$, it is possible to generate the magnetic field through decoupling. It is also worthy to mention that the two-fluid approximation is also consistent with the microscopic viewpoint: the rough criterion of a particle species to be either coupled or decoupled is usually by using the comparison between the interaction rate Γ and the expansion rate H. For the particle fully coupled with the plasma, its thermodynamical quantities are determined by the distribution function $f(T,mu)$. then while once the species totally decouples from the plasma, its evolution is simple: the number density decreased as a^{-3} and momentum decreased as a^{-1}. The decoupling process always described by the Boltzmann equation in an expanding universe (Kolb and Turner, 1990):

$$L=p^\alpha\frac{\partial}{\partial x^\alpha}-\Gamma^\alpha_{\beta\gamma}p^\beta p^\gamma\frac{\partial}{\partial p^\alpha}[f]=C[f], \tag{2.74}$$

where L is the Liouville operator and C is the collision term. Liouville operator usually have no spatial-derivative term due to the assumption of homogeneous and isotropic universe, but here, since the neutrino number distribution inhomogeneity is assumed, then one should have:

$$p^0\frac{\partial f}{\partial t}-H|\boldsymbol{p}|^2\frac{\partial f}{\partial p^0}+\boldsymbol{p}\nabla f=C[f], \tag{2.75}$$

where H is the Hubble expansion parameter, integrated by multiplying $\boldsymbol{p}$, one could obtain

$$\frac{\partial(\rho+p)\gamma^2\boldsymbol{u}}{\partial\tau}+4H\Big[(\rho+p)\gamma^2\boldsymbol{u}\Big]+\nabla\cdot\Big[(\rho+p)\gamma^2\boldsymbol{u}\otimes\boldsymbol{u}+p\mathbf{I}\Big]=\eta_{com}\nabla^2\boldsymbol{u}_{rel}-C_n, \tag{2.76}$$

which exact the momentum conservation for the neutrinos as discussed. Compare Eq. 2.76 with Dolgov and Grasso (2002), apparently the neutrino pressure and viscosity term are ignored, in that specific model, the lepton number density of neutrinos is locally imbalanced (i.e., the number density difference between neutrinos and anti-neutrinos) over a length scale λ, then, during the decoupling, the collision between neutrinos and plasma will also be inhomogeneous on the scale λ.

In conclusion, the "two-fluid" model (Eq. 2.71 to Eq. 2.73) contains detailed analyze of the different phases in the plasma, only requirement is the decoupled species velocity has non-zero vorticity. This model can be extended to a general aspect that induce inhomogeneous magnetic field via the collision inside the relativistic plasma in the early universe.

2.5 Conclusions

2.5.1 "Cosmic Li Problem": Current Status

The standard BBN model has three parameters: the effective neutrino number N_ν, the neutron lifetime τ_n, and the baryon to photon ratio (the baryonic density) of the

universe η. The former two parameters have been fairly well determined from experiments (Patrignani, 2016; Descouvemont et al., 2004; Coc et al., 2015) and η is obtained from the analysis of cosmic microwave background (CMB) power spectrum analysis (Bennett, 2013; Planck Collaboration et al., 2016a; Aghanim, 2020). Theoretical calculations of light element abundances in standard BBN are now well defined and precise (Cyburt et al., 2016; Mathews, Kusakabe, and Kajino, 2017). For the value of η derived from Planck (Bennett, 2013; Planck Collaboration et al., 2016a; Aghanim, 2020), there is excellent agreement between BBN and the observed primordial abundances of D and ^{4}He (Cyburt, Fields, and Olive, 2003; Cyburt et al., 2016; Pitrou et al., 2018). However the observed abundance of ^{7}Li in metal-poor dwarf halo stars (Spite and Spite, 1982; Sbordone, 2010) implies A(Li)=2.23 dex which disagrees with the theoretical prediction by about a factor of 3 (Li/H$=5.1\times10^{-10}$ from Cyburt et al. (2016), see Fig. 2.17).

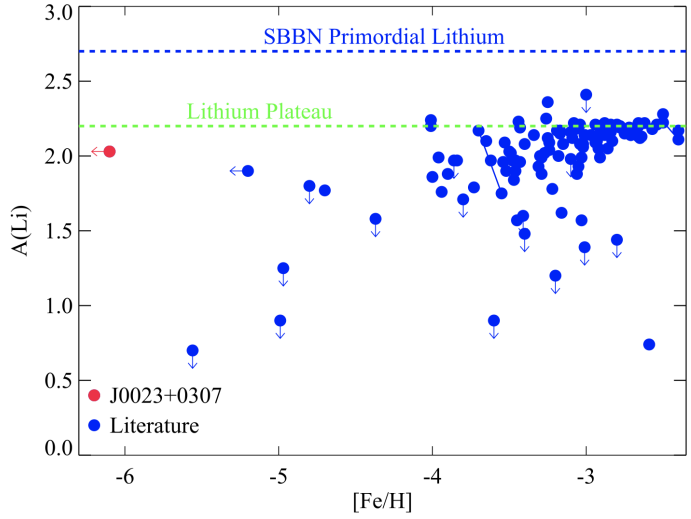

FIGURE 2.17: The current status of the lithium observations for metal poor stars. For metal poor stars, there is the Spite plateau (green dashed line), which is lower than the standard BBN prediction (blue dashed line). For extremely metal poor stars [Fe/H]<-3.0, the observed Li abundances drop below Spite plateau. The recent observation (Aguado et al., 2019) on a [Fe/H]<-6.0 star shows a recovered Li abundance on Spite plateau (red dot). This figure is taken from Aguado et al. (2019).

The ^{7}Li is a fragile element and could be easily produced in many astrophysical sites such as cosmic ray nucleosynthesis, stellar nucleosynthesis and the novae explosion nucleosynthesis, these activities could take part in ^{7}Li production for metallicity [Fe/H]>-1.0. Therefore in order to probe the ^{7}Li abundance in the early epoch, the old objects are the important keys, the metal-poor dwarf halo stars with [Fe/H]$\leq$-1.5 and surface temperature about 6000 K $\sim$ 6700 K are believed to have the un-evolved primordial ^{7}Li abundance, these stars are old enough to exclude the activities that produce ^{7}Li, also the narrow temperature region ensures that the ^{7}Li could not be destroyed in stars since the critical temperature for ^{7}Li(p, α)α reaction occurs is 10^6 K; for lower temperature, ^{7}Li dramatically decreases due to the deep convention during the stellar evolution.

The studies on the ^{7}Li observations start from the dwarf halo stars by pioneers (Spite and Spite, 1982; Bonifacio and Molaro, 1997) who found those stars are mostly

lying on the same level of the ^{7}Li abundance, i.e., A(^{7}Li)=2.23 dex, which is also called Spite plateau. The later on observations found that Spite plateau seems not only exist in our Galaxy, but also in Globular Cluster (Mucciarelli et al., 2014), dwarf galaxies (Hill et al., 2019) and ω Centauri (Monaco et al., 2010). These observations suggest that the ^{7}Li abundance of old stars is not affected by environments. Another interesting fact is the last years' observations (Sbordone, 2010; Bonifacio, 2018) on the extremely metal poor stars (i.e., [Fe/H]<-4.0) show a break down of Spite plateau, those stars have ^{7}Li abundance lower than spite plateau, and more interestingly, one of the recent observations on a star with [Fe/H]<-6.0 has ^{7}Li abundance lying back on the Spite plateau (Aguado et al., 2019) (high resolution with UVES at VLT infer the ^{7}Li abundance of this star is A(Li)=2.02$\pm$0.08).

These extremely metal poor stars are rare in galactic halos and are mainly carbon enhanced without excess of neutron-capture elements (CEMP-no stars), such facts lead to a possible solution to decrease the ^{7}Li abundance from BBN prediction to the Spite plateau as the lithium astration in Pop III stars (Piau et al., 2006): those observed metal poor stars are mainly from Pop III stars where the Li has already been depleted, the enhanced carbon abundance is the evidence for such a mechanism: Pop III stars ejected mostly outer layers Carbon, while other elements are fall backed (Tominaga, Iwamoto, and Nomoto, 2014). However, the later observations (Matsuno et al., 2017) on the CEMP-no main-sequence turn-off stars with metallicities [Fe/H]$\sim$-3 shows normal ^{7}Li abundances, suggests that the Li depletion are more likely related to the low iron abundance instead of the processes of the Pop III stars.

Clearly the Spite plateau has much deeper physical meaning because: **1).** If the ^{7}Li abundance of the Spite plateau does not represents the primordial value, then, what kind of mechanism could deplete lithium for all metal poor stars to the same level. Especially the recent observations on extragalactic objects seem to indicate a universality of such Li plateau. From the GCE perspective, the recent computation of ^{7}Li evolution shows that in the dwarf spheroidal (dSphs) and ultra faint galaxies (UFDs) of the Local Group, the Spite plateau for [Fe/H]<-1.0 also exists, implies that the Spite plateau does not suffered from the star forming history especially these galaxies has much lower star forming rate than our Galaxy (Matteucci et al., 2021). Therefore one need 'some mechanism' to reproduce the the Spite plateau even for halo stars, especially some of them are from the mixing with dwarf galaxies, which should be totally under different condition. **2).** If the explanation of the Spite plateau truly comes from stellar evolution, such model need to satisfy the facts that for the stars with metallicity [Fe/H]<-4.0, the observed ^{7}Li abundance show a decreased trend as the decreasing of metallicities. **3).** Of course the easiest way to explain such trend is the primordial abundance of Li is the Spite plateau. But, if one admit that the Spite plateau does stands for the real primordial value, then, one shall seek for some unknown cosmological process(es) that could destroy the primordial ^{7}Li only, and more challengingly, such process(es) should pass the trial of all the present-day cosmological and elemental abundances observations.

From the nuclear physical perspective, the full solution seems impossible, the recent updated reaction rates even worsen the discrepancy (Coc et al., 2004; Coc et al., 2012; Coc et al., 2015). Current uncertainties in the cross sections of relevant nuclear reactions are reach the accurate level of 0.2% for ^{4}He, 5% for D and ^{3}He and 15% for ^{7}Li (Descouvemont et al., 2004; Cyburt and Davids, 2008), and the sensitive studies indicate that there is no unknown reactions that could affect the ^{7}Li abundance significantly. Theoretically, detailed nuclear reaction network calculations up to the CNO cycle have been carried out (Coc et al., 2012; Coc and Vangioni, 2017), as well

as a Monte Carlo likelihood analysis to make a rigorous approach of the theoretical BBN nuclear reaction networks (Iliadis et al., 2016). Those results, however, do not give solutions to the lithium problem. Experimentally, the reaction ^{7}Be(d,p)2α is promising to resolve "cosmic Li problem" if the reaction rate is enhanced by a factor of 100, the previous measurements of its average cross section (Angulo, 2005) or the possible resonances (O'Malley et al., 2011; Kirsebom and Davids, 2011) seem rule out the possibility of such a huge enhancement. One of the recent measurement of this reactions shows the maximum change of the rate is less than 10% (Rijal et al., 2019). Another recent measurement of the ^{7}Be(n,p)^{7}Li cross section offers a reduction of the predicted ^{7}Li abundance by one-tenth (Hayakawa et al., 2021), and the final state involving the first excited state of ^{7}Li* can also only contribute up to 1% of the total cross section (Iwasa et al., 2021). On the other hand, the possibility of new resonance reactions to destroy ^{7}Li such as ^{7}Be$(\alpha,\gamma)^{11}$C and ^{7}Be(^{3}He,2$p\alpha$)^{4}He will be explored in the near future, although the recent search (Hammache, 2013) for missing levels in the relevant excitation energy regions of ^{10}C and ^{11}C did not find any new level and it has been found that these resonances must have unrealistically large decay widths (Chakraborty, Fields, and Olive, 2011; Civitarese and Mosquera, 2013; Hammache, 2013).

In conclusion, the "cosmic Li problem" is still unresolved by far, the solution from nuclear physics seems to have low chance; the solution proposed via stellar evolution could reproduce the Spite plateau ^{7}Li abundance, however, none of these suggested solutions gives a clear explanation on the reason why ^{7}Li in all the halo stars, stars of external galaxies and stars of Gaia dataset (Molaro, Cescutti, and Fu, 2020), show the similar evolution trend; as for the solution from cosmological perspective, those models always encounter excess deuterium while the recent D/H abundance observation has reach to a very strict level (Pettini and Cooke, 2012; Cooke, Pettini, and Steidel, 2018) so that many models has been ruled out. In addition, for stars with metallicities below [Fe/H]<-3.0, the decreasing trend of the observed ^{7}Li abundance (Sbordone, 2010; Aoki, Ito, and Tajitsu, 2012; Bonifacio, 2018) is not fully understood, this suggests that lithium observations in metal poor stars cannot be used anymore to probe BBN models.

Instead of observing the ^{7}Li in stars, the most direct way to investigate the initial Li abundance is observing Li in the *interstellar medium* (ISM). Such observations can avoid possible Li depletion by stellar evolution, and as a complement to the stellar observations. Observations of the atomic lines of Li in the ISM, especially in metal-poor atomic gas clouds, are extremely challenging. The only detection of interstellar atomic Li is the observation toward an O-type supergiant star in the Small Magellanic Cloud (Howk et al., 2012). Meanwhile, it is believed that the majority of the interstellar Li is in the form of lithium hydride (LiH), which is well mixed in the molecular gas phase (Combes and Wiklind, 1998). The LiH molecule has the J=1-0 rotational transition at 443.95 GHz and the first level of its rotational energy is at $\sim$21 K above the ground level (Pearson and Gordy, 1969). This sub-mm spectral line is feasible to be observed via observing molecular clouds with strong background sub-mm continuum sources. However, the atmospheric transmission at the LiH J=1-0 frequency is very poor. Very few telescopes are equipped with receivers that work at this frequency band, and its frequency lies in the wing of a deep and highly pressure-broadened terrestrial water line (the 4_{23} - 3_{30} transition at 448.001 GHz), making it also difficult to observe from ground. The expected interstellar Li abundance should be akin to the meteoric value A(Li)=3.25 (Grevesse, Asplund, and Sauval, 2007). If the Li abundance of the cloud is similar to the conjecture, then it will be a strong confirmation that the stellar evolution indeed decrease the initial Li

abundance in the Galactic ISM because the current Solar photosphere has Li abundance as A(Li)=1.05 dex (this is the so called "lithium problem in the Sun"). Then the discrepancy between the stellar Li abundances and the ISM values must come from some destruction during star formation and stellar evolution, one should turn to the stellar physics to resolve the "cosmic Li problem".

2.5.2 Possible Solution from PMF

A number of suggestions have been proposed to solve the "cosmic Li problem". One possible solution is that ^{7}Li abundance can be significantly depleted via diffusion process in (pre) main sequence phase depletion accompanied by late mass accretion (Fu et al., 2015). Others have argued for the existence of a stellar mass-dependent mechanism to deplete stellar lithium (Richard, Michaud, and Richer, 2005). Motivated by recent observations (Piau et al., 2006) suggest that ISM is in fact quite dynamic, it has also been suggested that the ^{7}Li depleted ejecta from massive Pop III stars may be mixed inefficiently with the proto-Galactic ISM prior to the formation of the metal poor halo stars of the galactic halo. Beside these, a variety of nonstandard BBN models have also been proposed such as an Inhomogeneous BBN (Applegate, Hogan, and Scherrer, 1987; Alcock, Fuller, and Mathews, 1987; Fuller, Mathews, and Alcock, 1988; Kajino, 1991; Orito et al., 1997; Lara, Kajino, and Mathews, 2006; Nakamura et al., 2017), dark matter decay (Kusakabe et al., 2013), sterile neutrinos (Esposito et al., 2000; Ishida, Kusakabe, and Okada, 2014) and super symmetric particles (Arbey and Mahmoudi, 2008; Kusakabe, Kajino, and Mathews, 2011; Kusakabe et al., 2017). Those possibilities are discussed in Kurki-Suonio (2000), Mathews, Kusakabe, and Kajino (2017), and Mathews et al. (2018).

In this Chapter, I investigated the PMF and its impacts on BBN sophisticatedly. In Sect. 2.2.3, the formula of weak reaction rates under PMF are derived: the charged-particle distribution functions are altered and lead to a change in the momentum distribution function of electrons and positrons (Eq. 2.10); the screening potential depends on the thermodynamics of charged particles in the plasma, which could be altered by the magnetic field (Eq. 2.11). I studied the screening potential in PMF and include this corrections in the calculation of electron-capture rate (Eq. 2.12). However, due to the low density of the plasma during BBN epoch, screening could only make 0.1% changes of the final primordial abundances calculation (Fig 2.6). The impact from PMF itself is more interesting because the quantized $e^{\pm}$ momentum phase space could reduce the weak interaction rates drastically (Fig. 2.4). Such impacts are included in BBN network, compared the theoretical ^{4}He yield with observations, found that a late generation epoch of a frozen-in PMF at $T_9 < 15$ is more favored (Fig. 2.7). Moreover, the recent updated nuclear reaction cross sections results in a lower D abundance in the standard BBN calculation compared with observations, it is found that such D under prediction could be resolved an enhancement of weak reaction rates caused by PMF (Table 2.1).

In Sect. 2.3, a static inhomogeneous PMF model is introduced and explored during the BBN epoch. The PMF is described by a stochastic field constrained by the observed CMB power spectrum under the assumption of a power-law correlation function. However, the strength of the magnetic field varies spatially once the magnetic field is generated before weak decoupling. We adopt a PMF energy density characterized by a Gaussian distribution in local field strength. This model implies the existence of an inhomogeneous PMF during the BBN epoch [Eq. (2.27)]. A homogeneous value of total energy density is assumed in the universe, and inhomogeneity of temperature along with that of the PMF. Locally, primordial baryons are in

TABLE 2.3: Predicted primordial light element abundances compared to the observational data for the case of a PMF with $\rho_{\rm Bc}/\rho_{\rm tot} = 0.11$ and $\sigma_{\rm B} = 0.53$.

Abundance	$\eta_{10} = 8.2$	Observation
Y_p	0.2568	0.2551±0.0022
D/H($\times 10^5$)	3.21	3.02±0.23
^{7}Li/H($\times 10^{10}$)	2.189	1.70±0.64

equilibrium with the same temperature which determines the photon energy density. Globally, due to the existence of an inhomogeneous PMF energy density, the temperature is inhomogeneous. This causes an effective non-MB distribution function for baryonic velocities during the BBN epoch. I derived an expression for the temperature distribution function [Eq. (2.31)] and calculated the effective baryonic distribution function in our PMF model (Eqs. 2.26-2.30). The reaction rates are analyzed and it is concluded that charged particle reactions are affected most due to the Coulomb barrier while neutron induced reactions are not (Fig. 2.14). The inhomogeneous PMF energy density was also added to the BBN network. It is found that the fluctuations of the PMF reduce the ^{7}Be production and enhance D production. It is also noticed that ^{4}He abundance is most sensitive to $\rho_{\rm Bc}$ (Fig. 2.12). I verified that under the limit of $\sigma_{\rm B} \to 0$, the abundances obtained from a homogeneous PMF strength are naturally recovered (Fig. 2.12).

In our model, D and ^{7}Li abundances are the most sensitive elements to the fluctuation parameter $\sigma_{\rm B}$ (Fig.2.13). By comparing our results with the Y_p constraints, it is found that $\rho_{\rm Bc}$ is less than 13% of the total energy density, and the range of $\rho_{\rm Bc}/\rho_{\rm tot} = 0.08 - 0.13$ provides the best fit to the observed abundances of for both Y_p and D. This amount of magnetic energy density corresponds to a present PMF of $1.18 - 1.51\mu$G. It is concluded that the constraints from both ^{4}He and D/H are satisfied with our PMF model for a fluctuation parameter $\sigma_{\rm B} = 0.04 - 0.17$. Moreover, the ^{7}Li abundance is reduced in our model to a value of $(3.35 - 3.52) \times 10^{-10}$, which is still above the Spite plateau (Table 2.2). If the baryon-to-photon ratio decreases from $\eta_{10} = 7.59 - 8.97$ during BBN to $\eta_{10} = 6.06 - 6.14$ of the Planck value by the time of photon last scattering, the Li problem could be solved for a fluctuation parameter of $\sigma_B = 0.45 - 0.61$ (Table 2.3). Such a high baryon-to-photon ratio does not result from the dissipation of PMF alone. However, if the present-day observed ^{7}Li abundance level of the Spite plateau is the result of stellar depletion during the evolutionary stage of the metal-poor stars, this tension would be relaxed in our PMF model. There is another possibility of finding a change of the baryon-to-photon ratio by the radiative decay of exotic particles. Therefore, the above parameter region which I find in the inhomogeneous PMF model cannot be excluded at this time.

Sect. 2.4 summarizes the MHD equations for an expanding relativistic plasma, and also magnetic field induction equation based on the two-fluid approximation is derived. As a preliminary model, the PMF generation via neutrino lepton number inhomogeneity is applied (Dolgov and Grasso, 2002). The neutrino number is presumed has excess $\delta n/n$ on the length scale λ. For the viscosity η in Eq. 2.41, The neutrino mean free path is given $l_\nu = \tau_w = \sigma^{-1}$, then it could be obtained that

$$l_\nu(t) = \tau_w = 2t_d \Big(\frac{t}{t_d}\Big)^{5/2}. \tag{2.77}$$

In the very early epoch, l_ν is much smaller than the length scale λ, as temperature decreases, since the reaction rate rapidly decrease $\sigma \propto T^5$, l_ν grows quickly comparable to λ, then when the neutrino starts decoupling, the inhomogeneous velocity could be induced. A multi-zone calculation of PMF is performed by assuming the initial parameters of the PMF generation model as $\delta n/n = 0.2$ and $\lambda = 0.01$ (Dolgov and Grasso, 2002). The magnetic field parameter in there study was defined as $b = e|B|/T^2$, while in BBN $\gamma = B/B_c$ is used:

$$\gamma(T) = \frac{B}{B_c} = \frac{b}{0.261}\Big(\frac{T}{\mathrm{MeV}}\Big)^2. \tag{2.78}$$

Then by applying the initial PMF strength $b = 0.07$ at $T = 1$ MeV before BBN start, I carried out the multi-zones BBN calculation, the PMF was set as satisfying the two-point correlation function with the power law spectrum as discussed in Sect. 2.3, $\lambda = 0.01$ corresponds to the present day 0.1 Mpc. For PMF strength of each zone, the Gaussian random field was applied. For each zone, the magnetic field impacts on electron capture rate (Eq. 2.12), thermodynamics (Eq. C.15), and time-temperature relation (Eq.C.20) are also taken into account, the screening effect has been proved not make big difference of the final abundance as discussed in 2.2.3, so it could be ignored. I evolved the BBN code for each zone and finally calculate the primordial

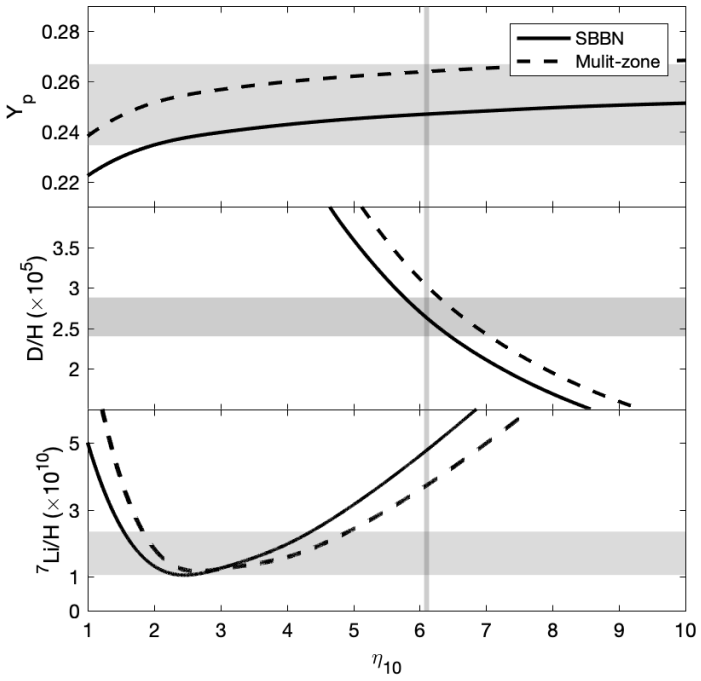

FIGURE 2.18: Y_p, D/H and ^{7}Li/H calculated abundance as a function of η_{10}, horizontal band in each element's panel represents the observational value. vertical band is the η_{10} value obtained from Planck analysis (Planck Collaboration et al., 2016a). Dashed line is the standard BBN calculation, solid line is our multi-zone results after averaging all zones.

elemental abundance of all zones, compare the averaged value with observations (Izotov, Thuan, and Guseva, 2014; Cooke, Pettini, and Steidel, 2018; Sbordone, 2010) as shown in Fig. 2.18. Although the ^{4}He and D abundances in this study touch the upper bounds of 2-σ from Cooke, Pettini, and Steidel (2018), however, unlike the homogeneous PMF, which could be simply treated as extra energy density so

that mainly ^{4}He is affected, the inhomogeneous PMF could deviate both ^{7}Li and D abundance which is consistent with Sect. 2.3. Also, although the co-moving PMF strength survive until today in this model is $B_0 \sim b \times 10^{-6}$ G, which is 1000 times larger than the IGMF limitation 10^{-9} G, however, as shown in Sect. 2.1, the co-moving strength of the field could decay if the turbulence is included.

In conclusion, this Chapter focuses on the PMF influence on BBN extensively. The thermodynamic conditions of the magnetized plasma are sophisticatedly investigated, however, because the relativistic plasma has low density during BBN epoch, these conditions could not change the primordial elemental abundance predictions significantly. Moreover, a static inhomogeneous PMF energy density model shows a completely new calculated result of primordial elemental abundances. A phenomenological model whereby sub-horizon iso-curvature temperature fluctuations arise from fluctuations in a PMF is explored. Previous studies (Cheng, Schramm, and Truran, 1994; Grasso and Rubinstein, 1996; Kernan, Starkman, and Vachaspati, 1996; Yamazaki and Kusakabe, 2012; Kawasaki and Kusakabe, 2012) introduced a constant PMF strength within a certain co-moving radius during the BBN epoch. However, if the inhomogeneous PMF exists, such a field could evolve and not keep the homogeneity. That could affect the temperature on large scales. I discussed a stochastic PMF and an ansatz for its strength distribution. BBN network calculations taking into account the PMF energy distribution is performed, it is found that the averaged charged-particle reaction rates are very different compared with those of a single temperature. As a result, the ^{7}Li abundance could be suppressed to $(3.35 \sim 3.52) \times 10^{-10}$ by such a static inhomogeneity arising from the PMF energy density, the D and ^{4}He abundances still satisfy the observational constraints. A multi-zone BBN calculation with spatial inhomogeneous PMF strength is also performed and obtains the similar reduction on ^{7}Li abundance. These facts stimulate us of the future works on building a realistic BBN model with MHD calculation to investigate the imprints of PMF dynamics in the primordial elemental abundances. I will try to clarify the potential solution of the "cosmic Li problem" from the fluctuated PMF in the future. Moreover, the dynamical PMF could leave imprints in the BBN calculation, then by comparing the final theoretical elemental abundance yields with observations, not only the strength could be constrained, but also the co-moving length scale of PMF.

Chapter 3

Strong Magnetic Field & Explosive Nucleosynthesis[1]

3.1 Introduction

In the explosive astrophysical sites such as the SNe explosion, the collapsar and the merging event, the particles interact strongly with each other via weak force and (or) electromagnetic force. The reaction rates are basically described by the probability of the scattering events and it could be differed due to the change in the microscopic and thermodynamic states of the environment. The interaction rates therefore, could be drastically varied from the theoretical estimation in the vacuum due to the many-body effect inside the plasma. One of the many-body effect that draws the attention recently is the Coulomb correction due to the electron-positron gas of the astrophysical sites: the electron positron gas in the fully ionized plasma could form a "effective shield" so that the the Coulomb barrier becomes lower. Previously, there are many studies on this effect: for the non-degenerate electron gas, the screening effect has been studied by Wang, Bertulani, and Balantekin (2011) for the non-relativistic contribution in the primordial nucleosynthesis, then Famiano, Balantekin, and Kajino (2016) included the relativistic contribution from the electron-positron plasma by solve the Schwinger-Dyson equation.

In a hot plasma, the background electrons create a "screening" effect between two reacting charged particles (Wu and Pálffy, 2017; Liu, 2016; Spitaleri et al., 2016; Kravchuk and Yakovlev, 2014; Potekhin and Chabrier, 2013; Quarati and Scarfone, 2007; Shaviv and Shaviv, 2000; Adelberger et al., 1998; Shalybkov and Yakovlev, 1987; Wang, Bertulani, and Balantekin, 2011; Wallace, Woosley, and Weaver, 1982; Itoh, Totsuji, and Ichimaru, 1977; Jancovici, 1977; Graboske et al., 1973; Dewitt, Graboske, and Cooper, 1973; Salpeter and van Horn, 1969; Salpeter, 1954). Coulomb screening reduces their Coulomb barrier because the effective charge between two particles is reduced. The commonly-used "extended" screening (Jancovici, 1977; Itoh, Totsuji, and Ichimaru, 1977) and recent evaluations of screening from relativistic effects have been explored (Famiano, Balantekin, and Kajino, 2016; Luo et al., 2020). In evaluating the screening effect, even a small shift in the potential energy can result in significant changes in the classical turning points of the WKB approximation, resulting in an increase in the reaction rate. It should be noted that other positively charged nuclei in a plasma also increase the reaction rate as positive and negative charges are redistributed in the presence of a "point-like" nuclear potential.

Though this adjustment to thermonuclear rates has been known for a long time (Salpeter, 1954), effects from relativistic, magnetized plasmas have not been fully addressed: the magnetic field could affects the motion of electrons and positrons inside

[1] This chapter is based on the paper Famiano et al. (2020)

the plasma, results in a change of their thermodynamics; also, electron momentum transverse to the field direction is quantized into Landau levels, the phase space integral is replace by a summation of the finite Landau levels. As discussed in Chapter 2, even the weak PMF could suppress the weak interaction rates and finally leave imprints in the predicted primordial abundances. For stronger astrophysical magnetic fields such as the collapsar jets and NSMs, the field strength could be as high as 10^{17} G (Nakamura et al., 2015; Kiuchi et al., 2015; Kiuchi et al., 2014; Takiwaki, Kotake, and Sato, 2009; Price and Rosswog, 2006; Ruiz, Tsokaros, and Shapiro, 2020). However, a few study focused on the magnetic field imprints in the nucleosynthetic yields in these astrophysical sites.

Another interesting process is the electrons and positrons pair production which is closely tied to the equilibrium abundances. It could occur at high-enough temperatures in which the tail of the Fermi distribution exceeds the pair-production threshold. Pair production has been studied in stellar cores of very massive stars (Kozyreva et al., 2017; Woosley, 2017; Spera and Mapelli, 2017; Takahashi, Yoshida, and Umeda, 2018) and as a neutrino cooling mechanism (Itoh et al., 1996). Also, though electron capture reactions have been previously studied (Itoh et al., 2002; Liu, Zhang, and Luo, 2007), the simultaneous effects of external magnetic fields and relativistic pair production on reaction rate screening (fusion and electron capture) in magnetized plasmas have not been fully considered. For temperatures and magnetic fields that are high enough, electrons and positrons can exist in non-negligible equilibrium abundances. In a magnetized plasma, the electron and positron energy distributions are altered by the external field.

The goal of this Chapter is to evaluate the effects of screening potential in both low and high density relativistic electron-positron plasmas of highly magnetized stellar environments, and also to investigate the magnetized plasma impacts on the weak interaction rates at the same time. In Sect. 3.2, the effects of weak screening corrections in a magnetized, relativistic plasma are studied, a useful approximation which can be used effectively in computational applications is developed. The results are finally applied to an example nucleosynthesis process in a MHD collapsar jet. In Sect. 3.3, I focus on high density plasma, the electrons (positrons) phase space's occupation is in a degenerate state, so that the screening potential strongly depends on the Fermi energy E_F. I investigate such strong screening corrections, and discuss the impacts on the weak interaction rates from such highly magnetized degenerate plasma. A profile from the 15 $M_\odot$ core collapsing SNe progenitor model is applied to calculate the electron capture rates of iron group nuclei, namely, ^{54}Fe and ^{70}Zn since they are the representative nuclides for pre-SNe and post-collapsing and bouncing calculation (Heger et al., 2001; Liebendörfer et al., 2001), separately. The results are essential to determine the electron fraction Y_e at the final stage evolution of massive star and the iron core mass before the SNe explosion.

3.2 Nuclear Reaction Weak Screening in High Magnetic Field

3.2.1 Weak Screening Limit

In a hot plasma, the background charges include the surrounding positrons, electrons and other nuclei. Classically, for a non-relativistic charge-neutral medium the electrostatic potential ϕ of a charge Ze in the presence of a background charge density can be computed via the Poisson-Boltzmann equation, i.e., Eq. 2.1. This description is almost universally used in astrophysical calculations involving nuclear

reactions. Here, the electron degeneracy must be calculated or estimated explicitly to accurately determine the energy and density distribution. However, for hot, magnetized plasmas electrons and positrons must be expressed in equilibrium using Fermi-Dirac statistics. The lepton number density in the presence of an external field is modified by the presence of Landau levels and changes from the zero-field form (Grasso and Rubinstein, 2001; Kawasaki and Kusakabe, 2012):

$$n(B \neq 0, T) = \frac{eB}{2\pi^2} \sum_{n=0}^{\infty} (2 - \delta_{n0}) \times \left[\int_0^{\infty} \frac{dp_z}{\exp\left[\frac{\sqrt{E^2+2neB}-\mu}{T}\right] + 1} - \int_0^{\infty} \frac{dp_z}{\exp\left[\frac{\sqrt{E^2+2neB}+\mu}{T}\right] + 1} \right]. \quad (3.1)$$

In the above Equation, $E = \sqrt{p_z^2 + m^2}$, where the z direction is parallel to the magnetic field. The term δ_{n0} accommodates the degeneracy for the higher Landau levels, and the index n takes into account the Landau level as well as the z-component of electron spin. As $B \to 0$, the summation in the second relationship in Eq. 3.1 becomes an integral, and the zero-field number density results.

The Poisson-Boltzmann equation must then be replaced with the equivalent equation assuming Fermi statistics with a magnetic field, B, and chemical potential, μ:

$$\begin{aligned} \nabla^2\phi(r) = & -4\pi Ze\delta^3(\mathbf{r}) - 4\pi \sum_{z>0} zen_z \exp\left[-\frac{ze\phi_r}{T}\right] \\ & + \frac{eB}{\pi} \sum_{n=0}^{\infty} g_n \int_0^{\infty} dp \Big[\frac{1}{\exp(\sqrt{E^2+2neB} - \mu - e\phi_r)/T + 1} \\ & - \frac{1}{\exp(\sqrt{E^2+2neB} + \mu + e\phi_r)/T + 1} \Big] + 4\pi \sum_{z>0} zen_z \\ & - \frac{eB}{\pi} \sum_{n=0}^{\infty} g_n \int_0^{\infty} dp \Big[\frac{1}{\exp(\sqrt{E^2+2neB} - \mu)/T + 1} \\ & - \frac{1}{\exp(\sqrt{E^2+2neB} + \mu)/T + 1} \Big] \end{aligned} \quad (3.2)$$

where the sum in the third term accounts for the quantized transverse momentum of electrons and positrons in a high magnetic field, and $g_n = 2 - \delta_{n0}$ accounts for Landau level degeneracy. The relativistic effects come from the high thermal energy, $T \sim m_e$, the Landau level spacing for field strengths with $\sqrt{eB} \sim m_e$, or both (Kawasaki and Kusakabe, 2012; Grasso and Rubinstein, 2001). The last two terms in Eq. 3.2 account for the redistribution of charge on the uniform charge background. For a charge-neutral plasma, the sum of these last two terms is zero before the charge Ze is introduced. Here, electrons are assumed to be relativistic while ions are still treated classically; the non-relativistic nuclei are treated with Boltzmann statistics.

The "screening enhancement factor" (SEF) f, relates the screened rate to the unscreened rate by $\langle \sigma v \rangle_{scr} = f \langle \sigma v \rangle_{uns}$. The value of f can be deduced from the WKB approximation in the thermonuclear reaction rates as $f = e^H$ (Graboske et al., 1973; Jancovici, 1977; Salpeter, 1954; Salpeter and van Horn, 1969; Wallace, Woosley, and Weaver, 1982), where H is a dimensionless value derived from the specific type of screening employed (Sahoo and Das, 2016; Kravchuk and Yakovlev,

2014; Itoh, Totsuji, and Ichimaru, 1977; Alastuey and Jancovici, 1978; Dewitt, Graboske, and Cooper, 1973; Quarati and Scarfone, 2007). As mentioned above, the intermediate exponent H_I is often determined using strong and weak screening values, $H_I = H_S H_W / \sqrt{H_S^2 + H_W^2}$. This method is used commonly in astrophysics codes incorporating nuclear reaction networks (Paxton et al., 2011; Paxton et al., 2015; Paxton et al., 2018; Meyer and Adams, 2007).

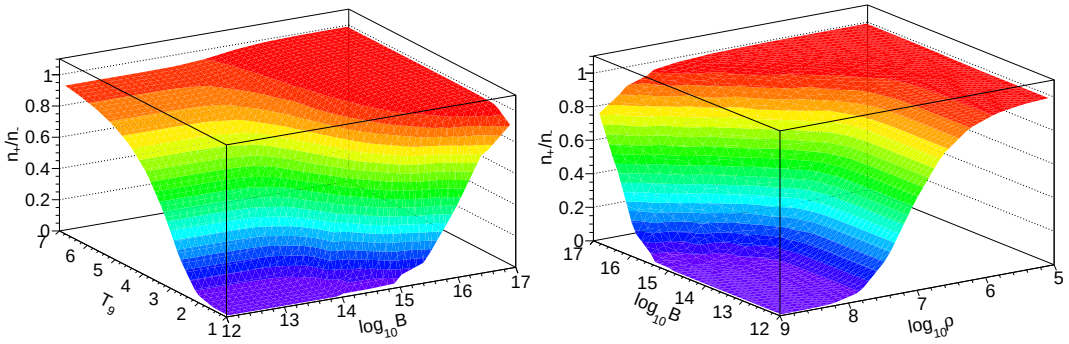

FIGURE 3.1: (a) Positron-electron ratio as a function of temperature and magnetic field in a neutral plasma at $\rho Y_e = 5 \times 10^5$ g/cm^3. (b) Positron-electron ratio as a function of density and magnetic field in a neutral plasma at temperature $T_9 = 7$ and $Y_e = 0.5$. The number densities are computed up to 2000 Landau levels.

An example of the importance of including thermal and magnetic field effects is shown in Fig. 3.1. Shown in the figure is the ratio of positron to electron number density as a function of temperature and magnetic field (where T_9 is the temperature in billions of K) at a density and electron fraction $\rho Y_e = 5 \times 10^5$ g/cm^3 taking into account the electron chemical potential at high density. Relativistic effects become increasingly important in this region as the positron number density becomes a significant fraction of the electron number density. The increased overall number of charges of any sign contribute to the screening effect, and this will be explored in this Chapter.

In the high temperature, low density "weak screening" limit, the Coulomb energy E_C between two reacting nuclei is lower than the thermal energy: $E_C/kT \ll 1$, as is the electron chemical potential. The electrons are mostly non-degenerate, and Eqs 3.2 can be expanded to first order in potential, $\mathcal{O}(\phi)$, known as the Debye-Hückel approximation. A corresponding Debye length, λ_D can be derived, resulting in a Yukawa-type potential, $\phi(r) \propto (e^{-r/\lambda_D})/r$ as opposed to the usual $1/r$ unscreened Coulomb relationship. For lower temperatures and higher densities resulting in higher electron degeneracy, the Thomas-Fermi (TF) screening length is more appropriate by solving the Schwinger-Dyson equation for the photon propagator (Kapusta and Gale, 2006) as discussed in Eq. 2.4 of Chapter. 2. The contribution to the screening length from the surrounding nuclei must also be included, and this can be significant in some cases. The chemical potential can be determined using Eq. 3.1 for a plasma of density ρ, electron fraction Y_e, and net electron density $n_- - n_+$. For most astrophysical applications, a static plasma is assumed with a net charge density of zero. The ratio of the relativistic Thomas-Fermi electron-positron screening length, λ_{TF}, to the classical Debye length, λ_D, is shown in Fig. 3.2 as a function of temperature and magnetic field at $\rho Y_e = 5 \times 10^6$ g/cm^3. In this figure, only the electron-positron screening length ratio is shown to emphasize the difference that high temperature and magnetic fields can induce in a plasma. In

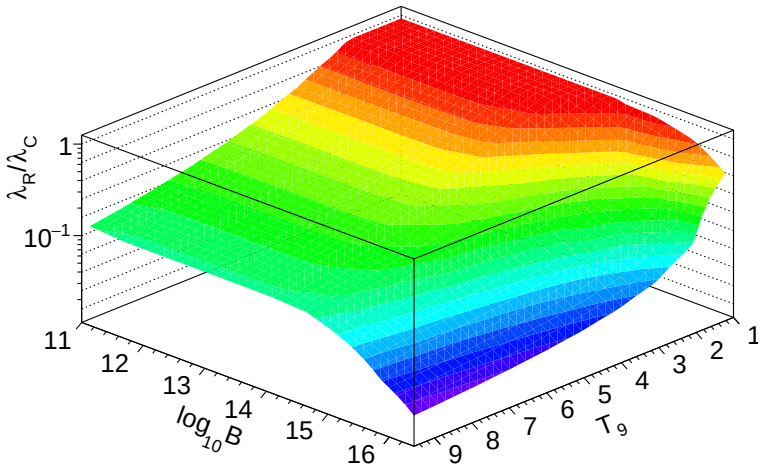

FIGURE 3.2: The ratio of classical to relativistic electron screening lengths for a neutral plasma as a function of temperature and magnetic field (G) at a constant electron density, $\rho Y_e = 5 \times 10^5$ g/cm^3.

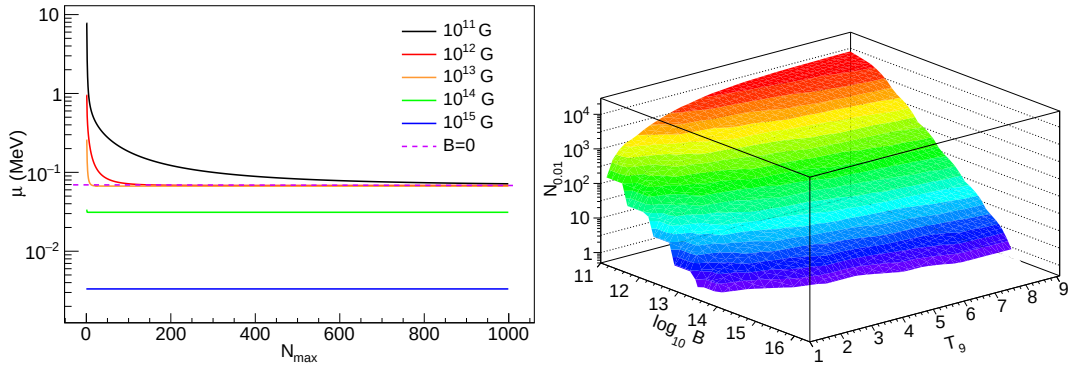

FIGURE 3.3: (a) Electron chemical potential as a function of the maximum number of Landau levels included in summation over Landau levels at $T_9 = 2$, $\rho Y_e = 5 \times 10^4$ g cm^{-3} for various magnetic fields. The dashed line is the chemical potential for an ideal Fermi gas. (b) Number of Landau levels necessary to approach an equilibrium electron number density with a maximum uncertainty of 1%, $N_{0.01}$ at a $\rho Y_e = 5 \times 10^4$ g cm^{-3} as a function of magnetic field (G) and T_9.

astrophysical calculations, the screening length from other nuclei must also be included, $1/\lambda^2 = 1/\lambda^2_{ion} + 1/\lambda^2_{-,+}$. There is a significant difference between the classical and relativistic screening lengths at high temperature and field. Because the screened rates depend exponentially on the screening lengths at low density/high-temperature, even small changes in the screening length can be significant. The relativistic electron screening length can be quite small at high-enough temperature or B field.

It is noted that at higher density or lower temperature, intermediate screening depends more heavily on the electron chemical potential. The increased electron chemical potential results in the electron-positron number densities which approach classical (non-relativistic) values. That is $n_- \rightarrow \rho N_A Y_e$ and $n_+ \rightarrow 0$. Because of this, first-order weak screening is replaced by an ion-sphere screening model or a type of geometric mean between the ion-sphere and weak screening model (Wallace, Woosley, and Weaver, 1982; Salpeter and van Horn, 1969).

In determining the equilibrium electron-positron number density and the screening lengths, computational models may truncate the number of Landau levels that are counted in the evaluation, or the sum may be replaced by an integral in a low-field approximation (Kawasaki and Kusakabe, 2012). For high fields, one can determine the number of Landau levels necessary to sum over to obtain a certain accuracy in the computation. This is illustrated in Fig. 3.3. In Fig. 3.3a, the computed electron chemical potential is shown as a function of the maximum Landau level, N_{max} included in the sum in Eq. 3.1 for $T_9 = 2$, and $\rho Y_e = 5 \times 10^4$ g cm^{-3}. As the number of Landau levels summed over increases, the chemical potential converges to its equilibrium value. For a field of 10^{15} G, the convergence is immediate, and the approximation where only the lowest Landau level is considered is valid. For 10^{14} G, the convergence occurs rapidly at $N_{max} = 1$, and the difference between this approximation and the $N_{max} = 1$ summation is small. At lower fields, a summation over more Landau levels is necessary in order to achieve a reasonable accuracy.

It is also interesting to note that at higher fields, the electron chemical potential is reduced as the level density is adjusted by the presence of Landau levels. At the highest fields, the electron transverse momentum is discrete and increases with field. The energy necessary to fill higher Landau levels is large compared to the thermal energy of the plasma, kT, and electrons are forced into the lowest-energy levels. However, if the field is low-enough such that $\sqrt{eB} \ll kT$, the chemical potential approaches that of an ideal Fermi gas, and the plasma can be treated as such. In this case, the field can be ignored.

Similarly, in Fig.3.3 (b), truncating the sum over Landau levels at a specific number is explored by examining the number of Landau levels necessary to achieve a desired uncertainty. Shown on the right side of this figure is the number of Landau levels necessary, $N_{0.01}$, such that the relative difference between the sum over $N_{0.01}$ Landau levels and the equilibrium number density is less than 1%:

$$1 - \frac{\sum_{i=0}^{N_{0.01}-1} h_i}{\sum_{i=0}^{N_{large}} h_i} < 0.01, \tag{3.3}$$

where h_i are individual terms in the number density in Eq. 3.1. That is, the relative difference between the number density if only $N_{0.01}$ Landau levels are used and if a sufficiently large number of Landau levels is used is less than 0.01. For this figure, the density times the electron fraction is $\rho Y_e = 5 \times 10^4$ g cm^{-3}. For fields that are high-enough, $B \gtrsim 10^{13}$ G, each successive term in the sum drops by roughly an order of magnitude, $h_{i+1}/h_i \sim 0.1$. Here, a value of N_{large} of 10^4 is assumed. From the left side of the figure, it is seen that even at low fields, sums up to terms less than 10^4 Landau levels are sufficient to characterize the plasma, indicating a choice of $N_{large} = 10^4$ to be sufficient. Even at low fields, the last $\sim$ 3000 Landau levels in the sum contribute less than 1% to the total electron-positron number density. For a lower field, it is necessary to include several hundred (or more) Landau levels in the sum for an accurate calculation. For the very high field, however, one can achieve a high accuracy by including only the lowest Landau level, known as the *lowest Landau level* (LLL) approximation. A discussion of the accuracy and utility of the LLL approximation in evaluating the TF length will be given later.

As can be seen from Figs. 3.1 and 3.3a, the effect of the magnetic field becomes negligible roughly below 10^{13} G. The electron-positron population is determined

almost exclusively by the system temperature and density. In this region, the thermally calculated chemical potential without magnetic fields is almost identical to that computed if magnetic field effects are accounted for and the positron number density approaches zero as stated previously. For the temperature and density used for Fig. 3.3a, the electron chemical potential if no field were present would be 0.76 MeV. Above 10^{13} G, the chemical potential decreases with field. At high fields and high temperatures, the chemical potential is low, and the electron-positron Fermi distribution is constrained to relatively low momentum. In this case, one should consider an Euler-MacLaurin expansion in momentum using the Euler-MacLaurin formula. The net electron number density can be written as:

$$n_e = eB\frac{T}{2\pi^2}\sum_{\tilde{p},n=0}^{\infty} g_n \left(\frac{2-\delta_{p0}}{2}\right)\frac{\sinh\tilde{\mu}}{\cosh\sqrt{\tilde{p}^2+\tilde{m}^2+n\gamma}+\cosh\tilde{\mu}}, \tag{3.4}$$

where $\gamma \equiv 2eB/T^2$ and terms with a tilde are divided by T, $\tilde{x} \equiv x/T$. These terms are unitless. It is noteworthy that, for the Euler-MacLaurin formula, the higher-order derivatives are zero, meaning that the sum above is complete. In the case of a strong magnetic field, the LLL approximation yields:

$$n_e = eB\frac{T}{2\pi^2}\sum_{\tilde{p}=0}^{\infty} \left(\frac{2-\delta_{p0}}{2}\right)\frac{\sinh\tilde{\mu}}{\cosh\sqrt{\tilde{p}^2+\tilde{m}^2}+\cosh\tilde{\mu}}, \tag{3.5}$$

resulting in a linear dependence on the external magnetic field.

The Thomas-Fermi screening length in a strong magnetic field is derived as:

$$\begin{aligned}\frac{1}{\lambda_{TF}^2} = 4\pi e^2\frac{\partial n}{\partial\mu} &= eB\frac{e^2}{\pi}\frac{\partial}{\partial\tilde{\mu}}\sum_{n=0}^{\infty} g_n\int_0^{\infty}\frac{d\tilde{p}}{\exp\left[\sqrt{\tilde{p}^2+\tilde{m}^2+n\gamma}\mp\tilde{\mu}\right]+1}\\ &= eB\frac{e^2}{\pi}\sum_{n=0}^{\infty} g_n\int_0^{\infty}\frac{\partial}{\partial\tilde{\mu}}\frac{d\tilde{p}}{\exp\left[\sqrt{\tilde{p}^2+\tilde{m}^2+n\gamma}\mp\tilde{\mu}\right]+1}\\ &= eB\frac{e^2}{\pi}\sum_{n=0}^{\infty} g_n\int_0^{\infty}\frac{d\tilde{p}}{1+\cosh\left(\sqrt{\tilde{p}^2+\tilde{m}^2+n\gamma}\mp\tilde{\mu}\right)},\end{aligned} \tag{3.6}$$

where the $\mp$ corresponds to the electron/positron number density, and the sum over both electron and positron densities is implied. The Euler-MacLaurin formula, expanded in momentum, yields an easily-computed form for the integral term above:

$$\frac{1}{\lambda_{TF}^2} = eB\frac{e^2}{\pi}\sum_{\tilde{p},n=0}^{\infty} g_n\left(\frac{2-\delta_{p0}}{2}\right)\frac{1+\cosh\tilde{\mu}\cosh\sqrt{\tilde{p}^2+\tilde{m}^2+n\gamma}}{\left(\cosh\tilde{\mu}+\cosh\sqrt{\tilde{p}^2+\tilde{m}^2+n\gamma}\right)^2} \tag{3.7}$$

where the sum over n is a sum over Landau Levels and the sum over $\tilde{p} = p/T$ results from the Euler-MacLaurin formula for Eq. 3.6.

One can approximate a sum over several Landau levels and only up to a maximum value of $\tilde{p}$ in the above equation:

$$\frac{1}{\lambda_{TF}^2} \propto \sum_{n=0}^{\infty} g_n\left[\sum_{\tilde{p}=0}^{\infty}\ldots\right] \rightarrow \sum_{n=0}^{n_{max}} g_n\left[\sum_{\tilde{p}=0}^{\tilde{p}_{max}}\ldots\right] + R_{\tilde{p}}, \tag{3.8}$$

where n_{max} is the highest Landau level included in the sum, and $\tilde{p}_{max}$ is the highest term included in the Euler-MacLaurin formula. The remainder induced by truncating the sum is $R_{\tilde{p}}$.

At high magnetic field, the electron chemical potential is much smaller than the Landau level spacing. In this case, the sum over $\tilde{p}$ converges rapidly, and the summation can be truncated to a few terms. For the purposes of computation, the limitation of the sum may be determined to truncate at $\tilde{p}_{max}$ where the difference in successive terms is smaller than some uncertainty, ε:

$$\frac{f_{\tilde{p}_{max}} - f_{(\tilde{p}_{max}-1)}}{f_{\tilde{p}_{max}}} < \varepsilon \tag{3.9}$$

As an example, the relative error in λ_{TF}, $\Delta\lambda/\lambda = 1 - \lambda_{McL}/\lambda_{exact}$ (where the Thomas-Fermi length deduced from the truncated sum is λ_{McL} and that deduced from Eq. 3.6 is λ_{exact}) induced by truncating the Euler-MacLaurin sum to a maximum index of $\tilde{p}_{max}$ is shown in Fig. 3.4 for temperatures T_9=7 and 2, at $\rho Y_e = 5{\times}10^4$ g cm^{-3}, and three values of the external magnetic field. Even for a low value of $\tilde{p}_{max} = 5$, the uncertainty is less than 1%.

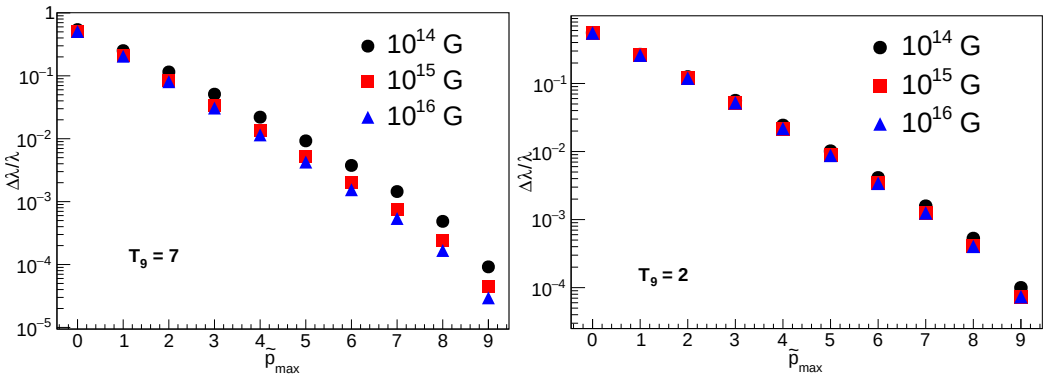

FIGURE 3.4: Relative error in Euler-MacLaurin formula compared to exact numerical computation for the integration in Eq. 3.6 as a function of maximum $\tilde{p}$ in the sum. Computations are for $\rho Y_e = 5 \times 10^4$ g cm^3 at temperatures (a) $T_9 = 7$ and (b) $T_9 = 2$. The maximum Landau level calculated in each case is $N_{max} = 2000$.

The validity of this approximation in determining the screening length at temperatures $T_9 = 2$ and 7 at $\rho Y_e = 5{\times}10^4$ g cm^{-3} is shown in Fig. 3.5. In this figure, the approximation given in Eq. 3.7 is used to determine the TF screening lengths. For each line in the figure, only the lowest 12 terms in the sum over $\tilde{p}$ are used. That is $\tilde{p}_{max} = 12$. The maximum number of Landau levels summed over is indicated for the various results in the figure. One sees that the lowest Landau level (LLL, N_{max} = 0) approximation performs quite well at high fields (log(B)$\gtrsim$14). At lower fields, more Landau levels must be included in the sum.

For completeness, the dependence of this approximation on temperature and density is shown in Fig. 3.6, which shows the relative error in the TF length computed with Eq. 3.7 compared to that computed with Eq. 3.6. It is seen that – in the weak screening regime – there is almost no dependence on density and a small dependence on temperature. Even at low fields (Fig. 3.6b), the error is relatively small. At lower temperatures, the error is somewhat larger. However, this area would very likely correspond to non-relativistic or intermediate screening.

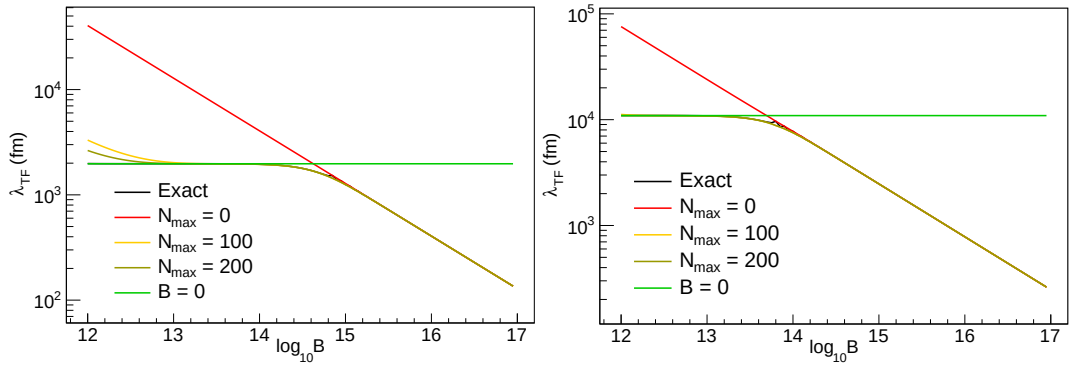

FIGURE 3.5: Electron Thomas-Fermi screening length using the approximation described in Eq. 3.6 for sums up to various maximum Landau levels, as indicated in the figure. In both figures, $\rho Y_e = 5 \times 10^4$ g cm^{-3}. The temperature is (a) $T_9 = 7$ and (b) $T_9 = 2$. For the panel (b), the lines corresponding to $n = 100$ and $n = 200$ lie on top of each other. In this figure, only the lowest 12 terms in the Euler-MacLaurin sum are computed, $\tilde{p}_{max} = 12$.

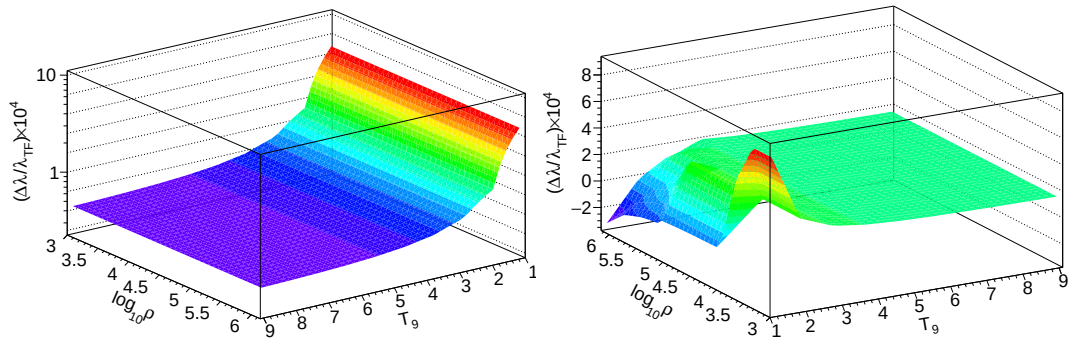

FIGURE 3.6: Relative difference in TF screening length Euler-MacLaurin approximation to the exact computation as a function of T and ρ for (a)$B = 10^{16}$ G and (b)$B = 10^{13}$ G for various temperatures and densities. Here, only the LLL approximation is used for the 10^{16} G case and the lowest 2000 Landau levels are used for the 10^{13} G case. In both panels, $Y_e = 0.5$.

For a lower field of $B = 10^{13}$ G, the approximation of Eq. 3.7 is shown in Fig. 3.6b, including the lowest 2000 Landau levels ($N_{max} = 2000$) and $\tilde{p}_{max} = 12$. The TF screening length is still fairly well approximated over a wide range of temperatures and densities even at lower B field if a sufficient number of Landau levels are included in the sum. For most temperatures and densities, the screening length is within about 10% of the actual Thomas-Fermi length. However, it is also noted that if the field is low enough, λ_{TF} for $B = 0$ is an excellent approximation, and the effect of the field can be ignored.

3.2.2 Weak Interactions

In addition to the inclusion of magnetized plasma effects on screening of the Coulomb potential and modifications to the electron-positron chemical potential, effects on weak interaction rates have also been examined. Weak interactions can be altered by changes to the electron Fermi-Dirac distribution function and the electron energy spectrum in weak decays (Luo et al., 2020; Grasso and Rubinstein, 2001; Fassio-Canuto, 1969). In addition, the shifts to the electron-positron chemical potentials in

the thermal plasma are also modified. The shift in chemical potentials can change the Fermi-Dirac functions, altering the available states for capture and decay as well as the Pauli blocking factors. This can influence all of the weak interactions. Also, the electrons and positrons involved in weak interactions are constrained to Landau levels, creating nearly-discrete energy spectra, especially at high fields.

In the presence of magnetic fields, the phase space $d^3\boldsymbol{p}$ of the interactions is changed by the presence of Landau Levels (see Eq. 2.10). The corresponding shift in the lepton energy spectra can have dramatic effects on the weak interaction rates in a magnetized plasma. With the inclusion of density distributions modified by the existence of Landau levels, the approximate weak interaction rates can be rewritten with the momentum component parallel to the magnetic field vector and the discrete transverse momentum components (Luo et al., 2020; Grasso and Rubinstein, 2001; Fassio-Canuto, 1969):

$$\Gamma_{\beta^-} = \kappa \frac{eB}{2} \sum_{n=0}^{N_{max}} (2-\delta_{n0}) \int_{\omega_\beta}^{Q} \frac{E(Q-E)^2}{\sqrt{E^2-m_e^2-2neB}} g(E,\mu_e) g(Q-E,-\mu_\nu) dE, \tag{3.10}$$

$$\Gamma_{\beta^+} = \kappa \frac{eB}{2} \sum_{n=0}^{N_{max}} (2-\delta_{n0}) \int_{\omega_\beta}^{-Q} \frac{E(-Q-E)^2}{\sqrt{E^2-m_e^2-2neB}} g(E,-\mu_e) g(-Q-E,-\mu_\nu) dE, \tag{3.11}$$

$$\Gamma_{EC} = \kappa \frac{eB}{2} \sum_{n=0}^{N_{max}} (2-\delta_{n0}) \int_{\omega_{EC}}^{\infty} \frac{E(E-Q)^2}{\sqrt{E^2-m_e^2-2neB}} f_{FD}(E,\mu_e) g(E-Q,\mu_\nu) dE, \tag{3.12}$$

$$\Gamma_{PC} = \kappa \frac{eB}{2} \sum_{n=0}^{N_{max}} (2-\delta_{n0}) \int_{\omega_{PC}}^{\infty} \frac{E(E+Q)^2}{\sqrt{E^2-m_e^2-2neB}} f_{FD}(E,-\mu_e) g(E+Q,-\mu_\nu) dE, \tag{3.13}$$

where f_{FD} is the Fermi-Dirac distribution and g is the Pauli blocking factor, also with the following quantities are defined (Arcones, Martinez-Pinedo, and Woosley, 2010; Hardy and Towner, 2009):

$$\begin{aligned} \omega_{EC/PC} \equiv & \max\left[\pm Q, m_e\right], \quad \omega_\beta \equiv \sqrt{m_e^2+2neB}; \\ N_{max} \leq & \frac{Q^2-m_e^2}{2eB}, \quad \kappa \equiv \frac{B \ln 2}{K m_e^5}; \\ B \equiv & 1+3g_A^2 = \begin{cases} 5.76, \text{nucleons}, \\ 4.6, \text{nuclei}, \end{cases} \\ K \equiv & \frac{2\pi^3\hbar^7 \ln 2}{G_V^2 m_e^5} = 6144 \text{ s}. \end{aligned} \tag{3.14}$$

Here the transition Q value is the difference in nuclear masses.

Unlike the case of an ideal Fermi gas, the electron-positron energy spectrum in weak interactions is not thermal, and the LLL approximation is not necessarily applicable. For example, the evolution with magnetic field of the β^- spectrum for a nuclei with a decay Q value of 12 MeV at $T_9 = 2$ and $\rho Y_e = 500$ g cm^{-3} is shown in Fig. 3.7. This spectrum is the integrand of Eq. 3.10. In the case of a non-zero field, the β spectrum is a sum of individual spectra for each Landau level with the maximum Landau level energy less than the decay Q value, $\sqrt{2neB+m_e^2} \leq Q$.

For a lower field, the Landau level spacing is much less than the Q value of the decay $\sqrt{eB} \ll Q$. An electron can be emitted into any of a large number of Landau

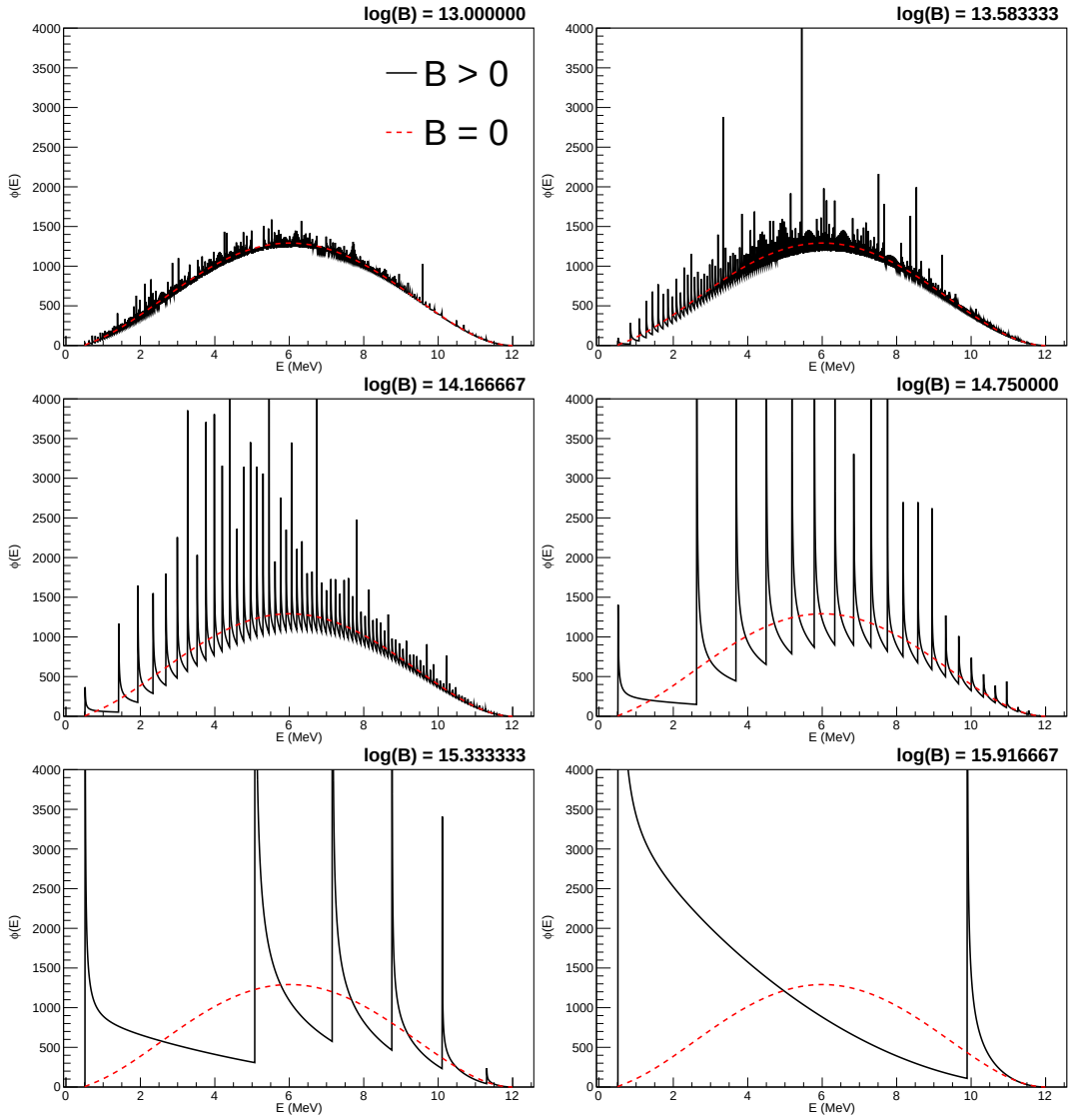

FIGURE 3.7: Evolution of the β^--decay spectrum with magnetic field for six different fields indicated in each panel. The red, dashed line indicates the spectrum for $B = 0$, and the black line indicates the spectrum for the magnetic field indicated in each figure. For this series of figures, the decay Q value is 12 MeV, and the values of T_9 and ρY_e are 2 and 500 g cm^{-3} respectively. The magnetic field units are G.

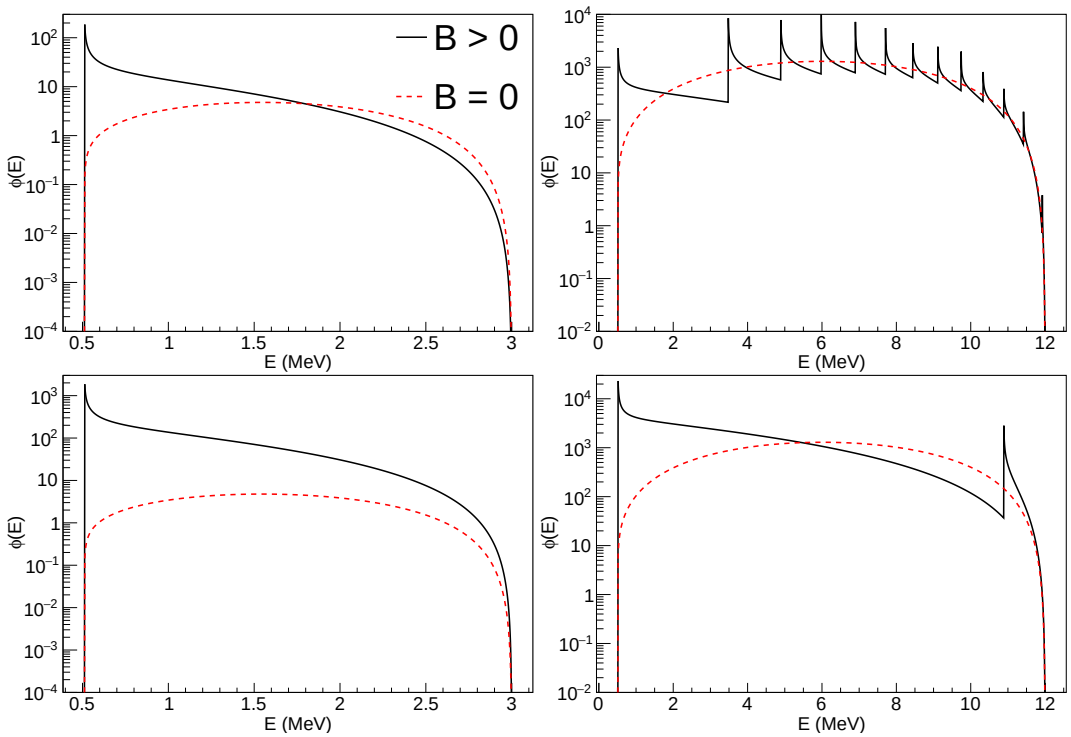

FIGURE 3.8: Electron β-decay spectra for $B = 10^{15}$ G (a,b) and 10^{16} G (c,d) for low Q values (a,c) and high Q values (b,d). The spectra are calculated at $T_9 = 2$ and ρY_e=500. The red, dashed lines correspond to the spectra for $B = 0$.

levels with level energies less than the electron energy. The Landau level spacing is quite small in this case. For decays to many possible Landau levels, the integrated spectrum is closer in value to the zero-field spectrum. In other words, as $eB \to 0$, the integrated non-zero-field spectrum approaches the zero-field spectrum. The sum in Eq. 3.10 becomes an integral, and the Landau level spacing $eB = \Delta p^2 \to d^2p$. The sum over all Landau levels approaches the zero-field spectrum. As the magnetic field increases, such that $\sqrt{2neB} \sim Q$, fewer Landau levels contribute to the total spectrum. For a very few levels, the zero-field and non-zero-field spectra can be dramatically different, and the decay rates can be magnified for higher fields. This could be potentially important for an r-process that proceeds in a high magnetic field, such as in a collapsar jet or NS merger, for example. Because the r-process encompasses nuclei with a wide range of β^- decay Q values, the effects of an external magnetic field can be significant. This is shown in Fig. 3.8, which shows the electron energy spectrum in β^- decay for several cases of Q-value and magnetic fields. This spectrum is also the integrand of Eq. 3.10. Spectra are computed for β^- decays at T_9=2 and ρY_e = 500 g cm^{-3}.

In this figure, four cases are shown for each combination of two Q values of 3 MeV and 12 MeV and two cases of magnetic field of 10^{15} G and 10^{16} G. For the low Q value of 3 MeV, the electrons can only be emitted into the lowest Landau level for both fields, i.e., $N_{max} = 0$. However, at a higher Q value of 12 MeV, the electron can be emitted into any of a number of Landau levels. For example, an electron emitted with an energy of 6 MeV could fall into the $N = 0$, 1, or 2 Landau level. The integration is thus a sum over all Landau levels up to the maximum possible Landau level within the β spectrum; $N_{max} = 11$ in this case. For a field of 10^{15} G, the Landau level spacing $\sqrt{eB} = 2.43$ MeV, which is less than the decay Q value, so

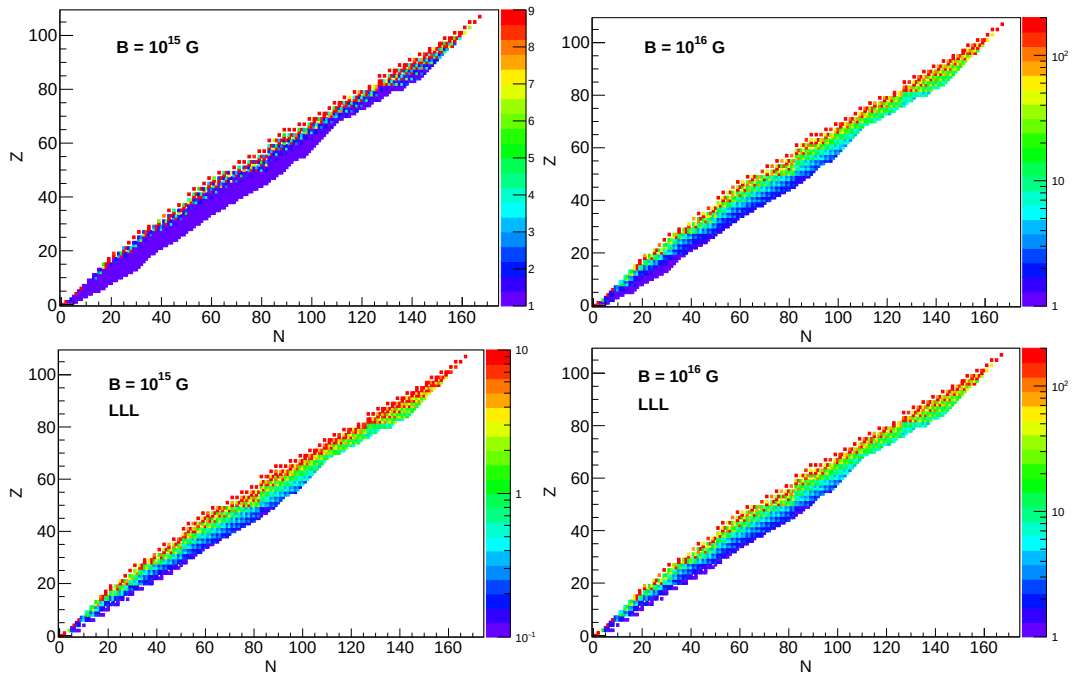

FIGURE 3.9: Ratio of β^- decay rates for decays of nuclei unstable against β^- decay in a non-zero field to those in a zero field, $\Gamma(B \neq 0)/\Gamma(B = 0)$ for magnetic fields $B = 10^{15}$ G (a,c) and $B = 10^{16}$ G (b,d). The top row corresponds to ratios for which all relevant Landau levels are included in the decay calculation, while the bottom row is for calculations for which only the lowest Landau level is included in the calculations. In all figures, $T_9 = 2$, $\rho Y_e = 500$ g cm^{-3}. Note the difference in scales in each figure.

multiple Landau levels contribute to the β spectrum.

For a higher field of 10^{16} G, with a Landau level spacing of 7.69 MeV, even at high β^- decay Q values, only a few (or one) Landau levels can be occupied by the emitted electrons. Further, as indicated in Fig. 3.8, for decay spectra that occupy very few Landau levels, the integrated spectrum, which is proportional to the total decay rate, can be significantly higher than the zero-field spectrum. The relationship between the Landau level spacing and the β-decay Q value is important in considering the astrophysical r-process. Because the r-process proceeds along a path of potentially very neutron-rich nuclei, the β^- decay Q values can be quite large, ~ 10 MeV. Thus, for an r-process in a high-field environment, the decay rates could be quite sensitive to the field. However, because the Q values are large, one cannot necessarily assume that the decay rates can be computed with just the LLL approximation.

The influence of high magnetic fields on β^- decay is shown in Fig. 3.9 for two assumptions of the magnetic field and two assumptions of Landau levels (whether the LLL approximation is used or not) at a temperature $T_9 = 2$ and $\rho Y_e = 500$. Here, the ratios of decay rates in a non-zero field to those in a zero field $\Gamma(B \neq 0)/\Gamma(B = 0)$ are plotted for each β^- unstable nuclei with Q values taken from the AME2016 evaluation (Wang et al., 2017).

Several findings are noted in this figure. First, for nuclei closer to stability, the Q values are much lower, and the rate ratio is higher. This is because electrons are emitted in only a few (or one) Landau levels. These nuclei would correspond to the schematic cases of Figs. 3.8a and c. For the higher field of 10^{16} G, the figures for the LLL assumption and the assumption for all relevant Landau levels are very similar,

indicating that the LLL is the primary contributor to the electron spectra in β^- decay for all nuclei at this field strength. At this field, the difference between the zero-field and non-zero-field computations is significant, and the increase in rates is much higher. However, for a field of 10^{15} G, inclusion of only the LLL underestimates the total rate. Including all relevant Landau levels in the rate computation is necessary. For more neutron-rich nuclei, more Landau levels are filled by the emitted electron, and the β spectrum more closely matches the zero-field spectrum. Thus, the ratio approaches unity. This would correspond to the case represented schematically in Fig. 3.8b. For a higher field, the ratio is close to unity only for the most neutron-rich nuclei, where the Q values are high enough fill multiple Landau levels in the decay. For the nuclei closer to stability, the Q values are low enough that only a single Landau level is filled by the ejected electron, resulting in a decay spectrum that is significantly different than the zero-field case. For the $B = 10^{16}$ G case for nuclei close to stability, the larger rates would correspond to the decay spectrum represented schematically in Fig. 3.8c.

3.2.3 Effects of External Magnetic Fields in *r*-Process Nucleosynthesis

As an example, *r*-process nucleosynthesis in a collapsar jet trajectory is examined. It is thought that the magnetic fields associated with collapsar jets and NSMs could be as high as 10^{16} G (Nakamura et al., 2015; Kiuchi et al., 2015; Kiuchi et al., 2014; Takiwaki, Kotake, and Sato, 2009). Such strong fields are formed by amplifying initially weak fields associated with the accretion region. While these fields may be near the surface of the objects, these will be considered as a possible upper limit in nucleosynthesis associated with collapsars and NSMs. Within the actual jet region in this model, fields have been computed to be $\sim 10^{12-14}$ G (Harikae, Takiwaki, and Kotake, 2009). Other evaluations of magnetic fields in collapsars or neutron star mergers have resulted in similar fields near the surface or the accretion disk, with some estimates up to and exceeding 10^{17} G (Price and Rosswog, 2006; Ruiz, Tsokaros, and Shapiro, 2020). While the field in the actual nucleosynthesis site may vary significantly, a few field cases are examined here to show the field magnitudes necessary to result in significant differences in the final *r*-process abundance distribution. Some of the fields investigated in the *r*-process nucleosynthesis studied here may very well exceed realistic values or those in nature and are thus illustrative in conveying field-strength effects in nucleosynthesis processes. Temperature effects, on the other hand are computed for the actual computed environmental temperature of the *r*-process site. Here, the effects of Coulomb screening in the early stages of the *r*-process as well as the effects from the enhancement of weak interaction rates by the external field are examined.

Several nucleosynthesis scenarios are investigated to evaluate the effects on *r*-process nucleosynthesis. These scenarios are listed in Table 3.1, where the notation $\mathrm{X(F)}_{\log B}$ is used; the label 'X' refers to a specific screening and weak interaction treatment at a field B, and 'F' indicates the inclusion of fission cycling or not. For example, model A_{14} is model A at a magnetic field of 10^{14} G without fission cycling while model AF_{14} is the same model with fission cycling included. The various models summarized are:

- No Coulomb screening and no magnetic field effects. (Models $\mathrm{A}_{\log B}$ and $\mathrm{AF}_{\log B}$)

TABLE 3.1: Models used to evaluate the effects of screening from temperature and magnetic fields as well as effects from magnetic fields on weak interactions. For each model, the subscript is the magnetic field strength.

Model	Screening	Weak Interactions
$\mathrm{A(F)}_{\log B}$	None	$B = 0$
$\mathrm{B(F)}_{\log B}$	Classical	$B = 0$
$\mathrm{C(F)}_{\log B}$	Relativistic ($B = 0$)	$B = 0$
$\mathrm{D(F)}_{\log B}$	Relativistic (B$\neq$0)	$B = 0$
$\mathrm{E(F)}_{\log B}$	Relativistic ($B \neq 0$)	$B \neq 0$, LLL only
$\mathrm{F(F)}_{\log B}$	Relativistic ($B \neq 0$)	$B \neq 0$, All LL

- Default classical screening in which weak screening is determined by electrons in a Maxwell distribution (Jancovici, 1977; Itoh et al., 1979). (Models $\mathrm{B}_{\log B}$ and $\mathrm{BF}_{\log B}$.)
- Relativistic screening in which the weak screening TF length is determined from electrons in an ideal Fermi gas (Famiano, Balantekin, and Kajino, 2016). (Models $\mathrm{C}_{\log B}$ and $\mathrm{CF}_{\log B}$.)
- Relativistic screening including effects on the TF length from an external magnetic field on the Fermi gas (Luo et al., 2020). (Models $\mathrm{D}_{\log B}$ and $\mathrm{DF}_{\log B}$.)
- Relativistic including effects on the TF length plus magnetic field effects on weak interaction rates assuming the LLL approximation. (Models $\mathrm{E}_{\log B}$ and $\mathrm{EF}_{\log B}$.)
- Relativistic including effects on the TF length plus effects on weak interaction rates including all contributing Landau levels to the β^- decays. (Models $\mathrm{F}_{\log B}$ and $\mathrm{FF}_{\log B}$.)

In Table 3.1, the models indicated by $B = 0$ are those for which the magnetic field effects are not included in the evaluation of screening or weak interactions. Model E includes effects of the magnetic field on weak interactions, but only the LLL approximation is used. Model F includes weak interaction effects for all relevant Landau levels in β^- decays.

In order to evaluate the effects of magnetic fields on screening and weak interactions in a possibly highly magnetized plasma in the *r*-process, a single trajectory from the MHD jet model of Nakamura et al. (2015) was used. This trajectory is shown in Fig. 3.10. Several values of a static, external magnetic field were evaluated. Because the field may not be well understood in many sites, this evaluation is taken to be qualitative only as a demonstration of the magnitude of the effects of strong external fields in nucleosynthetic sites. Nucleosynthesis in static fields, $14 \leq \log(B) \leq 16$, was evaluated. For the *r*-process calculation, the initial composition was assumed to be protons and neutrons with $Y_e = 0.05$ as given in Nakamura et al., 2015. The nuclear reaction network code `NucnetTools` (Meyer and Adams, 2007) was modified to include thermodynamic effects and screening effects at high temperature and magnetic fields. The reaction network was a full network which was truncated at $Z = 98$.

The weak interaction rates were computed using the relationships in Eqs. 3.10 – 3.13. These rates are ground-state transitions only. However, the purpose of this initial evaluation is not an evaluation of accurate weak interaction rates, but a description of the effects of strong magnetic fields on nucleosynthetic processes. If transitions to excited states are included, the rates are expected to be even more sensitive to external fields because of the smaller transition Q value relative to the Landau level spacing (Fig. 3.8), while transitions from excited states may be less sensitive as the Q values are larger, though one must also account for changes in transition order when including excited states.

The nucleosynthesis was computed to 6000 s. In order to do this, an extrapolation of the Nakamura et al., 2012 trajectories to low T and low ρ was made because the published trajectories stop at 2.8s. At low-enough temperatures and densities, neutron captures decline, and only β-decays and subsequent smoothing ensues. The temperature and density extrapolation was done assuming an adiabatic expansion for $t > 2.8$ s, $\log(T_9) \propto \log(\rho) \propto \log(t)$. This extrapolation allows the temperature and density to drop significantly to follow the processing further in time while examining effects from late-time fission cycling. Clearly, there is still some nucleosynthesis during this phase, and this is used to evaluate long-term effects of the nucleosynthesis.

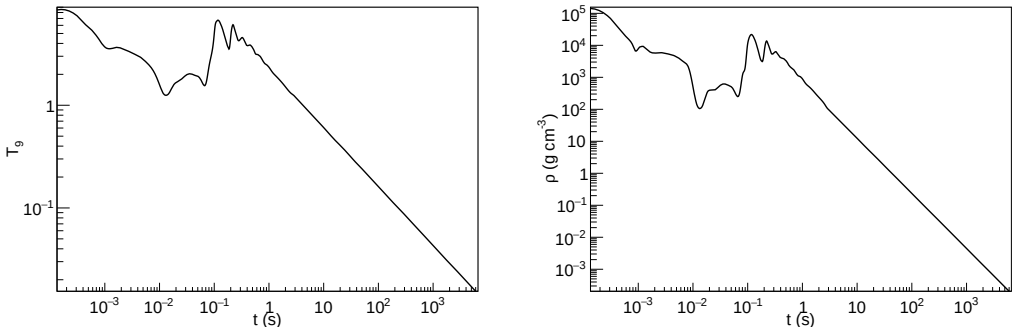

FIGURE 3.10: Trajectory used for the MHD *r*-process nucleosynthesis calculation. (a) Temperatures, T_9. (b) Density.

To include screening effects, relativistic weak screening was used for $T_9 > 0.3$. For lower temperatures, the classical Debye-Hückel screening was used in models C - F (see Fig. 3.2). In model B, classical Debye-Hückel screening was used for all temperatures. For the strong magnetic field, the Thomas-Fermi length of Eq. 3.7 was used. For weaker fields, the difference between the screening lengths for the relativistic case at $B = 0$ and at $B \neq 0$ is negligible as shown in Fig. 3.5. Thus, to improve the speed of the network calculations, the LLL approximation was assumed with the expansion of Eq. 3.7. In order to determine whether to use the LLL approximation or the thermal screening length (with $B = 0$), the inverse screening length, $k \propto 1/\lambda$, was computed in each case, and the maximum value was used:

$$k \rightarrow \max\left[k(B=0), k(B\neq 0)\right] \tag{3.15}$$

The resultant corresponding screening length is then determined by Eq. 3.7 at high fields and the relativistic length computed in prior work (Famiano, Balantekin, and Kajino, 2016) at lower fields. Certainly, there is a small transition region between the low-field and the high-field values shown in Fig. 3.5 where the screening length is overestimated slightly. In this region, the screening length could be overestimated

by as much at ∼15%, with a resultant shift in the overall reaction rates of about 15%. This can be corrected by relaxing the LLL approximation and including as few as 10 Landau levels in the length calculation. However, it is ignored in this evaluation because the correction is small compared to the change in screening length from the magnetic field. The *r*-process is not expected to be dominated by screening as it is primarily a neutron capture process, and the time spent in this transition region for the *r*-process is expected to be brief compared to the entire *r*-process. Future, more accurate evaluations may include this small correction. Effects from fission cycling were included in a rudimentary fashion following the prescription of Shibagaki et al. (2016). In this model, fission was implemented for the Cf isotopic chain, $^{270-295}$Cf. Fission rates were assumed to be 100 s^{-1} for all nuclei in this isotopic chain. Clearly, this fission model is overly simplistic and does not represent the full details of the nuclear structure necessary for a proper determination of fission. However, as we will discuss later, it is necessary to include fission in a collapsar/NSM *r*-process, and this model provides an appropriate level of detail to capture the overall effects of intense magnetic fields on β decays in this site.

3.2.4 *r*-process Abundance Distributions

The final abundance distributions for all six models studied with and without fission are shown in Fig. 3.11 for a field of 10^{15} G. Fig. 3.12 shows the final abundance distributions for models including fission at a field of 10^{14} G. (All models except E_{14} and EF_{14} shown in Figure 3.12.) The electron fraction Y_e is plotted for all models in Fig. 3.13.

In all cases, Coulomb screening of nuclear reactions has a minimal effect on the overall reaction network. This is not surprising as the primary fusion reaction is neutron capture, which is immune to screening. While the inclusion of magnetic fields creates a slight enhancement in the overall abundance for the heavier nuclei due to the enhancement of charged-particle reactions early in the *r*-process (e.g., proton and alpha captures), this enhancement is minimal. Likewise, the effects from default screening and relativistic screening are negligible in this treatment.

However, the inclusion of enhanced weak rates does have an effect on the overall resultant reactions. For a full treatment, including accurate computations of the weak rates with contributions from all relevant Landau levels, the overall β^- rates are higher, resulting in a more rapid progression to the heaviest nuclei. As can be seen in the case for no fission in Fig. 3.11, the rapid β-decay rates results in a large abundance of nuclei near the endpoint of the reaction network ($Z = 98$). The nucleosynthesis progresses to the Cf isotopic chain, where the abundance builds up. At this point, the only possible reactions are (n,γ), (n,α), neutron-induced fission, and photospallation reactions as a result of truncating the network at Z=98. This results in additional neutron production and minimal production of α particles. Of course, this is an unrealistic scenario because of the artificial termination point in the nucleosynthesis, but it does convey the increased nucleosynthesis speed from the high magnetic field in a very neutron-rich environment.

The LLL approximation for β^- decay rates is also shown in this figure. In this case, the Landau level spacing is generally less than the decay Q value, except for a few low mass nuclei with $Z \lesssim 20$. This results in overall slower β decay rates, resulting in a slower progress to the heavy mass nuclei and a larger relative abundance at the low mass nuclei.

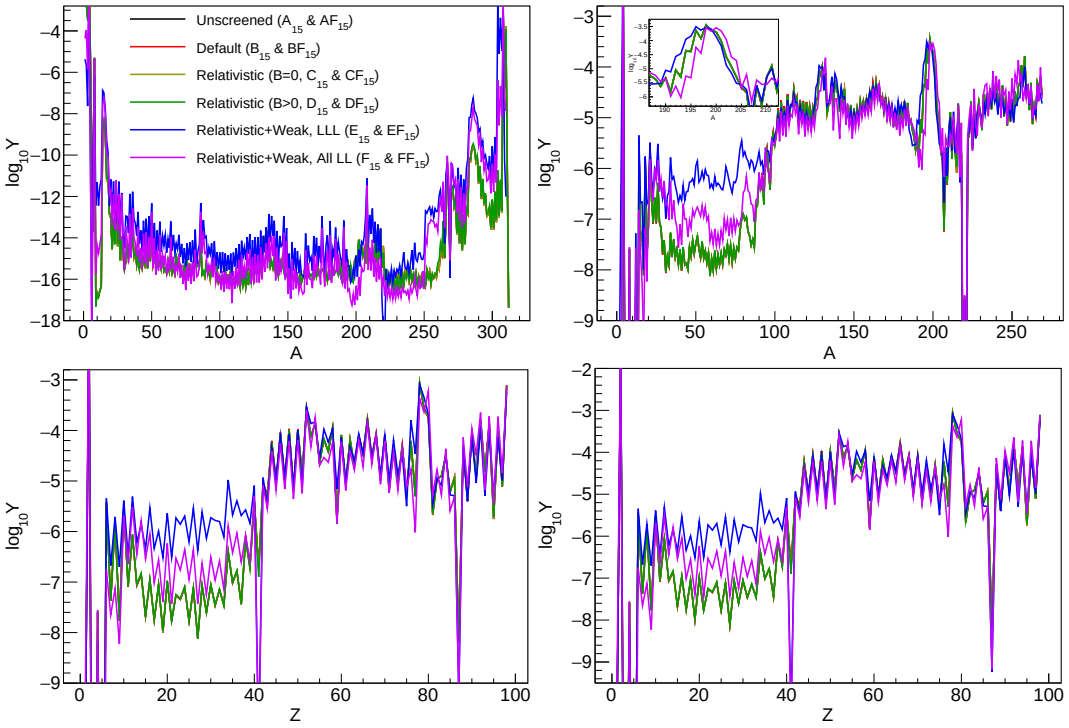

FIGURE 3.11: Abundances at $t = 6000$ s for MHD models for the adiabatic trajectory in Fig. 3.10 with an external field of 10^{15} G. Plots (a) and (c) show nucleosynthesis results without fission, and plots (b) and (d) shows nucleosynthesis results with fission. For the models with fission, the points for the default screening model nearly coincide with those for the unscreened model, and the points for the relativistic screening model for $B = 0$ nearly coincide with those for the relativistic screening model with $B = 10^{15}$ G.

The right side of Fig. 3.11 shows the final abundance distributions if fission cycling is included in the network calculation. As expected, there is very little difference between the abundance distributions if nuclear screening is included in the reaction network. However, the inclusion of β^- decay enhancement results in a an enhancement of the low-mass nuclei, $(Z, A) \lesssim (40, 100)$. For the heavier mass nuclei, fission products dominate the abundance distribution. As fission becomes dominant, heavier-mass nuclei are enhanced in abundance relative to that of the low-mass nuclei, and one notices a relative increase in abundance for $Z \gtrsim 40$ for all models.

However, there is also an enhancement of the abundances of the low-mass nuclei with field-enhanced decay rates relative to the abundances of nuclei without them. This is likely a result of the more rapid progression of the *r*-process to the fissile nuclei. There are two effects that can be considered in this case. First, from Fig. 3.9, it can be seen that the enhancement of the β^- decay rates is less for lower mass nuclei than for the higher mass nuclei. While this enhancement is small, it results in a somewhat slower progression of the *r*-process through these lower-mass progenitors relative to the progression through higher mass nuclei. Thus, a slight buildup of abundance relative to the high-mass nuclei can result. This is particularly noticeable if only the LLL is taken into account. The rate differences are more pronounced, and the the enhancement of low-mass nuclear abundance is larger.

To a lesser extent, the neutrons produced in fission can also slightly enhance the production of lower-mass nuclei. It is assumed that two neutrons are produced in

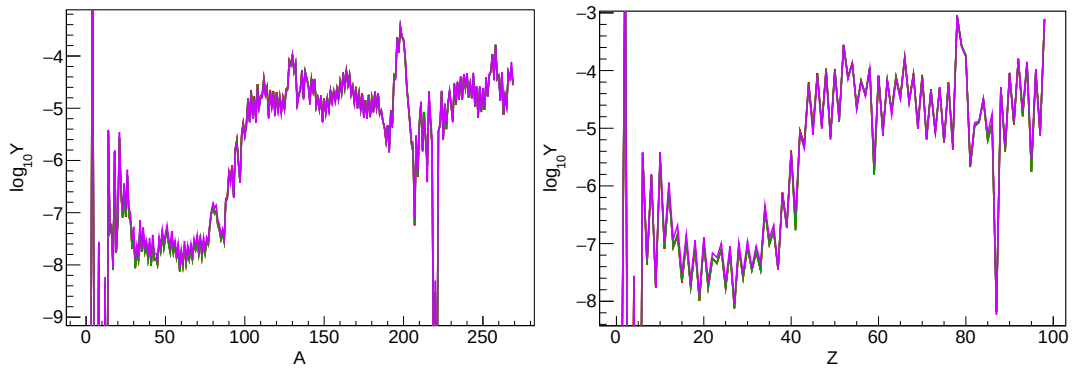

FIGURE 3.12: Abundances at $t = 6000$ s for MHD models for the adiabatic trajectory in Fig. 3.10 for a field of 10^{14} G including fission. The colors are the same as those in Fig. 3.11. The LLL approximation is not shown.

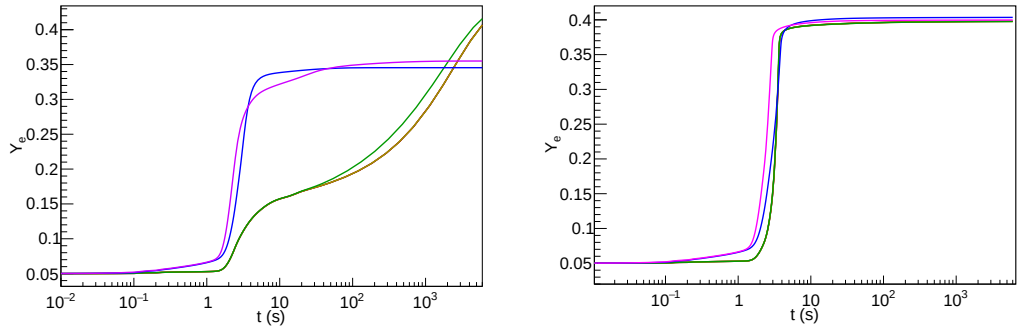

FIGURE 3.13: Electron fractions as a function of time for trajectories without fission (a) and with fission (b). In both figures the lines for no screening, default screening, and relativistic ($B = 10^{15}$ G) screening coincide. In the right figure, screening with enhanced weak interactions deviates from the other models. The colors are the same as those shown in Figure 3.11.

each fission in this model. Because of the very large initial neutron abundance, the progression to fission is not surprising in this scenario. However, for the the case in which decays are enhanced by the magnetic field, the progress to fissile nuclei is more rapid. Thus, more fission neutrons are produced in the *r*-process. These can be used as fuel for subsequent processing. Of course, neutrons produced in fission are captured by all progenitor nuclei, and not just the low-mass nuclei. The slightly less-enhanced decay rates of the low-mass nuclei, on the other hand, result in an abundance that is likely even more enhanced than in the absence of fission.

From Fig. 3.11, one also notes that there is a slight shift to higher mass in the final abundance distribution for the field-enhanced case. This is because the more rapid decay rates result in a slight shift of the *r*-process path closer to stability than in the case with zero field. This shift is prominent at the abundance peaks. For an *r*-process path that is closer to stability, the path intersects the magic numbers at a higher mass, resulting in the slight shift by a few mass units. This is shown in the inset for the A$\sim$195 abundance peak in Fig. 3.11b.

An evaluation at a field of 10^{14} G is shown in Fig. 3.12. In this figure, the abundances at $t = 6000$ s for a calculation including fission are shown, and the LLL approximation has been removed for clarity. As expected, for the lower field, the decay

rates are closer to the zero field decay rates, and the overall shift in the abundance distribution is smaller, though a small increase in abundance is noted for $A < 100$. This trend is consistent with the non-zero field trends observed but to a lesser extent.

The electron fraction Y_e as a function of time is shown for all six models with and without fission cycling in Fig. 3.13 at a field of 10^{15} G. For each case, it is observed that screening has a minimal effect on the evolution of the electron fraction. During the early stages of the *r*-process, the high-temperature environment is in nuclear statistical equilibrium (NSE). As the environment cools and expands, reactions dominate with a small time window during which charged-particle reactions (e.g., (α,γ), (α,n), etc.) may occur. These would be affected by Coulomb screening. Without fission, the dominant contribution to Y_e is from the Cf isotopic chain. In the case of field-enhanced decay rates, because the progression to the Cf chain is more rapid, an equilibrium Y_e occurs very rapidly, with a more rapid progression if all Landau levels are included in the decays, as expected. It is also noted that a complete inclusion of all Landau levels results in a slightly higher equilibrium Y_e as the *r*-process path is closer to stability. For the other calculations, the Y_e is lower as the *r*-process path is more neutron-rich as explained previously.

Fig. 3.13b shows the evolution of Y_e in the more realistic case including fission cycling in the calculation. Here, as the *r*-process becomes dominated by fission products, the equilibrium Y_e is similar in all cases. However, it can be seen that inclusion of the field-enhanced rates results in an earlier rise in the electron fraction owing to a more rapid *r*-process combined with a more rapid decay to stability.

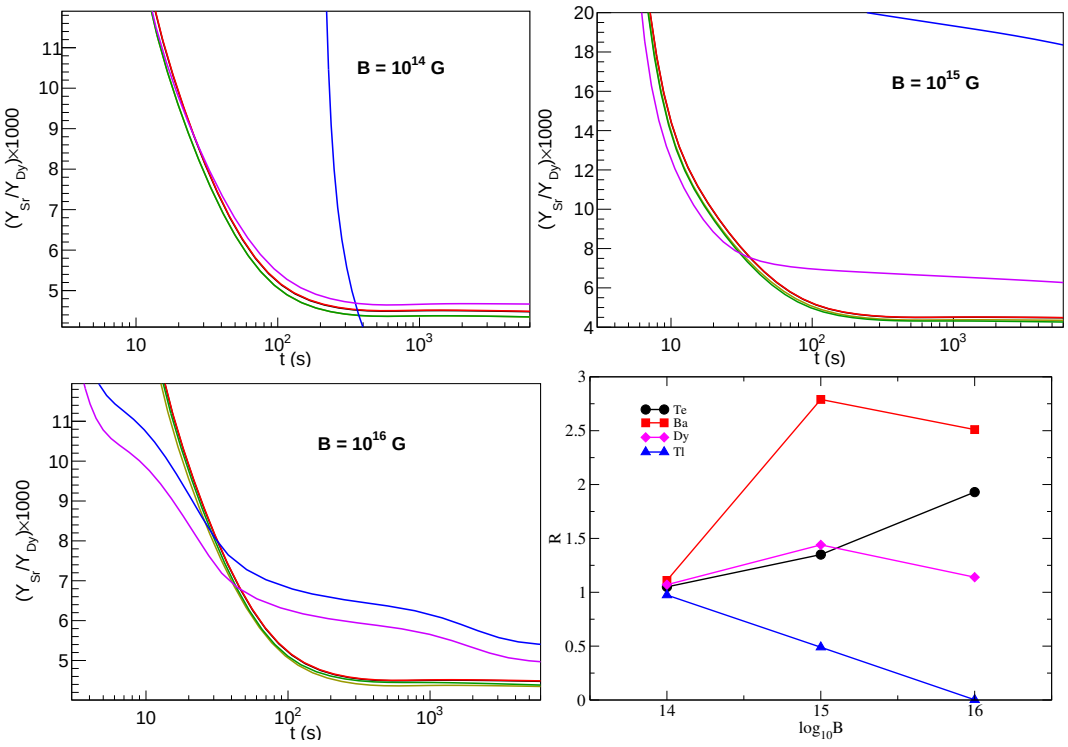

FIGURE 3.14: Sr/Dy abundance ratios for the collapsar network calculation for all models in Table 3.1 for (a) $B = 10^{14}$ G, (b) $B = 10^{15}$ G, and (c) $B = 10^{16}$ G. The colors are the same as those shown in Fig. 3.11. Panel (d) shows abundance double ratios given by Eq. 3.16 for four elements as a function of magnetic field.

3.2.5 Abundance Ratios

The overall final abundance distribution can be characterized by various abundance ratios. This is particularly helpful in that these provide a characteristic number to gauge the relative contribution from fission compared to the abundance buildup of light nuclei. This ratio is shown for three fields as a function of time in Fig. 3.14 for all six models studied. The zero-field cases are represented by the unscreened and screened relativistic models. The figure shows the abundance ratio for the cases in which fission cycling is accounted for.

In all cases, the value of the abundance ratio, Y_{Sr}/Y_{Dy} drops rapidly as the *r*-process path moves to the heavier nuclei and into the fissile nuclei, after which an equilibrium abundance of Dy begins to be produced via fission. The abundance ratio continues to drop more gradually with time after $\sim$4 s, when the Dy continues to build more slowly, and an equilibrium abundance of Sr is approached. This evolution continues into the post-processing of the *r*-process. It's also noticed the relativistic screening effect – though small – is more prominent than effects from classical screening, resulting in a slight reduction in the Sr/Dy ratio. While this reduction is small compared to effects from the magnetic field on β decays, it can be seen in the figures.

For the lowest field, the effect of the enhanced rates is small because the field-enhanced rates – consisting of decays to many Landau levels – are similar to the non-enhanced rates. If only the LLL approximation is used (model EF_{14}), the evolution is significantly different as the rates are grossly underestimated, resulting in a very slow *r*-process evolution, and the Sr/Dy abundance ratio does not drop until much later in the evolution. For the highest field, on the other hand, there is a smaller difference between the LLL approximation (model EF_{16}) and the inclusion of all Landau levels (model FF_{16}) in the decay rates because only a few Landau levels are populated in beta decays at this field.

Shown in Fig. 3.14d are various abundance ratios Y_{Sr}/Y_X (where X indicates an arbitrary element) at t=6000 s as a function of the magnetic field. Plotted in the figure is the relative elemental abundance double ratio, R, defined as:

$$R \equiv \frac{(Y_{Sr}/Y_X)_B}{(Y_{Sr}/Y_X)_{B=0}} \tag{3.16}$$

which shows the evolution of the elemental abundance ratios as the field increases. For low fields, all values are expected to converge at unity as seen in the figure. However, as fields increase, different physical processes affect the ratios.

For the lowest Z element (Te), which can be weakly populated by fission at all fields, a more rapid progression to the fission products can result in a slightly increased production of Te. However, production of Sr via neutron capture is enhanced by the strong magnetic field. Also, the Sr decay rates are not as enhanced as much as those of Te. Thus the Sr/Te ratio increases with field. For Ba and Dy, however, there is an increase, followed by a decrease. This is because the population of Ba and Dy by fission not only depends on the rate of progression to the fissile nuclei, but also the final fission distribution. As the *r*-process path progression to fission for $B = 10^{15}$ G is similar to that for $B = 10^{14}$ G, the production of the Ba and Dy progenitors is faster as the field increases up to $B = 10^{15}$ G. However, above this field, the β^- decay rates are fast enough such that the *r*-process path itself – being dynamic in nature – shifts sufficiently such that the distribution of fissile nuclei changes, and the fission product distribution changes somewhat. One might imagine the peaks of the fission distribution shifting to lower mass, thus raising or lowering abundances

of the progenitors of Ba and Dy. Clearly, the fission model used in this work is too simplistic to make a more than qualitative conclusion, but the interplay between the fission product distribution and the magnetic fields compels further investigation.

The element Tl is also fascinating. It is seen that the Sr/Tl ratio decreases with field. Tl lies above the fission products in mass and Z. However, it also lies just above the A=195 peak in the *r*-process distribution. Recall from Fig. 3.11 that the *r*-process distribution shifts slightly to higher mass as the field increases, shifting the $A = 195$ abundance peak as well. This shift, in turn increases the Tl abundance dramatically, thus reducing the Sr/Tl abundance ratio. This effect of the magnetic field on the shape of the final *r*-process abundance distribution, and hence, the Sr/X abundance ratio is compelling as an *r*-process from a single collapsar site can be characterized by the abundance distribution, and the magnetic field may be constrained by the abundance ratios. Obviously, a more thorough evaluation incorporating a more realistic fission model is necessary (Beun et al., 2008; Mumpower et al., 2018; Suzuki et al., 2018; Vassh et al., 2019), but the effect on the shape of the abundance distribution can still be made.

The ratios studied here may be of particular interest to astronomers in evaluating elemental abundance ratios in stars enriched in single sites. These ratios are generally low compared to solar *r*-process abundance values (Arlandini et al., 1999) owing to the fact that the single neutron-rich trajectory presented here results in a large abundance of massive elements. The range of observed values from the SAGA database (Suda et al., 2008) are also large compared to the values here. This may likely result from a both a detection limit as well as from the fact that if collapsar jets contribute to the galactic *r*-process abundance distribution, they contribute in combination with other sites.

3.2.6 Results & Discussions

Plasma effects on nuclear fusion and weak interactions in hot, highly-magnetized plasmas were evaluated, and the example of *r*-processing in a collapsar MHD jet site were examined. Two primary effects were analyzed. The first is the effect of Coulomb screening on fusion reactions of charged particles. Because the *r*-process is dominated by neutron captures, screening has a small effect on the overall evolution and final abundance distribution of the *r*-process. However, charged-particle reactions in the early stages (e.g., (α,n) and (α,γ) reactions) may be affected. Coulomb screening is affected by both the temperature and the magnetic field of the environment. While the default classical weak screening commonly used in astrophysics codes was found to have virtually no effect on the final *r*-process abundance distribution, relativistic effects from high temperatures and high magnetic fields were found to have a slight effect on the *r*-process evolution.

The second effect studied is the effect of high magnetic fields on nuclear weak interaction rates. As fields increase in strength, electron momentum transverse to the field direction is quantized into Landau levels. This alters the Fermi-Dirac distribution, resulting in a shift in the electron spectrum. While the magnetic field was found to have a small effect on Coulomb screening, strong fields may have a larger effect on nucleosynthesis when applied to weak interaction rates. This is because – particularly in the case of the finite β-decay spectrum – only a limited number of Landau levels can be occupied by the emitted charged lepton, as indicated in Figs. 3.7 and 3.8. For very high fields, $\sqrt{eB} \sim Q$, only a couple of Landau levels are available to the emitted electron or positron. The electron energy spectra have strong peaks where the electron longitudinal momentum is zero. The integrated spectrum, which

is proportional to the decay rate, is thus much larger than that for the zero-field case. Large fields can affect the *r*-process evolution.

A simple MHD collapsar jet model was adapted from the hydrodynamics calculations of Nakamura et al. (2012) as an illustrative model. In this model, static fields of various strengths were assumed. Various effects of thermal and field effects were studied individually in a systematic manner to gauge the effects of individual environmental parameters. While the temperature was treated dynamically following a single trajectory, which was assumed to decay adiabatically after 2.8 s, the magnetic field in this case was assumed constant. One interesting result of magnetic-field effects on the *r*-process studied was that β^- decay rates increase with field strength. Because of this, the *r*-process path, which changes dynamically in time, may shift somewhat closer to stability for very strong fields. This has multiple effects. First, the point at which the *r*-process path crosses the magic numbers change, thus shifting the abundance peaks of the final distribution. This shape can be evaluated using elemental abundance ratios, such as Y_{Sr}/Y_{Tl}. Second, the fissile nuclei produced in the *r*-process will be different, resulting in potentially different fission rates and distributions. This could possibly be studied using abundance ratios such as Y_{Sr}/Y_{Ba}, Y_{Sr}/Y_{Dy}, or something similar. Finally, the fission cycling time decreases somewhat with increasing field, resulting in an increase in fission products as well as a slight addition of neutrons to the *r*-process environment.

3.3 Strong Screening in Highly Magnetized Degenerate Plasma

3.3.1 Review of the Screening Effect in Degenerate Gas

For the degenerate plasma, the situation is more difficult to tackle since the first-order aprroximated solution to the Poisson equation is invalid. At a lower temperature case (i.e., non-relativistic), the linear response theory is useful to calculate the dielectric coefficient of the gas (Linhard, 1954) which further show its importance on determining the screening potential. The only mattered state is the ground state of the electron gas in the system. However, in astrophysics, a more interesting environment is the degenerate relativistic electron positron plasma, Jancovici, 1962 calculated the screening potential of a relativistic ultra-degenerate plasma, and the studies indicate that the screening potential could affect β-decay rate (Morita, 1973; Matese and Johnson, 1965) as well as the electron capture rate (Glauber et al., 1956; Takahashi, El Eid, and Hillebrandt, 1978; Fuller, Fowler, and Newman, 1980), these weak interactions play essential roles in the astrophysics because the interaction itself determines the pre-SNe stellar evolution and stellar nucleosynthesis, the detailed calculation has been performed by McLaughlin, Fuller, and Wilson (1996), Heger et al. (2001), and Wanajo et al. (2003). Heger et al. (2001) noticed that electron captures on iron group nuclei of the final stage stellar evolution decrease the electron fraction Y_e which lead to a further variation of the iron core mass; McLaughlin, Fuller, and Wilson (1996) pointed out that right after the SNe explosion, Y_e in the region above the hot proto-neutron star could shifting of nuclear abundance critically. Therefore, it is extremely important to calculate accurately the weak interaction rates in dense stars which contains the relativistic degenerate electron liquid (Takahashi, El Eid, and Hillebrandt, 1978; García-Berro, Ritossa, and Iben, 1997; Bravo and García-Senz, 1999; Itoh et al., 2002). For such a environment, the chemical potential must be accounted for in the relativistic treatment of Eq. 3.2 and computed using the electron-positron number density assuming charge neutrality. The screening corrections is not negligible, and $E_C/kT \gg 1$. The thermal energy is less

important, and the potential is modified by the difference in Coulomb energy before and after the reaction – the so-called ion sphere model (Clayton, 1983; Salpeter and van Horn, 1969; Salpeter, 1954).

On the other hand, the magnetic field also plays an important role in terms of affecting the the weak interaction rate in dense plasma, our previous work (Luo et al., 2020; Famiano et al., 2020) have calculated the contributions to the weak interaction rate from non-degenerate screening potential for both weak and strong magnetic field strength. It is believed that some astrophysical sites such as magnetars (i.e., the rotating neutron stars) could consist a relativistic degenerate electron gas in a strong magnetic field of the order of 10^{14-16} G (Rea and Esposito, 2011; Kaspi and Beloborodov, 2017) in the inner region. However, the screening potential in such a highly magnetized dense plasma has not been investigated thoroughly. Prompted by this fact, in this section, a generalization of the Hartree self-consistent field method of the relativistic degenerate electron gas is applied(Delsante and Frankel, 1978; Delsante and Frankel, 1980). By taking into account the background magnetic field, the dielectric coefficient which could further determine the screening potential is calculated. The results are applied to calculate the electron capture rate of ^{54}Fe and ^{70}Zn since they determine the electron fraction of the plasma and electron fraction is one of the most important variables determines the neutron-richness for nucleosynthesis and finally could change the isotopic abundances (McLaughlin, Fuller, and Wilson, 1996; Langanke and Martinez-Pinedo, 2000; Langanke and Martinez-Pinedo, 2003; Nishimura, Takiwaki, and Thielemann, 2015).

In this section, the cgs unit is used, so $\alpha = e^2/\hbar c$ where α is the fine structure constant. The Coulomb potential V at a point with a relative position $\boldsymbol{r}$ to the center nuclei is given by

$$V(\boldsymbol{r}) = \frac{\alpha\hbar c Q}{\boldsymbol{r}}. \tag{3.17}$$

Consider that the electron-positron gas which form a self-consistent internal field $A_0(\boldsymbol{x}, t)$ at the position $\boldsymbol{x}$ and time t, this field should satisfy the Poisson equation:

$$\nabla^2 \mathbf{A}_0(\boldsymbol{x}, t) = -4\pi\rho(\boldsymbol{x}, t), \tag{3.18}$$

the solution of Eq. D.2 can be obtained by the inverse-Fourier transform of $A_0(\boldsymbol{q}, t)$:

$$A_0(\boldsymbol{x}, t) = \sum A_0(\boldsymbol{q}, t) e^{i\boldsymbol{q}\boldsymbol{x}}, \tag{3.19}$$

where $A_0(\boldsymbol{q}, t)$ is given by

$$A_0(\boldsymbol{q}, t) = \frac{4\pi}{q^2}\rho(\boldsymbol{q}, t). \tag{3.20}$$

The screening potential is the electrostatic field that trigger by a electric charge Q (i.e., the nuclei in the astrophysical sites):

$$V(\boldsymbol{r}) \equiv A_0(\boldsymbol{r}, 0) = -\frac{1}{(2\pi)^3}\int d\boldsymbol{q} e^{i\boldsymbol{q}\boldsymbol{r}} V(\boldsymbol{q}) = -\frac{2}{\pi}\frac{Ze^2}{r}\int_0^\infty \frac{sin(rq)}{q\epsilon(q, 0)} dq, \tag{3.21}$$

where

$$V(\boldsymbol{q}) = \frac{4\pi Q}{q^2}\frac{1}{\epsilon(\boldsymbol{q}, 0)}, \tag{3.22}$$

here, $\epsilon(\boldsymbol{q}, 0)$ is the dielectric coefficient of the plasma, clearly $\epsilon(\boldsymbol{q}, 0) = 1$ corresponds to the pure Coulomb potential $V_{Coul}(\boldsymbol{r}) = \alpha Q/\boldsymbol{r}$ of a bare nuclei with charge Q. Then, the problem to solve the screening potential $V(\boldsymbol{r}, 0)$ becomes to solve the dielectric

coefficient $\epsilon(\boldsymbol{q},0)$. By manipulating the self-consistent potential together with the Hartree approximation (Delsante and Frankel, 1980) (see derivation in Appendix. D), $\epsilon(\boldsymbol{q},\omega)$ reads

$$\epsilon(\boldsymbol{q},\omega) = 1 + \frac{4\pi e^2}{Vq^2}\sum_{aa'}\frac{|\langle a'|e^{i\boldsymbol{qx}}|a\rangle|^2}{\hbar\omega - (E'_a - E_a)}[F(a') - F(a)]. \tag{3.23}$$

where ω is the plasma frequency, V is the volume of the system,$F(a)$ is the general distribution function which is the probability of state a could exist, and

$$\langle a'|e^{i\boldsymbol{qx}}|a\rangle = \int \phi_a^\dagger(\boldsymbol{x})\phi_a(\boldsymbol{x})e^{-i\boldsymbol{qx}}d^3x, \tag{3.24}$$

where $\phi_a(\boldsymbol{x})$ stands for the eigenfunction of the electron wave and E_a is the corresponding energy.

For a quick check, firstly let's consider the case that without background field. The wave function ϕ_a of the electrons is given by

$$\phi_a(\boldsymbol{x}) = \frac{1}{V^{1/2}}u_s(\boldsymbol{p})e^{i(\boldsymbol{p}\cdot\boldsymbol{x} - E_p\cdot t)\hbar} \tag{3.25}$$

where $u_s(\boldsymbol{p})$ is the spinor representation with momentum $\boldsymbol{p}$:

$$u_1(\mathbf{p}) = N\begin{bmatrix}1\\0\\p_3c/(E_p+E_0)\\c(p_1+ip_2)/(E_p+E_0)\end{bmatrix}$$

$$u_2(\mathbf{p}) = N\begin{bmatrix}0\\1\\c(p_1-ip_2)/(E_p+E_0)\\-p_3c/(E_p+E_0)\end{bmatrix}$$

where $N = \sqrt{(E_p+E_0)/2E_p}$ and $E_0 = mc^2$. Under this representation, $\langle a'|e^{i\boldsymbol{qx}}|a\rangle$ is given by

$$\langle \boldsymbol{p},s|e^{i\boldsymbol{qx}}|\boldsymbol{p}',s'\rangle = u_s^\dagger(\boldsymbol{p})u_{s'}(\boldsymbol{p}')\delta_{\boldsymbol{p}',\boldsymbol{p}+\hbar\boldsymbol{q}}. \tag{3.26}$$

Consider the infinite space, the summation $\sum_a$ becomes $\frac{V}{(2\pi\hbar)^3}\int d\boldsymbol{p}$, one may have

$$\epsilon(\boldsymbol{q},\omega) = 1 + \frac{4\pi e^2}{(2\pi\hbar)^3q^2}\int d\boldsymbol{p}\sum_{ss'}\frac{\left[u_s^\dagger(p)u_{s'}(p+\hbar q)\right]^2}{\hbar\omega - (E_{p+\hbar q} - E_p)}[F(p+\hbar q) - F(p)]. \tag{3.27}$$

For the non-relativistic electrons, i.e., $E_p << E_0$, it has

$$u_s^\dagger(p)u_{s'}(p')\delta_{p',p+\hbar q} = 2, \tag{3.28}$$

which is exact the Lindhard formula (Linhard, 1954) including electron spin 2 for the longitudinal dielectric function.

Further more, for the long distance static limit, i.e., $q \to 0$, it has

$$\epsilon(\boldsymbol{q},0) = 1 + \lim_{q\to 0}\frac{4\pi e^2}{(2\pi\hbar)^3q^2}\int d\boldsymbol{p}\frac{[F(p+\hbar q) - F(p)]}{E_p - E_{p+\hbar q}} = 1 - \frac{4\pi e^2}{q^2}\int dp\frac{\partial F}{\partial E}, \tag{3.29}$$

then the longitudinal dielectric coefficient reads

$$\epsilon(\boldsymbol{q},0) = 1 - \frac{4\pi e^2}{q^2}\frac{\partial n}{\partial E} = 1 + \frac{4\pi e^2}{q^2}\frac{\partial n}{\partial \mu}, \tag{3.30}$$

which is exact the Thomas-Fermi screening formula where TF vector k_{TF} is given by

$$k_{TF}^2 \equiv \frac{1}{\lambda_{TF}^2} = 4\pi e^2 \frac{\partial n}{\partial \mu}. \tag{3.31}$$

3.3.2 Screening Effect in the Highly Magnetized Plasma

The above results are also consistent with Jancovici (1962) since they also consider the degenerate plasma but field-free scenario. In the magnetic field, the wave functions of electrons reads

$$\psi_{n,p_x,p_z,\sigma} = \frac{1}{L^2} H_{n,p_z,\sigma} e^{ip_x x/\hbar} e^{ip_z z/\hbar}, \tag{3.32}$$

where n is the Landau quantum number, σ is the spin quantum number and also

$$H_{n,p_z,1} = \frac{1}{\sqrt{2E(E+E_0)}} \begin{bmatrix} (E+E_0)G_n(y) \\ 0 \\ cp_z G_n(y) \\ -i(2e\hbar cBn)^{1/2} G_{n-1}(y) \end{bmatrix}$$

for spin up, and

$$H_{n,p_z,-1} = \frac{1}{\sqrt{2E(E+E_0)}} \begin{bmatrix} 0 \\ (E+E_0)G_n(y) \\ i(2e\hbar cB(n+1))^{1/2} G_{n+1}(y) \\ -cp_z G_n(y) \end{bmatrix}$$

for spin down. The electron energy in the magnetic field is given by $E^2 = E_0^2 + p_z^2c^2 + e\hbar Bc(2n - \sigma + 1)$, $G_n(y)$ is given by

$$G_n(y) = N_n H_n\Big[\big(\frac{m\omega_c}{\hbar}\big)^{1/2} y\Big] \exp\big(-\frac{m\omega_c y^2}{2\hbar}\big) \tag{3.33}$$

$$N_n = \Big(\frac{m\omega_c}{\pi\hbar c}\Big)^{1/4} (2^n n!)^{-1/2}, \tag{3.34}$$

where H_n is the Harmonic oscillator function. The final result of the dielectric coefficient is (Delsante and Frankel, 1980)

$$\begin{aligned} \epsilon(q,\omega,B) =& 1 + \frac{\pi e^2}{q^2}\frac{m\omega_c}{(2\pi\hbar)^2}\int_{-p_F(n,\sigma)}^{p_F(n,\sigma)} dp_z \\ &\times \sum_{n,n',\sigma,\sigma'} \frac{N_{n,n'}^2(p_z,\sigma,\sigma',q)[F(n',\sigma',p_z') - F(n,\sigma,p_z)]}{\hbar\omega + E_{n,p_z,\sigma} - E_{n',p_z',\sigma'}} \end{aligned} \tag{3.35}$$

and

$$N^2_{n,n'}(p_z,\sigma,\sigma',q) = N^2N'^2\Big\{\delta_{\sigma,\sigma'}\big[(E_TE'_T + c^2p_zp'_z)|M_{nn'}| + c^2p_\perp p'_\perp|M_{n-\sigma,n'-\sigma}|\big]^2 + \delta_{\sigma,-\sigma'}[c^2p'_\perp p_z|M_{n,n'+\sigma}| - c^2p_\perp p'_z|M_{n-\sigma,n'}|]^2\Big\}; \quad (3.36)$$

for the case $n \leq n'$,

$$M_{n,n'} = \Big(\frac{n'!}{n!}\Big)^{1/2} e^{-q^2_\perp/4\beta^2}\Big(\frac{q_\perp}{2^{1/2}\beta}\Big)^{n-n'} L^{n-n'}_{n'}\Big(\frac{q^2_\perp}{2\beta^2}\Big)e^{-iq_y(q_x+2k_x)/\beta^2}e^{-i\phi_q(n-n')}, \quad (3.37)$$

and for $n < n'$,

$$M_{n,n'} = \Big(\frac{n!}{n'!}\Big)^{1/2} e^{-q^2_\perp/4\beta^2}\Big(\frac{q_\perp}{2^{1/2}\beta}\Big)^{n'-n} L^{n'-n}_{n}\Big(\frac{q^2_\perp}{2\beta^2}\Big)e^{-iq_y(q_x+2k_x)/\beta^2}e^{i\phi_q(n'-n)}(-1)^{n'-n}. \quad (3.38)$$

Here, $\beta = m\omega_c/\hbar$, $q_x + iq_y = q_\perp e^{i\phi_q}$, and $L^{n'-n}_n(x)$ is the generalized Laguerre polynomial. Here, the notation of the direction of momentum has been changed, i.e., q_z corresponds to the momentum parallel to the magnetic field and $q_\perp$ corresponds to that perpendicular to the magnetic field. Some other parameters are (and all the parameters with $'$ follow the same manner but with $p' = p + \hbar q$):

$$\omega_c = \frac{eB}{m_ec}; N^2 = \frac{1}{EE_T}; E_T = E + E_0; p_\perp = \sqrt{e\hbar Bc(2n - \sigma + 1)}/c. \quad (3.39)$$

The screening potential then is given by

$$\begin{aligned} V(\boldsymbol{r},B) &= -\frac{1}{(2\pi)^3}\int d\boldsymbol{q}e^{i\boldsymbol{qr}}V(\boldsymbol{q},B) \\ &= -\frac{1}{\pi}\frac{Ze^2}{r}\int_0^\pi\int_0^\infty sin\theta\frac{sin(rq)}{q\epsilon(q\cdot sin\theta, q\cdot cos\theta, 0, B)}d\theta dq \end{aligned} \quad (3.40)$$

where the azimuth angle integration $d\theta$ has been included.

Inside the degenerate plasma, all the electrons and positrons should have energy less than the Fermi energy: $E \leq E_F$. The E_F in general is proportional to the $(\rho Y_e)^{1/3}$, however, inside the magnetic field, E_F also depends on the magnetic field as well (See Appendix D for the detailed derivation), the E_F should satisfy the following condition:

$$\rho Y_e = \frac{2m\omega_c}{(2\pi\hbar)^2c}\Big[(E_F^2 - E_0^2)^{1/2} + 2\sum_{n=1}^{n_{max}}\sqrt{E_F^2 - E_0^2 - 2e\hbar cBn}\Big], \quad (3.41)$$

where *rho* is the density and Y_e is the electron fraction. n_{max} is given by

$$[E_0^2 + 2e\hbar cBn_{max}] < E_F^2 < [E_0^2 + 2e\hbar cB(n_{max}+1)]. \quad (3.42)$$

Fig.3.15 shows Fermi energy E_F as a function of magnetic field strength for different set of (ρ_6, Y_e) where $\rho_6 \equiv \rho/10^6$. For an extremely strong magnetic field, only the LLL is occupied, so E_F decreases monotonically as a function of B, $E_F \to E_0$, with limit that $B \to \infty$, $B \to m_e$. The critical magnetic field B_{crit} for the scenario that only LLL is occupied is

$$B_{crit} = \frac{\pi\hbar c}{e}\Big[2\pi(\rho Y_e)^2\Big]^{1/3}, \quad (3.43)$$

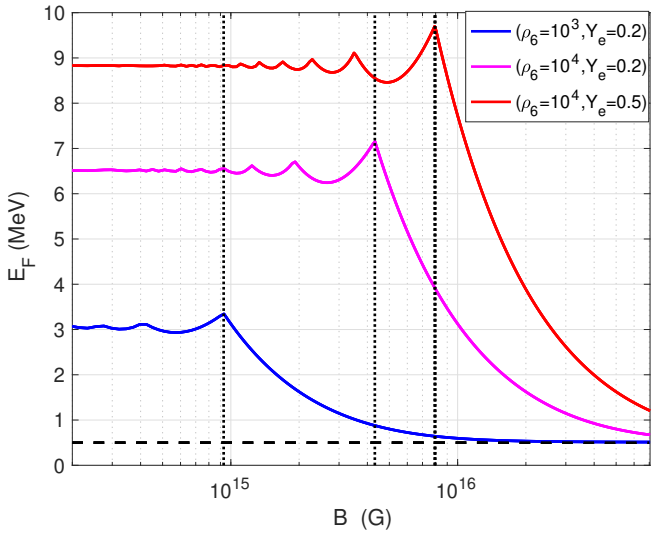

FIGURE 3.15: Fermi energy E_F as a function of magnetic field strength. In this figure, ρ_6, Y_e are set for different combinations as $(10^3, 0.2)$,$(10^4, 0.2)$ and $(10^4, 0.5)$, respectively. If magnetic field is relatively weak, E_F becomes the same as the field-free case. For each line, E_F approaches to $E_0 = 0.511$ MeV when $B > B_{crit}$ which represented by black dotted line.

with decreasing of the magnetic field strength, the new Landau level pops up, then to cancel the extra energy that carried by magnetic field, E_F decrease firstly then increasing since the canceling effect decreases monotonically with decreasing of magnetic field. Until the next Landau level pops up, such patterned will be repeated. For the weak magnetic field, E_F becomes the value that without filed, i.e., for these combinations, $E_F(B = 0) = 3.01$ MeV, 6.51 MeV and 8.82 MeV, separately.

The potential described by Eq. 3.40 are shown in Fig. 3.16, the $V_{scr}(B, \boldsymbol{r})/V_{un}(B = 0, \boldsymbol{r})$ value which is the ratio that screening compared with the Coulomb potential of bare nuclei.

Fig. 3.16 shows the combination of $(\rho_6, Y_e) = (10^4, 0.5)$. The radius range is set as $1 \sim 20$ fm which is enough since in general the nuclei has the radius as $r = 1.3A^{1/3}$, and most interactions can be considered as occur at position r. From Fig. 3.16, the same patterns appeals as in Fig. 3.15 due to the popping up of the Landau level as decreasing of the field strength. $r \sim 5$ is the most radius of nuclei, as shown on the figure, only few percent of the Coulomb potential is suppressed, however, this correction is not negligible since it corresponds to ~ 100 keV of the electrons kinetic energy.

3.3.3 Electron Capture Rate in Strong Magnetic Field

As discussed in Chapter 1, weak interactions could be mainly divided into two compositions: Fermi and GT transitions. The treatment of Fermi transition is straight forward while GT transition strongly depends on the nuclear structure. In a fully ionized degenerate plasma, the β-decay is strongly blocked by the degenerate electron gas. However, the continuum electron capture from the degenerate electron plasma is possible due to the high energies of the electrons, and it is also possible to induce the transitions to the GT resonance. Among the studies on the weak interaction, one of the most important work is the tabulations made by Fuller, Fowler, and Newman (1980), Fuller, Fowler, and Newman (1982a), and Fuller, Fowler, and

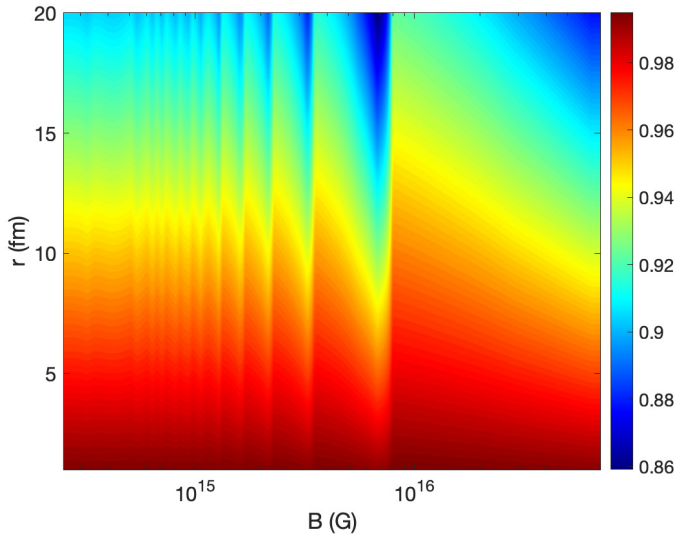

FIGURE 3.16: Contour map of $V_{scr}(B, \boldsymbol{r})/V_{un}(B = 0, \boldsymbol{r})$ of magnetic field strength B and distance to the central nuclei r. Usually $r \sim 5$ fm, the screening potential in this region could suppress the Coulomb potential for few percent.

Newman (1982b) (FFN). They calculated the rates for the nuclei with mass number $A = 21 \sim 60$ which are the main nuclei relevant to the astrophysical interesting. The calculation was based on the the available experiment data in 1980's for individual transitions between ground states and the lowing lying excited states. However, the later experiments (Goodman et al., 1980; Alford, 1990; Osterfeld, 1992; Alford, 1993) show that the GT strength actually could be strongly quenched, the reaction could be fragmented over many states in the daughter nuclei. Such facts urge us to find an accurate description of the correlations between the residual interaction among valence nucleons. From a theoretical site, the shell model is the only known tool that could predict the GT distribution in the nuclei reliably, it has been proved that the shell model could reproduce the GT_+ transition measurement as well the lifetime predictions of the pf-shell nuclei (Caurier et al., 1999). The shell-model rates has been calculated for sd-shell nuclei ($A = 17 \sim 39$) (Oda et al., 1994) and pf-shell nuclei:$A = 45 \sim 65$) (Langanke and Martínez-Pinedo, 2001), $A = 65 \sim 80$ (Pruet and Fuller, 2003) based on the recent experiments. Compare with FFN, the updated rates are lower than the previous results which possibly due to: 1) the quenched Gamow-Teller strength value that deviated from the independent-particle-model; 2). the systematic misplacement of GT centroid in nuclei with certain pairing structure; 3). the much complete experimental data.

The importance of the shell-model rates in the late-stage evolution of massive stars has been investigated previously (Heger et al., 2001; Langanke and Martinez-Pinedo, 2003), it was shown that for the pre-SNe models, by replacing the FFN electron capture rates, the central electron fraction Y_e, the entropy and the iron core mass could be significantly deviated. Especially during the final stage of the stellar evolution, the inner region of a star approaches to high density, the mass of the star is determined by Chandrasekhar mass, which is proportional to Y_e^2. Electron capture process could reduces the electron number density, on the other hand, the neutrino emission from electron capture could carry away the energy and entropy of the core.

Therefore, it is essential to carried on a reliable evaluation of the stellar weak interaction rates, particularly of the stellar electron capture rates.

Previously, the correction from screening effect has been studied (Juodagalvis et al., 2010), the main contribution of the correction comes from the relativistic degenerate electron plasma and the typical corrections are with order of a few percent. However, the scenario of the magnetized plasma has not been investigated in detail, magnetic field could affect: 1). the electron capture rate itself due to the quantized of phase space. 2). the screening correction also could be contributed from magnetic field because of the changing in electronic thermodynamics, which could leave further imprints in the nucleosynthesis as well as the astrophysical observational signals.

The electron capture rate for kth nuclei (Z,A) is given by the initial states i and final states j (Fuller, Fowler, and Newman, 1980; Fuller, Fowler, and Newman, 1982a; Langanke and Martínez-Pinedo, 2001; Pruet and Fuller, 2003)

$$\lambda_k = \sum_i \frac{(2J_i+1)e^{-E_i/k_BT}}{G(Z,A,T)} \sum_f \lambda_{if} \tag{3.44}$$

Here, J_i and E_i are the spin and excitation energy of the parent states, respectively. k_B is Boltzmann factor. $G(Z,A,T)$ is the nuclear partition function, λ_{if} is the electron capture rate from one of the initial states to all possible final states:

$$\lambda_{if} = \frac{ln2}{(ft)_{if}} f_{if}. \tag{3.45}$$

As have been discussed in Chapter. 1, the allowed transition can only occur if certain selection rules are satisfied for the nuclear spin (J_i, J_f) and parities (π_i, π_f) which i and f stands for the initial and final states. So one may have:

$$\frac{1}{(ft)_{if}} = \frac{1}{(ft)^F_{if}} + \frac{1}{(ft)^{GT}_{if}}, \tag{3.46}$$

where ft_{if} corresponds to Fermi transition and Gamow-Teller transition matrix elements:

$$\frac{1}{(ft)^F_{if}} \sim \frac{10^{3.79}}{|M_F|^2_{if}} \tag{3.47}$$

$$\frac{1}{(ft)^{GT}_{if}} \sim \frac{10^{3.59}}{|M_{GT}|^2_{if}}. \tag{3.48}$$

Considering the background magnetic field, the integrand in phase space should be replaced with

$$\omega p S_e(\omega, \mu_e, T)\, d\omega \to \frac{eB}{4} \sum_{n=0}^{max} (2-\delta_{n0}) \frac{\omega_B}{p_B} S_e(\omega_B, \mu_B, T)\, d\omega, \tag{3.49}$$

here the relation $\omega_B^2 = p^2 + 1 + 2n\gamma$ is used where ω_B is the total electron energy in the unit of m_e, p is the electron momentum in the unit of m_e. μ_B denotes for the

chemical potential within the background magnetic field, and it is calculated via

$$\rho N_A Y_e = \frac{m_e^3}{\pi^2}\frac{eB}{4}\sum_{n=0}^{max}(2-\delta_{n0})\int_0^\infty dp_z\,(S_e - S_p). \tag{3.50}$$

where S_p is the distribution function of positron. Then the phase space integral over df_{if} reads

$$f_{if} = \frac{eB}{4}\sum_{n=0}^{max}(2-\delta_{n0})\int_{\omega_l'}^\infty d\omega_B\,\frac{\omega_B}{p_B}(Q_{if}^s+\omega_B)^2 F(Z,\omega_B)S_e(\omega_B,\mu_B,T) \tag{3.51}$$

The bounds of integration are set by the reaction threshold ω_l', which is the value for the electron capture is energetically feasible; $\omega_l = 1$ if $Q_{if} > -1$ and $\omega_l = |Q_{if}|$ for $Q_{if} < -1$. For $Q_{if} < -1$, the electron must have enough kinetic energy to make the reaction possible, and $\omega_l > 1$. Q_{if} is the electron capture transition energy divided by the electron mass, determined from the nuclear masses.

The only remaining factor appearing in the phase space integrals is the Fermi function $F(Z,\omega)$ which corrects the distortion of the electron wave function (Juodagalvis et al., 2010):

$$F(Z,\omega) = 2(1+\gamma)(2pR)^{-2(1-\gamma)}\frac{|\Gamma(\gamma+iy)|^2}{|\Gamma(2\gamma+1)|^2}e^{\pi y}, \tag{3.52}$$

where $\gamma = \sqrt{1-(\alpha Z)^2}$, $y = \alpha Z\omega/p$, α is the fine structure constant and R is the nuclei radius.

There are two places that screening could mainly change (Bravo and García-Senz, 1999; Juodagalvis et al., 2010; Liu, Zhang, and Luo, 2007): (1). due to the fact that the chemical potential depends on Z, screening effects will change the threshold energy for the capture by the amount (Couch and Loumos, 1974):

$$Q_{if}^s = Q_{if} + \Delta Q_c; \quad \Delta Q_c = \mu_c(Z-1) - \mu_c(Z), \tag{3.53}$$

where μ_c is the Coulomb chemical potential given by (Shalybkov and Yakovlev, 1987):

$$\mu_c = T f_C(\Gamma_i), \tag{3.54}$$

f_C is the Coulomb free energy per ion in units of T, Γ_i is the ion-coupling parameter for species i (detailed equation see in Juodagalvis et al. (2010)).

(2). The energy of the captured electron is affected by the presence of the background electron gas. The energy ω is reduced to $\omega - \Delta_V$ where Δ_V is the screening potential. In the presence of magnetic field, it should have $\omega_B' = \sqrt{p_B^2+1+2n\gamma} - \Delta V(B)$, where $\Delta V(B)$ is given by Eq. 3.40 as

$$\Delta V(B) = V(\boldsymbol{r},B) - \frac{Ze^2}{\boldsymbol{r}}. \tag{3.55}$$

Fig. 3.17 shows the contribution from screening and the magnetic field to the phase space integral, i.e., Eq. 3.51. f_{ij} under different density (ρY_e) and field strength B are compared, temperature was set as $T = 10$ GK, the diagonal lines on both panels represent the relation $B_{crit} \propto (\rho Y_e)^{2/3}$. The left panel shows the ratio between screened and unscreened f_{ij}, it is clear that the screening could suppress f_{ij} for about 20% under high density and strong magnetic field case (the right bottom part), while

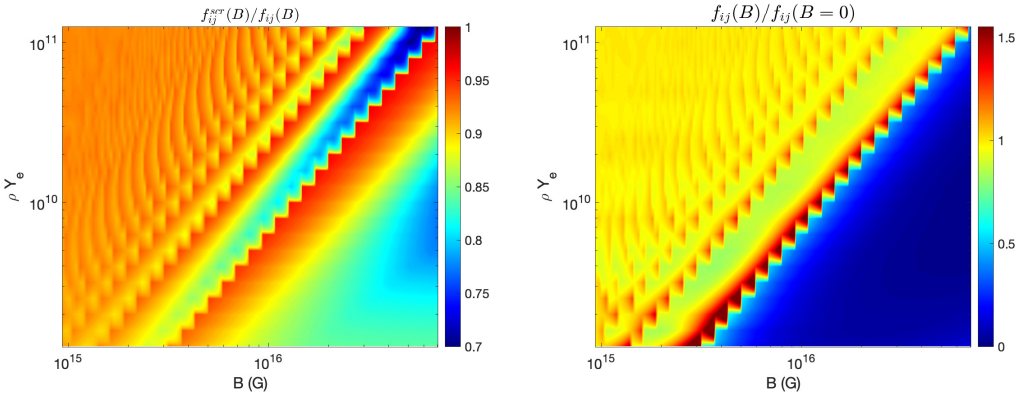

FIGURE 3.17: The left panel: The ratio between screened and unscreened f_{ij}. For the field-free situation, only few percent deviation of f_{ij} could be found (i.e., left-upper region of this panel). For the high field and relative low density case ($B > 10^{16}$ G and $\rho Y_e \sim 10^9$), screening effect could suppress f_{ij} about 20%. The right panel: The f_{ij} in a background magnetic field compared with field-free case. f_{ij} could be enhanced about 1.5 times when the field strength just corresponds to a new popped-up Landau level, for the extremely high field case, only the LLL allowed for electron to occupied, then f_{ij} is drastically reduced (i.e., left-upper region of this panel). The calculation here sets $T = 10\ GK$.

for most of the cases, screening could reduce f_{ij} for few percent, this is consistent with the previous study (Juodagalvis et al., 2010) where only the field-free screening is taken into account. On the right panel, the results are more interesting, here, I compare the ratio of f_{ij} between the scenario with and without magnetic field. Beyond the B_{crit}, f_{ij} value dramatically drops, this is due to the LLL occupation. For $B < B_{crit}$, for every $(\rho Y_e, B)$ combinations that corresponds to a state that popped-up a new Landau level, f_{ij} value could be enlarged for 1.5 times due to the larger value of E_F. Clearly once the field strength become lower than 10^{14} G, more Landau levels contribute to the integral of f_{ij}, then it becomes the same value as $B = 0$ scenario.

Since electron capture rate $\lambda_{ij} \propto f_{ij}$, the impacts on the phase space should leave imprints in the final electron capture rates. After the Oxygen burning, the inner regions of the star are mainly the iron peak nuclei, therefore, it is worth to discuss the iron group nuclei firstly.

The commonly accepted explosion mechanism is called "delayed mechanism": at the very end stage of stellar evolution, electron degeneracy pressure finally could not support the gravity so the core starts contracting, leading to an increasing temperature and density, when the density approaches to $\rho \sim 10^{11}$ g cm^{-3}, the neutrinos cannot escape from the center, so that a homologous core could form. The later increasing of the density finally make the core excess the nuclear matter density ($\rho \sim 10^{14}$ g cm^{-3}), then a spring-like bounce is formed, the "oscillation" of the core trigger a shock wave at the surface of the core, although the shock tries to traverse the material, it loses energies quickly via the interactions with the in-falling matter and the neutrino emission. The explosion could not be formed during this phase. Finally, the shock could revived due to the energy deposition from the neutrinos generated by cooling of the proto-neutron star and make the explosion (Bethe, 1990; Burrows, Hayes, and Fryxell, 1995; Janka and Mueller, 1996; Burrows et al., 2000; Langanke and Wiescher, 2001; Woosley, Heger, and Weaver, 2002).

The study on the electron capture rates of iron-group nuclei have been included

in the previous study (Heger et al., 2001) for the final stage evolution. For both 15 $M_\odot$ and 25 $M_\odot$ stellar models, the new electron capture rates for nuclei with mass number $A = 45 \sim 65$ (Langanke and Martínez-Pinedo, 2001) together with the supplemented rates of lighter nuclei (Oda et al., 1994) could enlarge the electron fraction Y_e of the onset of a collapsing core by $0.01 \sim 0.015$ because of the reduction of electron capture rate; the entropy of the cores are also increased for stars with $M > 20\ M_\odot$ while for stars with $M < 20\ M_\odot$, the entropy is lower compared with old models. As a consequence, the changes of entropy profile in silicon burning stage suppressed the growth of iron cores prior to collapse, so that the iron cores are in general are reduced by about $0.05\ M_\odot$ (Heger et al., 2001). As a result, the larger Y_e value could result in a larger homologous core, while a smaller iron core is obtained, so the shock is much easily to traverse. On the other hand, the weak-interaction processes shift the matter composition to smaller Y_e and hence more neutron-rich nuclei, subsequently affecting nucleosynthesis (McLaughlin, Fuller, and Wilson, 1996; Langanke and Martinez-Pinedo, 2000; Langanke and Martinez-Pinedo, 2003). The detailed analysis of Y_e change after Oxygen burning also finds that the important flow during the final stages of stellar evolution is much closer to valley of stability, several of the most important electron capturing nuclei (e.g., ^{54,56,58}Fe, ^{55}Mn, ^{53}Cr) are identified (Heger et al., 2001; Langanke and Martinez-Pinedo, 2003). Inspired by previous study, one should first focus on the rate of electron capture on ^{54}Fe. The reaction rates are calculated in different set of stellar conditions (i.e., combination of density, temperature and Y_e), those combinations are appropriate for the inner core of a collapsing 15 $M_\odot$ star, the star's profile is taken from Juodagalvis et al. (2010).

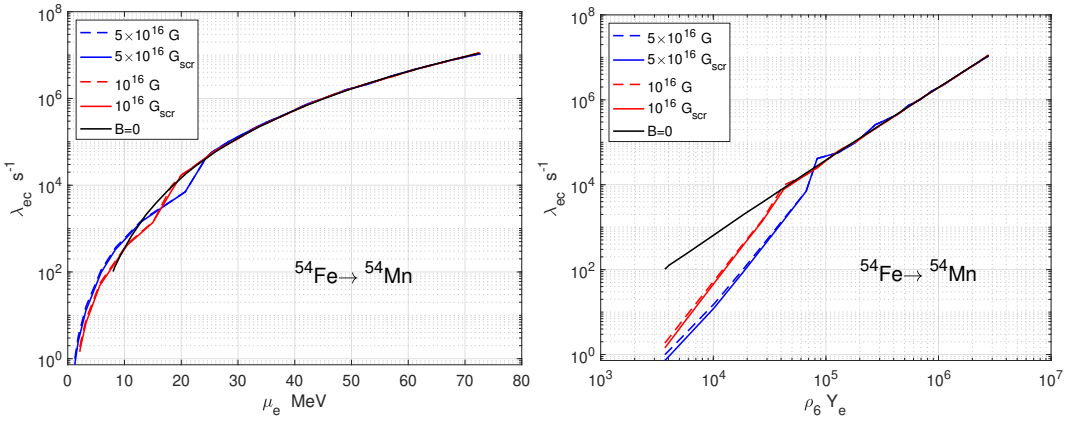

FIGURE 3.18: The reaction rate of $^{54}\mathrm{Fe}(e^-, \nu_e)^{54}\mathrm{Mn}$ as functions of chemical potential μ_e and ρY_e, respectively. Blue lines correspond to a 10^{15} G magnetic field, red lines correspond to a 10^{16} G magnetic field, black lines are field-free case. The screening corrections are also included as solid lines.

Fig. 3.18 shows the reaction rate of $^{54}\mathrm{Fe}(e^-, \nu_e)^{54}\mathrm{Mn}$ as a function of chemical potential μ_e and ρY_e, respectively. All the rates are converged to values for electron chemical potentials μ_e larger than about 25 MeV, while at lower μ_e values, the capture rates are more sensitive to the magnetic field strengths. The screening could suppress the electron capture rates as expected, and the suppression is stronger for the lower μ_e value. It is also worthy to mention that due to the magnetic field, μ_e is also a function of B as discussed, therefore, for the same combination of (ρ, Y_e), μ_e decreased as the increasing field strength, the electron capture rate could be reduced almost two orders of magnitude for the low density and high field region. At high density region, the field strength that allowed only the LLL occupation is also

high (i.e., $B_{crit} \propto \rho^{2/3}$), therefore $B < B_{crit}$ makes the indistinguishable trend of the reaction rates at high density region.

The aforementioned pre-supernova models are the initial input for the collapse and post-bounce stage. During the collapse, since the density is as high as 10^{14} g cm^{-3}, the elastic scattering between neutrino and nuclei $\nu + N \leftrightarrow \nu + N$ strongly trapped the neutrinos, also, the temperature and density during the collapsing and explosion are high, so that nuclear matter composition is determined by NSE, the detailed reaction network calculation is unnecessary. However, (Liebendörfer et al., 2001) pointed out that that electron capture is still important for the early phase of the collapse. Intuitively, the electron captured by protons are more favored due to the small Q-value compared with nuclei, however, the number fraction Y_p (i.e., the number of free protons divided by the total number of nucleons) is quite low especially for the 15 $M_\odot$ model. Since the electron fraction Y_e is enlarged by replacing the FFN rate with LMP, the material is less neutron rich so that the Q-value of the electron capture on nuclei could drop further. The neutron capture rates, $p + e^- \leftrightarrow n + \nu_e$ and $(A, Z) + e^- \leftrightarrow (A, Z-1) + \nu_e$ are sensitive to the phase-space due to the strong energy dependence E_e^5 of the integrand, the cross sections are enhanced rapidly during the collapse with the increasing of density and temperature. For the low entropy environment, the heavy nuclei is the main component of the collapsing matter, and due to the decreasing of Y_e, those nuclei will mostly located in the neutron rich region. Previous study concluded that it is safe to consider only the most abundant nuclei in the nuclear statistical equilibrium during the collapsing calculation, i.e., the ^{70}Zn and ^{88}Kr at different stages of collapse(Mezzacappa, 2001).

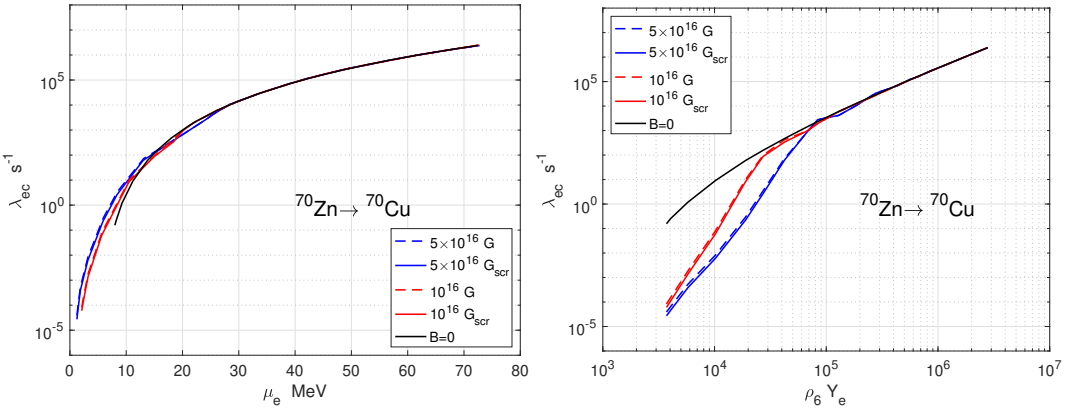

FIGURE 3.19: Same plot as Fig. 3.18 but for electron capture reaction ^{70}Zn$(e^-, \nu_e)^{70}$Cu.

Fig. 3.19 shows the same plot as Fig. 3.18 but for ^{70}Zn$(e^-, \nu_e)^{70}$Cu, the electron capture rates could be suppressed drastically in the region $\rho_6 Y_e \leq 10^5$, so $N \sim 50$ isotopic abundance could be deviated. One should notice that the most abundant nuclei are not necessary to represent all the heavy nuclei since such an approximation assumes the electron capture vanishes for nuclei with $Z < 40$ and $N \leq 40$ due to the completely blocked GT transitions. However, such an assumption is not accurate since the thermal excited states could pop up, then the proton could transfer from pf-shell to g-shell which lead to a possible transition (Cooperstein and Wambach, 1984). Therefore this reduction due to the strong field strength should be applied to other $N \sim 50$ isotope extensively in the near future.

For the high magnetic field and high density plasma, the chemical potential of electrons is simply the Fermi energy E_F, which has shown the field strength dependence. Once the Q-value is under the chemical potential μ_e, for a low chemical

potential value, the capture rate is sensitive to the μ_e, which could lead to further impacts on all the heavy nuclei in the collapsing and bouncing phases. Especially, it has been noticed that only the most abundant nuclei is not enough to represent the electron capture process in SNe (Langanke and Martinez-Pinedo, 2003). Moreover, the electron capture of heavy nuclei could generate low-energy neutrinos, and the inverse reaction of the electron capture affects the neutrino absorption of heavy nuclei which could deviate the emission of low-energy neutrinos. It is also shown that the number abundance of heavy nuclei is larger than the free protons during the collapse (Sampaio et al., 2003), although the capture rates of protons are much larger, they play the equal important roles for the Y_e evolution. Therefore, it is expected that the magnetic field could make significant impact during the collapsing and bouncing phases.

3.4 Conclusions

In this Chapter, plasma effects in highly-magnetized plasmas were evaluated. As field increases in strength, electron momentum transverse to the field direction is quantized into Landau levels. This alters the Fermi-Dirac distribution, resulting in a shift in the electron spectrum. Such shift leads to several consequences: the phase space integral in weak interactions is replace by a summation of the finite Landau levels; the Fermi energy E_F, which is the maximum energy that electrons could occupy in the plasma is changed because of the quantization of phase space. The screening correction to the bare Coulomb potential of nuclei also shift the value since electrons and positrons carry on extra electromagnetic energy. These microscopic effects could contribution to the nuclear weak interactions as well as the fusion reactions.

Specifically, for the non-degenerate plasma, an example of *r*-processing in a collapsar MHD jet site was examined by including all these effects from magnetic field. Thomas-Fermi description provides quite a good approximation on calculating the screening potential. Since the *r*-process is dominated by neutron captures, Coulomb screening only has a small effect on the overall evolution and final abundance distribution of the *r*-process. However, the strong field strength may have a larger effect on nucleosynthesis when it is applied to weak interaction rates. This is because particularly in the case of the finite β-decay spectrum – only a limited number of Landau levels can be occupied by the emitted charged lepton, as indicated in Figs. 3.7 and 3.8. For very high fields, $\sqrt{eB} \sim Q$, only a couple of Landau levels are available to the emitted electron or positron. A simple MHD collapsar jet model from the hydrodynamics calculations of Nakamura et al., 2012 is applied as an illustrative model. Large fields were found could affect the *r*-process evolution since the β^- decay rates increase with field strength. Because of this, it is found that the point at which the *r*-process path crosses the magic numbers change, results in shifting the abundance peaks of the final distribution and eventually affect the abundance ratios such as $\mathrm{Y}_{Sr}/\mathrm{Y}_{Tl}$. Also, the fissile nuclei produced in the *r*-process will be different, resulting in potentially different fission rates and distributions. This could possibly be studied using abundance ratios such as $\mathrm{Y}_{Sr}/\mathrm{Y}_{Ba}$, $\mathrm{Y}_{Sr}/\mathrm{Y}_{Dy}$.

For the degenerate plasma, the electron capture rates of iron group nuclei are re-evaluated by including the magnetic field impacts. The thermodynamic properties of electrons are strongly rely on the Fermi energy E_F, so I evaluate E_F value at high field, find E_F is monotonically decreased with the increasing of magnetic field if only the lowest Landau level is allowed to be occupied. The degeneracy of the plasma

makes the Thomas-Fermi approximation invalid, a relativistic generalization of the Hartree self-consistent field method is applied to calculate the dielectric longitudinal coefficient, finally obtained the screening potential of the strongly-magnetized degenerate plasma (Eq. 3.40). Unlike the field-free degenerate situation that only few percent deviation of the interaction rates could be found, the screening potential could reduce the electron capture rate for about 20% (left panel of Fig. 3.17). Moreover, the strong field strength only allow the lowest Landau level, therefore the phase space integral f_{ij} is dramatically suppressed when $B > B_{crit}$ (right panel of Fig. 3.17). A profile from a 15 $M_\odot$ core collapsing SNe progenitor model is applied to calculate the electron capture rates of ^{54}Fe and ^{70}Zn, it is noticed that a two orders of magnitude reduction for plasma with density $\rho \sim 10^9 \sim 10^{11}$ and magnetic field $B > 10^{14}$ G (Figs. 3.18 and 3.19). This is because E_F is the maximum energy that electrons could have in degenerate plasma, the amount of electrons with energy higher than the threshold energy of electron capture is small in strong magnetic field. These impacts have potential significance on the MHD-Jet SNe since $^{54}\mathrm{Fe}(e^-, \nu_e)^{54}\mathrm{Mn}$ is the leading reaction that reduces Y_e, the entropy of central region and the iron core mass are sensitive to Y_e value during the final stage evolution of massive star. These two parameters are crucial inputs of SNe explosion calculation. ^{70}Zn is one of the most abundant nuclei during the collapsing and bouncing stage, although the electron capture on proton is easier to occur compare with heavier nuclei, the relative smaller proton fraction suggests that the reduction of electron capture rates under strongly-magnetized degenerate plasma could further suppress the neutron richness; moreover, the changes on electron capture rate could also affect the emitted neutrino spectrum and the neutrino absorption rates.

Chapter 4

Summary and Future Aspects

4.1 Summary

This thesis focuses on the magnetic field and the induced influence on the nucleosynthesis in both cosmology and astrophysics. For the cosmological magnetic field, I sophisticatedly study the BBN in the context of PMF; for the magnetic field in astrophysics, I extensively investigate the *r*-process nucleosynthesis and the electron capture on iron group nuclei. The magnetic field affects the motion of electrons and positrons, results in a change of the plasma's thermodynamic condition. Electron momentum transverse to the field direction is quantized into Landau levels, then the phase space integral to calculate the weak interaction rates is replaced by a summation of the finite Landau levels; the Fermi energy E_F in the plasma is also affected because of the quantization of phase space. The screening correction to the Coulomb potential of bare nuclei shifts the value since electrons and positrons carry on extra electromagnetic energy. These microscopic effects could contribution to the nuclear weak interactions significantly. On the other hand, thermonuclear reactions strongly depend on the background temperature and density of the reactant nuclei species, these two properties of the plasma could easily affected by dynamical evolution of magnetic field due to the induced energy fluctuation, results in a further change of the abundance flow.

In Chapter 2, the property of relativistic plasma in early universe with background PMF is investigated in detail. Specifically, the weak screening effect from the magnetized plasma is clarified, the screening depends on the thermodynamics of charged particles in the plasma which could be altered by PMF, the screening potential under PMF is derived in Eq. 2.11 and the electron-capture rate including such corrections is derived in Eq. 2.12. The screening has only 0.1% impact on the final abundances yields (Fig 2.6) because of the low density of plasma during BBN. However, by including the PMF impacts on weak interactions, the generation epoch of a frozen-in PMF could be constrained. Comparing the theoretical ^{4}He yield with observations, it is found that a late PMF generation epoch at $T < 1.5 \times 10^{10}$K is more favored (Fig. 2.7). Moreover, the recent updated nuclear reaction cross sections results in a lower D abundance in the standard BBN calculation compared with observations, such D under prediction could be resolved an enhancement of weak reaction rates caused by PMF (Table 2.1).

Then, a static inhomogeneous PMF energy density model is proposed during BBN in Sect. 2.3. Our static model shows a completely new calculated result of primordial elemental abundances (Fig. 2.13). The main effect of fluctuated PMF is the inhomogeneity of energy density which can lead to a deviation from classical Maxwellian distribution for baryons. The PMF in this work is described as a stochastic field. PMF energy density obeys a narrow Gaussian distribution under the presumption of a constant value of total energy density. The expression for the

temperature distribution function is derived (Eq. 2.31). In this model, primordial baryons are in local equilibrium with the same temperature and obey Maxwellian distribution; Globally, due to the existence of a fluctuated PMF, radiation energy density becomes inhomogeneous as the radiation temperature does. This inhomogeneity eventually leads to a non-Maxwellian baryonic distribution function (Fig 2.11). It is found that $\rho_{Bc}/\rho_{tot} = 0.08 - 0.13$ and $\sigma_B = 0.04 - 0.17$ provides the best fit to the observations for both Y_p and D (Fig. 2.12). This amount of magnetic energy density corresponds to a present PMF of $1.18 - 1.51$ μG. Moreover, the ^{7}Li abundance is reduced in our model to a value of $^7\mathrm{Li/H} = (3.35 - 3.52) \times 10^{-10}$ which is lower compare with standard BBN but still not enough to solve the "cosmic Li problem" (Table 2.2).

In Sect. 2.4, the relativistic MHD equations are derived in an expanding universe (Eqs. 2.54 to 2.56) which could be used for the realistic calculation of BBN with dynamical PMF evolution. The PMF generation from decoupling of particles is studied extensively, this model can be extended to a general aspect that induce inhomogeneous magnetic field via the collision inside the relativistic plasma in the early universe. By applying the the"two-fluid" model (Eqs. 2.54 to 2.56), it is possible to generate PMF from the collisions between different phases of the plasma, the only requirement is the decoupled species velocity has non-zero vorticity (Eqs. 2.54 to 2.56). The equations could be numerically solved in the future dynamical PMF study.

Finally, the present status of the "cosmic Li problem" is summarized, there is no clear resolution at present, the solution from nuclear physics side seems impossible; the stellar astrophysical solution requires a universal mechanism that should explain not only the metal poor dwarf halo stars, but also the extra-galactic metal poor observations. From cosmological perspective, the recent study shows that the Hubble tension could be alleviated by inducing the magnetic field (Jedamzik and Pogosian, 2020), indicates the possible existence of PMF. A multi-zone BBN model with inhomogeneous PMF strength is performed, our results shows the light elemental abundance also could be significantly deviated due to the inhomogeneity from PMF energy density. The PMF in our model has the survival co-moving strength as $B_0 \sim 10^{-6}$ G, which is larger than the IGMF limitation, however, the turbulence decay could reduce the co-moving strength of PMF, therefore, a much more reliable conclusion should be obtained from a much realistic numerical calculation of the dynamical PMF evolution including turbulence.

In Chapter 3, the plasma effect from strongly-magnetized plasma is investigated in the astrophysical sites. Sect. 3.2 analyzes the high field and non-degenerate scenario, electron momentum transverse to the field direction is quantized into limited Landau levels. This alters the Fermi-Dirac distribution significantly, resulting in a shift in the electron spectrum (Fig. 3.7). The screening correction to the bare Coulomb potential of nuclei also shifts its value (Fig. 3.6), Thomas-Fermi description provides quite good approximation on calculating the screening potential, however, since the *r*-process is dominated by neutron captures, screening only has a small effect on the overall evolution and final abundance distribution of the *r*-process. More interesting impacts come from the high fields: only a limited number of Landau levels can be occupied by the emitted charged lepton for β-decay spectrum (Figs. 3.7 and 3.8); and for very high fields, $\sqrt{eB} \sim Q$, only a couple of Landau levels are available to the emitted electron or positron. Consequently, the weak interaction rates are deviated from field-free case which leads to further changes on the *r*-process nucleosynthesis. An example of *r*-processing in a collapsar MHD-jet site is applied in this chapter, large fields were found could affect the *r*-process evolution since the

β^- decay rates increase with field strength. It is found that the point at which the *r*-process path crosses the magic numbers change, results in shifting the abundance peaks of the final distribution and eventually affect the abundance ratios such as Y_{Sr}/Y_{Tl}. Also, the fissile nuclei produced in the *r*-process will be different, resulting in potentially different fission rates and distributions. This could possibly be studied using abundance ratios such as Y_{Sr}/Y_{Ba}, Y_{Sr}/Y_{Dy}.

Then in Sect. 3.3, the effects from magnetized degenerate plasma are studied. The Thomas-Fermi approximation of calculating the screening potential is invalid, a relativistic generalization of the Hartree self-consistent field method is applied to calculate the dielectric longitudinal coefficient, obtained the screening potential of the highly-magnetized degenerate plasma (Eq. 3.40). The electron capture rates of iron group nuclei under highly-magnetized degenerate plasma are evaluated, about 20% reduction of the capture rates is result from Coulomb screening (left panel of Fig. 3.17). Moreover, the strong field strength only allow the lowest Landau level, therefore the phase space integral f_{ij} is dramatically suppressed when $B > B_{crit}$ (right panel of Fig. 3.17). A profile from a 15 $M_\odot$ core collapsing SNe progenitor model is applied to calculate the electron capture rate of ^{54}Fe and ^{70}Zn, it is noticed a two orders of magnitude reduction for plasma with density $\rho \sim 10^9 \sim 10^{11}$ g cm^{-3} and $B > 10^{14}$ G (Figs. 3.18 and 3.19). Such effects have potential significance on the MHD-Jet SNe since ^{54}Fe$\rightarrow{}^{54}$Mn is the leading reaction that reduce Y_e during the final stage of stellar evolution, and Y_e decided the entropy of central region as well as the iron core mass, which are the crucial initial inputs of SNe explosion calculation; ^{70}Zn is one of the most abundant nuclei during the collapsing and bouncing stage, the reduction of electron capture rates on heavy nuclei under highly-magnetized degenerate plasma could further suppress the neutron richness; moreover, the changes on electron capture rate could also affect the emitted neutrino spectrum and the neutrino absorption rate.

4.2 Future Plan

The present constraints on IGMFs provide us with a magnetic field strength of $\sim$ nG for a co-moving length scale $\sim$ kpc, which could be correspond to a survival relic PMF generated in the very early universe. However, the predicted magnetic field strength due to the galaxies or the AGN activities also has the same strength and scale (Fig. 2.1), therefore, the origin of the IGMFs unfortunately could not be clarified by far. To avoid the contamination from later epoch galactic activities, one should seek for another probe that could constraint both the field strength and correlation length in the very early universe. The primordial nucleosynthesis is an important process after weak interaction decoupling, the observed primordial elemental abundances have been proved to be the most powerful tool to probe the very early universe from many aspects (Luo et al., 2021; Kawasaki et al., 2020; Mori and Kusakabe, 2019). Once PMF was generated during inflation, phase transition or(and) weak interaction decoupling, its evolution should leave an imprint in light elemental abundances. However, since standard BBN calculation does not consider the effect from PMF fluctuation, only an upper limit of averaged PMF co-moving energy density can be deduced from primordial elemental observations. Our static inhomogeneous PMF shows the significance on deviating the BBN predictions, and the MHD equations of PMF generation in expanding universe are also derived. In the future, I will mainly focus on constructing BBN reaction network with PMF evolution to build a realistic PMF-BBN dynamical model: 1). the comparison between

the predicted elemental production in our calculation and the observed primordial elemental abundances; 2). the comparison between the calculated final PMF pattern and the CMB spectrum observed by Planck satellite, these two evidences could finally provide a more precise constraint on PMF generation, field strength and correlation scale.

Moreover, the recent studies of stellar evolution show that ^{7}Li abundance could be significantly depleted via diffusion process in main sequence phase or the pre-main sequence depletion accompanied by a late mass accretion. However, the stellar evolution theory of metal-poor stars has large uncertainty because of the limitation from observations, it is hard to conclude that the stellar evolution is the solution of "cosmic Li problem". PMF could alleviate this problem, the observed A(^{7}Li)=2.23 dex could be reproduced from an initial Li abundance as A(^{7}Li)=2.5 dex theoretically in the depletion models, which indicates that the relic ^{7}Li abundance after BBN could be an intermediate value between standard BBN prediction and Spite plateau. Therefore, studying of the dynamical PMF impact on BBN could build a bridge to link the ^{7}Li abundance from BBN to stellar evolution, in the future, this study could help to push the theoretical ^{7}Li abundance limit in both BBN calculation and stellar evolution.

Recent consensus of the origin of *r*-process is that collapsars, which are the supernovae leaving black hole as remnant, and supernovae, leaving neutron star as remnant, are the major sites of providing r-process elements in the entire history of Galactic chemical evolution and that neutron star mergers make minor additional contribution in recent epoch. Although the gravitational wave event GW170817 and its electromagnetic counterpart GRB170817 (Abbott, 2017; Abbott et al., 2017) is consistent with the present understanding of the NSM, there is unfortunately no clear evidence for the r-process elements except for the blue-to-red light curve change. Our results on the strongly magnetized astrophysical plasma shows the explosive nucleosynthesis of *r*-process elements could provide an observational signal for such a strong magnetic field through the change of weak electron-capture rates. In the future, I would like to carry on more precise evaluations, it is interesting to note that – in a highly-magnetized *r*-process site – the elemental abundance ratios can constrain the magnetic field of the site and vice-versa, such influence could be utilized to clarify the *r*-process site. The limitations of our test model presented here are noted. These include primarily the static field assumption and the simplified fission model used. If the static field is assumed to be the maximum field in the site, then the results could be thought of as upper limits. Also, the simplified fission model was used as the primary evaluation of this study was on the effects of strong magnetic fields in nucleosynthesis sites. The progenitor nuclei examined in the *r*-process site in this study – being quite far from stability – were treated in this much simpler matter. In the future I will carry on much extensive study with a dynamic treatment of the magnetic field.

For MHD-Jet SNe, electron fraction Y_e is the most important variable because it determines the neutron-richness. For the very end phase of stellar evolution as well as in the region above neutrino sphere during the bouncing, the evolution of Y_e depends on the weak interactions rate. The electron capture rates for two iron group nuclei have been calculated, I would like to extend the study to other nuclei and carry out the systematic study of the weak interactions rates in the magnetized degenerate plasma, then including the rates into the SNe model. Such effects are non-trivial because the isotopic abundances at high temperature region are obtained by solving the nuclear Saha equation, which determined by Y_e, so that any changes of the electron fraction finally could leave the observational signals in the final yields;

since the low-energy neutrinos are main come from the electron capture of heavy nuclei,it is also expected that magnetic field leave some imprints in neutrino spectrum. Further, the ejected material from those explosive activity could may change the contribution to currently observed elements in GCE models. Future work will also concentrate on a more thorough treatment of fission in the collapsar/MHD site and its effects on GCE.

Another interesting point is that the dielectric coefficient also determine the effective electron collision frequencies significantly, which deviates the electrical and thermal conductivity and could result in a modification of magnetars cooling curve. The theoretical cooling calculations serve as a principal window on the properties of super-dense hadronic matter and neutron star structure. Therefore in the strong magnetized degenerate plasma, by studying the similar impact as screening, new information about neutron star such as *equation of state* (EOS) and internal pulsar heating mechanism could be provided.

Appendix A

Thermonuclear reaction rate

A.1 Cross Section

The cross section σ describes how much the probability is that an interaction could occur. Suppose a beam carries N_b particles per unit time t, with a covering area A, is incident on a target. The number of target nuclei (we assume non-overlapping case) within the beam is N_t. We define the total number of interactions occur per unit time is N_R/t, then the cross section is defined as

$$\begin{aligned}\sigma &= \frac{number\ of\ interactions\ per\ time}{number\ of\ incident\ particles\ per\ area\ time \times number\ of\ target\ nuclei\ within\ beam} \\ &= \frac{N_R/t}{[N_b/(tA)]N_t}. \end{aligned} \tag{A.1}$$

This is the general definition to describe reaction probabilities in astrophysical environment and in laboratory measurements of nuclear reactions. Usually the total cross section σ is given in terms of $d\sigma/d\Omega$, which is a differential cross section determine by emit angle θ. $d\sigma/d\Omega$ is

$$\frac{d\sigma}{d\Omega} = \frac{N_R^{d\Omega}/(tN_t)}{(N_b/t)(1/A)}\frac{1}{d\Omega}. \tag{A.2}$$

With the definition of a current density j as the number of particles per time per area, the beam and emitted interaction products reads

$$j_b = \frac{N_b/t}{A}; \tag{A.3}$$

$$j_{et} = \frac{N_R^{d\Omega}/(tN_t)}{dF}. \tag{A.4}$$

In conclusion,

$$\sigma = \int \left(\frac{d\sigma}{d\Omega}\right) d\Omega, \tag{A.5}$$

where

$$\sigma = \frac{j_{et}r^2}{j_b}. \tag{A.6}$$

The common units of cross sections are

$$1\text{b} := 10^{-24}\text{cm}^2; 1\text{fm}^2 = 10^{-2}\text{b} \tag{A.7}$$

A.2 Particle-Induced Reactions

Consider a reaction which involves four species $0+1 \rightarrow 2+3$, using Eq.A.1, we can write the reaction rate per unit time t and per unit volume V as

$$r_{01} = \frac{N_R}{V \cdot t} = \sigma N_t \Big(\frac{N_b}{V \cdot A \cdot t} \Big) = n_t n_b \sigma v, \tag{A.8}$$

here we define the number density of interacting particles as

$$n_0 = \frac{N_t}{V}; n_1 = \frac{N_b}{V}. \tag{A.9}$$

In a thermodynamic equilibrium, the relative velocity of the two interacting species 0 and 1 is not a constant, it may follow a certain distribution function $P(v)$, in this case, $P(v)\mathrm{d}v$ is the probability that the relative velocity is in the range of $v \sim v + \mathrm{d}v$, and $P(v)$ naturally should be normalized to unity as

$$\int_0^\infty P(v)\mathrm{d}v = 1. \tag{A.10}$$

In general, $P(v)$ is the Maxwell-Boltzmann distribution

$$P(v)\mathrm{d}v = \Big(\frac{m_{01}}{2\pi kT} \Big)^{3/2} e^{-m_{01}v^2/2kT} 4\pi v \mathrm{d}v, \tag{A.11}$$

here the Boltzmann constant k is given by $k = 8.6173 \times 10^{-5}\mathrm{eV/K}$, T is the temperature, m_{01} is the reduced mass $m_{01} = m_0 m_1/(m_0 + m_1)$.

With the variable transform $E = m_{01}v^2/2$, $dE/dv = m_{01}v$, we may write the velocity distribution as the energy distribution

$$\begin{aligned} P(E)\mathrm{d}E &= \Big(\frac{m_{01}}{2\pi kT} \Big)^{3/2} e^{-E/kT} 4\pi \frac{2E}{m_{01}} \frac{dE}{m_{01}} \sqrt{\frac{m_{01}}{E}} \\ &= \frac{2}{\sqrt{\pi}} \frac{\sqrt{E}}{(kT)^{3/2}} e^{-E/kT} dE \end{aligned} \tag{A.12}$$

then the reaction rate per particle pair $\langle \sigma v \rangle_{01}$ is given by

$$\langle \sigma v \rangle_{01} = \int_0^\infty v P(v) \sigma(v) \mathrm{d}v. \tag{A.13}$$

Numerically, in BBN epoch, we can calculate the reaction rate at a given temperature $T_9 := T/10^9\mathrm{K}$

$$N_A \langle \sigma v \rangle_{01} = \frac{3.7318 \times 10^{10}}{T_9^{3/2}} \sqrt{\frac{M_0 + M_1}{M_0 M_1}} \int_0^\infty E\sigma(E) e^{-11.905E/T_9} dE \tag{A.14}$$

which is in the unit of $\mathrm{cm^3 mol^{-1} s^{-1}}$.
Then the reaction rate is given by

$$\begin{aligned} r_{01} &= n_0 n_1 \int_0^\infty v P(v) \sigma(v) \mathrm{d}v \\ &= n_0 n_1 \langle \sigma v \rangle_{01}. \end{aligned} \tag{A.15}$$

For the identical particles, when n_0 is a large number, the total number density is given by

$$\frac{n_0(n_0-1)}{2} \to \frac{n_0^2}{2}, \tag{A.16}$$

the more general case reads

$$r_{01} = \frac{n_0 n_1 \langle \sigma v \rangle_{01}}{1+\delta_{01}}. \tag{A.17}$$

A.3 Photon-Induced Reactions

For photon-induced reaction $\gamma + 1 \to 1 + 2$, since photon only travel with speed of light c, therefore similar to Eq. A.8, the reaction rate $r_{\gamma 1} = N_R/(Vt)$ is given by

$$r_{\gamma 1} = n_1 n_\gamma c \sigma(E_\gamma), \tag{A.18}$$

here the cross section depends on the γ-ray energy, there is no such a term same as $\langle \sigma v \rangle$ since the relative velocity here is always a constant value c. Moreover, in a plasma which at the thermodynamic equilibrium state, the number density of photons is not a constant, it depends on the background temperature and γ-ray energy, therefore $r_{\gamma 1}$ can be rewritten as

$$r_{\gamma 3} = n_3 \int_0^\infty c n_\gamma(E_\gamma) \sigma(E_\gamma) \mathrm{d}E_\gamma, \tag{A.19}$$

The energy density of electromagnetic waves within the frequencies ranged between $\nu \sim \nu + \mathrm{d}\nu$ is describe by Planck radiation law

$$u(\nu)\mathrm{d}\nu = \frac{8\pi h \nu^3}{c^3} \frac{1}{e^{h\nu/kT}-1} \mathrm{d}\nu, \tag{A.20}$$

with the variable transformation $E_\gamma = h\nu$,

$$u(E_\gamma)\mathrm{d}E_\gamma = \frac{8\pi}{(hc)^3} \frac{E_\gamma^3}{e^{E_\gamma/kT}-1} \mathrm{d}E_\gamma. \tag{A.21}$$

Then the number density of photons with in the energy range $E_\gamma \sim E_\gamma + \mathrm{d}E_\gamma$ at a certain temperature T is

$$\begin{aligned} n_\gamma(E_\gamma)\mathrm{d}E_\gamma &= \frac{u(E_\gamma)}{E_\gamma}\mathrm{d}E_\gamma \\ &= \frac{8\pi}{(hc)^3} \frac{E_\gamma^2}{e^{E_\gamma/kT}-1} \mathrm{d}E_\gamma, \end{aligned} \tag{A.22}$$

together with Eq. A.19, we obtain for the reaction rate $r_{\gamma 1}$

$$r_{\gamma 1} = \frac{n_1 8\pi}{h^3 c^2} \int_0^\infty \frac{E_\gamma^2}{e^{E_\gamma/kT}-1} \sigma(E_\gamma) \mathrm{d}E_\gamma \tag{A.23}$$

Appendix B

Friedmann Equation & Cosmology

B.1 Basic Quantities

The line element in spacially flat FRW space-time can be written as

$$ds^2 = -dt^2 + a^2(t)\delta_{ij}dx^i dx^j = a^2(\tau)\eta_{\mu\nu}dx^\mu dx^\nu, \tag{B.1}$$

Metric Tensor

Metric tensor read as

$$(g_{\mu\nu}) = \begin{pmatrix} -1 & & & \\ & a^2(t) & & \\ & & a^2(t) & \\ & & & a^2(t) \end{pmatrix}, \tag{B.2}$$

$$(g^{\mu\nu}) = \begin{pmatrix} -1 & & & \\ & \frac{1}{a^2(t)} & & \\ & & \frac{1}{a^2(t)} & \\ & & & \frac{1}{a^2(t)} \end{pmatrix}, \tag{B.3}$$

for the coordinate (t, x, y, z), and

$$(g_{\mu\nu}) = a^2(\tau)\begin{pmatrix} -1 & & & \\ & 1 & & \\ & & 1 & \\ & & & 1 \end{pmatrix}, \tag{B.4}$$

$$(g^{\mu\nu}) = \frac{1}{a^2(\tau)}\begin{pmatrix} -1 & & & \\ & 1 & & \\ & & 1 & \\ & & & 1 \end{pmatrix}, \tag{B.5}$$

for the coordinate (τ, x, y, z).

Christoffel Symbols

$$\boldsymbol{\Gamma^\lambda_{\alpha\beta} = \frac{1}{2}g^{\lambda\rho}(\partial_\alpha g_{\alpha\gamma} + \partial_\beta g_{\rho\alpha} - \partial_\rho g_{\alpha\beta})}$$

We have

$$\Gamma^0_{00} = \Gamma^0_{0i} = 0,\ \ \Gamma^0_{ij} = \delta_{ij}\dot{a}a = a^2 H\delta_{ij},\ \ \Gamma^i_{0j} = \delta^i_j\frac{\dot{a}}{a} = H\delta^i_j \tag{B.6}$$

for the coordinate (t, x, y, z), and

$$\Gamma^0_{00} = \frac{a'}{a} = \mathcal{H}, \;\; \Gamma^0_{ij} = \delta_{ij}\frac{a'}{a} = \mathcal{H}\delta_{ij}, \;\; \Gamma^i_{0j} = \delta^i_j\frac{a'}{a} = \mathcal{H}\delta^i_j \tag{B.7}$$

for the coordinate (τ, x, y, z). Here after, H and $\mathcal{H}$ denote the following quantities

$$H = \frac{da/dt}{a} = \frac{\dot{a}}{a}; \quad \mathcal{H} = \frac{da/d\tau}{a} = \frac{a'}{a}. \tag{B.8}$$

Riemann Tensors

$$\boldsymbol{R^\lambda_{\mu\rho\nu} = \partial_\rho \Gamma^\lambda_{\mu\nu} - \partial_\nu \Gamma^\lambda_{\mu\rho} + \Gamma^\sigma_{\mu\nu}\Gamma^\lambda_{\rho\sigma} + \Gamma^\sigma_{\mu\rho}\Gamma^\lambda_{\nu\sigma}}$$

We have

$$\begin{aligned}
&R^0_{i0j} = \delta_{ij}a\ddot{a}, R^0_{ij0} = -\delta_{ij}a\ddot{a}, R^i_{00j} = \delta^i_j\frac{\ddot{a}}{a}, R^i_{0j0} = -\delta^i_j\frac{\ddot{a}}{a},\\
&R^1_{212} = R^1_{313} = \dot{a}^2, R^1_{221} = R^1_{331} = -\dot{a}^2,\\
&R^2_{121} = R^2_{323} = \dot{a}^2, R^2_{112} = R^2_{332} = -\dot{a}^2,\\
&R^3_{131} = R^3_{232} = \dot{a}^2, R^3_{113} = R^3_{223} = -\dot{a}^2
\end{aligned} \tag{B.9}$$

for the coordinate (t, x, y, z), and

$$\begin{aligned}
&R^0_{i0j} = \delta_{ij}\left[\frac{a''}{a} - \left(\frac{a'}{a}\right)^2\right], R^0_{ij0} = -\delta_{ij}\left[\frac{a''}{a} - \left(\frac{a'}{a}\right)^2\right],\\
&R^i_{00j} = \delta^i_j\left[\frac{a''}{a} - \left(\frac{a'}{a}\right)^2\right], R^i_{0j0} = -\delta^i_j\left[\frac{a''}{a} - \left(\frac{a'}{a}\right)^2\right],\\
&R^1_{212} = R^1_{313} = \left(\frac{a'}{a}\right)^2, R^1_{221} = R^1_{331} = -\left(\frac{a'}{a}\right)^2,\\
&R^2_{121} = R^2_{323} = \left(\frac{a'}{a}\right)^2, R^2_{112} = R^2_{332} = -\left(\frac{a'}{a}\right)^2,\\
&R^3_{131} = R^3_{232} = \left(\frac{a'}{a}\right)^2, R^3_{113} = R^3_{223} = -\left(\frac{a'}{a}\right)^2
\end{aligned} \tag{B.10}$$

for the coordinate (τ, x, y, z).

Ricci Tensors

$$\boldsymbol{R_{\mu\nu} = R^\rho_{\mu\rho\nu}}$$

We have

$$\begin{aligned}
R_{00} &= -3\frac{\ddot{a}}{a} = -3(\dot{H} + H^2)\\
R_{ij} &= \delta_{ij}(2\dot{a}^2 + a\ddot{a}) = a^2\delta_{ij}(\dot{H} + 3H^2)
\end{aligned} \tag{B.11}$$

for the coordinate (t, x, y, z), and

$$\begin{aligned}
R_{00} &= -3\frac{a''}{a} + 3\left(\frac{a'}{a}\right)^2 = -3\mathcal{H}'\\
R_{ij} &= \delta_{ij}\left[\frac{a''}{a} + \left(\frac{a'}{a}\right)^2\right] = \delta_{ij}(\mathcal{H}' + 2\mathcal{H}^2)
\end{aligned} \tag{B.12}$$

for the coordinate (τ, x, y, z).

Scalar Curvature

$$R = 6\left[\frac{\ddot{a}}{a} + \left(\frac{\dot{a}}{a}\right)^2\right] = 6(\dot{H} + 2H^2) \tag{B.13}$$

for the coordinate (t, x, y, z), and

$$R = \frac{6}{a^2}\frac{a''}{a} = 6a^{-2}(\mathcal{H}' + \mathcal{H}^2) \tag{B.14}$$

for the coordinate (τ, x, y, z).

Einstein tensors

$$\boldsymbol{G_{\mu\nu} = R_{\mu\nu} - \frac{1}{2}g_{\mu\nu}R}$$

We have

$$\begin{aligned} G_{00} &= 3\left(\frac{\dot{a}}{a}\right)^2 = 3H^2 \\ G_{ij} &= \delta_{ij}\left(-\dot{a}^2 - 2a\ddot{a}\right) = -a^2\delta_{ij}(2\dot{H} + 3H^2) \end{aligned} \tag{B.15}$$

for the coordinate (t, x, y, z), and

$$\begin{aligned} G_{00} &= 3\left(\frac{a'}{a}\right)^2 = 3\mathcal{H}^2 \\ G_{ij} &= \delta_{ij}\left[-2\frac{a''}{a} + \left(\frac{a'}{a}\right)^2\right] = -\delta_{ij}(2\mathcal{H}' + \mathcal{H}^2) \end{aligned} \tag{B.16}$$

for the coordinate (τ, x, y, z).

B.2 Friedmann Equation

In cosmology, Einstein equation reads as

$$R_{\mu\nu} - \frac{1}{2}g_{\mu\nu}R + \Lambda g_{\mu\nu} = 8\pi G T_{\mu\nu}, \tag{B.17}$$

the FLRW metric is given by

$$ds^2 = -dt^2 + a(t)^2\Big[\frac{dr^2}{1-kr^2} + r^2(d\theta^2 + sin^2\theta d\phi^2)\Big], \tag{B.18}$$

where k determines the closed ($k = +1$), Open ($k = -1$) or flat ($k = 0$) Universe, a is the scale factor to describe the scale of the Universe.

With a very prior assumption on the right hand side of Eq. B.17, we can treat the total stress-energy tensor $T_{\mu\nu}$ as a diagonal and its space components must be equal. This assumption is consistent with the symmetries of the metric, and easy to be proceed without detailed knowledge of the properties of the fundamental fields which contribute to $T_{\mu\nu}$. This simplest presumption imply a perfect homogeneous fluid which characterized by a time-dependent energy density $\rho(t)$ and pressure $p(t)$:

$$T_{\mu\nu} = \text{diag}(\rho, -p, -p, -p). \tag{B.19}$$

Then plug in the metric (Eq. B.18) to the Einstein equation, we can obtain that for $0-0$ component

$$\left(\frac{\dot{a}}{a}\right)^2 = \frac{8\pi G}{3}\rho - \frac{k}{a^2} + \frac{\Lambda}{3} \tag{B.20}$$

for $i-j$ component

$$\frac{\ddot{a}}{a} = -\frac{4\pi G}{3}(\rho + p) + \frac{\Lambda}{3}. \tag{B.21}$$

However, these two equation are not independent to each other, when we introduce the energy conservation of stress-energy tensor $T_{\mu\nu}$, i.e., $T^{\mu\nu}_{\ ;\nu} = 0$, we can obtain

$$\frac{\mathrm{d}}{\mathrm{d}t}(\rho a^3) + p\frac{\mathrm{d}(a^3)}{\mathrm{d}t} = 0, \tag{B.22}$$

combine this with Eq. B.21, Eq. B.20 can be recovered. Therefore, in order to solve the equations with three variables ρ, p and a, we need an extra independent equations, i.e., the *equation of state* (EOS) which describes the relation between pressure and density as $p = f(\rho)$. For the perfect fluid we assumed, EOS can be expressed as $p = \omega\rho$, for relativistic matter, $p = \rho/3$, for non-relativistic matter, $p = 0$, for vacuum, $p = -\rho$. Then combine these relations with Eq. B.22, one can obtain

$$Relativistic : p = \frac{1}{3}\rho \Longrightarrow \rho \propto a^{-4} \tag{B.23}$$

$$Non-relativisitc : p = 0 \Longrightarrow \rho \propto a^{-3} \tag{B.24}$$

$$Vacuum : p = -\rho \Longrightarrow \rho = const. \tag{B.25}$$

Then in the Friedmann model ($k = 0$, $\Lambda = 0$), Eq. B.20 becomes

$$\dot{a}^2 = \frac{8\pi G}{3}\rho a^2 \tag{B.26}$$

the solution of Eq. B.20 is

$$\dot{a} = a_0 H_0 \left(\frac{a_0}{a}\right)^{\frac{1+3\omega}{2}} \tag{B.27}$$

$$a(t) = a_0 \left(\frac{t}{t_0}\right)^{\frac{2}{3(1+\omega)}} \tag{B.28}$$

$$a(t) \propto \begin{cases} t^{1/2} & \omega = \frac{1}{3}\ (Radiation-dominated) \\ t^{2/3} & \omega = 0\ (Matter-dominated) \end{cases} \tag{B.29}$$

Appendix C

Electronic Thermodynamics

C.1 Field-free Thermodynamics

In the early Universe, the dilute weakly-interacting gas of particles can be treat as in a thermal equilibrium, so that the number density n, the energy density ρ and pressure p can be given in terms of the distribution function $f(\mathbf{p})$ with the degrees of freedom g:

$$\begin{aligned} n &= \frac{g}{(2\pi)^3}\int f(\mathbf{p})d^3\mathbf{p} \\ \rho &= \frac{g}{(2\pi)^3}\int E(\mathbf{p})f(\mathbf{p})d^3\mathbf{p} \\ p &= \frac{g}{(2\pi)^3}\int \frac{|\mathbf{p}^2|}{3E}f(\mathbf{p})d^3\mathbf{p}, \end{aligned} \tag{C.1}$$

where $E^2 = \mathbf{p}^2 + m^2c^4$. For the particles in kinetic equilibrium, the distribution function f within the phase space is given by

$$f(\mathbf{p}) = \frac{1}{\exp\left[(E-\mu)/kT\right] \pm 1}, \tag{C.2}$$

here μ is the chemical potential of the particles, $+1$ and -1 corresponds to Fermi-Dirac distribution and Bose-Einstein distribution respectively.
With the energy-momentum relation, Eq. C.1 can be expressed as

$$n = \frac{g}{2\pi^2}\int_m^\infty \frac{(E^2-m^2)^{1/2}}{\exp\left[(E-\mu)/kT\right] \pm 1}E^2dE \tag{C.3}$$

$$\rho = \frac{g}{2\pi^2}\int_m^\infty \frac{(E^2-m^2)^{1/2}}{\exp\left[(E-\mu)/kT\right] \pm 1}EdE \tag{C.4}$$

$$p = \frac{g}{6\pi^2}\int_m^\infty \frac{(E^2-m^2)^{3/2}}{\exp\left[(E-\mu)/kT\right] \pm 1}dE, \tag{C.5}$$

the results of the integration is

$$n = \frac{\xi(3)}{\pi^2}g'T^3(Boson); \frac{3\xi(3)}{4\pi^2}g'T^3(Fermion) \tag{C.6}$$

$$\rho = \frac{\pi^2}{30}gT^4(Boson); \frac{7\pi^2}{240}gT^4(Fermion) \tag{C.7}$$

$$p = \rho/3. \tag{C.8}$$

In the expanding universe, the second law of thermodynamics with a volume of $V = a^3$ is

$$TdS = d(\rho V) + pdV = d[(\rho + p)V] - Vdp, \tag{C.9}$$

under the integrability condition:

$$\frac{\partial^2 S}{\partial T \partial V} = \frac{\partial^2 S}{\partial V \partial T}, \tag{C.10}$$

the energy density could be linked to pressure:

$$T\frac{dp}{dT} = \rho + p \Longrightarrow dp = \frac{\rho + p}{T}dT, \tag{C.11}$$

together with Eq. C.9, we can obtain

$$dS = \frac{1}{T}d[(\rho + p)V] - (\rho + p)V\frac{dT}{T^2} = d\Big[\frac{(\rho + p)V}{T} + const\Big], \tag{C.12}$$

which implies that the entropy for per co-moving volume is $a^3(\rho + p)/T$. Then consider energy conservation Eq.B.22, we have

$$d\Big[\frac{(\rho + p)V}{T}\Big] = 0, \tag{C.13}$$

so for the entropy density $s = S/V$, one can obtain

$$s = \frac{\rho + p}{T} = \frac{2\pi^2}{45}gT^3. \tag{C.14}$$

C.2 Thermodynamics inside Magnetic Field

Due to the larger magnetic momentum of electrons and positrons compared with charged baryons, magnetic field could deviate the electrons and positrons thermodynamics dramatically. The thermodynamics of $e^{\pm}$ will be affected via *Landau quantization* (Kawasaki and Kusakabe, 2012):

$$n_{e^{\pm}} = \frac{eB}{(2\pi)^2}\sum_{n=0}^{\infty}(2 - \delta_{n0})\int_{-\infty}^{\infty} f_{FD}(E_B, T_\gamma)dp_z \tag{C.15}$$

$$\rho_{e^{\pm}} = \frac{eB}{(2\pi)^2}\sum_{n=0}^{\infty}(2 - \delta_{n0})\int_{-\infty}^{\infty} E_B f_{FD}(E_B, T_\gamma)dp_z \tag{C.16}$$

$$P_{e^{\pm}} = \frac{eB}{(2\pi)^2}\sum_{n=0}^{\infty}(2 - \delta_{n0})\int_{-\infty}^{\infty} \frac{E_B^2 - m_e^2}{3E_B} f_{FD}(E_B, T_\gamma)dp_z \tag{C.17}$$

here,f_{FD} is the *Fermi-Dirac distribution*, T_γ is the photon temperature, $E_B = p_z^2 + m_e^2 + 2neB$. $n_{e^{\pm}}$, $\rho_{e^{\pm}}$ and $P_{e^{\pm}}$ represents the number density,the energy density and the pressure of $e^{\pm}$ in the early universe. After neutrino decoupling, neutrinos became free particles so that their temperature decrease as $T_\nu \propto R^{-1}$ where R is the scale factor of the Universe. On the other hand, the conservation of energy requires

$$d[(\rho_{em} + P_{em})R^3] = R^3 dP_{em} \tag{C.18}$$

with $\rho_{em} = \rho_e + \rho_\gamma$ and $P_{em} = P_e + P_\gamma$ (here, ρ_e and P_e are the summation quantity for both electron and positron), after taking into account the magnetic field, the Hubble

expansion rate now reads

$$H = \frac{\dot{R}}{R} = \sqrt{\frac{8\pi G \rho_{tot}}{3}}, \tag{C.19}$$

where $\rho_{tot} = \rho_{em} + \rho_{PMF}$. The photon temperature as a function of time with the existence of magnetic field reads (Kernan, Starkman, and Vachaspati, 1996):

$$\frac{dT_\gamma}{dt} = -3H \frac{\rho_{em} + P_{em}}{d\rho_{em}/dT_\gamma}, \tag{C.20}$$

in this equation, the electron energy density and pressure are described as the formalism in C.15-C.16 as a function of magnetic field strength.

Appendix D

Hartree Approximation

D.1 Hartree Self-consistent Field Method

The Hamiltonian under the Heisenberg representation of the entire electron gas system is

$$H(t) = \int d^3x\psi^\dagger(x)\Big[c\alpha\cdot(p - e\mathbf{A^e}(\boldsymbol{x})) + \beta mc^2\Big]\psi(x) + \frac{1}{2}\int\int d^3x d^3x' \frac{\rho(\boldsymbol{x},t)\rho(\boldsymbol{x}',t)}{|\boldsymbol{x}-\boldsymbol{x}'|}. \tag{D.1}$$

The first term describes the electrons' motion in an external field $\mathbf{A}^{ext}(\boldsymbol{x},t)$, the second term is the electron self consistent interaction, $\rho(\boldsymbol{x},t)$ is the charge density at position $\boldsymbol{x}$ and is given by $e\psi^\dagger(\boldsymbol{x},t)\psi(\boldsymbol{x},t)$. The electrons' self-consistent potential $\mathbf{A}_0(x)$ follows the solution of Poisson equation:

$$\nabla^2 \boldsymbol{A}_0(\boldsymbol{x},t) = -\rho(\boldsymbol{x},t). \tag{D.2}$$

The solution of Eq.D.2 can be obtained by the inverse-Fourier transform of $\boldsymbol{A}_0(\boldsymbol{q},t)$:

$$\boldsymbol{A}_0(\boldsymbol{x},t) = \sum \boldsymbol{A}_0(\boldsymbol{q},t)e^{i\boldsymbol{q}\boldsymbol{x}}; \tag{D.3}$$

$$\boldsymbol{A}_0(\boldsymbol{q},t) = \frac{4\pi}{q^2}\rho(\boldsymbol{q},t). \tag{D.4}$$

The Fourier expansion of the charge density is given by

$$\rho(\boldsymbol{x},t) = \sum \rho(\boldsymbol{q},t)e^{i\boldsymbol{q}\boldsymbol{x}}; \tag{D.5}$$

$$\rho(\boldsymbol{q},t) = \frac{1}{V}\int d^3x\rho(\boldsymbol{x},t)e^{-i\boldsymbol{q}\boldsymbol{x}}. \tag{D.6}$$

Also, the term $\psi(\boldsymbol{x},t)$ can be expanded by the set of eigenfunctions $\psi_a(x)$ that satisfy the time-independent Dirac Hamiltonian:

$$H_D = c\alpha\cdot(p - e\mathbf{A^e}(\boldsymbol{x},\mathbf{t})) + \beta mc^2; H_D\psi_a(\boldsymbol{x}) = E_a\psi_a(\boldsymbol{x}), \tag{D.7}$$

here a denotes a set of quantum number $\{a\} = \{n,s\}$. Then the wave function $\psi(\boldsymbol{x},t)$ reads

$$\psi(\boldsymbol{x},t) = \sum C_a(t)\psi_a(\boldsymbol{x}). \tag{D.8}$$

Combine Eq.D.2, Eq.D.5 and Eq.D.8, we can rewrite the Hamiltonian $H(t)$ as

$$H(t) = \sum_a C_a^\dagger(t)C_a(t)E_a + \frac{1}{2}V\sum\rho(\boldsymbol{q},t)\rho(-\boldsymbol{q},t)\frac{4\pi}{q^2}, \tag{D.9}$$

Since the charge density is given by

$$\rho(\boldsymbol{x},t) = e\psi^{\dagger}(\boldsymbol{x},t)\psi(\boldsymbol{x},t), \tag{D.10}$$

then from Eq. D.6, $\rho(\boldsymbol{q},t)$ reads

$$\rho(\boldsymbol{q},t) = \frac{e}{V}\sum_{aa'}\langle a|e^{-i\boldsymbol{qx}}|a'\rangle C_a^{\dagger}(t)C_{a'}(t) \tag{D.11}$$

where

$$\langle a|e^{-i\boldsymbol{qx}}|a'\rangle = \int \psi_a^{\dagger}(\boldsymbol{x})\psi_a'(\boldsymbol{x})e^{-i\boldsymbol{qx}}d^3x. \tag{D.12}$$

From Eq. D.9, we can obtain the Heisenberg equations of $B(a,a',t) \equiv C_a^{\dagger}(t)C_a'(t)$ as

$$\begin{aligned}\frac{\partial B(a,a',t)}{\partial t} = -\frac{i}{\hbar}\Big[H(t),B(a,a',t)\Big] =& -\frac{i}{\hbar}(E_a'-E_a)B(a,a',t)\\ &-\frac{i}{2\hbar}\sum_q\sum_a\frac{4\pi e}{q^2}\Big\{\rho(\boldsymbol{q},t)\Big[\langle b'|e^{i\boldsymbol{qx}}|a\rangle B(b,a,t)\\ &-\langle a|e^{i\boldsymbol{qx}}|b\rangle B(a,b',t)\Big] + \Big[\langle b'|e^{-i\boldsymbol{qx}}|a\rangle B(b,a,t)\\ &-\langle a|e^{-i\boldsymbol{qx}}|b\rangle B(a,b',t)\Big]\rho(-\boldsymbol{q},t)\Big\}.\end{aligned} \tag{D.13}$$

The next step is to take the average observable quantities of each side. A generalized distribution function is defined as

$$F(b,b',t) = \langle B(b,b',t)\rangle = \sum_A P_A\langle A|C_b^{\dagger}(t)C_{b'}(t)|A\rangle, \tag{D.14}$$

where A is the complete set of plasma state, and P_A is the probability of finding the system with state A. Then the Heisenberg equation becomes

$$\begin{aligned}\frac{\partial F(b,b',t)}{\partial t} =& -\frac{i}{\hbar}(E_b'-E_b)F(b,b',t) - \frac{i}{2\hbar}\sum_q\sum_a\frac{4\pi e}{q^2}\\ &\times\Big\{\langle b'|e^{i\boldsymbol{qx}}|a\rangle\langle\rho(\boldsymbol{q},t)B(b,a,t)\rangle - \langle a|e^{i\boldsymbol{qx}}|b\rangle\langle\rho(\boldsymbol{q},t)B(a,b',t)]\rangle\\ &+\langle b'|e^{-i\boldsymbol{qx}}|a\rangle\langle\rho(\boldsymbol{q},t)B(b,a,t)\rangle - \langle a|e^{-i\boldsymbol{qx}}|b\rangle\langle\rho(\boldsymbol{q},t)B(a,b',t)\rangle\Big\}.\end{aligned} \tag{D.15}$$

Using the Hartree self-consistent field approximation (Hartree approximation):

$$\langle B(b,b',t)\rho(\boldsymbol{q},t)\rangle \sim \langle B(b,b',t)\rangle\langle\rho(\boldsymbol{q},t)\rangle = F(b,b',t)\rho(\boldsymbol{q},t), \tag{D.16}$$

and also the linear perturbation theory to $F(b,a,t)$ and $\rho(\boldsymbol{q},t)$ as

$$F(b,a,t) = \delta_{ab}F(a) + F_1(b,a,t) \tag{D.17}$$

$$\rho(\boldsymbol{q},t) = 0 + \rho_1(\boldsymbol{q},t), \tag{D.18}$$

where $F(a)$ is the Fermi-Dirac distribution. Applying

$$F(b,a,t)\rho(\boldsymbol{q},t) \sim \delta_{ab}F(a)\rho_1(\boldsymbol{q},t), \tag{D.19}$$

then Eq. D.13 becomes

$$\frac{\partial F_1(b',b,t)}{\partial t}+\frac{i}{\hbar}(E'_b-E_b)F_1(b,b',t)=\frac{i}{\hbar}[F(b')-F(b)]\sum_q\frac{4\pi e}{q^2}\langle b'|e^{i\boldsymbol{qx}}|b\rangle\rho(\boldsymbol{q},t). \tag{D.20}$$

Taking the Laplace transforms of D.20 gives us

$$\begin{aligned}&\omega F_1(b',b,\omega)-F_1(b',b,0)+\frac{i}{\hbar}(E'_b-E_b)F_1(b,b',\omega)\\&=\frac{i}{\hbar}[F(b')-F(b)]\sum_q\frac{4\pi e}{q^2}\langle b'|e^{i\boldsymbol{qx}}|b\rangle\rho(\boldsymbol{q},\omega),\end{aligned} \tag{D.21}$$

From Eqs. D.4 and D.11,

$$A_0(\boldsymbol{q},t)=\frac{e}{V}\sum_{aa'}\langle a|e^{-i\boldsymbol{qx}}|a'\rangle F_1(a,a',t) \tag{D.22}$$

so finally, the solution of Eq. D.20 is

$$\begin{aligned}A_0(\boldsymbol{q},\omega)=&\frac{4\pi ie}{Vq^2}\sum_{aa'}\frac{\langle a|e^{-i\boldsymbol{qx}}|a'\rangle F(a,a',0)}{\omega-(E'_a-E_a)/\hbar}\\&-\frac{F(a')-F(a)}{\omega-(E'_a-E_a)/\hbar}\frac{4\pi e^2}{Vq^2}\sum_{aa'}\sum_{q'}\Big[\langle a'|e^{i\boldsymbol{q}'\boldsymbol{x}'}|a\rangle A_0(\boldsymbol{q}',\omega)\Big].\end{aligned} \tag{D.23}$$

the second term can be taken as

$$\frac{F(a')-F(a)}{\omega-(E'_a-E_a)/\hbar}\frac{4\pi e^2}{Vq^2}\sum_{aa'}|\langle a'|e^{i\boldsymbol{qx}'}|a\rangle|^2A_0(\boldsymbol{q},\omega) \tag{D.24}$$

so finally we have

$$A_0(\boldsymbol{q},\omega)=\frac{1}{\epsilon(\boldsymbol{q},\omega)}\frac{4\pi ie}{Vq^2}\sum_{aa'}\frac{\langle a|e^{-i\boldsymbol{qx}}|a'\rangle F(a,a',0)}{\hbar\omega-(E'_a-E_a)}, \tag{D.25}$$

where $\epsilon(\boldsymbol{q},\omega)$ is the longitudinal dielectric function written as

$$\epsilon(\boldsymbol{q},\omega)=1+\frac{4\pi e^2}{Vq^2}\sum_{aa'}\frac{|\langle a'|e^{i\boldsymbol{qx}'}|a\rangle|^2}{\hbar\omega-(E'_a-E_a)}[F(a')-F(a)]. \tag{D.26}$$

D.2 Fermi Energy of Strongly Magnetized Degenerate Plasma

Inside strongly magnetized degenerate plasma, the momentum of test charge along with magnetic field q_z cannot exceed the Fermi momentum $p_F(n,\sigma)$:

$$\sqrt{E_F^2-E_0^2-e\hbar cB(2n-\sigma+1)}, \tag{D.27}$$

all the electrons should have energy that $E\leq E_F$, i.e.,

$$-\sqrt{E_F^2-E_0^2-2e\hbar cBn}/c\leq p_z\leq\sqrt{E_F^2-E_0^2-2e\hbar cBn}, \tag{D.28}$$

also,

$$\begin{aligned} F(n,\sigma,p_z) =& 0 \quad if \;\; E(n,\sigma,p_z) > E_F \\ =& 1 \quad if \;\; E(n,\sigma,p_z) \leq E_F. \end{aligned}$$

Moreover, within the magnetic field background, there is no positron exists, Fermi energy E_F also is a function of field strength: the charge density of the plasma is given by $\rho = (N_+ + N_-)/V$ where $N_+(N_-)$ stands for the number of electrons with spin up(down). We have:

$$\begin{aligned} \frac{N_+}{V} =& \frac{m\omega_c}{(2\pi\hbar)^2} \cdot \int_0^\infty dp_z \sum_{n=0}^{n_{max}} F(n,p_z,1) \\ =& \frac{m\omega_c}{(2\pi\hbar)^2} \cdot 2 \sum_{n=0}^{n_{max}} p_F(n,p_z,1) \\ =& \frac{m\omega_c}{(2\pi\hbar)^2} \cdot 2 \sum_{n=0}^{n_{max}} \sqrt{E_F^2 - E_0^2 - 2e\hbar cBn}/c \end{aligned} \tag{D.29}$$

and similarly:

$$\frac{N_-}{V} = \frac{m\omega_c}{(2\pi\hbar)^2} \cdot 2 \sum_{n=0}^{n_{max}} \sqrt{E_F^2 - E_0^2 - 2e\hbar cB(n+1)}/c. \tag{D.30}$$

The requirement of charge conservation fix the ρ, so that we have

$$\rho = \frac{2m\omega_c}{(2\pi\hbar)^2 c} \left[(E_F^2 - E_0^2)^{1/2} + 2 \sum_{n=1}^{n_{max}} \sqrt{E_F^2 - E_0^2 - 2e\hbar cBn} \right] \tag{D.31}$$

and n_{max} is given by

$$[E_0^2 + 2e\hbar cBn_{max}] < E_F^2 < [E_0^2 + 2e\hbar cB(n_{max}+1)] \tag{D.32}$$

because $E_F^2 - E_0^2 - 2e\hbar cBn$ should be non-negative.

Bibliography

Abbott, B. P. et al. (2017). "GW170817: Observation of Gravitational Waves from a Binary Neutron Star Inspiral". In: *Phys. Rev. Lett.* 119.16, p. 161101. DOI: 10.1103/PhysRevLett.119.161101. arXiv: 1710.05832 [gr-qc].

Abbott, B. P. et al. (2017). "Multi-messenger Observations of a Binary Neutron Star Merger". In: *Astrophys. J. Lett.* 848.2, L12, p. L12. DOI: 10.3847/2041-8213/aa91c9. arXiv: 1710.05833 [astro-ph.HE].

Adahchour, Abderrahim and Pierre Descouvemont (2003). "R-matrix analysis of the3He(n, p)3H and7Be(n, p)7Li reactions". In: *J. Phys. G: Nucl. Part. Phys.* 29.2, pp. 395–403. DOI: 10.1088/0954-3899/29/2/315. URL: https://doi.org/10.1088/0954-3899/29/2/315.

Adamek, Julian et al. (2011). "A large scale coherent magnetic field: interactions with free streaming particles and limits from the CMB". In: *J. Cosmol. Astropart. Phys.* 2011.6, 017, p. 017. DOI: 10.1088/1475-7516/2011/06/017. arXiv: 1102.5235 [astro-ph.CO].

Adelberger, E. G. et al. (1998). "Solar fusion cross sections". In: *Rev. Mod. Phys.* 70, pp. 1265–1291. DOI: 10.1103/RevModPhys.70.1265. eprint: astro-ph/9805121.

Aghanim, N. et al. (2020). "Planck 2018 results. VI. Cosmological parameters". In: *Astron. Astrophys.* 641, A6. DOI: 10.1051/0004-6361/201833910. arXiv: 1807.06209 [astro-ph.CO].

Aguado, David S. et al. (2019). "Back to the Lithium Plateau with J0023+0307 with [Fe/H]<-6". In: *Astrophys. J. Lett.* 874, p. L21. DOI: 10.3847/2041-8213/ab1076. arXiv: 1904.04892 [astro-ph.SR].

Akhiezer, A. I. et al. (1975). "Plasma electrodynamics. Volume 1 - Linear theory. Volume 2 - Non-linear theory and fluctuations". In: *Oxford Pergamon Press International Series on Natural Philosophy* 1.

Alastuey, A. and B. Jancovici (1978). "Nuclear reaction rate enhancement in dense stellar matter". In: *Astrophys. J.* 226, pp. 1034–1040. DOI: 10.1086/156681.

Alcock, C., G. M. Fuller, and G. J. Mathews (1987). "The Quark - hadron phase transition and primordial nucleosynthesis". In: *Astrophys. J.* 320, pp. 439–447. DOI: 10.1086/165560.

Alford, W. P. et al. (1990). "Gamow-teller Strength Observed in the ^{48}Ti (n, p) ^{48}Sc Reaction: Implications for the Double Beta Decay of ^{48}Ca". In: *Nucl. Phys. A* 514, pp. 49–65. DOI: 10.1016/0375-9474(90)90331-F.

— (1993). "Spin-isospin strength distributions in f-p shell nuclei: A study of the V-51 (n, p) and Co-59 (n, p) reactions at 198 MeV". In: *Phys. Rev. C* 48, pp. 2818–2827. DOI: 10.1103/PhysRevC.48.2818.

Alpher, R. A., H. Bethe, and G. Gamow (1948). "The origin of chemical elements". In: *Phys. Rev.* 73, pp. 803–804. DOI: 10.1103/PhysRev.73.803.

Angulo, C. et al. (2005). "The $Be^7(d,p)2\alpha$ cross section at big bang energies and the primordial Li^7 abundances". In: *Astrophys. J. Lett.* 630, pp. L105–L108. DOI: 10.1086/491732. arXiv: astro-ph/0508454.

Aoki, Wako, Hiroko Ito, and Akito Tajitsu (2012). "Examination of the mass-dependent Li depletion hypothesis by the Li abundances of the very metal-poor double-lined spectroscopic binary G166-45". In: *Astrophys. J. Lett.* 751, p. L6. DOI: 10.1088/2041-8205/751/1/L6. arXiv: 1204.3952 [astro-ph.SR].

Applegate, J. H., C. J. Hogan, and R. J. Scherrer (1987). "Cosmological Baryon Diffusion and Nucleosynthesis". In: *Phys. Rev. D* 35, pp. 1151–1160. DOI: 10.1103/PhysRevD.35.1151.

Arbey, A. and F. Mahmoudi (2008). "SUSY constraints from relic density: High sensitivity to pre-BBN expansion rate". In: *Phys. Lett. B* 669, pp. 46–51. DOI: 10.1016/j.physletb.2008.09.032. arXiv: 0803.0741 [hep-ph].

Arcones, A., G. Martinez-Pinedo, and S. E. Woosley (2010). "Electron fraction constraints based on Nuclear Statistical Equilibrium with beta equilibrium". In: *Astron. Astrophys.* 522, A25. DOI: 10.1051/0004-6361/201014276. arXiv: 1002.3854 [astro-ph.SR].

Arlandini, C. et al. (1999). "Neutron capture in low mass asymptotic giant branch stars: cross-sections and abundance signatures". In: *Astrophys. J.* 525, pp. 886–900. DOI: 10.1086/307938. arXiv: astro-ph/9906266.

Aver, Erik, Keith A. Olive, and Evan D. Skillman (2010). "A New Approach to Systematic Uncertainties and Self-Consistency in Helium Abundance Determinations". In: *J. Cosmol. Astropart. Phys.* 05, p. 003. DOI: 10.1088/1475-7516/2010/05/003. arXiv: 1001.5218 [astro-ph.CO].

— (2015). "The effects of He I λ10830 on helium abundance determinations". In: *J. Cosmol. Astropart. Phys.* 07, p. 011. DOI: 10.1088/1475-7516/2015/07/011. arXiv: 1503.08146 [astro-ph.CO].

Bahcall, J.N. (1989). *Neutrino Astrophysics*. Cambridge University Press. ISBN: 9780521379755.

Banerjee, Robi and Karsten Jedamzik (2004). "The Evolution of cosmic magnetic fields: From the very early universe, to recombination, to the present". In: *Phys. Rev. D* 70, p. 123003. DOI: 10.1103/PhysRevD.70.123003. arXiv: astro-ph/0410032.

Bania, T. M., Robert T. Rood, and Dana S. Balser (2002). "The cosmological density of baryons from observations of 3He+ in the Milky Way". In: *Nature* 415, pp. 54–57. DOI: 10.1038/415054a.

Barbagallo, M. et al. (2016). "^{7}Be$(n,\alpha)^4$He Reaction and the Cosmological Lithium Problem: Measurement of the Cross Section in a Wide Energy Range at n_TOF at CERN". In: *Phys. Rev. Lett.* 117.15, p. 152701. DOI: 10.1103/PhysRevLett.117.152701. arXiv: 1606.09420 [nucl-ex].

Baumann, Daniel (2009). "TASI Lectures on Inflation". In: *arXiv*. arXiv: 0907.5424v2.

Baym, Gordon and Henning Heiselberg (1997). "The Electrical conductivity in the early universe". In: *Phys. Rev. D* 56, pp. 5254–5259. DOI: 10.1103/PhysRevD.56.5254. arXiv: astro-ph/9704214.

Beck, Christian (2001). "Dynamical foundations of nonextensive statistical mechanics". In: *Phys. Rev. Lett.* 87, p. 180601. DOI: 10.1103/PhysRevLett.87.180601. arXiv: cond-mat/0105374.

Bennett, C. L. et al. (2013). "Nine-Year Wilkinson Microwave Anisotropy Probe (WMAP) Observations: Final Maps and Results". In: *Astrophys. J. Suppl.* 208, p. 20. DOI: 10.1088/0067-0049/208/2/20. arXiv: 1212.5225 [astro-ph.CO].

Bernui, Armando, Constantino Tsallis, and Thyrso Villela (2007). "Deviation from Gaussianity in the cosmic microwave background temperature fluctuations". In: *EPL* 78.1, p. 19001. DOI: 10.1209/0295-5075/78/19001. arXiv: astro-ph/0703708.

Bertone, Serena, Corina Vogt, and Torsten Ensslin (2006). "Magnetic Field Seeding by Galactic Winds". In: *Mon. Notices Royal Astron. Soc.* 370, pp. 319–330. DOI: 10.1111/j.1365-2966.2006.10474.x. arXiv: astro-ph/0604462.

Bertulani, C. A., J. Fuqua, and M. S. Hussein (2013). "Big Bang nucleosynthesis with a non-Maxwellian distribution". In: *Astrophys. J.* 767, p. 67. DOI: 10.1088/0004-637X/767/1/67. arXiv: 1205.4000 [nucl-th].

Bertulani, C. A. and T. Kajino (2016). "Frontiers in Nuclear Astrophysics". In: *Prog. Part. Nucl. Phys.* 89, pp. 56–100. DOI: 10.1016/j.ppnp.2016.04.001. arXiv: 1604.03197 [nucl-th].

Bethe, H. A. (1949). "Theory of the Effective Range in Nuclear Scattering". In: *Phys. Rev.* 76, pp. 38–50. DOI: 10.1103/PhysRev.76.38.

— (1990). "Supernova mechanisms". In: *Rev. Mod. Phys.* 62, pp. 801–866. DOI: 10.1103/RevModPhys.62.801.

Bethe, H. A. and Conrad Longmire (1950). "The effective range of nuclear forces 2. photo-disintegration of the deuteron". In: *Phys. Rev.* 77, pp. 647–654. DOI: 10.1103/PhysRev.77.647.

Beun, J. et al. (2008). "Fission cycling in a supernova *r* process". In: *Phys. Rev. C* 77 (3), p. 035804. DOI: 10.1103/PhysRevC.77.035804.

Biermann, L. (1950). "Über den Ursprung der Magnetfelder auf Sternen und im interstellaren Raum (miteinem Anhang von A. Schlüter)". In: *Zeitschrift Naturforschung Teil A* 5, p. 65.

Bird, Chris, Kristen Koopmans, and Maxim Pospelov (2008). "Primordial Lithium Abundance in Catalyzed Big Bang Nucleosynthesis". In: *Phys. Rev. D* 78, p. 083010. DOI: 10.1103/PhysRevD.78.083010. arXiv: hep-ph/0703096.

Bjorken, J.D. and S.D. Drell (1964). *Relativistic Quantum Mechanics*. International series in pure and applied physics. McGraw-Hill. ISBN: 9780070054936.

Blatt, John M. and J. David Jackson (1949). "On the Interpretation of Neutron-Proton Scattering Data by the Schwinger Variational Method". In: *Phys. Rev.* 76, pp. 18–37. DOI: 10.1103/PhysRev.76.18.

Bonifacio, P. and P. Molaro (1997). "The Primordial lithium abundance". In: *Mon. Notices Royal Astron. Soc.* 285, pp. 847–861. DOI: 10.1093/mnras/285.4.847. arXiv: astro-ph/9611043.

Bonifacio, P. et al. (2018). "TOPoS - IV. Chemical abundances from high-resolution observations of seven extremely metal-poor stars". In: *Astron. Astrophys.* 612, A65. DOI: 10.1051/0004-6361/201732320. arXiv: 1801.03935 [astro-ph.SR].

Born, Max (1949). "Reciprocity Theory of Elementary Particles". In: *Rev. Mod. Phys.* 21.3, pp. 463–473. DOI: 10.1103/RevModPhys.21.463.

Braginskii, S. I. (1965). "Transport Processes in a Plasma". In: *Rev. Mod. Plasma Phys.* 1, p. 205.

Brandenburg, Axel (2001). "The Inverse cascade and nonlinear alpha-effect in simulations of isotropic helical hydromagnetic turbulence". In: *Astrophys. J.* 550, pp. 824–840. DOI: 10.1086/319783. arXiv: astro-ph/0006186.

Brandenburg, Axel, Kari Enqvist, and Poul Olesen (1996). "Large scale magnetic fields from hydromagnetic turbulence in the very early universe". In: *Phys. Rev. D* 54, pp. 1291–1300. DOI: 10.1103/PhysRevD.54.1291. arXiv: astro-ph/9602031.

Brandenburg, Axel and Kandaswamy Subramanian (2005). "Astrophysical magnetic fields and nonlinear dynamo theory". In: *Phys. Rept.* 417, pp. 1–209. DOI: 10.1016/j.physrep.2005.06.005. arXiv: astro-ph/0405052.

Bravo, E. and D. García-Senz (1999). "Coulomb corrections to the equation of state of nuclear statistical equilibrium matter: implications for SNIa nucleosynthesis and

the accretion-induced collapse of white dwarfs". In: *Mon. Notices Royal Astron. Soc.* 307.4, pp. 984–992. DOI: 10.1046/j.1365-8711.1999.02694.x.

Brune, C. R., R. W. Kavanagh, and C. Rolfs (1994). "H-3 (alpha, gamma) Li-7 reaction at low energies". In: *Phys. Rev. C* 50, pp. 2205–2218. DOI: 10.1103/PhysRevC.50.2205.

Brune, C. R. et al. (1999). "Total cross-section of the H-3 (p, n) He-3 reaction from threshold to 4.5-MeV". In: *Phys. Rev. C* 60, p. 015801. DOI: 10.1103/PhysRevC.60.015801. arXiv: nucl-ex/9902010.

Burbidge, Margaret E. et al. (1957). "Synthesis of the elements in stars". In: *Rev. Mod. Phys.* 29, pp. 547–650. DOI: 10.1103/RevModPhys.29.547.

Burrows, Adam, John Hayes, and Bruce A. Fryxell (1995). "On the Nature of Core-Collapse Supernova Explosions". In: *Astrophys. J.* 450, p. 830. DOI: 10.1086/176188. arXiv: astro-ph/9506061 [astro-ph].

Burrows, Adam et al. (2000). "A New Algorithm for Supernova Neutrino Transport and Some Applications". In: *Astrophys. J.* 539.2, pp. 865–887. DOI: 10.1086/309244. arXiv: astro-ph/9905132 [astro-ph].

Cameron, A. G. W., J. J. Cowan, and J. W. Truran (1983). "The Waiting Point Approximation in R-Process Calculations". In: *Astrophys. Space Sci.* 91.2, pp. 235–243. DOI: 10.1007/BF00656112.

Cameron, A. G. W. et al. (1983). "Steady Flow Approximations to the Helium R-Process". In: *Astrophys. Space Sci.* 91.2, pp. 221–234. DOI: 10.1007/BF00656111.

Caprini, Chiara, Ruth Durrer, and Geraldine Servant (2009). "The stochastic gravitational wave background from turbulence and magnetic fields generated by a first-order phase transition". In: *J. Cosmol. Astropart. Phys.* 12, p. 024. DOI: 10.1088/1475-7516/2009/12/024. arXiv: 0909.0622 [astro-ph.CO].

Caprini, Chiara et al. (2009). "The cosmic microwave background temperature bispectrum from scalar perturbations induced by primordial magnetic fields". In: *J. Cosmol. Astropart. Phys.* 06, p. 021. DOI: 10.1088/1475-7516/2009/06/021. arXiv: 0903.1420 [astro-ph.CO].

Carlson, J. and R. Schiavilla (1998). "Structure and Dynamics of Few Nucleon Systems". In: *Rev. Mod. Phys.* 70, pp. 743–842. DOI: 10.1103/RevModPhys.70.743.

Casella, C. et al. (2002). "First measurement of the d(p,γ) ^{3}He cross section down to the solar Gamow peak". In: *Nucl. Phys.* 706.1, pp. 203–216. DOI: 10.1016/S0375-9474(02)00749-2.

Caurier, E. et al. (1999). "Shell model calculations of stellar weak interaction rates. 1. Gamow-Teller distributions and spectra of nuclei in the mass range A = 45 - 65". In: *Nucl. Phys. A* 653, pp. 439–452. DOI: 10.1016/S0375-9474(99)00240-7. arXiv: nucl-th/9903042.

Chakraborty, Nachiketa, Brian D. Fields, and Keith A. Olive (2011). "Resonant Destruction as a Possible Solution to the Cosmological Lithium Problem". In: *Phys. Rev. D* 83, p. 063006. DOI: 10.1103/PhysRevD.83.063006. arXiv: 1011.0722 [astro-ph.CO].

Cheng, B., D. N. Schramm, and J. W. Truran (1993). "Interaction rates at high magnetic field strengths and high degeneracy". In: *Phys. Lett. B* 316, pp. 521–527. DOI: 10.1016/0370-2693(93)91038-O. arXiv: astro-ph/9308035.

Cheng, Baolian, David N. Schramm, and James W. Truran (1994). "Constraints on the strength of a primordial magnetic field from big bang nucleosynthesis". In: *Phys. Rev. D* 49.10, pp. 5006–5018. DOI: 10.1103/PhysRevD.49.5006. arXiv: astro-ph/9308041 [astro-ph].

Christensson, Mattias, Mark Hindmarsh, and Axel Brandenburg (2001). "Inverse cascade in decaying three-dimensional magnetohydrodynamic turbulence". In:

Phys. Rev. E 64.5, p. 056405. DOI: 10.1103/PhysRevE.64.056405. arXiv: astro-ph/0011321 [astro-ph].

Civitarese, O. and M. E. Mosquera (2013). "Nuclear structure constrains on resonant energies: A solution of the cosmological Li-7 problem?" In: *Nucl. Phys. A* 898, pp. 1–13. DOI: 10.1016/j.nuclphysa.2012.11.012.

Clayton, Donald D. (1983). *Principles of Stellar Evolution and Nucleosynthesis*. The University of Chicago Press (Chicago), pp. 357 –359.

Coc, Alain and Elisabeth Vangioni (2017). "Primordial nucleosynthesis". In: *Int. J. Mod. Phys. E* 26.08, p. 1741002. DOI: 10.1142/S0218301317410026. arXiv: 1707.01004 [astro-ph.CO].

Coc, Alain et al. (2004). "Updated Big Bang Nucleosynthesis Compared with Wilkinson Microwave Anisotropy Probe Observations and the Abundance of Light Elements". In: *Astrophys. J.* 600.2, pp. 544–552. DOI: 10.1086/380121. arXiv: astro-ph/0309480 [astro-ph].

Coc, Alain et al. (2012). "Standard Big-Bang Nucleosynthesis up to CNO with an improved extended nuclear network". In: *Astrophys. J.* 744, p. 158. DOI: 10.1088/0004-637X/744/2/158. arXiv: 1107.1117 [astro-ph.CO].

Coc, Alain et al. (2015). "New reaction rates for improved primordial D/H calculation and the cosmic evolution of deuterium". In: *Phys. Rev. D* 92.12, p. 123526. DOI: 10.1103/PhysRevD.92.123526. arXiv: 1511.03843 [astro-ph.CO].

Combes, F. and T. Wiklind (1998). "Search for LiH in the ISM towards B0218+357". In: *Astron. Astrophys.* 334, pp. L81–L84. arXiv: astro-ph/9804303 [astro-ph].

Cooke, Ryan J., Max Pettini, and Charles C. Steidel (2018). "One Percent Determination of the Primordial Deuterium Abundance". In: *Astrophys. J.* 855.2, p. 102. DOI: 10.3847/1538-4357/aaab53. arXiv: 1710.11129 [astro-ph.CO].

Cooperstein, J. and J. Wambach (1984). "Electron capture in stellar collapse". In: *Nucl. Phys. A* 420, pp. 591–620. DOI: 10.1016/0375-9474(84)90673-0.

Couch, R. G. and G. L. Loumos (Dec. 1974). "The Urca process in dense stellar interiors." In: *Astrophys. J.* 194, pp. 385–392. DOI: 10.1086/153255.

Cyburt, R. H. and B. Davids (Dec. 2008). "Evaluation of modern He3(α, γ)Be7 data". In: *Phys. Rev. C* 78.6, 064614, p. 064614. DOI: 10.1103/PhysRevC.78.064614. arXiv: 0809.3240 [nucl-ex].

Cyburt, Richard H., Brian D. Fields, and Keith A. Olive (2003). "Primordial nucleosynthesis in light of WMAP". In: *Phys. Lett. B* 567.3-4, pp. 227–234. DOI: 10.1016/j.physletb.2003.06.026. arXiv: astro-ph/0302431 [astro-ph].

Cyburt, Richard H. et al. (2010). "The JINA REACLIB Database: Its Recent Updates and Impact on Type-I X-ray Bursts". In: *Astrophys. J., Suppl. Ser.* 189.1, pp. 240–252. DOI: 10.1088/0067-0049/189/1/240.

Cyburt, Richard H. et al. (2016). "Big Bang Nucleosynthesis: 2015". In: *Rev. Mod. Phys.* 88, p. 015004. DOI: 10.1103/RevModPhys.88.015004. arXiv: 1505.01076 [astro-ph.CO].

Damone, L. et al. (2018). "^{7}Be(n,p)^{7}Li Reaction and the Cosmological Lithium Problem: Measurement of the Cross Section in a Wide Energy Range at n_TOF at CERN". In: *Phys. Rev. Lett.* 121.4, p. 042701. DOI: 10.1103/PhysRevLett.121.042701. arXiv: 1803.05701 [nucl-ex].

Daugherty, J. K. and A. K. Harding (1983). "Pair production in superstrong magnetic fields." In: *Astrophys. J.* 273, pp. 761–773. DOI: 10.1086/161411.

Davies, R. D. (May 1968). "Structure of the Galactic Magnetic Field". In: *Nature* 218.5140, pp. 435–437. DOI: 10.1038/218435a0.

Davies, R. D., R. S. Booth, and A. J. Wilson (1968). "Interstellar Magnetic Fields determined from Zeeman Effect Measurements". In: *Nature* 220.5173, pp. 1207–1210. DOI: 10.1038/2201207a0.

Delsante, A.E. and N.E. Frankel (1978). "Relativistic degenerate electron plasma in an intense magnetic field". In: *Phys. Lett. A* 67.4, pp. 279–281. DOI: 10.1016/0375-9601(78)90303-1.

— (1980). "Dielectric response of a relativistic degenerate electron plasma in a strong magnetic field". In: *Annals of Physics* 125.1, pp. 135–175. DOI: https://doi.org/10.1016/0003-4916(80)90122-0.

Demozzi, Vittoria, Viatcheslav Mukhanov, and Hector Rubinstein (2009). "Magnetic fields from inflation?" In: *J. Cosmol. Astropart. Phys.* 08, p. 025. DOI: 10.1088/1475-7516/2009/08/025. arXiv: 0907.1030 [astro-ph.CO].

Dendy, R.O. (1990). *Plasma Dynamics*. Oxford science publications. Clarendon Press. ISBN: 9780198520412.

Descouvemont, Pierre et al. (2004). "Compilation and R-matrix analysis of Big Bang nuclear reaction rates". In: *Atom. Data Nucl. Data Tabl.* 88, pp. 203–236. DOI: 10.1016/j.adt.2004.08.001. arXiv: astro-ph/0407101.

Dettmann, C. P., N. E. Frankel, and V. Kowalenko (1993). "Plasma electrodynamics in the expanding Universe". In: *Phys. Rev. D* 48, pp. 5655–5667. DOI: 10.1103/PhysRevD.48.5655.

Dewitt, H. E., H. C. Graboske, and M. S. Cooper (1973). "Screening Factors for Nuclear Reactions. I. General Theory". In: *Astrophys. J.* 181, pp. 439–456. DOI: 10.1086/152061.

Dimopoulos, Konstantinos and Anne-Christine Davis (1997). "On the evolution of primordial magnetic fields". In: *Phys. Lett. B* 390, pp. 87–96. DOI: 10.1016/S0370-2693(96)01366-4. arXiv: astro-ph/9610013.

Dolgov, A. (1993). "Breaking of conformal invariance and electromagnetic field generation in the universe". In: *Phys. Rev. D* 48, pp. 2499–2501. DOI: 10.1103/PhysRevD.48.2499. arXiv: hep-ph/9301280.

Dolgov, Alexander D. and Dario Grasso (2002). "Generation of cosmic magnetic fields and gravitational waves at neutrino decoupling". In: *Phys. Rev. Lett.* 88, p. 011301. DOI: 10.1103/PhysRevLett.88.011301. arXiv: astro-ph/0106154.

Durrer, R., P. G. Ferreira, and T. Kahniashvili (2000). "Tensor microwave anisotropies from a stochastic magnetic field". In: *Phys. Rev. D* 61, p. 043001. DOI: 10.1103/PhysRevD.61.043001. arXiv: astro-ph/9911040.

Durrer, Ruth and Andrii Neronov (2013). "Cosmological magnetic fields: their generation, evolution and observation". In: *Astron. Astrophys. Rev.* 21, 62, p. 62. DOI: 10.1007/s00159-013-0062-7. arXiv: 1303.7121 [astro-ph.CO].

Einstein, Albert (Jan. 1948). "A Generalized Theory of Gravitation". In: *Rev. Mod. Phys.* 20.1, pp. 35–39. DOI: 10.1103/RevModPhys.20.35.

Esmailzadeh, Rahim, Glenn D. Starkman, and Savas Dimopoulos (Sept. 1991). "Primordial Nucleosynthesis without a Computer". In: *Astrophys. J.* 378, p. 504. DOI: 10.1086/170452.

Esposito, S. et al. (2000). "Nonequilibrium spectra of degenerate relic neutrinos". In: *Nucl. Phys. B* 590, pp. 539–561. DOI: 10.1016/S0550-3213(00)00554-X. arXiv: astro-ph/0005573.

Famiano, Michael et al. (Aug. 2020). "Nuclear Reaction Screening, Weak Interactions, and r-process Nucleosynthesis in High Magnetic Fields". In: *Astrophys. J.* 898.2, 163, p. 163. DOI: 10.3847/1538-4357/aba04d. arXiv: 2006.14148 [astro-ph.HE].

Famiano, Michael A., A. Baha Balantekin, and Toshitaka Kajino (2016). "Low-lying Resonances and Relativistic Screening in Big Bang Nucleosynthesis". In: *Phys.*

Rev. C 93.4, p. 045804. DOI: 10.1103/PhysRevC.93.045804. arXiv: 1603.03137 [astro-ph.CO].

Fassio-Canuto, L. (1969). "Neutron Beta Decay in a Strong Magnetic Field". In: *Phys. Rev.* 187 (5), pp. 2141–2146. DOI: 10.1103/PhysRev.187.2141. URL: https://link.aps.org/doi/10.1103/PhysRev.187.2141.

Feng, Jonathan L., Arvind Rajaraman, and Fumihiro Takayama (2003). "Superweakly interacting massive particle dark matter signals from the early Universe". In: *Phys. Rev. D* 68.6, 063504, p. 063504. DOI: 10.1103/PhysRevD.68.063504. arXiv: hep-ph/0306024 [hep-ph].

Fields, Brian D. and Keith A. Olive (Oct. 2006). "Big bang nucleosynthesis". In: *Nucl. Phys. A* 777, pp. 208–225. DOI: 10.1016/j.nuclphysa.2004.10.033.

Fowler, William A., Georgeanne R. Caughlan, and Barbara A. Zimmerman (Jan. 1967). "Thermonuclear Reaction Rates". In: *Annu. Rev. Astron. Astrophys.* 5, p. 525. DOI: 10.1146/annurev.aa.05.090167.002521.

Friedan, Daniel, Zongan Qiu, and Stephen Shenker (Apr. 1984). "Conformal Invariance, Unitarity, and Critical Exponents in Two Dimensions". In: *Phys. Rev. Lett.* 52.18, pp. 1575–1578. DOI: 10.1103/PhysRevLett.52.1575.

Friedmann, A. (Jan. 1922). "Über die Krümmung des Raumes". In: *Zeitschrift fur Physik* 10, pp. 377–386. DOI: 10.1007/BF01332580.

Fu, X. et al. (Feb. 2018). "The Gaia-ESO Survey: Lithium enrichment histories of the Galactic thick and thin disc". In: *Astron. Astrophys.* 610, A38, A38. DOI: 10.1051/0004-6361/201731677. arXiv: 1711.04829 [astro-ph.GA].

Fu, Xiaoting et al. (Sept. 2015). "Lithium evolution in metal-poor stars: from pre-main sequence to the Spite plateau". In: *Mon. Not. Royal Astron. Soc.* 452.3, pp. 3256–3265. DOI: 10.1093/mnras/stv1384. arXiv: 1506.05993 [astro-ph.SR].

Fuller, G. M., W. A. Fowler, and M. J. Newman (1980). "Stellar weak-interaction rates for sd-shell nuclei. I - Nuclear matrix element systematics with application to Al-26 and selected nuclei of importance to the supernova problem". In: *Astrophys. J., Suppl. Ser.* 42, pp. 447–473. DOI: 10.1086/190657.

— (1982a). "Stellar weak interaction rates for intermediate-mass nuclei. II - A = 21 to A = 60". In: *Astrophys. J.* 252, pp. 715–740. DOI: 10.1086/159597.

— (1982b). "Stellar weak interaction rates for intermediate mass nuclei. III - Rate tables for the free nucleons and nuclei with A = 21 to A = 60". In: *Astrophys. J., Suppl. Ser.* 48, pp. 279–319. DOI: 10.1086/190779.

— (1985). "Stellar weak interaction rates for intermediate-mass nuclei. IV - Interpolation procedures for rapidly varying lepton capture rates using effective log (ft)-values". In: *Astrophys. J.* 293, pp. 1–16. DOI: 10.1086/163208.

Fuller, G. M., G. J. Mathews, and C. R. Alcock (1988). "Quark-hadron phase transition in the early Universe: Isothermal baryon-number fluctuations and primordial nucleosynthesis". In: *Phys. Rev. D* 37.6, pp. 1380–1400. DOI: 10.1103/PhysRevD.37.1380.

Furlanetto, Steven R. and Abraham Loeb (Jan. 2002). "Intergalactic Magnetic Fields from Quasar Outflows". In: *Lighthouses of the Universe: The Most Luminous Celestial Objects and Their Use for Cosmology*. Ed. by Marat Gilfanov, Rashid Sunyeav, and Eugene Churazov, p. 450. DOI: 10.1007/10856495_64. arXiv: astro-ph/0110090 [astro-ph].

Gailis, R. M., N. E. Frankel, and C. P. Dettmann (1995). "Magnetohydrodynamics in the expanding Universe". In: *Phys. Rev. D* 52.12, p. 6901. DOI: 10.1103/PhysRevD.52.6901.

Gailis, R. M. et al. (1994). "Magnetized plasmas in the early universe". In: *Phys. Rev. D* 50.6, pp. 3847–3858. DOI: 10.1103/PhysRevD.50.3847.

García-Berro, Enrique, Claudio Ritossa, and Jr. Iben Icko (1997). "On the Evolution of Stars that Form Electron-Degenerate Cores Processed by Carbon Burning. III. The Inward Propagation of a Carbon-Burning Flame and Other Properties of a 9 M Model Star". In: *Astrophys. J.* 485.2, pp. 765–784. DOI: 10.1086/304444.

Georgi, Howard and S. L. Glashow (1974). "Unity of All Elementary-Particle Forces". In: *Phys. Rev. Lett.* 32.8, pp. 438–441. DOI: 10.1103/PhysRevLett.32.438.

Gervais, J. L. and B. Sakita (1971). "Field theory interpretation of supergauges in dual models". In: *Nucl. Phys. B* 34, p. 632.

Glauber, R. J. et al. (1956). "Relativistic and Screening Effects in Radiative Electron Capture". In: *Phys. Rev.* 101, pp. 905–905. DOI: 10.1103/PhysRev.101.905.

Goodman, C. D. et al. (1980). "Gamow-Teller Matrix Elements from 0-degrees (p, n) Cross Sections". In: *Phys. Rev. Lett.* 44, pp. 1755–1759. DOI: 10.1103/PhysRevLett.44.1755.

Graboske, H. C. et al. (1973). "Screening Factors for Nuclear Reactions. II. Intermediate Screen-Ing and Astrophysical Applications". In: *Astrophys. J.* 181, pp. 457–474. DOI: 10.1086/152062.

Grasso, Dario and Antonio Riotto (1998). "On the nature of the magnetic fields generated during the electroweak phase transition". In: *Phys. Lett. B* 418, pp. 258–265. DOI: 10.1016/S0370-2693(97)01224-0. arXiv: hep-ph/9707265.

Grasso, Dario and H. R. Rubinstein (1995). "Limits on possible magnetic fields at nucleosynthesis time". In: *Astropart. Phys.* 3, pp. 95–102. DOI: 10.1016/0927-6505(94)00030-7. arXiv: astro-ph/9409010.

Grasso, Dario and Hector R. Rubinstein (1996). "Revisiting nucleosynthesis constraints on primordial magnetic fields". In: *Phys. Lett. B* 379, pp. 73–79. DOI: 10.1016/0370-2693(96)00416-9. arXiv: astro-ph/9602055.

— (2001). "Magnetic fields in the early universe". In: *Phys. Rept.* 348, pp. 163–266. DOI: 10.1016/S0370-1573(00)00110-1. arXiv: astro-ph/0009061.

Grevesse, N., M. Asplund, and A. J. Sauval (2007). "The Solar Chemical Composition". In: *Space Sci. Rev.* 130.1-4, pp. 105–114. DOI: 10.1007/s11214-007-9173-7.

Hammache, F. et al. (2013). "Search for new resonant states in 10C and 11C and their impact on the cosmological lithium problem". In: *Phys. Rev. C* 88.6, p. 062802. DOI: 10.1103/PhysRevC.88.062802. arXiv: 1312.0894 [nucl-ex].

Hardy, J. C. and I. S. Towner (2009). "Superallowed 0^+0^+ nuclear β decays: A new survey with precision tests of the conserved vector current hypothesis and the standard model". In: *Phys. Rev. C* 79.5, 055502, p. 055502. DOI: 10.1103/PhysRevC.79.055502. arXiv: 0812.1202 [nucl-ex].

Harikae, Seiji., Tomoya. Takiwaki, and Kei. Kotake (2009). "Long-Term Evolution of Slowly Rotating Collapsar in Special Relativistic Magnetohydrodynamics". In: *Astrophys. J.* 704, pp. 354–371. DOI: 10.1088/0004-637X/704/1/354. arXiv: 0905.2006 [astro-ph.HE].

Hawking, S.W. and G.F.R. Ellis (1973). *The Large Scale Structure of Space-Time*. Cambridge Monographs on Mathem. Cambridge University Press. ISBN: 9780521099066.

Hayakawa, S. et al. (2021). "Constraining the Primordial Lithium Abundance: New Cross Section Measurement of the 7Be n Reactions Updates the Total 7Be Destruction Rate". In: *Astrophys. J. Lett.* 915.1, p. L13. DOI: 10.3847/2041-8213/ac061f.

Heger, A. et al. (2001). "Presupernova collapse models with improved weak interaction rates". In: *Phys. Rev. Lett.* 86, pp. 1678–1681. DOI: 10.1103/PhysRevLett.86.1678. arXiv: astro-ph/0007412.

Heger, Alexander and Stan Woosley (2020). "Production of Lithium in Primordial Supernovae". In: *Mem. Soc. Ast. It.* 91, p. 58. arXiv: 2002.04749 [astro-ph.SR].

Hill, V. et al. (2019). "VLT/FLAMES high-resolution chemical abundances in Sculptor: a textbook dwarf spheroidal galaxy". In: *Astron. Astrophys.* 626, A15, A15. DOI: 10.1051/0004-6361/201833950. arXiv: 1812.01486 [astro-ph.GA].

Hinshaw, G. et al. (2013). "Nine-year Wilkinson Microwave Anisotropy Probe (WMAP) Observations: Cosmological Parameter Results". In: *Astrophys. J., Suppl. Ser.* 208.2, 19, p. 19. DOI: 10.1088/0067-0049/208/2/19. arXiv: 1212.5226 [astro-ph.CO].

Hix, W. Raphael and Bradley S. Meyer (2006). "Thermonuclear kinetics in astrophysics". In: *Nucl. Phys. A* 777, pp. 188–207. DOI: 10.1016/j.nuclphysa.2004.10.009. arXiv: astro-ph/0509698 [astro-ph].

Hou, S. Q. et al. (2017). "Non-extensive Statistics to the Cosmological Lithium Problem". In: *Astrophys. J.* 834.2, p. 165. DOI: 10.3847/1538-4357/834/2/165. arXiv: 1701.04149 [astro-ph.CO].

Howk, J. Christopher et al. (2012). "Observation of interstellar lithium in the low-metallicity Small Magellanic Cloud". In: *Nature* 489.7414, pp. 121–123. DOI: 10.1038/nature11407. arXiv: 1207.3081 [astro-ph.CO].

Ichiki, Kiyotomo et al. (2006). "Cosmological Magnetic Field: A Fossil of Density Perturbations in the Early Universe". In: *Science* 311.5762, pp. 827–829. DOI: 10.1126/science.1120690.

Iliadis, Christian (2007). *Nuclear Physics of Stars*. Wiley-VCH (Weinheim). DOI: 10.1002/9783527692668.

Iliadis, Christian et al. (2016). "Bayesian Estimation of Thermonuclear Reaction Rates". In: *Astrophys. J.* 831.1, p. 107. DOI: 10.3847/0004-637X/831/1/107. arXiv: 1608.05853 [astro-ph.SR].

Ishida, Hiroyuki, Motohiko Kusakabe, and Hiroshi Okada (2014). "Effects of long-lived 10 MeV-scale sterile neutrinos on primordial elemental abundances and the effective neutrino number". In: *Phys. Rev. D* 90.8, p. 083519. DOI: 10.1103/PhysRevD.90.083519. arXiv: 1403.5995 [astro-ph.CO].

Itoh, N., H. Totsuji, and S. Ichimaru (1977). "Enhancement of thermonuclear reaction rate due to strong screening". In: *Astrophys. J.* 218, pp. 477–483. DOI: 10.1086/155701.

Itoh, N. et al. (1979). "Enhancement of thermonuclear reaction rate due to strong screening. II - Ionic mixtures". In: *Astrophys. J.* 234, pp. 1079–1084. DOI: 10.1086/157590.

Itoh, N. et al. (1983). "Electrical and thermal conductivities of dense matter in the liquid metal phase. I - High-temperature results". In: *Astrophys. J.* 273, pp. 774–782. DOI: 10.1086/161412.

Itoh, N. et al. (1996). "Neutrino Energy Loss in Stellar Interiors. VII. Pair, Photo-, Plasma, Bremsstrahlung, and Recombination Neutrino Processes". In: *Astrophys. J., Suppl. Ser.* 102, p. 411. DOI: 10.1086/192264.

Itoh, Naoki et al. (2002). "Screening Corrections to the Electron Capture Rates in Dense Stars by the Relativistically Degenerate Electron Liquid". In: *Astrophys. J.* 579.1, pp. 380–385. DOI: 10.1086/342726. arXiv: astro-ph/0207132 [astro-ph].

Iwasa, N. et al. (2021). "Experimental study of the Γ_{p1}/Γ_{p0} ratios of resonance states in ^{8}Be for deducing the ^{7}Be(n ,p_1)^{*7}Li reaction rate relevant to the cosmological lithium problem". In: *Phys. Rev. C* 103.1, 015801, p. 015801. DOI: 10.1103/PhysRevC.103.015801.

Izotov, Y. I., T. X. Thuan, and N. G. Guseva (2014). "A new determination of the primordial He abundance using the He i λ10830 *Aemissionline* : *cosmologicalimplications*". In: *Mon. Notices Royal Astron. Soc.* 445.1, pp. 778–793. DOI: 10.1093/mnras/stu1771. arXiv: 1408.6953 [astro-ph.CO].

Jancovici, B. (1962). "On the relativistic degenerate electron gas". In: *Il Nuovo Cimento* 25.2, pp. 428–455. DOI: 10.1007/BF02731458.

— (1977). "Pair correlation function in a dense plasma and pycnonuclear reactions in stars". In: *J. Stat. Phys.* 17, pp. 357–370. DOI: 10.1007/BF01014403.

Janka, H. T. and E. Mueller (1996). "Neutrino heating, convection, and the mechanism of Type-II supernova explosions." In: *Astron. Astrophys.* 306, p. 167.

Jedamzik, Karsten, Visnja Katalinic, and Angela V. Olinto (1998). "Damping of cosmic magnetic fields". In: *Phys. Rev. D* 57, pp. 3264–3284. DOI: 10.1103/PhysRevD.57.3264. arXiv: astro-ph/9606080.

Jedamzik, Karsten and Levon Pogosian (2020). "Relieving the Hubble Tension with Primordial Magnetic Fields". In: *Phys. Rev. Lett.* 125.18, 181302, p. 181302. DOI: 10.1103/PhysRevLett.125.181302. arXiv: 2004.09487 [astro-ph.CO].

Jedamzik, Karsten and Andrey Saveliev (2019). "Stringent Limit on Primordial Magnetic Fields from the Cosmic Microwave Background Radiation". In: *Phys. Rev. Lett.* 123.2, p. 021301. DOI: 10.1103/PhysRevLett.123.021301. arXiv: 1804.06115 [astro-ph.CO].

Jittoh, Toshifumi et al. (2007). "Possible solution to the Li-7 problem by the long lived stau". In: *Phys. Rev. D* 76, p. 125023. DOI: 10.1103/PhysRevD.76.125023. arXiv: 0704.2914 [hep-ph].

Juodagalvis, A. et al. (2010). "Improved estimate of electron capture rates on nuclei during stellar core collapse". In: *Nucl. Phys. A* 848.3-4, pp. 454–478. DOI: 10.1016/j.nuclphysa.2010.09.012. arXiv: 0909.0179 [nucl-th].

Kajino, T. (1991). "Can quark - gluon plasma formation in relativistic heavy ion collisions constrain inhomogeneous cosmologies?" In: *Phys. Rev. Lett.* 66, pp. 125–128. DOI: 10.1103/PhysRevLett.66.125.

Kajino, T. et al. (2019). "Current status of r-process nucleosynthesis". In: *Progress in Particle and Nuclear Physics* 107, pp. 109–166. DOI: 10.1016/j.ppnp.2019.02.008. arXiv: 1906.05002 [astro-ph.HE].

Kandus, Alejandra, Kerstin E. Kunze, and Christos G. Tsagas (2011). "Primordial magnetogenesis". In: *Phys. Rept.* 505, pp. 1–58. DOI: 10.1016/j.physrep.2011.03.001. arXiv: 1007.3891 [astro-ph.CO].

Kapusta, J. I. and C. Gale (2006). *Finite-Temperature Field Theory: Principles and Applications*. Cambridge University Press (Cambridge).

Kaspi, Victoria M. and Andrei M. Beloborodov (2017). "Magnetars". In: *Annu. Rev. Astron. Astrophys.* 55.1, pp. 261–301. DOI: 10.1146/annurev-astro-081915-023329. arXiv: 1703.00068 [astro-ph.HE].

Kawabata, T. et al. (2017). "Time-Reversal Measurement of the p -Wave Cross Sections of the Be7(n,α)He4 Reaction for the Cosmological Li Problem". In: *Phys. Rev. Lett.* 118.5, p. 052701. DOI: 10.1103/PhysRevLett.118.052701.

Kawano, Lawrence (1992). *Let's go: Early universe 2. Primordial nucleosynthesis the computer way*. NASA STI/Recon Technical Report N.

Kawasaki, Masahiro and Motohiko Kusakabe (2011). "Destruction of ^{7}Be in big bang nucleosynthesis via long-lived sub-strongly interacting massive particles as a solution to the Li problem". In: *Phys. Rev. D* 83, p. 055011. DOI: 10.1103/PhysRevD.83.055011. arXiv: 1012.0435 [hep-ph].

— (2012). "Updated constraint on a primordial magnetic field during big bang nucleosynthesis and a formulation of field effects". In: *Phys. Rev. D* 86, p. 063003. DOI: 10.1103/PhysRevD.86.063003. arXiv: 1204.6164 [astro-ph.CO].

Kawasaki, Masahiro et al. (2020). "Big-bang nucleosynthesis with sub-GeV massive decaying particles". In: *J. Cosmol. Astropart. Phys.* 12, p. 048. DOI: 10.1088/1475-7516/2020/12/048. arXiv: 2006.14803 [hep-ph].

Kernan, Peter J., Glenn D. Starkman, and Tanmay Vachaspati (1996). "Big bang nucleosynthesis constraints on primordial magnetic fields". In: *Phys. Rev. D* 54, pp. 7207–7214. DOI: 10.1103/PhysRevD.54.7207. arXiv: astro-ph/9509126.

— (1997). "Comment on 'Constraints on the strength of primordial B fields from big bang nucleosynthesis reexamined'". In: *Phys. Rev. D* 56, pp. 3766–3767. DOI: 10.1103/PhysRevD.56.3766. arXiv: astro-ph/9612101.

Khatri, Rishi and Rashid A. Sunyaev (2011). "Time of primordial Be-7 conversion into Li-7, energy release and doublet of narrow cosmological neutrino lines". In: *Astron. Lett.* 37, p. 367. DOI: 10.1134/S1063773711060041. arXiv: 1009.3932 [astro-ph.CO].

Khomenko, E. et al. (Sept. 2014). "Fluid description of multi-component solar partially ionized plasma". In: *Phys. Plasmas* 21.9, 092901, p. 092901. DOI: 10.1063/1.4894106. arXiv: 1408.1871 [astro-ph.SR].

Kievsky, A. et al. (2008). "TOPICAL REVIEW: A high-precision variational approach to three- and four-nucleon bound and zero-energy scattering states". In: *J Phys G Nucl Part Phys* 35.6, 063101, p. 063101. DOI: 10.1088/0954-3899/35/6/063101. arXiv: 0805.4688 [nucl-th].

Kirsebom, O. S. and B. Davids (2011). "One fewer solution to the cosmological lithium problem". In: *Phys. Rev. C* 84.5, 058801, p. 058801. DOI: 10.1103/PhysRevC.84.058801. arXiv: 1109.4690 [astro-ph.CO].

Kiuchi, Kenta et al. (2014). "High resolution numerical relativity simulations for the merger of binary magnetized neutron stars". In: *Phys. Rev. D* 90 (4), p. 041502. DOI: 10.1103/PhysRevD.90.041502. URL: https://link.aps.org/doi/10.1103/PhysRevD.90.041502.

Kiuchi, Kenta et al. (2015). "Efficient magnetic-field amplification due to the Kelvin-Helmholtz instability in binary neutron star mergers". In: *Phys. Rev. D* 92 (12), p. 124034. DOI: 10.1103/PhysRevD.92.124034. URL: https://link.aps.org/doi/10.1103/PhysRevD.92.124034.

Kolb, Edward W. and Robert J. Scherrer (1982). "Massive neutrinos and primordial nucleosynthesis". In: *Phys. Rev. D* 25.6, pp. 1481–1491. DOI: 10.1103/PhysRevD.25.1481.

Kolb, Edward W. and Michael S. Turner (1990). *The Early Universe*. Vol. 69. ISBN: 978-0-201-62674-2.

Korn, Andreas J. et al. (2006). "A probable stellar solution to the cosmological lithium discrepancy". In: *Nature* 442, pp. 657–659. DOI: 10.1038/nature05011. arXiv: astro-ph/0608201.

Kozyreva, A. et al. (2017). "Fast evolving pair-instability supernova models: evolution, explosion, light curves". In: *Mon. Notices Royal Astron. Soc.* 464, pp. 2854–2865. DOI: 10.1093/mnras/stw2562. arXiv: 1610.01086 [astro-ph.HE].

Kravchuk, P. A. and D. G. Yakovlev (2014). "Strong plasma screening in thermonuclear reactions: Electron drop model". In: *Phys. Rev. C* 89.1, 015802, p. 015802. DOI: 10.1103/PhysRevC.89.015802. arXiv: 1401.2539 [astro-ph.SR].

Kronberg, P. P. (1994). "Extragalactic magnetic fields". In: *Rep. Prog. Phys.* 57.4, pp. 325–382. DOI: 10.1088/0034-4885/57/4/001.

Kurki-Suonio, H. (2000). "Alternative Solutions to Big Bang Nucleosynthesis (Invited Paper)". In: *The Light Elements and their Evolution*. Ed. by L. da Silva, R. de Medeiros, and M. Spite. Vol. 198. IAU Symposium.

Kusakabe, Motohiko, Toshitaka Kajino, and Grant J. Mathews (2011). "SUSY-catalyzed big bang nucleosynthesis as a solution of lithium problems". In: *Journal of Physics Conference Series*. Vol. 312. J. Phys. Conf. Ser. P. 042012. DOI: 10.1088/1742-6596/312/4/042012.

Kusakabe, Motohiko and Masahiro Kawasaki (2015). "Chemical separation of primordial Li^+ during structure formation caused by nanogauss magnetic field". In: *Mon. Notices Royal Astron. Soc.* 446, pp. 1597–1624. DOI: 10.1093/mnras/stu2115. arXiv: 1404.3485 [astro-ph.CO].

Kusakabe, Motohiko and Masahiro Kawasaki (2019). "Initial Li Abundances in the Proto-Galaxy and Globular Clusters Based upon the Chemical Separation and Hierarchical Structure Formation". In: *Astrophys. J. Lett.* 876.2, L30, p. L30. DOI: 10.3847/2041-8213/ab1a38. arXiv: 1903.08035 [astro-ph.SR].

Kusakabe, Motohiko et al. (2013). "Big-bang nucleosynthesis limit on the neutral fermion decays into neutrinos". In: *Phys. Rev. D* 87.8, p. 085045. DOI: 10.1103/PhysRevD.87.085045. arXiv: 1303.2291 [astro-ph.CO].

Kusakabe, Motohiko et al. (2013). "Solution to Big-Bang nucleosynthesis in hybrid axion dark matter model". In: *Phys. Lett. B* 718.3, pp. 704–708. DOI: 10.1016/j.physletb.2012.11.007. arXiv: 1202.5603 [astro-ph.CO].

Kusakabe, Motohiko et al. (2017). "Review on effects of long-lived negatively charged massive particles on Big Bang Nucleosynthesis". In: *Int. J. Mod. Phys. E* 26.8, 1741004-64, pp. 1741004–64. DOI: 10.1142/S021830131741004X. arXiv: 1706.03143 [astro-ph.CO].

Kusakabe, Motohiko et al. (2019). "On the relative velocity distribution for general statistics and an application to big-bang nucleosynthesis under Tsallis statistics". In: *Phys. Rev. D* 99.4, p. 043505. DOI: 10.1103/PhysRevD.99.043505. arXiv: 1806.01454 [astro-ph.CO].

Lamia, L. et al. (2019). "Cross-section Measurement of the Cosmologically Relevant 7Be(n, α)4He Reaction over a Broad Energy Range in a Single Experiment". In: *Astrophys. J.* 879.1, p. 23. DOI: 10.3847/1538-4357/ab2234.

Langanke, K. and G. Martinez-Pinedo (2000). "Shell model calculations of stellar weak interaction rates: 2.. Weak rates for nuclei in the mass range A = 45-65 in supernovae environment". In: *Nucl. Phys. A* 673, pp. 481–508. DOI: 10.1016/S0375-9474(00)00131-7. arXiv: nucl-th/0001018.

Langanke, K. and G. Martínez-Pinedo (2001). "Rate Tables for the Weak Processes of pf-SHELL Nuclei in Stellar Environments". In: *At. Data Nucl. Data Tables* 79.1, pp. 1–46. DOI: 10.1006/adnd.2001.0865.

Langanke, K. and G. Martinez-Pinedo (2003). "Nuclear Weak Interaction Processes in Stars". In: *Rev. Mod. Phys.* 75, pp. 819–862. DOI: 10.1103/RevModPhys.75.819. arXiv: nucl-th/0203071.

Langanke, K. and M. Wiescher (2001). "Nuclear reactions and stellar processes". In: *Rep. Prog. Phys.* 64.12, pp. 1657–1701. DOI: 10.1088/0034-4885/64/12/202.

Lara, Juan F., Toshitaka Kajino, and Grant J. Mathews (2006). "Inhomogeneous big bang nucleosynthesis revisited". In: *Phys. Rev. D* 73, p. 083501. DOI: 10.1103/PhysRevD.73.083501. arXiv: astro-ph/0603817.

Lee, T. D. and Chen-Ning Yang (1957). "Parity Nonconservation and a Two Component Theory of the Neutrino". In: *Phys. Rev.* 105. Ed. by G. Feinberg, pp. 1671–1675. DOI: 10.1103/PhysRev.105.1671.

Liddle, A.R. and D.H. Lyth (2000). *Cosmological Inflation and Large-Scale Structure*. Cosmological Inflation and Large-scale Structure. Cambridge University Press. ISBN: 9780521575980.

Liebendörfer, Matthias et al. (2001). "Probing the gravitational well: No supernova explosion in spherical symmetry with general relativistic Boltzmann neutrino transport". In: *Phys. Rev. D* 63.10, 103004, p. 103004. DOI: 10.1103/PhysRevD.63.103004. arXiv: astro-ph/0006418 [astro-ph].

Linhard, J. (1954). "On the properties of a gas of charged particles". In: *Dan. Vid. Selsk Mat.-Fys. Medd.* 28, p. 8. URL: https://ci.nii.ac.jp/naid/10013390197/en/.

Liu, J.-J. (2016). "Strong screening effects on resonant nuclear reaction ^{23}Mg (p, γ) ^{24}Al in the surface of magnetars". In: *Res. Astron. Astrophys.* 16, 83, p. 83. DOI: 10.1088/1674-4527/16/5/083. arXiv: 1602.05501 [astro-ph.SR].

Liu, M. Q., J. Zhang, and Z. Q. Luo (2007). "Screening effect on electron capture in presupernova stars". In: *Astron. Astrophys.* 463.1, pp. 261–264. DOI: 10.1051/0004-6361:20065689.

Livadiotis, G. and D. J. McComas (2010). "Exploring Transitions of Space Plasmas Out of Equilibrium". In: *Astrophys. J.* 714.1, pp. 971–987. DOI: 10.1088/0004-637X/714/1/971.

Lodders, Katharina (2003). "Solar System Abundances and Condensation Temperatures of the Elements". In: *Astrophys. J.* 591.2, pp. 1220–1247. DOI: 10.1086/375492.

Luo, Yudong et al. (2019). "Big Bang Nucleosynthesis with an Inhomogeneous Primordial Magnetic Field Strength". In: *Astrophys. J.* 872.2, p. 172. DOI: 10.3847/1538-4357/ab0088. arXiv: 1810.08803 [astro-ph.CO].

Luo, Yudong et al. (2020). "Screening corrections to electron capture rates and resulting constraints on primordial magnetic fields". In: *Phys. Rev. D* 101.8, 083010, p. 083010. DOI: 10.1103/PhysRevD.101.083010. arXiv: 2002.08636 [astro-ph.CO].

Luo, Yudong et al. (2021). "Impacts of Hawking Radiation from Primordial Black Holes in Critical Collapse Model on the Light Element Abundances". In: *J. Cosmol. Astropart. Phys.* 05, p. 042. DOI: 10.1088/1475-7516/2021/05/042. arXiv: 2011.10937 [astro-ph.CO].

Lutz, Eric (2003). "Anomalous diffusion and Tsallis statistics in an optical lattice". In: *Phys. Rev. A* 67.5, 051402, p. 051402. DOI: 10.1103/PhysRevA.67.051402. arXiv: cond-mat/0210022 [cond-mat.stat-mech].

Lyth, D. H. D. H. and A. A. Riotto (1999). "Particle physics models of inflation and the cosmological density perturbation". In: *Phys. Rep.* 314.1-2, pp. 1–146. DOI: 10.1016/S0370-1573(98)00128-8. arXiv: hep-ph/9807278 [hep-ph].

Ma, L. et al. (1997). "Measurements of ^{1}H(d–>,γ)^{3}He and ^{2}H(p–>,γ)^{3}He at very low energies". In: *Phys. Rev. C* 55.2, pp. 588–596. DOI: 10.1103/PhysRevC.55.588.

Mack, Andrew, Tina Kahniashvili, and Arthur Kosowsky (2002). "Microwave background signatures of a primordial stochastic magnetic field". In: *Phys. Rev. D* 65, p. 123004. DOI: 10.1103/PhysRevD.65.123004. arXiv: astro-ph/0105504.

Marcucci, L. E. et al. (2005). "Electromagnetic structure of A=2 and 3 nuclei and the nuclear current operator". In: *Phys. Rev. C* 72.1, 014001, p. 014001. DOI: 10.1103/PhysRevC.72.014001. arXiv: nucl-th/0502048 [nucl-th].

Marshall, J. F. and E. Guth (1950). "Photo-Disintegration of the Deuteron at High Energies". In: *Phys. Rev.* 78.6, pp. 738–744. DOI: 10.1103/PhysRev.78.738.

Martin, Jerome and Jun'ichi Yokoyama (2008). "Generation of Large-Scale Magnetic Fields in Single-Field Inflation". In: *J. Cosmol. Astropart. Phys.* 01, p. 025. DOI: 10.1088/1475-7516/2008/01/025. arXiv: 0711.4307 [astro-ph].

Martínez-Gómez, David, Roberto Soler, and Jaume Terradas (2016). "Multi-fluid Approach to High-frequency Waves in Plasmas: I. Small-amplitude Regime in Fully Ionized Medium". In: *Astrophys. J.* 832.2, 101, p. 101. DOI: 10.3847/0004-637X/832/2/101. arXiv: 1609.06190 [astro-ph.SR].

Martínez-Gómez, David et al. (2021). "Simulations of the Biermann battery mechanism in two-fluid partially ionised plasmas". In: *arXiv*. eprint: 2104.06956.

Martínez-Pinedo, G. et al. (2007). "The role of fission in the r-process". In: *Prog. Part. Nucl. Phys.* 59.1, pp. 199–205. DOI: 10.1016/j.ppnp.2007.01.018.

Matese, J. J. and W. R. Johnson (1965). "Influence of Screening on the Atomic Photoeffect". In: *Phys. Rev.* 140, A1–A7. DOI: 10.1103/PhysRev.140.A1.

Mathews, Grant J., Motohiko Kusakabe, and Toshitaka Kajino (2017). "Introduction to big bang nucleosynthesis and modern cosmology". In: *Int. J. Mod. Phys. E* 26.8, 1741001, p. 1741001. DOI: 10.1142/S0218301317410014. arXiv: 1706.03138 [astro-ph.CO].

Mathews, Grant J. et al. (2018). "Big bang nucleosynthesis, the CMB, and the origin of matter and space-time". In: *AIP Conference Proceedings* 1947.1, p. 020014. DOI: 10.1063/1.5030818.

Matsuno, Tadafumi et al. (2017). "Lithium in CEMP-no stars: A new constraint on the lithium depletion mechanism in the early universe*". In: *Publ. Astron. Soc. Jpn.* 69.2, 24, p. 24. DOI: 10.1093/pasj/psw129. arXiv: 1612.06624 [astro-ph.SR].

Matteucci, Francesca et al. (2021). "The evolution of Lithium: implications of a universal Spite plateau". In: *Mon. Notices Royal Astron. Soc.* DOI: 10.1093/mnras/stab1234. arXiv: 2104.11504 [astro-ph.GA].

Mazurek, T. J., J. W. Truran, and A. G. W. Cameron (1974). "Electron Capture in Carbon Dwarf Supernovae". In: *Astrophys. Space Sci.* 27.2, pp. 261–291. DOI: 10.1007/BF00643877.

McLaughlin, Gail C., George M. Fuller, and James R. Wilson (Dec. 1996). "The Influence of Nuclear Composition on the Electron Fraction in the Post–Core Bounce Supernova Environment". In: *Astrophys. J.* 472, p. 440. DOI: 10.1086/178077. arXiv: astro-ph/9701114 [astro-ph].

Mestel, L. and I. W. Roxburgh (1962). "On the Thermal Generation of Toroidal Magnetic Fields in Rotating Stars." In: *Astrophys. J.* 136, p. 615. DOI: 10.1086/147412.

Metzger, B. D. et al. (2010). "Electromagnetic Counterparts of Compact Object Mergers Powered by the Radioactive Decay of R-process Nuclei". In: *Mon. Notices Royal Astron. Soc.* 406, p. 2650. DOI: 10.1111/j.1365-2966.2010.16864.x. arXiv: 1001.5029 [astro-ph.HE].

Meyer, B. S. and D. C. Adams (2007). "Libnucnet: A Tool for Understanding Nucleosynthesis". In: *Meteoritics and Planetary Science Supplement* 42, p. 5215.

Mezzacappa, A. (2001). "Simulations of stellar core collapse, bounce, and postbounce evolution with boltzmann neutrino transport, and implications for the core collapse supernova mechanism". In: *Nucl. Phys. B Proc. Suppl.* 91. Ed. by J. Law, R. W. Ollerhead, and J. J. Simpson, pp. 338–344. DOI: 10.1016/S0920-5632(00)00960-9. arXiv: astro-ph/0010579.

Minoda, Teppei et al. (2017). "Thermal Sunyaev-Zel'dovich effect in the intergalactic medium with primordial magnetic fields". In: 96.12, 123525, p. 123525. DOI: 10.1103/PhysRevD.96.123525. arXiv: 1705.10054 [astro-ph.CO].

Molaro, P., G. Cescutti, and X. Fu (2020). "Lithium and beryllium in the Gaia-Enceladus galaxy". In: *Mon. Notices Royal Astron. Soc.* 496.3, pp. 2902–2909. DOI: 10.1093/mnras/staa1653. arXiv: 2006.00787 [astro-ph.GA].

Monaco, L. et al. (2010). "The lithium content of ω Centauri. New clues to the cosmological Li problem from old stars in external galaxies". In: *Astron. Astrophys.* 519, L3, p. L3. DOI: 10.1051/0004-6361/201015162. arXiv: 1008.1817 [astro-ph.GA].

Mori, Kanji and Motohiko Kusakabe (2019). "Roles of $^7\mathrm{Be}(n,p)^7\mathrm{Li}$ resonances in big bang nucleosynthesis with time-dependent quark mass and Li reduction by a heavy quark mass". In: *Phys. Rev. D* 99.8, p. 083013. DOI: 10.1103/PhysRevD.99.083013. arXiv: 1901.03943 [astro-ph.CO].

Morita, M. (1973). *Beta Decay and Muon Capture*. W. A. Benjamin, Advanced Book Program. ISBN: 9780805371529.

Mucciarelli, A. et al. (2014). "The Abundance of Lithium Measured for the First Time Beyond Our Galaxy". In: *The Messenger* 158, pp. 45–47.

Mumpower, M. R. et al. (2018). "β-delayed Fission in r-process Nucleosynthesis". In: *Astrophys. J.* 869.1, 14, p. 14. DOI: 10.3847/1538-4357/aaeaca. arXiv: 1802.04398 [nucl-th].

Nagai, Y. et al. (2006). "Measurement of the H2(n,γ)H3 reaction cross section between 10 and 550 keV". In: *Phys. Rev. C* 74.2, 025804, p. 025804. DOI: 10.1103/PhysRevC.74.025804.

Nakamura, K. et al. (2012). "Neutrino-driven supernova explosions powered by nuclear reactions". In: *Death of Massive Stars: Supernovae and Gamma-Ray Bursts*. Ed. by P. Roming, N. Kawai, and E. Pian. Vol. 279. IAU Symposium, pp. 365–366. DOI: 10.1017/S1743921312013373.

Nakamura, K. et al. (2015). "r-process nucleosynthesis in the MHD+neutrino-heated collapsar jet". In: *Astron. Astrophys.* 582, A34. DOI: 10.1051/0004-6361/201526110.

Nakamura, Riou et al. (2017). "Big-Bang nucleosynthesis: Constraints on nuclear reaction rates, neutrino degeneracy, inhomogeneous and Brans-Dicke models". In: *Int. J. Mod. Phys. E* 26.8, 1741003, p. 1741003. DOI: 10.1142/S0218301317410038. arXiv: 1710.08153 [astro-ph.CO].

Nishimura, N., T. Takiwaki, and F. K. Thielemann (2015). "The r-process nucleosynthesis in the various jet-like explosions of magnetorotational core-collapse supernovae". In: *Astrophys. J.* 810.2, p. 109. DOI: 10.1088/0004-637X/810/2/109. arXiv: 1501.06567 [astro-ph.SR].

Oda, T. et al. (1994). "Rate Tables for the Weak Processes of sd -Shell Nuclei in Stellar Matter". In: *Atom. Data Nucl. Data Tabl.* 56, pp. 231–403. DOI: 10.1006/adnd.1994.1007.

Olive, K. A. and Particle Data Group (2014). "Review of Particle Physics". In: *Chin. Phys. C* 38.9, 090001, p. 090001. DOI: 10.1088/1674-1137/38/9/090001.

Olive, Keith A. et al. (2012). "Higher D or Li: probes of physics beyond the standard model". In: *Mon. Notices Royal Astron. Soc.* 426.2, pp. 1427–1435. DOI: 10.1111/j.1365-2966.2012.21703.x. arXiv: 1203.5701 [astro-ph.CO].

O'Malley, P. D. et al. (2011). "Search for a resonant enhancement of the ^{7}Be + d reaction and primordial ^{7}Li abundances". In: *Phys. Rev. C* 84.4, 042801, p. 042801. DOI: 10.1103/PhysRevC.84.042801.

Orito, M. et al. (1997). "Geometrical effects of baryon density inhomogeneities on primordial nucleosynthesis". In: *Astrophys. J.* 488, p. 515. DOI: 10.1086/304716. arXiv: astro-ph/9609130.

Osterfeld, Franz (1992). "Nuclear spin and isospin excitations". In: *Rev. Mod. Phys.* 64, pp. 491–558. DOI: 10.1103/RevModPhys.64.491.

Patrignani, C. et al. (2016). "Review of Particle Physics". In: *Chin. Phys. C* 40.10, p. 100001. DOI: 10.1088/1674-1137/40/10/100001.

Pavlos, G P (2012). "Understanding the Multi-Scale and Multi-fractal Dynamics of Space Plasmas Through Tsallis Non-Extensive Statistical Theory". In: *arXiv*. arXiv: 1203.4003.

Paxton, B. et al. (2011). "Modules for Experiments in Stellar Astrophysics (MESA)". In: *Astrophys. J., Suppl. Ser.* 192, 3, p. 3. DOI: 10.1088/0067-0049/192/1/3. arXiv: 1009.1622 [astro-ph.SR].

Paxton, B. et al. (2015). "Modules for Experiments in Stellar Astrophysics (MESA): Binaries, Pulsations, and Explosions". In: *Astrophys. J., Suppl. Ser.* 220, 15, p. 15. DOI: 10.1088/0067-0049/220/1/15. arXiv: 1506.03146 [astro-ph.SR].

Paxton, Bill et al. (2018). "Modules for Experiments in Stellar Astrophysics (MESA): Convective Boundaries, Element Diffusion, and Massive Star Explosions". In:

Astrophys. J., Suppl. Ser. 234.2, 34, p. 34. DOI: 10.3847/1538-4365/aaa5a8. arXiv: 1710.08424 [astro-ph.SR].

Peacock, J.A. (1999). *Cosmological Physics*. Cambridge Astrophysics. Cambridge University Press. ISBN: 9780521422703.

Pearson, Edwin F. and Walter Gordy (1969). "Millimeter-Wave Spectra and Molecular Constants of ^{6}LiD and ^{7}LiD". In: *Phys. Rev.* 177.1, pp. 59–61. DOI: 10.1103/PhysRev.177.59.

Pettini, Max and Ryan Cooke (2012). "A new, precise measurement of the primordial abundance of deuterium". In: *Mon. Notices Royal Astron. Soc.* 425.4, pp. 2477–2486. DOI: 10.1111/j.1365-2966.2012.21665.x. arXiv: 1205.3785 [astro-ph.CO].

Piau, L. et al. (2006). "From First Stars to the Spite Plateau: a Possible Reconciliation of Halo Stars Observations with Predictions from Big Bang Nucleosynthesis". In: *Astrophys. J.* 653, pp. 300–315. DOI: 10.1086/508445. arXiv: astro-ph/0603553.

Pitrou, Cyril et al. (2018). "Precision big bang nucleosynthesis with improved Helium-4 predictions". In: *Phys. Rept.* 754, pp. 1–66. DOI: 10.1016/j.physrep.2018.04.005. arXiv: 1801.08023 [astro-ph.CO].

Planck Collaboration et al. (2016a). "Planck 2015 results. XIII. Cosmological parameters". In: *Astron. Astrophys.* 594, A13, A13. DOI: 10.1051/0004-6361/201525830. arXiv: 1502.01589 [astro-ph.CO].

Planck Collaboration et al. (2016b). "Planck 2015 results. XIX. Constraints on primordial magnetic fields". In: *Astron. Astrophys.* 594, A19, A19. DOI: 10.1051/0004-6361/201525821. arXiv: 1502.01594 [astro-ph.CO].

Potekhin, A. Y. and G. Chabrier (2013). "Electron Screening Effect on Stellar Thermonuclear Fusion". In: *Contrib. Plasma Phys.* 53, pp. 397–405. DOI: 10.1002/ctpp.201200094. arXiv: 1310.3162 [physics.plasm-ph].

Price, Daniel and Stephan Rosswog (2006). "Producing ultra-strong magnetic fields in neutron star mergers". In: *Science* 312, p. 719. DOI: 10.1126/science.1125201. arXiv: astro-ph/0603845.

Pruet, Jason and George M. Fuller (2003). "Estimates of stellar weak interaction rates for nuclei in the mass range A = 65-80". In: *Astrophys. J. Suppl.* 149, p. 189. DOI: 10.1086/376753. arXiv: astro-ph/0211262.

Qian, Y. Z. and S. E. Woosley (1996). "Nucleosynthesis in neutrino driven winds: 1. The Physical conditions". In: *Astrophys. J.* 471, pp. 331–351. DOI: 10.1086/177973. arXiv: astro-ph/9611094.

Quarati, P. and A. M. Scarfone (2007). "Modified Debye-Hückel Electron Shielding and Penetration Factor". In: *Astrophys. J.* 666, pp. 1303–1310. DOI: 10.1086/520058. arXiv: 0705.3545.

Rea, Nanda and Paolo Esposito (2011). "Magnetar outbursts: an observational review". In: *Astrophys. Space Sci. Proc.* 21, p. 247. DOI: 10.1007/978-3-642-17251-9_21. arXiv: 1101.4472 [astro-ph.GA].

Richard, Olivier, Georges Michaud, and Jacques Richer (2005). "Implications of WMAP observations on Li abundance and stellar evolution models". In: *Astrophys. J.* 619, pp. 538–548. DOI: 10.1086/426470. arXiv: astro-ph/0409672.

Rijal, N. et al. (2019). "Measurement of $d+^7$Be cross sections for Big-Bang nucleosynthesis". In: *Phys. Rev. Lett.* 122.18. [Erratum: Phys.Rev.Lett. 123, 239902 (2019)], p. 182701. DOI: 10.1103/PhysRevLett.122.182701. arXiv: 1808.07893 [nucl-ex].

Rossani, A. and A.M. Scarfone (2000). "Tsallis distribution functions for charged particles in electric and magnetic fields". In: *Physica A* 282.1, pp. 212–224. DOI: https://doi.org/10.1016/S0378-4371(00)00079-0.

Ruiz, Milton, Antonios Tsokaros, and Stuart L. Shapiro (2020). "Magnetohydrodynamic simulations of binary neutron star mergers in general relativity: Effects

of magnetic field orientation on jet launching". In: *Phys. Rev. D* 101.6, 064042, p. 064042. DOI: 10.1103/PhysRevD.101.064042. arXiv: 2001.09153 [astro-ph.HE].

Saha, M. N. (1921). "On a Physical Theory of Stellar Spectra". In: *Proceedings of the Royal Society of London Series A* 99.697, pp. 135–153. DOI: 10.1098/rspa.1921.0029.

Sahoo, B. K. and M. Das (2016). "Plasma-screening effects in the astrophysically relevant He-like and Li-like Mg and Fe ions*". In: *Eur. Phys. J. D* 70, 270, p. 270. DOI: 10.1140/epjd/e2016-70541-6. arXiv: 1608.07919 [physics.atom-ph].

Salpeter, E. E. (1951). "The Effective Range of Nuclear Forces. Effect of the Potential Shape". In: *Phys. Rev.* 82.1, pp. 60–66. DOI: 10.1103/PhysRev.82.60.

— (1954). "Electrons Screening and Thermonuclear Reactions". In: *Aust. J. Phys.* 7, p. 373. DOI: 10.1071/PH540373.

Salpeter, E. E. and H. M. van Horn (1969). "Nuclear Reaction Rates at High Densities". In: *Astrophys. J.* 155, p. 183. DOI: 10.1086/149858.

Sampaio, J. M. et al. (2003). "Electron capture rates for core collapse supernovae". In: *Nucl. Phys. A* 718. Ed. by S. Kubono et al., pp. 440–442. DOI: 10.1016/S0375-9474(03)00832-7. arXiv: nucl-th/0209057.

Sbordone, L. et al. (2010). "The metal-poor end of the Spite plateau. 1: Stellar parameters, metallicities and lithium abundances". In: *Astron. Astrophys.* 522, A26. DOI: 10.1051/0004-6361/200913282. arXiv: 1003.4510 [astro-ph.GA].

Scherrer, Robert J. and Michael S. Turner (1988a). "Primordial Nucleosynthesis with Decaying Particles. I. Entropy-producing Decays". In: *Astrophys. J.* 331, p. 19. DOI: 10.1086/166534.

— (1988b). "Primordial Nucleosynthesis with Decaying Particles. II. Inert Decays". In: *Astrophys. J.* 331, p. 33. DOI: 10.1086/166535.

Schiff, L. I. (1950). "Deuteron Photo-Effect at High Energies". In: *Phys. Rev.* 78.6, pp. 733–737. DOI: 10.1103/PhysRev.78.733.

Seeger, Philip A., William A. Fowler, and Donald D. Clayton (Feb. 1965). "Nucleosynthesis of Heavy Elements by Neutron Capture." In: *Astrophys. J., Suppl. Ser.* 11, p. 121. DOI: 10.1086/190111.

Seshadri, T. R. and Kandaswamy Subramanian (2009). "CMB bispectrum from primordial magnetic fields on large angular scales". In: *Phys. Rev. Lett.* 103, p. 081303. DOI: 10.1103/PhysRevLett.103.081303. arXiv: 0902.4066 [astro-ph.CO].

Shalybkov, D. A. and D. G. Yakovlev (Sept. 1987). "Simple model for taking into account the effects of plasma screening in thermonuclear reactions". In: *Astrophys.* 27.2, pp. 562–568. DOI: 10.1007/BF01006020.

Shaviv, G. and N. J. Shaviv (2000). "Is There a Dynamic Effect in the Screening of Nuclear Reactions in Stellar Plasmas?" In: *Astrophys. J.* 529, pp. 1054–1069. DOI: 10.1086/308290.

Shibagaki, S. et al. (2016). "Relative Contributions of the Weak, Main, and Fission-recycling r-process". In: *Astrophys. J.* 816, 79, p. 79. DOI: 10.3847/0004-637X/816/2/79. arXiv: 1505.02257 [astro-ph.SR].

Smartt, S. J. et al. (2017). "A kilonova as the electromagnetic counterpart to a gravitational-wave source". In: *Nature* 551.7678, pp. 75–79. DOI: 10.1038/nature24303. arXiv: 1710.05841 [astro-ph.HE].

Smith, Michael S., Lawrence H. Kawano, and Robert A. Malaney (1993). "Experimental, computational, and observational analysis of primordial nucleosynthesis". In: *Astrophys. J. Suppl.* 85, pp. 219–247. DOI: 10.1086/191763.

Son, D. T. (1999). "Magnetohydrodynamics of the early Universe and the evolution of primordial magnetic fields". In: *Phys. Rev. D* 59.6, 063008, p. 063008. DOI: 10.1103/PhysRevD.59.063008. arXiv: hep-ph/9803412 [hep-ph].

Spera, M. and M. Mapelli (2017). "Very massive stars, pair-instability supernovae and intermediate-mass black holes with the sevn code". In: *Mon. Notices Royal Astron. Soc.* 470, pp. 4739–4749. DOI: 10.1093/mnras/stx1576. arXiv: 1706.06109 [astro-ph.SR].

Spitaleri, C. et al. (2016). "The electron screening puzzle and nuclear clustering". In: *Phys. Lett. B* 755, pp. 275 –278. DOI: https://doi.org/10.1016/j.physletb.2016.02.019.

Spite, F. and M. Spite (1982). "Abundance of lithium in unevolved stars and old disk stars : Interpretation and consequences." In: *Astron. Astrophys.* 115, pp. 357–366.

Spitzer, Lyman (1965). *Physics of fully ionized gases*.

Steigman, Gary (2007). "Primordial Nucleosynthesis in the Precision Cosmology Era". In: *Annu. Rev. Nucl. Part. Sci.* 57.1, pp. 463–491. DOI: 10.1146/annurev.nucl.56.080805.140437. arXiv: 0712.1100 [astro-ph].

Subramanian, K., D. Narasimha, and S. M. Chitre (1994). "Thermal generation of cosmological seed magnetic fields in ionization fronts". In: *Mon. Notices Royal Astron. Soc.* 271, p. L15. DOI: 10.1093/mnras/271.1.L15.

Subramanian, Kandaswamy (2010). "Magnetic fields in the early universe". In: *Astron. Nachr.* 331, pp. 110–120. DOI: 10.1002/asna.200911312. arXiv: 0911.4771 [astro-ph.CO].

— (2016). "The origin, evolution and signatures of primordial magnetic fields". In: *Rept. Prog. Phys.* 79.7, p. 076901. DOI: 10.1088/0034-4885/79/7/076901. arXiv: 1504.02311 [astro-ph.CO].

Subramanian, Kandaswamy and John D. Barrow (1998). "Magnetohydrodynamics in the early universe and the damping of noninear Alfven waves". In: *Phys. Rev. D* 58, p. 083502. DOI: 10.1103/PhysRevD.58.083502. arXiv: astro-ph/9712083.

Subramanian, Kandaswamy and John D. Barrow (1998). "Microwave Background Signals from Tangled Magnetic Fields". In: *Phys. Rev. Lett.* 81.17, pp. 3575–3578. DOI: 10.1103/PhysRevLett.81.3575. arXiv: astro-ph/9803261 [astro-ph].

Suda, Takuma et al. (2008). "Stellar Abundances for the Galactic Archeology (SAGA) Database — Compilation of the Characteristics of Known Extremely Metal-Poor Stars". In: *Publ. Astron. Soc. Jpn.* 60, p. 1159. DOI: 10.1093/pasj/60.5.1159. arXiv: 0806.3697 [astro-ph].

Suzuki, Toshio et al. (2018). "β-decay Rates for Exotic Nuclei and r-process Nucleosynthesis up to Thorium and Uranium". In: *Astrophys. J.* 859.2, 133, p. 133. DOI: 10.3847/1538-4357/aabfde.

Takahashi, K., M. F. El Eid, and W. Hillebrandt (1978). "Beta transition rates in hot and dense matter." In: *Astron. Astrophys.* 67.2, pp. 185–197.

Takahashi, K., T. Yoshida, and H. Umeda (2018). "Stellar Yields of Rotating First Stars. II. Pair-instability Supernovae and Comparison with Observations". In: *Astrophys. J.* 857, 111, p. 111. DOI: 10.3847/1538-4357/aab95f. arXiv: 1803.06630 [astro-ph.SR].

Takahashi, Keitaro et al. (2005). "Magnetic Field Generation from Cosmological Perturbations". In: *Phys. Rev. Lett.* 95 (12), p. 121301. DOI: 10.1103/PhysRevLett.95.121301. URL: https://link.aps.org/doi/10.1103/PhysRevLett.95.121301.

Takiwaki, Tomoya, Kei Kotake, and Katsuhiko Sato (2009). "Special Relativistic Simulations of Magnetically-dominated Jets in Collapsing Massive Stars". en. In: *Astrophys. J.* 691.2. arXiv: 0712.1949, pp. 1360–1379. DOI: 10.1088/0004-637X/691/2/1360.

Talmi, Igal and Bruce R. Barrett (1994). "Simple Models of Complex Nuclei: The Shell Model and Interacting Boson Model". In: *Phys. Today* 47.2, p. 102. DOI: 10.1063/1.2808408.

Taylor, A. M., I. Vovk, and A. Neronov (2011). "Extragalactic magnetic fields constraints from simultaneous GeV-TeV observations of blazars". In: *Astron. Astrophys.* 529, A144, A144. DOI: 10.1051/0004-6361/201116441. arXiv: 1101.0932 [astro-ph.HE].

Tominaga, Nozomu, Nobuyuki Iwamoto, and Ken'ichi Nomoto (2014). "Abundance Profiling of Extremely Metal-poor Stars and Supernova Properties in the Early Universe". In: *Astrophys. J.* 785.2, 98, p. 98. DOI: 10.1088/0004-637X/785/2/98. arXiv: 1309.6734 [astro-ph.SR].

Tumino, A. et al. (2014). "New Determination of the ^{2}H(d,p)^{3}H and ^{2}H(d,n)^{3}He Reaction Rates at Astrophysical Energies". In: *Astrophys. J.* 785.2, 96, p. 96. DOI: 10.1088/0004-637X/785/2/96.

Turner, Michael S. and Lawrence M. Widrow (1988). "Inflation Produced, Large Scale Magnetic Fields". In: *Phys. Rev. D* 37, p. 2743. DOI: 10.1103/PhysRevD.37.2743.

Vassh, N. et al. (2019). "Using excitation-energy dependent fission yields to identify key fissioning nuclei in r-process nucleosynthesis". In: *J Phys G Nucl Part Phys* 46.6, p. 065202. DOI: 10.1088/1361-6471/ab0bea. arXiv: 1810.08133 [nucl-th].

Verschuur, G. L. (1968). "Positive Determination of an Interstellar Magnetic Field by Measurement of the Zeeman Splitting of the 21-cm Hydrogen Line". In: *Phys. Rev. Lett.* 21.11, pp. 775–778. DOI: 10.1103/PhysRevLett.21.775.

Viviani, M. et al. (2000). "Photodisintegration and electrodisintegration of ^{3}He at threshold and pd radiative capture". In: *Phys. Rev. C* 61.6, 064001, p. 064001. DOI: 10.1103/PhysRevC.61.064001. arXiv: nucl-th/9911051 [nucl-th].

Wallace, R. K., S. E. Woosley, and T. A. Weaver (1982). "The thermonuclear model for X-ray transients". In: *Astrophys. J.* 258, pp. 696–715. DOI: 10.1086/160119.

Wanajo, Shinya et al. (2003). "The r-Process in Supernova Explosions from the Collapse of O-Ne-Mg Cores". In: *Astrophys. J.* 593.2, pp. 968–979. DOI: 10.1086/376617. arXiv: astro-ph/0302261 [astro-ph].

Wands, David (2007). *Multiple Field Inflation*. Ed. by Martin Lemoine, Jerome Martin, and Patrick Peter. Vol. 738, p. 275. DOI: 10.1007/978-3-540-74353-8_8.

Wang, Biao, C. A. Bertulani, and A. B. Balantekin (2011). "Electron screening and its effects on Big-Bang nucleosynthesis". In: *Phys. Rev. C* 83, p. 018801. DOI: 10.1103/PhysRevC.83.018801. arXiv: 1010.1565 [astro-ph.CO].

Wang, Meng et al. (2017). "The AME2016 atomic mass evaluation (II). Tables, graphs and references". In: *Chin. Phys. C* 41.3, 030003, p. 030003. DOI: 10.1088/1674-1137/41/3/030003.

Wasserman, I. (1978). "On the origins of galaxies, galactic angular momenta, and galactic magnetic fields." In: *Astrophys. J.* 224, pp. 337–343. DOI: 10.1086/156381.

Watson, Darach et al. (2019). "Identification of strontium in the merger of two neutron stars". In: *Nature* 574.7779, pp. 497–500. DOI: 10.1038/s41586-019-1676-3. arXiv: 1910.10510 [astro-ph.HE].

Weinberg, S. (2008). *Cosmology*. Cosmology. OUP Oxford. ISBN: 9780191523601.

Weinberg, Steven (1972). *Gravitation and Cosmology: Principles and Applications of the General Theory of Relativity*. New York: John Wiley and Sons. ISBN: 978-0-471-92567-5, 978-0-471-92567-5.

Widrow, Lawrence M. et al. (2012). "The First Magnetic Fields". In: *Space Sci. Rev.* 166, pp. 37–70. DOI: 10.1007/s11214-011-9833-5. arXiv: 1109.4052 [astro-ph.CO].

Wilk, G. and Z. Wlodarczyk (2000). "On the interpretation of nonextensive parameter q in Tsallis statistics and Levy distributions". In: *Phys. Rev. Lett.* 84, p. 2770. DOI: 10.1103/PhysRevLett.84.2770. arXiv: hep-ph/9908459.

Wilk, G. and Z. Wlodarczyk (2002). "The Imprints of nonextensive statistical mechanics in high-energy collisions". In: *Chaos Solitons Fractals* 13, pp. 581–594. DOI: 10.1016/S0960-0779(01)00041-8. arXiv: hep-ph/0004250.

Woosley, S. E. (2017). "Pulsational Pair-instability Supernovae". In: *Astrophys. J.* 836, 244, p. 244. DOI: 10.3847/1538-4357/836/2/244. arXiv: 1608.08939 [astro-ph.HE].

Woosley, S. E., A. Heger, and T. A. Weaver (Nov. 2002). "The evolution and explosion of massive stars". In: *Rev. Mod. Phys.* 74.4, pp. 1015–1071. DOI: 10.1103/RevModPhys.74.1015.

Wu, Y. and A. Pálffy (2017). "Determination of Plasma Screening Effects for Thermonuclear Reactions in Laser-generated Plasmas". In: *Astrophys. J.* 838, 55, p. 55. DOI: 10.3847/1538-4357/aa6252. arXiv: 1612.06884 [physics.plasm-ph].

Yamazaki, Dai G. (2016). "Evolution of the cosmic matter density field with a primordial magnetic field". In: *Phys. Rev. D* 93.4, p. 043004. DOI: 10.1103/PhysRevD.93.043004. arXiv: 1602.02750 [astro-ph.CO].

Yamazaki, Dai G., Kiyotomo Ichiki, and Keitaro Takahashi (2013). "Constraints on the multi-lognormal magnetic fields from the observations of the cosmic microwave background and the matter power spectrum". In: *Phys. Rev. D* 88.10, 103011, p. 103011. DOI: 10.1103/PhysRevD.88.103011. arXiv: 1311.2584 [astro-ph.CO].

Yamazaki, Dai G. and Motohiko Kusakabe (2012). "Effects of power law primordial magnetic field on big bang nucleosynthesis". In: *Phys. Rev. D* 86, p. 123006. DOI: 10.1103/PhysRevD.86.123006. arXiv: 1212.2968 [astro-ph.CO].

Yamazaki, Dai G. et al. (2008). "Effects of a Primordial Magnetic Field on Low and High Multipoles of the CMB". In: *Phys. Rev. D* 77, p. 043005. DOI: 10.1103/PhysRevD.77.043005. arXiv: 0801.2572 [astro-ph].

Yamazaki, Dai G. et al. (2012). "The Search for a Primordial Magnetic Field". In: *Phys. Rept.* 517, pp. 141–167. DOI: 10.1016/j.physrep.2012.02.005. arXiv: 1204.3669 [astro-ph.CO].

Yokoi, K., S. Neo, and K. Nomoto (1979). "Electron captures in nuclear statistical equilibrium." In: *Astron. Astrophys.* 77.1-2, pp. 210–213.

Zaqarashvili, T. V., M. L. Khodachenko, and H. O. Rucker (2011). "Magnetohydrodynamic waves in solar partially ionized plasmas: two-fluid approach". In: *Astron. Astrophys.* 529, A82, A82. DOI: 10.1051/0004-6361/201016326. arXiv: 1101.3913 [astro-ph.SR].